

# Sheffield Hallam University

*[57]Fe Mossbauer studies of surface interactions in a PVD process.*

DAVIDSON, John L.

Available from the Sheffield Hallam University Research Archive (SHURA) at:

<http://shura.shu.ac.uk/19536/>

## A Sheffield Hallam University thesis

This thesis is protected by copyright which belongs to the author.

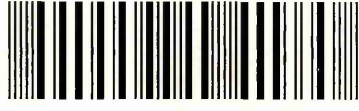
The content must not be changed in any way or sold commercially in any format or medium without the formal permission of the author.

When referring to this work, full bibliographic details including the author, title, awarding institution and date of the thesis must be given.

Please visit <http://shura.shu.ac.uk/19536/> and <http://shura.shu.ac.uk/information.html> for further details about copyright and re-use permissions.

CITY CAMPUS POND STREET  
SHEFFIELD S1 1WB

101 546 714 8



372558

**REFERENCE**

ProQuest Number: 10694417

All rights reserved

INFORMATION TO ALL USERS

The quality of this reproduction is dependent upon the quality of the copy submitted.

In the unlikely event that the author did not send a complete manuscript and there are missing pages, these will be noted. Also, if material had to be removed, a note will indicate the deletion.



ProQuest 10694417

Published by ProQuest LLC (2017). Copyright of the Dissertation is held by the Author.

All rights reserved.

This work is protected against unauthorized copying under Title 17, United States Code  
Microform Edition © ProQuest LLC.

ProQuest LLC.  
789 East Eisenhower Parkway  
P.O. Box 1346  
Ann Arbor, MI 48106 – 1346

# **$^{57}\text{Fe}$ Mössbauer Studies of Surface Interactions in a PVD Process**

John Lee Davidson

A thesis submitted in partial fulfilment of the requirements of Sheffield Hallam University for the degree of Doctor of Philosophy

September 1997

Sponsoring Establishment: Sheffield Hallam University



# **$^{57}\text{Fe}$ Mössbauer Studies of Surface Interactions in a PVD Process**

by John Lee Davidson submitted for the degree of Doctor of Philosophy

A critical stage of the combined steered arc and unbalanced magnetron process is the metal ion pre-treatment which improves the adhesion of the TiN coating. In this study, Conversion Electron Mössbauer Spectroscopy (CEMS) has been used to investigate surface interactions in a commercial Arc Bond Sputtering (ABS<sup>TM</sup>) coating system.

A novel application of the Liljequist theory of CEMS has been used to determine ion etch rates for deposited natural iron on stainless steel substrates, for various Ti ion pre-treatment processes. The approach has estimated an etch rate of 60 nm min.<sup>-1</sup> for samples positioned without substrate rotation at a cathode-sample distance of 250 mm. This has been calculated to correspond to a bias current density of 6.68 Amps m<sup>-2</sup>. Similar experiments involving modes of rotation yield an average etch rate of approximately 40 nm min.<sup>-1</sup>

To detect small quantities of iron containing phases formed during a pre-treatment process it has been necessary to enrich substrates with the Mössbauer isotope,  $^{57}\text{Fe}$  to achieve greater surface sensitivity. The enrichment used the technique of the deposition of an estimated 25 nm of  $^{57}\text{Fe}$  on polished mild steel substrates followed by annealing to generate an  $^{57}\text{Fe}$  diffusion profile into the near surface region. A diffusion model has been used to predict the  $^{57}\text{Fe}$  depth profile due to the adopted annealing process parameters. Verification of the estimated thickness of the deposited  $^{57}\text{Fe}$  overlayer and the diffusion profile has been provided by SIMS and SNMS.

Using the  $^{57}\text{Fe}$  enriched mild steel samples, CEMS has investigated the formation of iron-titanium phases after a typical industrial ten minute pre-treatment process using substrate rotation, at a substrate bias voltage of -1200 V. Significant phase formation of both crystalline FeTi and amorphous  $\text{Fe}_x\text{Ti}_{1-x}$  have been identified. The formation of the crystalline phase has been confirmed by XRD. Using a model of the  $^{57}\text{Fe}$  isomer shift dependence of  $x$ , in amorphous alloys yielded  $x=0.31 \pm 0.08$  for  $\text{Fe}_x\text{Ti}_{1-x}$ . Further experiments using an estimated 25 nm of  $^{57}\text{Fe}$  deposited on mild steel without annealing, showed the presence of magnetite and a small quantity of crystalline FeTi for a 25 s pre-treatment process. After a 300 s pre-treatment time the oxide layer is removed and significant quantities of both crystalline and amorphous FeTi are formed. CEMS has also showed increased  $^{57}\text{Fe}$  removal at a  $6 \times 10^{-5}$  mbar Ar operating pressure within the coating chamber compared with a pre-treatment performed at a higher Ar pressure of  $3 \times 10^{-3}$  mbar, showing the greater effect of the Ti ion etching under these conditions. During the experiments performed at different Ar pressures, CEMS also identified iron carbonitride phases. Similar phases have also been identified in the early growth stages of a compound layer in a process performed using a modified Balzers coating system.

CEMS has proved to be a powerful technique, enabling the investigation of surface interaction phenomena occurring in the near surface region of  $^{57}\text{Fe}$  enriched substrates treated by Physical Vapour Deposition (PVD) processes. The information provided by the technique makes it strategically important in the future research of interface regions generated by PVD processes.

# TABLE OF CONTENTS

## CHAPTER 1

### INTRODUCTION

<b>1.1 Background</b> .....	1
<b>1.2 Substrate Surface Pre-treatment</b> .....	4
<b>1.3 Studies of PVD Coatings</b> .....	5
1.3.1 Arc Discharge	
1.3.2 Plasma Sputtering	
1.3.3 Plasma Nitriding	
<b>1.4 Interface Studies of PVD Coatings</b> .....	9
<b>References</b> .....	14

## CHAPTER 2

### LITERATURE REVIEW

<b>2.1 Evaporative Techniques</b> .....	15
2.1.1 Resistive Heating Evaporation	
2.1.2 Inductive Heating Evaporation	
2.1.3 Electron Beam Evaporation	
2.1.4 Cathodic Arc Evaporation	
2.1.5 Random Arc Evaporation	
2.1.6 Macroparticles	
2.1.7 Steered Arc	
<b>2.2 Sputtering Techniques</b> .....	24
2.2.1 Ion Beam Sputtering	
2.2.2 Diode Sputtering using a Glow Discharge	
2.2.3 Triode Sputtering	
2.2.4 Glow Discharge Plasma	
2.2.5 Magnetron Sputtering	
2.2.6 Unbalanced Magnetron	
2.2.7 Magnetron Magnetic Arrangements	
<b>2.3 Arc Bond Sputtering (ABS<sup>TM</sup>)</b> .....	33
<b>2.4 Plasma and Surface Interactions</b> .....	35
2.4.1 Nucleation and Coating Growth	
2.4.2 Sputter Etching	
2.4.3 Structure Zone Models	
2.4.4 Interfaces	
2.4.5 Residual Stress	
<b>2.5 The Fe-Ti System</b> .....	44
2.5.1 The Fe-Ti Phase Diagram	
2.5.2 Identification and Analysis of Fe-Ti phases	
2.5.3 Single Crystals of FeTi	
2.5.4 Predicted Isomer Shift in Amorphous Fe based Alloys	
2.5.5 Amorphous Alloy Fe <sub>1-x</sub> Ti <sub>x</sub>	
<b>References</b> .....	61

**CHAPTER 3**  
**THE MÖSSBAUER EFFECT AND**  
**MÖSSBAUER SPECTROSCOPY**

<b>3.1 Theoretical Linewidth of the emitted 14.4 keV <math>\gamma</math>-ray</b> .....	64
<b>3.2 Mechanism of the Mössbauer Effect</b> .....	66
<b>3.3 The Quantised Lattice</b> .....	68
<b>3.4 Observation of the Mössbauer Effect</b> .....	69
<b>3.5 Hyperfine Interactions</b> .....	70
3.5.1 Isomer Shift	
3.5.2 Nuclear Quadrupole Interaction	
3.5.3 Magnetic Hyperfine Interaction	
<b>3.6 Backscatter Mössbauer Spectroscopy</b> .....	80
<b>3.7 Principles of CEMS</b> .....	81
3.7.1 Overview	
3.7.2 Electron Re-emission and Transport in $^{57}\text{Fe}$ CEMS	
<b>3.8 Applications of CEMS</b> .....	85
3.8.1 Characterization of the Surface Properties of Oxidised Steels	
3.8.2 Corrosion Studies of Steels in Aggressive Atmospheres	
3.8.3 Ion Implantation Studies	
3.8.4 Analysis of Hardened Steel Surfaces	
3.8.5 Surface Stress and Orientation of the Magnetic Field of Iron and Steel Substrates	
3.8.6 Intermetallic Compounds Formed at the Interface of Metal Coated Substrates	
<b>3.9 Mössbauer Spectroscopy Instrumentation</b> .....	94
3.9.1 Operation of the Spectrometer	
3.9.2 Electron Detection	
<b>3.10 Computer Fitting of Mössbauer Spectra</b> .....	100
3.10.1 Data Folding	
3.10.2 Data Fitting	
<b>3.11 Spectrometer Calibration</b> .....	102
<b>References</b> .....	105

**CHAPTER 4**  
**EXPERIMENTAL TECHNIQUE**

<b>4.1 Sample Preparation</b> .....	107
4.1.1 Evaporation	
4.1.2 Annealing Conditions	
<b>4.2 Diffusion Model</b> .....	110
4.2.1 Lattice Self Diffusion in Iron	
<b>4.3 ABS<sup>TM</sup> Experimental Arrangement</b> .....	114
<b>4.4 Complementary Techniques</b> .....	117
4.4.1 Secondary Electron Microscopy	
4.4.2 Glow Discharge Optical Electron Microscopy	
4.4.3 Secondary Ion Mass Spectrometry	
<b>References</b> .....	123

<b>CHAPTER 5</b>	
<b>PRELIMINARY MÖSSBAUER STUDIES AND SURFACE INTERACTIONS IN A PVD PROCESS</b>	
5.1 Surface Sensitivity of CEMS .....	124
5.2 Determination of Ion Etch Rates in the ABS <sup>TM</sup> Process.....	128
5.3 <sup>57</sup> Fe Enrichment.....	139
5.3.1 Ion Implantation	
5.3.2 Evaporation followed by Diffusion	
References.....	154
<b>CHAPTER 6</b>	
<b>INTERFACES IN PVD PROCESSES</b>	
6.1 Interfaces Generated by Ti Ions in a Steered Arc Discharge .....	155
6.1.1 Calculation of x in the Fe <sub>x</sub> Ti <sub>1-x</sub> Alloy	
6.1.2 Further Experiments using a Steered Arc Discharge	
6.2 Comparison with the ABS <sup>TM</sup> Process.....	168
References.....	172
<b>CHAPTER 7</b>	
<b>CONCLUSIONS AND FUTURE WORK.....</b>	<b>173</b>
References.....	177
<b>ACKNOWLEDGEMENTS .....</b>	<b>178</b>
<b>COURSES AND CONFERENCES ATTENDED.....</b>	<b>179</b>
<b>ANNEXE</b>	
<b>PRODUCTION OF SINGLE PHASE FeTi.....</b>	<b>180</b>
References.....	186
<b>APPENDIX 1</b>	
<b>CEMSN2 PROGRAM .....</b>	<b>187</b>
<b>APPENDIX 2</b>	
<b>CEMSN2 RESULTS .....</b>	<b>198</b>
<b>APPENDIX 3</b>	
<b>FORTRAN PROGRAM USED FOR SOLVING THE DIFFUSION PROBLEM .....</b>	<b>201</b>
<b>APPENDIX 4</b>	
<b>PUBLICATIONS .....</b>	<b>202</b>

# CHAPTER 1

## INTRODUCTION

### 1.1 Background

In recent years a variety of deposition methods have found widespread application in the deposition of hard ceramic coatings. These coatings are deposited for industrial protective or decorative purposes and are typically between 1 to 5  $\mu\text{m}$  in thickness. Typical coatings are binary compounds composed of a transition or refractory metal nitride or carbide e.g. TiC, TiN, CrN or ternary compounds with either two non-metals e.g. TiCN, TiBN or two metals eg TiAlN, TiZrN. The coatings exhibit extreme properties such as high melting point, high hardness and high chemical inertness [1] and are used in applications where corrosion and/or wear resistance are important. Typical applications include increasing the lifetime of high speed steel (HSS) drills, end mills etc. Other properties include smooth surface finish with a low coefficient of friction, making the coatings ideal for extrusion dies and punches. Since a range of attractive colours can be produced, the coatings have been used in decorative applications, in particular as an alternative to the more expensive and less hard-wearing coatings e.g. “gold” coloured watch cases and spectacle frames.

A number of deposition technologies are currently being used commercially to produce a variety of coatings for a particular application. These include electroplating, laser ablation and plasma spraying. However, one of the main technologies employed for enhancing the surface properties of a coated component is physical vapour deposition (PVD). The term “ion plating” refers to coating deposition by inert or reactive means with vacuum coating sources in a highly ionized atmosphere.

During a PVD process at least one of the deposited species is atomised from a solid target material within the coating chamber under vacuum conditions. This process may be plasma assisted (PAPVD) and is characterised by the temperature during deposition

being less than 500 °C. Thus, allowing the deposition on to a wide range of temperature sensitive substrate materials.

Atomisation of the depositing species in a PVD process can be achieved by two methods. The first method, evaporative PVD is a process in which the coating species is heated by resistive, inductive, electron beam or arc techniques until it evaporates into the vapour phase. The second method, sputter PVD involves bombarding a solid target with high kinetic energy ions and neutrals such that a momentum transfer occurs which removes or sputters atoms from the surface of the source material.. In both methods, the atomised species are mixed with a reactive gas for ceramic deposition.

All of the various PVD techniques differ essentially by the atomisation method employed. The most recent methods have undergone extensive development and are the least well understood. One of the most recent developments is Arc Bond Sputtering (ABS™). This technique combines the excellent adhesion associated with arc technology and the versatility of material selection and smoothness of coatings offered by using a magnetron source. Such a “hybrid” deposition process utilises a steered arc to etch the substrate prior to the coating, causing implantation of the deposited species, followed by the deposition of a dense coating using an unbalanced magnetron. The work reported in this thesis uses conversion electron <sup>57</sup>Fe Mössbauer spectroscopy (CEMS) to gain a greater understanding of the ABS™ process. The process joins the two branches of the PVD “family tree” as shown in fig 1.1 and allows for significant control over the coating-substrate interface and the associated growth characteristics of the deposited coating.

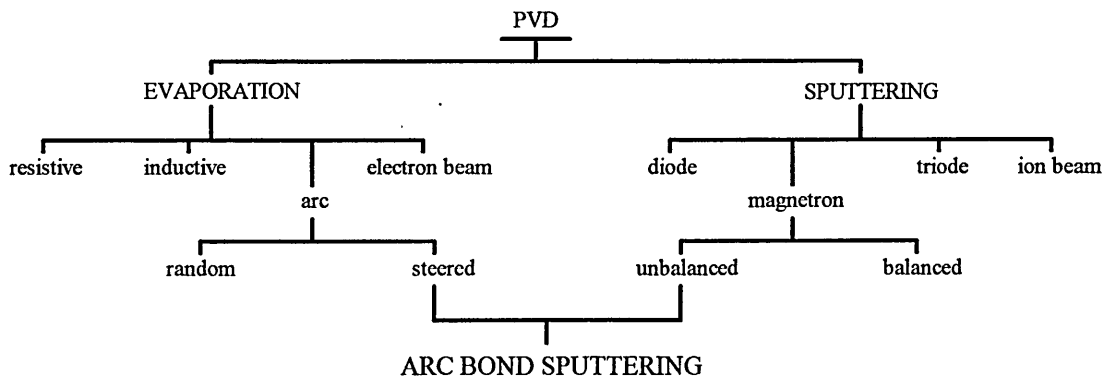


Fig 1.1 The PVD family tree.

The growth of hard coatings and their properties have been discussed by many authors [2-6]. The nature of film growth depends on both macro- and micro-scopic parameters. These include vapour source parameters, plasma and transport parameters, particle impact parameters and substrate parameters. Parameters of a microscopic nature include ion-neutral flux ratios and energies at the substrate surface, whilst examples of macroscopic parameters are vapour source power, total pressure and source substrate distances. Workers have usually reported the dependence of macroscopic properties of hard coatings on bias voltage, total pressure and substrate temperature [7, 8].

The classification of various types of microstructures associated with deposited thin films have been shown by structure zone models (SZMs) . These models [9, 10] show the dependence of formed microstructures on substrate temperature and total pressure within the coating chamber. They indicate that the microstructure is essentially influenced by the condensation conditions during film deposition. It is also noted that smooth dense coatings consist of columnar single crystals growing from the interface up to the film surface and that this is only obtained when the condensation temperature is within a sufficiently high range. The conclusions of these SZMs have been confirmed by many X-TEM studies of hard coatings.

The performance of a hard coating e.g. TiN can be significantly dependent on the process parameters used within the coating system [11, 12]. However, the literature to date, suggests that there is still a lack of fundamental knowledge, clarifying how the coating parameters influence the changes or formation of the microstructure of hard coatings. Hence microstructural studies of coatings are of significant importance because they provide an understanding of any relationships between the performance of a coating and the process parameters.

One of the most significant prerequisites for a high performance coating is good adhesion at the interface between the coating and the substrate material. The strength of this adhesion is dependent on the physical and chemical interactions between the coating and the substrate material, and in particular the microstructure of the interface

region. Poor adhesion has been attributed to poor interfacial contact, low fracture toughness, high compressive stresses within the coating and a low degree of chemical bonding. Therefore, the interface structure plays a significant role in determining the adhesive strength of a coating-substrate system. Hence it is of great importance to improve the understanding of the correlation between the interface structure and its related substrate adhesion.

## **1.2 Substrate Surface Pre-treatment**

Several workers [13-15] have reported that a thin layer of Ti at the interface results in adhesion improvement of TiN coatings deposited by ion plating. It has been suggested that this Ti intermediate layer behaves as a graded interface between the coating and the steel substrate. However, the effects of this Ti interlayer on the coating adhesion is still unclear, primarily due to a lack of extensive microstructural studies of the interface region.

The pretreatment process usually consists of chemical cleaning followed by etching and ion bombardment in the deposition chamber. These processes influence the performance of the coating, mainly adhesion and microstructural properties. During ion cleaning the significant processes at the substrate depend heavily on the type and energy of the ions and the substrate material. Differences exist between sputtering with gas and metallic ions. Essentially, the substrates heat up much faster during a metal ion etch due to the multiply charged ions compared with an argon ion etch.

During a typical etch process adsorbed impurities are removed at very low energies (<10 eV) [16] and at higher energies (10 - 30 eV) surface sputtering begins. During sputtering with gas ions, the main processes involve desorption, sputtering, implantation, particle trapping and diffusion. Sputtering with metallic ions e.g. Ti involves metal condensation, sputtering, implantation mixing and diffusion. Sputtering using Ti ions from cathodic arc processes results in a reduction in contamination at the

surface and an altered interface layer consisting of a mixture of iron and titanium containing phases [17]. The main processes involved in the formation of such interfaces are diffusion and ion mixing. These processes are highly dependent on substrate material and the associated depth profiles for various different etching ions and substrate materials have been measured using glow discharge optical emission spectroscopy (GDOES).

### 1.3 Studies of PVD Coatings

#### 1.3.1 Arc discharge

A number of studies have been reported which analyse the performance of PVD coatings. Until recently, the majority of the available results and data have been obtained from studies on the macroscopic scale. However any study of interface problems of this type, should be concerned with the microscopic and atomic scales. This requires investigations using modern analytical techniques such as transmission electron microscopy (TEM), scanning electron microscopy (SEM) with energy dispersive X-ray analysis (EDX), depth profiling using Auger electron spectroscopy (AES) and conversion electron Mössbauer spectroscopy (CEMS).

Cheng *et al.* [15] has shown that for reactive ion plated TiN coatings deposited at a temperature of 500 °C without a Ti interlayer, large compressive stresses accumulate in the coating. This was seen visually when the thickness of the steel substrate was reduced by grinding to around 200 µm, it assumed a convex dome shape due to the compressive stresses. This study also shows a strong adhesion between a TiN coating with a Ti interlayer for an AISI M50 substrate deposited at a temperature of 500 °C. AES identified that an interlayer had fully transformed into a fcc crystal structure TiC phase and no trace of  $\alpha$ -Ti was detected. It was also found that the interface between substrate and interlayer was sharp and straight, unlike the interlayer-TiN interface which had an irregular, distorted shape. It is suggested that this irregular shape of the

interlayer-TiN interface and the high interface contact between the substrate interlayer is responsible for the associated high adhesive strength. They conclude, like other workers [13, 14], that the Ti interlayer dramatically reduces the internal stress associated with the coating. It is also concluded for a coating deposited at a substrate temperature of 500 °C that carbon diffusion occurs from the steel matrix to the interface region. The diffusing carbon atoms react with the active Ti atoms at the interlayer forming TiC. This diffusion process also has the benefit of closing any vacancy gap between the substrate-interlayer, thereby increasing the interface contact and improving adhesion.

Román *et al.* [18] has investigated by AES the importance of oxygen at the interface of TiN and TiCN coatings deposited on M2 HSS substrates. It is reported that for TiN coated HSS at 720 K substrate temperature, a low level of oxygen is present at the interface and for a TiN coated HSS at 520 K, a high level of oxygen is reported at the interface. The greatest adhesion of the two samples was found to be for the coating deposited at the higher temperature. They also report that for TiCN coatings deposited at 725 K, oxygen is not present in significant quantities at the interface and that the adhesion is greater for TiCN coatings compared with TiN coatings. This non-development of the oxygen phase is explained by the cracking of the C<sub>2</sub>H<sub>2</sub> molecule within the plasma discharge producing hydrogen ions which react at the interface to produce H<sub>2</sub>O. This is later desorbed from the substrates as the temperature falls below 400 K.

A study by Navinsék *et al.* [14] has investigated the microstructure of TiN coatings and grain size distributions from TEM examinations. It is reported that the nature of any defects is strongly dependent upon the type of coating process and that a high quality coating should contain a typical grain size of 100 nm. This study estimates that the interface width is below 100 nm from AES analysis. It is noted from this study that TiN can behave as a diffusion barrier. The results indicate that for a TiN coating with a Ti interlayer a typical grain structure significantly suppresses the diffusion of metallic elements. However the diffusion of carbon is not hindered and so should lead to the formation of TiC and Ti(C,N) at the interface.

### 1.3.2 Plasma Sputtering

The main disadvantage of coatings produced by arc discharge methods is the occurrence of macroparticles. The formation of macroparticles significantly degrades the performance of coated components of a tribological nature such as bearings and high speed dry cutting. However studies have shown [19] that macroparticles do not occur for coatings produced by magnetron sputtering methods.

Initial results by Berg *et al.* [20] report that TiN coatings produced by magnetron sputtering under various oxygen residual gas pressures, with and without sputter cleaning with argon, show differences in mechanical properties. In particular, adhesive strength for TiN coatings investigated by scratch tests indicate better adhesion for increasing oxygen impurity gas content. However no adequate depth profiling of a TiN coating-substrate system is given and high levels of oxygen impurity gas content within the chamber do not necessarily imply a high oxygen content present at the interface region.

A study by Håkansson *et al.* [19] has investigated the film morphology of magnetron sputtered coatings by SEM examinations of various coated substrates. No macroparticle droplets were observed for TiN coatings deposited on HSS and stainless steel substrates. Cross-sectional TEM (XTEM) examinations revealed a substrate-film interfacial layer about 10 nm in thickness. The sputtered TiN coatings showed inter columnar porosity as reported by other workers [14]. It was also observed that a graded interface existed from a stainless steel substrate which extended about 80 nm into the film. This was found to be mostly comprised of iron, nickel, chromium and a small quantity of oxide residue was also detected. XRD analysis of the deposited coatings indicated a preferential (200) film growth orientation and that the TiN crystal structure was fcc.

Chen *et al.* [13] has studied the hardness and adhesive strength in Ti interlayer modified coatings deposited on stainless steel substrates. It is reported that films which have a random polycrystalline structure exhibit better adhesion than films with a strong preferred orientation (111). It is also reported from AES analysis that TiC and TiO

phases are present within the interface region. It is concluded that the structural orientation of a deposited coating plays a major role in film adhesion.

Grönig *et al.* [21] has reported an interface analysis of plasma deposited TiN coatings on stainless steel at 600 °C substrate temperatures. The chemical composition at the interface was investigated using XPS. The results indicate that at these deposition temperatures, chromium diffuses into the coating where nitriding occurs. The study concludes that the composition of the elements at the interface is strongly temperature dependent due to metal segregation from the bulk material to the interface and in some cases into the coating.

### 1.3.3 Plasma Nitriding

During the plasma nitriding process positive ions in the treatment gas accelerate towards the negatively biased component. The positive ions hit the surface of the component with high kinetic energy giving rise to heating of the component and sputtering of the surface. The plasma nitriding of titanium which causes the formation of TiN and the diffusion of nitrogen in to the substrate has been described by Grederic [22].

Quaeyhaegens *et al.* [23] has used AES to investigate the interface of a TiN coating on plasma nitrided tool steel. The deposited TiN coatings were estimated to be 1.0 µm in thickness over a titanium intermediate layer of about 0.2 µm in thickness. It was noted that by considering the Ti/N ratio over the interface region, nitrogen diffusion from the TiN layer towards the titanium interlayer had taken place. It is reported that it is not possible to estimate the thickness of the interface region from AES results since the sputter rate is unknown for the interface material and because of an interface broadening effect. This effect is due to non-uniform sputter removal which restricts the depth resolution of AES and can result in a broadening of the interface to about 150 nm.

D'Haen *et al.* [24] has investigated the interface of various TiN coatings on plasma nitrified stainless steel substrates. Bad adhesion is reported for the deposition of a TiN layer with a titanium interlayer. However, the thickness of this interlayer has not been estimated; an interlayer either too thick or too thin may result in poor adhesion. Phase composition studied by XRD indicates nitrogen diffusion within the TiN-Ti-substrate system. Hence an interlayer which is too thick may behave as a diffusion barrier thus preventing the formation of the gradual interfacial region. It is concluded that the adhesion is determined by the interface structure and the thickness of the interlayer itself.

#### 1.4 Interface Studies of PVD Coatings

Mössbauer spectroscopy has been shown to be sensitive regarding the detection and identification of phases within the Ti-Fe system. Phase identification for Ti-Fe binary systems have been studied by transmission Mössbauer spectroscopy by several workers [25-27]. In these studies room temperature Mössbauer parameters are quoted which enable phases to be identified and analysed by conversion electron Mössbauer spectroscopy (CEMS).

The most comprehensive CEMS characterisation of Fe-Ti and Fe-TiN systems prepared by PVD has been carried out by Hanzel *et al.* [28]. This study investigated the microstructure of the interface regarding the dependence of PVD parameters. The samples used were low carbon steel with a 25 nm  $^{57}\text{Fe}$  overlayer formed by evaporation in a vacuum at  $5 \times 10^{-7}$  mbar. Layers of Ti and TiN, both 25 nm in thickness, were sputtered deposited on to the  $^{57}\text{Fe}$  enriched samples at various substrate temperatures and bias voltages. CEMS identified an amorphous  $\text{Fe}_x\text{Ti}_{1-x}$  phase at the interface of the Fe-Ti system. The relative intensity of this phase was found to increase from 2.4 % to 6.4 % as the substrate bias voltage was increased from -100 V to -450 V. This can be explained by considering the behaviour of the accelerating Ti ions. For higher substrate bias, the more energetic Ti ions reach the substrate surface during the deposition process. Iron carbides and carbonitrides are also reported to be present within the

interface region. It is noted that the hyperfine parameters for some iron carbides, nitrides and carbonitrides are similar to each other. However, the presence of carbon within the interface region was supported by AES analysis. It is reported that for the Fe-TiN interfaces more iron carbide and/or nitride phases are present compared with the Fe-Ti system. In both systems oxides are present at the interface. The relative intensity of the oxides is dependent upon the cleaning process before deposition. Finally, during annealing of the samples at 773 K for 1 hr. the amorphous  $\text{Fe}_x\text{Ti}_{1-x}$  and TiN phases partially decompose. An earlier study by the same authors [29] proposed that during such annealing processes, nitrogen penetration occurs deeper into the substrate, while titanium oxidation occurs. Local reactions at the interface may take place such as:



This may explain the degradation of TiN coated cutting tools after prolonged use at excessive temperatures without sufficient cooling.

Similar interfacial local reactions involving iron oxides have been proposed by Helmersson *et al.* [30]. This study found by AES changes in the oxide layer at the interface for TiN layers deposited on HSS substrates by dc magnetron sputtering for deposition temperatures in the range 100-600 °C. On the basis of AES analysis, the oxides were predominantly  $\text{Fe}_2\text{O}_3$  and  $\text{Fe}_3\text{O}_4$  for low deposition temperatures, whilst at higher temperatures the oxide FeO predominates. The formation of FeO is due to Cr diffusion from the HSS substrate into the interface region as shown in fig 1.2.

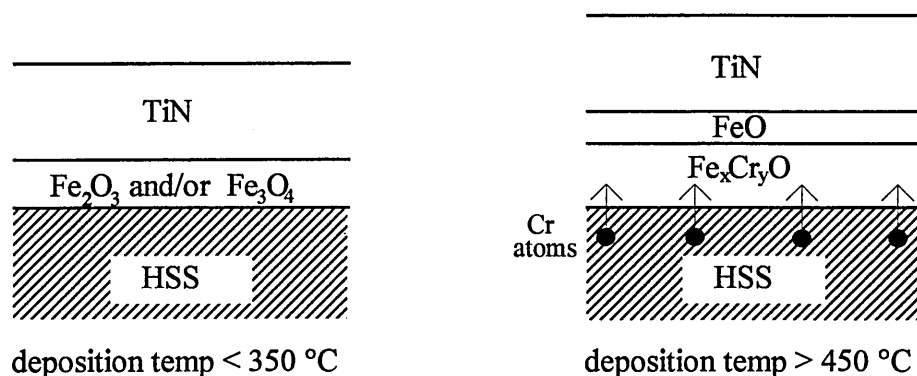


Fig 1.2 Schematic representation of a high speed steel coated with TiN without sputter etch cleaning prior to deposition.

Samples produced at the higher temperatures were found to exhibit greater adhesive strength. Their study suggests that the improved adhesion was due to the increased structural matching between TiN and FeO. Both crystal structures of FeO and TiN are NaCl type and the lattice mismatch between the two compounds is only 1.4 %. The study showed that sputter etching the samples, prior to deposition, removes virtually all surface oxides and increases the substrate-coating adhesion by a factor of 2. A further increase in the adhesion was observed by depositing a thin Ti interfacial layer. This layer reacts with any remaining oxygen and at 400 °C, carbon diffusion occurs and forms TiC. The increases in adhesion resulting from the formation of either TiC or FeO was discussed in terms of interfacial energies. In the case of FeO, low interfacial energy explained the improved adhesion by reducing the compressive stress between the coating and substrate.

A similar CEMS study of thin films of TiN with a Ti interlayer prepared by a reactive ion plated PVD method has been carried out by Carbuccichio *et al.* [31]. The samples studied were <sup>57</sup>Fe enriched Armco iron which were subjected to depositions at 500 °C after ion etching with argon at 0.1 Torr. They found that the Mössbauer spectrum associated with the samples after the deposition process could be interpreted as a superimposition of several sub spectra. Namely, a 6 line spectrum due to  $\alpha$ -Fe, a quadrupole doublet attributed to TiFe<sub>2</sub> intermetallic compound, a central singlet due to  $\alpha$ -Ti(Fe) solid solution and a ferromagnetic phase described by 2 superimposed contributions due to Fe atoms in  $\alpha$ -Fe(Ti) solid solution. Comparison between spectra associated with Fe-Ti-TiN systems for different Ti deposition times suggest that both TiFe<sub>2</sub> and  $\alpha$ -Ti(Fe) phases are located at the substrate-coating interface. Also for decreasing amounts of deposited Ti and therefore decreasing Ti interlayer thickness, the sub spectra contributions from all phases containing Ti decreases. This indicates that Ti alloying of the iron substrate is a result of the pre-deposited Ti. It was also discovered that a shot-peening treatment of the substrate before deposition, leads to higher amounts of  $\alpha$ -Fe(Ti) and consequently improved adhesion. They conclude that the increased adhesive strength obtained by pre-deposition of Ti is due to the formation of a Fe-Fe(Ti)-Ti(Fe)-TiN sequence and the formation of Fe-Ti inter metallic compounds.

The presence of Fe-Ti intermetallic compounds has also been observed by Young *et al.* [32] for Ti-B-N films deposited by using N bombardment on an electron beam ion plated Ti-B film. In this study, Auger electron spectroscopy depth profiling indicated N and Ti penetration into the substrate, resulting in a wide interfacial diffusion zone, estimated to be  $150 \pm 30$  nm thick. XTEM observations showed the interface to have a dense and fine nanocrystalline structure which by microdiffraction was identified to contain the phases FeTi, Fe<sub>2</sub>Ti and Ti<sub>2</sub>N. The results indicated that the method using N ions to bombard the film produces the film-substrate interfacial diffusion zone by stimulating the interfacial chemical reaction.

Another study by Navinsék *et al.* [14] has investigated the interaction between Ti and Fe atoms by CEMS. The substrates were low carbon steel, cleaned and enriched with a <sup>57</sup>Fe overlayer measuring 28 nm in thickness. The substrates were further coated with a 25 nm layer of pure Ti or TiN using an arc discharge process at 50 °C. Phases similar to that reported in reference 32 were detected. It was also discovered that for substrate surface roughness extending greater than  $R_a = 0.05$  µm up to a few microns, increased the chance of poorer adhesion.

A study of the literature suggests that the performance of a PVD hard coating is significantly dependent on the process parameters used within the coating chamber. It also reveals that a deeper understanding is required in the following areas:-

- (i) The formation of the interface layers and the role of ion cleaning process before film deposition.
- (ii) The effect of plasma processes on film growth.

However, there exists an agreement within the literature regarding the following areas:-

- (i) Chemical and physical interactions between the coating and the substrate play a significant role in determining the adhesive strength of the coating.
- (ii) Reduced compressive stresses within the coating lead to improved adhesion.
- (iii) The growth of carbides within the interfacial region and the interaction between metallic and gaseous atoms at the interface significantly affect the performance of the coating.

Finally, the interface studies which have used CEMS to investigate the Fe-Ti interaction have proved particularly sensitive in detecting amorphous and intermetallic phases which remain undetected by complementary techniques.

It has become clear, by studying the recent literature, that CEMS is a powerful tool for investigating the interface between a PVD hard coating and a steel substrate is CEMS. This study seeks to gain greater understanding of the role of the interface layer on coating-substrate adhesion by identification of the constituent phases within the interface region using CEMS and other complementary techniques. A major part of the project is concerned with improving the surface sensitivity of the backscatter Mössbauer technique. From the literature it can be seen that due to the small physical thickness of the interface layer very high sensitivity is required to identify the phases present. Such a sensitivity can be achieved using substrate material enriched in the Mössbauer sensitive isotope  $^{57}\text{Fe}$ . This enrichment can be achieved by either an ion implantation process or by diffusion. By using enriched samples it has been possible to detect iron containing phases during various Ti ion pretreatment processes used within the ABS<sup>TM</sup> method.

## References

- [1] R. F. Bunsham, *Phys. and Chem. of Protective Coatings* **149** (1986) 131.
- [2] H. Holleck, *J. Vac. Sci. Technol. A* **4** (1986) 2661.
- [3] O. Knotek, F. Jungblut and R. Breidenbach, *Vacuum* **41** (1991) 2184.
- [4] C. Deshpandey and R. F. Bunshah, *Thin Solid Films* **163** (1988) 131.
- [5] B. M. Kramer and P. K. Judd, *J. Vac. Sci. Technol. A* **3** (1985) 2439.
- [6] H. W. Holleck, *Vacuum* **41** (1991) 2220.
- [7] J. A. Thornton, *J. Vac. Sci. Technol. A* **4** (1986) 3059.
- [8] C. Fountzoulas and W. B. Nowak, *J. Vac. Sci. Technol. A* **9** (1991) 2128.
- [9] J. A. Thornton, *J. Vac. Sci. Technol.* **11** (1974) 666.
- [10] R. Messier, A. P. Giri and R. A. Roy, *J. Vac. Sci. Technol. A* **2** (1984) 500.
- [11] D. S. Rickerby and P. J. Burnett, *Thin Solid Films* **157** (1988) 195.
- [12] J. E. Sundgren, *Thin Solid Films* **128** (1985) 21.
- [13] Y. I. Chen and J. G. Duh, *Mater. Chem. Phys.* **32** (1992) 352.
- [14] B. Navinsék, S. Novak and A. Zalar, *Mater. Sci. Eng. A* **139** (1991) 249.
- [15] C. C. Cheng, A. Erdemir and G. R. Fenske, *Surf. Coat. Technol.* **39/40** (1989) 365.
- [16] J. Vyskocil and J. Musil, *J. Vac. Sci. Technol. A* **10(4)** (1992) 1740.
- [17] S. Kadlec, J. Musil and J. Vyskocil, *Surf. Coat. Technol.* **54/55** (1992) 287.
- [18] E. Román, J. L. deSegovia, A. Alberdi, J. Calvo and J. Laucirica, *Mater. Sci. Eng. A* **163** (1993) 197.
- [19] G. Håkansson, L. Hultman, J. -E. Sundgren, J. E. Greene and W. -D. Münz, *Surf. Coat. Technol.* **48** (1991) 51.
- [20] S. Berg, S. W. Kim, V. Grajewski and E. Fromm, *Mater. Sci. Eng. A* **139** (1991) 345.
- [21] P. Gröning, S. Novak, L. Schlapbach and H. E. Hinterman, *Appl. Surf. Sci.* **62** (1992) 209.
- [22] T. Gredic, M. Zlatanovic and W. -D. Münz, *Surf. Coat. Technol.* **61** (1993) 338.
- [23] C. Quaeyhaegens, M. Van Stappen, L. M. Stals, F. Bodart, G. Terwagne and R. Vlaeminck, *Surf. Coat. Technol.* **54/55** (1992) 279.
- [24] J. D'Haen, C. Quaeyhagens, G. Knuyt, L. De Schepper, L. M. Stals and M. Van Stappen, *Surf. Coat. Technol.* **60** (1993) 468.
- [25] H. Harada, S. Ishibe, R. Konishi and H. Sasakura, *Jap. J. Appl. Phys.* **24(9)** (1985) 1141.
- [26] M. M. Stupel, B. Z. Weiss and M. Ron, *Acta Metal.* **25** (1977) 667.
- [27] M. M. Stupel, B. Z. Weiss and M. Ron, *J. Appl. Phys.* **47(1)** (1976) 6.
- [28] D. Hanzel, W. Meisel, D. Hanzel, P. Griesbach, B. Navinsek, P. Panjan and P. Gütlich, *J. Vac. Sci. Technol. A* **11(6)** (1993) 3034.
- [29] D. Hanzel, W. Meisel, D. Hanzel and P. Gütlich, *Hyp. Int.* **69** (1991) 807.
- [30] U. Helmersson, B. O. Johansson, J. E. Sundgren, H. T. G. Hentzell and P. Billgren, *J. Vac. Sci. Technol. A* **3(2)** (1985) 308.
- [31] M. Carbucicchio and G. Palombarini, *Hyp. Int.* **57** (1990) 1783.
- [32] Q. Q. Yang, L. H. Zhao, H. Q. Du and L. S. Wen, *Surf. Coat. Technol.* **81** (1996) 287.

## CHAPTER 2

### LITERATURE REVIEW

#### 2.1 Evaporative Techniques

Evaporation is the conversion of a substance into a vapour at high temperatures either from the liquid state or by sublimation from the solid material. By evaporating under vacuum a flux of atomised material, usually a metal, can be used to produce thin films on a substrate. A variety of heating techniques to provide the atomised material have been devised.

##### 2.1.1 Resistive Heating Evaporation

In the resistive heating process [1], the evaporant is held in a crucible or a filament made from a high melting point resistive material such as refractory metal e.g. W, Mo or Ta. The evaporant can be in the form of powder, chips or wire and to prevent reaction between the crucible and the evaporant, the crucible may be coated or made from a metal oxide or nitride e.g.  $\text{Al}_2\text{O}_3$ , BeO, BN with the resistive tungsten wire coiled around the crucible. On the application of a high current in the order of 10's of amps through the resistive wire, heat is liberated by the Joule effect and after melting the material eventually evaporates. A schematic of the process using a filament wire to provide the heating is shown in fig. 2.1.

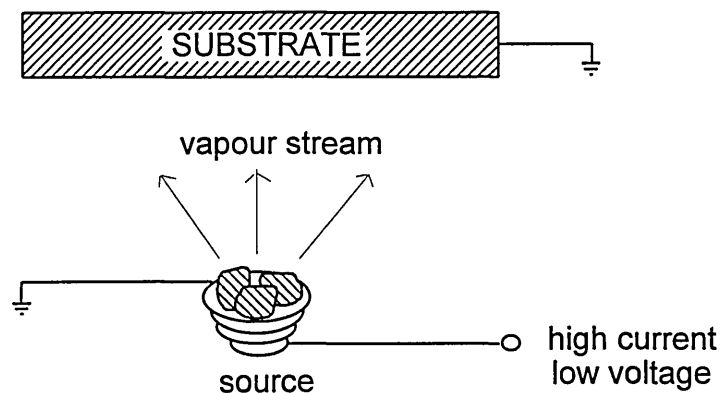


Fig. 2.1 Schematic of resistive heating evaporation.

### 2.1.2 Inductive Heating Evaporation

An alternative method to resistive heating is to use an inductively heated source. Similarly, a refractory metal oxide or nitride crucible is used, but has the advantage that no direct thermal coupling between the evaporant and the heating coil takes place, thus the crucible temperature remains lower. This method employs the application of radio frequency (rf) AC to the coil causing a varying magnetic field and inducing eddy currents in the conducting evaporant material. The current flow in the material causes heating by the Joule effect. Subsequently the metal starts to evaporate and the eddy currents set up circular motions that stir the remaining melt ensuring even evaporation.

### 2.1.3 Electron Beam Evaporation

Another more advanced method, utilises an electron beam evaporation source [2-4]. In this method a range of materials can be evaporated by using an electron beam which causes ionisation of the gas and vapour species so forming a plasma that assists the deposition process. The electron gun consists of a heated tungsten filament, by application of an electric current which causes thermionic emission of electrons. The electron gun is differentially pumped to prevent oxidation and premature failure of the filament. The generated electron beam is magnetically deflected onto the crucible containing the evaporant material. The crucible is typically made of copper and is water cooled so that a molten pool is surrounded by a solid shell of evaporant material. This prevents any evaporant-crucible interaction and ensures only high purity vapour is produced. A schematic of the electron beam evaporation is shown in fig. 2.2.

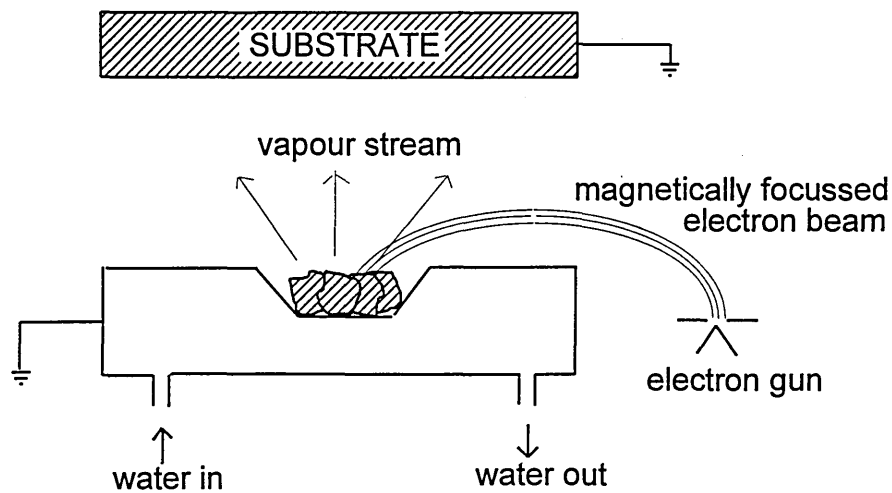


Fig. 2.2 Schematic of electron beam evaporation.

An alternative to this arrangement is to use a plasma electron beam gun involving a hollow cathode in which a glow discharge and a plasma are generated. By inert gas ion bombardment within the hollow cathode electron emission is produced by either secondary and/or thermionic emission and a beam is magnetically or electrostatically extracted. The advantage of this type of gun is that a higher pressure can be used and consequently no separate pumping is required.

All the previously described techniques cause the evaporation of the bulk material by melting in such a way that the liberated vapour originates from a molten pool. This severely restricts the orientation and positioning of the source-substrate geometry and may not be suitable for coating large objects. Also the resistive and inductive heating methods require some form of ionisation enhancement to generate a plasma. However, the cathodic arc evaporation method does not suffer from these limitations.

#### 2.1.4 Cathodic Arc Evaporation

In recent years commercially useful deposition systems utilising cathodic arc evaporation sources have become available. This PVD technique is an ion-plating process that was pioneered and further developed by several workers [5-7], during the early 1970's. In the cathodic arc evaporation process, an electric arc is struck on the

surface of the material to be evaporated which acts as a cathode, while the coating chamber is grounded and acts as the anode. The process of arc triggering can be either by electrical or mechanical means. By mechanical triggering a grounding probe is brought into contact with the cathode during the application of a current pulse. An alternative is to use an electrical means of thermally breaking down a thin, poorly conducting film between the cathode and an ignition wire. Once initiated, the arc is self-sustaining and operates at a high current and low voltage; typically 50 - 400 A and - 20 - -60 V. The arc is supported in the generated flux and can be maintained under high vacuum operating conditions. However, the coating chamber is usually back-filled with either an inert gas used to sustain the arc , or a reactive gas such as nitrogen so that compound films may be deposited. Fig. 2.3 shows a schematic of the cathodic arc evaporation process. Application of the cathodic arc in thin film technology has the following important features:

- (i) a source of a highly ionised dense accelerated metallic plasma
- (ii) the arc can be operated under ultra high vacuum conditions up to atmospheric pressure
- (iii) multi-component cathodes can be formed e.g. TiAl.

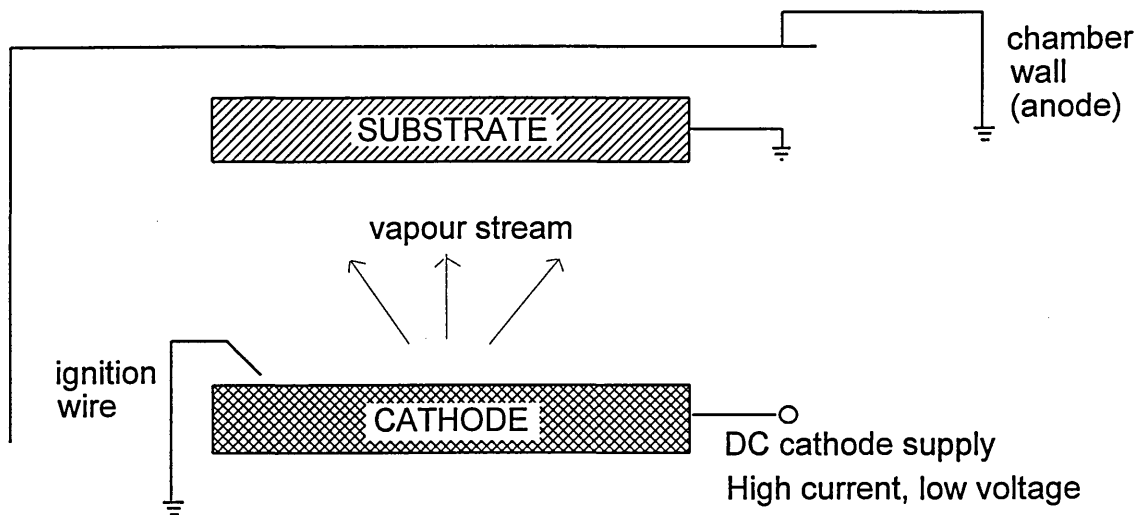


Fig. 2.3 The cathodic arc evaporation process.

### 2.1.5 Random Arc

During the arc discharge process, a cathode spot is focused on the cathode surface moving with a velocity between 1 - 100 m s<sup>-1</sup>. At low currents in the range 10 - 100 A and depending on the cathode material, all the arc current is concentrated on one spot. At higher currents, the spot divides and two or more spots exist simultaneously. The direction of movement of the spots is influenced by any surface defects on the cathode with the arc showing a preference for microscopic protrubences or gullies. Several processes take place at the surface of the cathode. In particular, heating of the material occurs at power densities in the range 10<sup>2</sup> - 10<sup>6</sup> W m<sup>-2</sup>. However if the cathode is cooled adequately, material may pass into the vapour phase without the cathode undergoing bulk melting. Thus the evaporation source may be mounted in any orientation, even inverted.

At the cathode spot a current density of 10<sup>10</sup> A m<sup>-2</sup> exists. This high current density causes significant heating producing a liquid molten pool which is vigorously evaporated and acts as a source of various species. These form a high velocity jet of atomistic material, both highly ionised and neutral, and various sized clusters of atoms and ions. Electrons are also emitted by a combination of thermionic emission mechanisms, and are accelerated away from the cathode surface. The produced electrons collide with the evaporating neutral atoms and cause ionisation, creating a dense plasma above the spot. The plasma expands rapidly, but the electrons move more quickly than the larger atoms, thus leaving behind a positive space charge which retards further electrons and accelerates ions in all directions as shown in fig. 2.4.

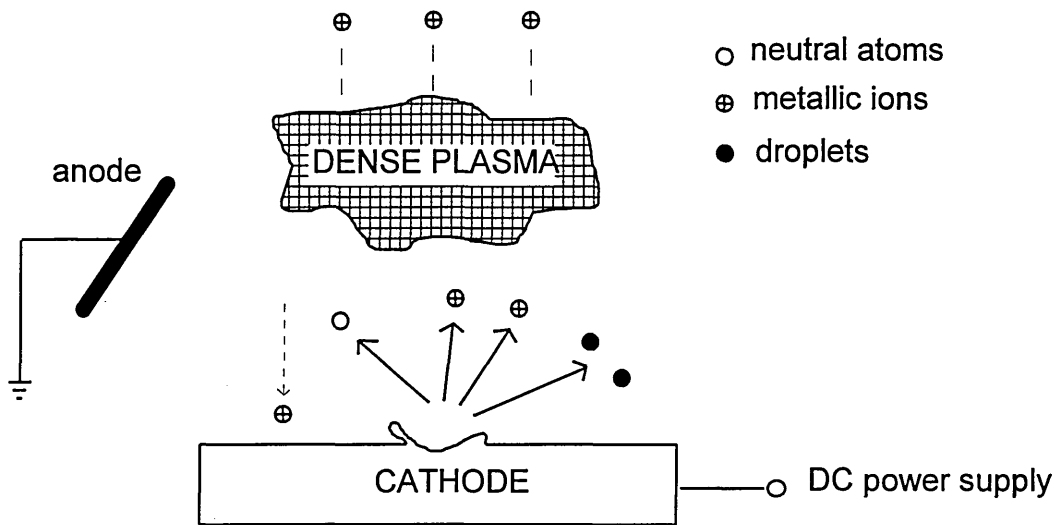


Fig. 2.4 Plasma generation by cathodic arc.

The produced plasma jet peaks in a direction normal to the cathode surface and is highly ionised; approximately 90 % of the evaporated species. For refractory metals, the evaporated species are multiply ionised e.g. for titanium the charge distribution is approximately 27 % of  $Ti^+$ , 67 % of  $Ti^{2+}$  and 6 % of  $Ti^{3+}$  [8].

### 2.1.6 Macroparticles

During operation of the arc, the random arc spots have a tendency to concentrate in specific areas of the cathode, producing large localised molten pools. The positive space charge which accelerates ions away from the cathode, also accelerates some ions towards the surface of the cathode. The impinging ionic jet on a liquid pool surface may cause ejection of droplets or macroparticles measuring several tens of microns in diameter [9-11]. These droplets are undesirable due to their detrimental effect on surface roughness and adhesion of the deposited film, along with the wastage of cathode material.

During the coating process, providing sufficient reactive gas is used, then contamination or poisoning of the cathode occurs. This raises the melting point of the cathode material and hence reducing the size of the molten pools, and also increases the arc velocity due

to liberation of the reactive gas when intensely heating the arc. This results in fewer macroparticles and the process of deliberately poisoning the cathode is known as the modified arc process [12]. Other processes have been developed to reduce macroparticle formation. These include filtering the produced flux using a magnetic coil (plasma duct) [13], using a conventional arc as an ion source for ion beam self-sputtering [14] and the use of pure cathode material without gases [11]. Another method exists and has been successful in reducing macroparticles. This method relies on increasing the speed at which the arc spot moves over the cathode surface by magnetic confinement or steering the arc.

### 2.1.7 Steered Arc

The motion of a cathode spot can be influenced by the application of an external magnetic field. This is due to the arc sitting preferentially at the point on the cathode surface where the normal of the magnetic field is zero. The magnetic field can be produced by a magnet, or more commonly a coil and is circular or oval in shape and thus a “racetrack” of zero normal field generates the region on which the arc traverses. Due to the Hall effect of the transverse field, the arc travels around the racetrack at high velocity in the range 1 - 100 m s<sup>-1</sup>. However, there is an unexpected phenomenon regarding the direction of arc motion.

Ampere’s rule states that for a conductor carrying a current of electric current density,  $\mathbf{J}$ , in the presence of a magnetic flux density,  $\mathbf{B}$ , is subject to a force given by  $\mathbf{J} \wedge \mathbf{B}$ ; the Hall effect. However, high speed photography has revealed that the arc traverses the racetrack in the opposite direction predicted by the Hall effect. This retrograde motion [15] is a consequence of the Hall effect contribution from the Lorentz force acting on the charge carriers, which are normally electrons. The Lorentz force is given by:

$$\mathbf{F} = q(\mathbf{E} + \mathbf{v} \wedge \mathbf{B})$$

where  $\mathbf{F}$  is the force,  $q$  is the moving charge,  $\mathbf{E}$  is the electric field and  $\mathbf{v} \wedge \mathbf{B}$  is the vector product of the particles’ velocity and the magnetic flux density. According to the Hall effect a sideways shift is imposed on the motion of the electrons by their passage

through the magnetic field. However, in the case of a magnetically steered arc operating at low pressure, electrons are partially confined to cycloid paths in the magnetic field and thus return to the cathode without contributing to the net current flow. Since the plasma surrounding the cathode consists of an intense flux of ionised material, the current is mainly carried away by positive charge carriers and the Hall field is reversed. At higher operating pressures (not usually found in PVD) the arc motion reverts to the usual Ampere direction. The differences in cathode spot direction for high and low gas pressures have been observed by Robson and Von Engel [16]. The direction of the cathode spot at high pressures can be explained by a shorter mean free path for the ion flux, resulting in kinetic energy loss collisions such that fewer positive ions escape the cathode. Thus the majority current carriers are electrons as in the normal situation of obeying Ampere's rule. The exact mechanism of cathode spot motion is not fully understood, but this does not unduly effect the use of magnetically steered arcs in PVD. However, a model of the motion of the cathode spot based upon the local nature of the cathode surface and variance of the heat flux within the spot has been described by Nemichinskii [17]. The predicted arc velocities were found to agree well with measured experimental values. In one study by Fang [18], the arc motions for copper, stainless steel and titanium targets were observed. The highest measured arc velocities were associated with titanium, for which  $40 \text{ m s}^{-1}$  was observed under the test conditions. The maximum velocities for stainless steel and copper were found to be  $15$  and  $2 \text{ m s}^{-1}$  respectively. It was also shown that the retrograde motion of the arc can be treated as a function of arc voltage, thermal conductivity and atomic mass, and that the arc velocity was reduced with increasing ambient gas pressure.

Electrical or mechanical changes in the profile of the magnetic field allow for the precise control of the arc motion and the ability to steer the arc in a predetermined closed-path of variable radius on the cathode surface. The confinement of the arc can be implemented by using either electro or permanent magnets. Early steered arc methods used a small permanent magnet attached to a rotating arm behind the cathode. The rotation of the arm during evaporation caused the arc to follow a circular path on the cathode surface, the diameter of the circle being a function of the intensity of the magnetic field. More recently, steering the arc has been achieved using stationary

magnetic field coils behind the cathode to both guide the arc and increase its velocity. By varying the current in the coils, and hence the magnetic field strength, the path diameter of the arc can be changed. Both methods ensure the resultant motion of the arc spot has improved erosion uniformity, reduced frequency and the size of macroparticles, and reduced arc instability due to travel beyond the edge of the cathode. Using such methods the steered arc technique offers precise control of the evaporation area and hence the possibility of using segmented cathodes for the deposition of graded and multilayered coatings.

Confinement of the arc to the cathode surface is also possible by using a “passive border”, having predetermined electronic characteristics. The major requirement of the material used in a passive border is very low secondary electron emission. This results in reduced ionisation and a weakened plasma jet, causing the arc to travel away from the border. Since the passive border does not extinguish the arc, the evaporation source operates with improved stability and for longer periods of time without re-ignition. The preferred material for passive confinement is boron nitride, and the method is normally used in conjunction with magnetic confinement.

## **2.2 Sputtering Techniques**

When a solid surface is bombarded with energetic particles such as ions or neutrals, material from the surface of the solid is ejected during the process of momentum transfer. This phenomenon is known as sputtering. The sputter yield,  $s$ , is the number of atoms ejected from the target per incident ion. The yield is affected by the surface structure, the mass of the bombarding ion and the associated incident energy. The sputter yield increases rapidly with relatively small increases in bombarding ion energy after a threshold energy typically between 10 to 30 eV for metal targets. From about 100 eV upwards, the yield increases approximately linearly with ion energy. At this kind of energy and higher, the sputter deposition of films becomes practical. Further increases in the ion energy, also increases  $s$  to a maximum and then decreases slowly. This decrease in  $s$  with increasing ion energy is due to the penetration of ions into the target,

and consequently not all the atoms ejected from their lattice sites reach the surface as sputtered material. Such sputtering processes are utilised for thin film deposition via a variety of techniques.

### 2.2.1 Ion Beam Sputtering

The bombarding species on a cathode surface may originate from an external source using either an arc or a glow discharge plasma. The ions are extracted electrostatically and magnetically directed onto the cathode surface. This type of technique is commonly used for ion implantation and surface modification in the semiconductor industry [19]. However, to achieve a greater ionic flux over a wider area of the cathode, an alternative method is to generate a glow discharge directly in front of the cathode.

### 2.2.2 Diode Sputtering using a Glow Discharge

A glow discharge can be easily generated by applying a high potential between 300 - 5000 V between two electrodes in a vacuum chamber containing an inert work gas such as argon. This is achieved by using a cathode of the material to be deposited and the chamber walls act as the anode, hence the diode arrangement name as shown in fig. 2.5.

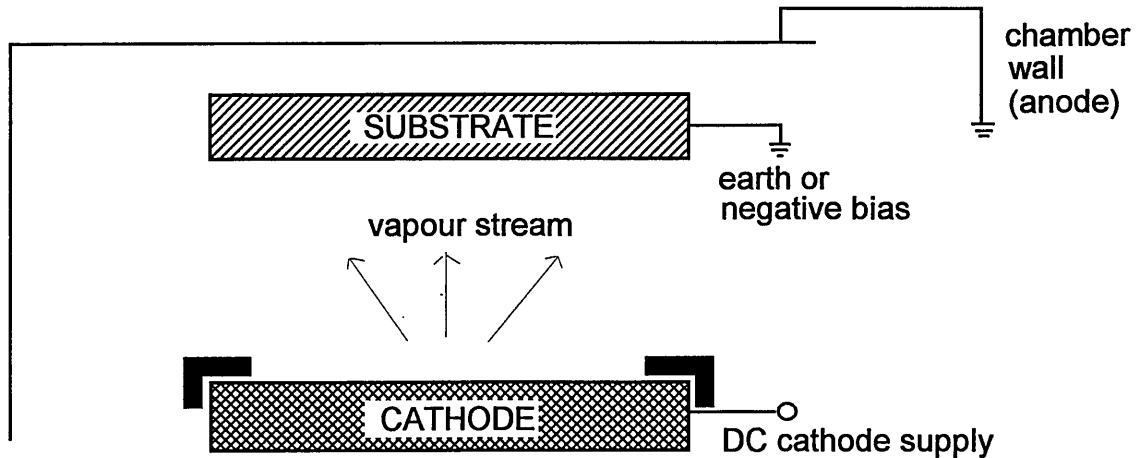


Fig 2.5 Diode sputter source.

If the applied potential to the cathode is greater than the breakdown voltage of the gas then an electric current will flow. This is initiated by the acceleration of gas ions towards the cathode and electrons towards the anode. The accelerated ions lose most of their energy on collision with the cathode. Similarly the ions also lose their charge and are either elastically recoiled or implanted. Momentum transfer from the incident ions to the cathode generates a “collision cascade” within the near surface region of the target material. The transferred energy,  $E_t$  during such binary collisions is given by:

$$E_t = 4m_i m_t / (m_i + m_t)^2$$

where  $m_i$  and  $m_t$  are the masses of the incident and the target atoms. The resulting collision cascade may travel deep into the cathode dissipating its energy by increased lattice vibrations, or it may recoil to the surface and cause the ejection of an atom or a cluster of atoms providing the remaining energy is greater than the surface binding energy. A schematic of the sputtering process is shown in fig. 2.6.

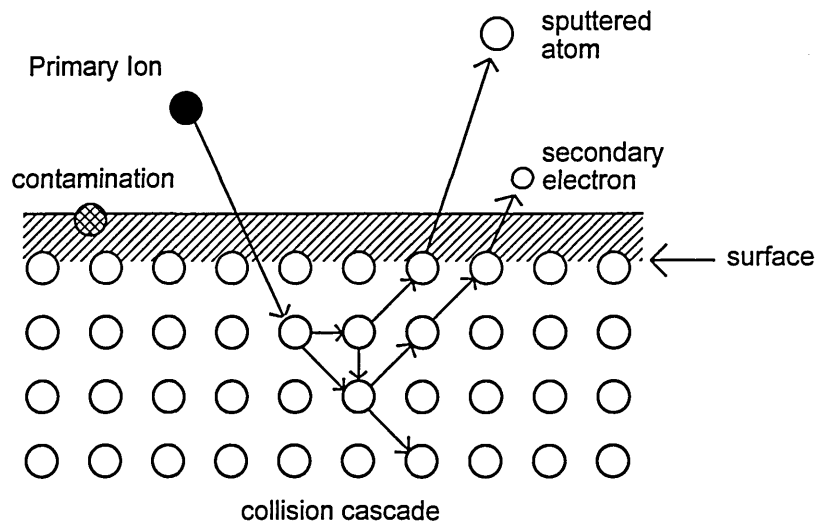


Fig. 2.6 Schematic of the sputtering process showing the formation of a collision cascade generating defects, ion implantation and the removal of a surface atom.

The process of sputtering is very inefficient and typically only 1 % of the incident energy reappears as the energy associated with the sputtered atoms. Approximately 90 % of the ejected atoms are neutral and have a low kinetic energy i.e. a few eV. The bombardment also causes the emission of secondary electrons, X-rays, photon generation and the desorption of trapped gas atoms from the cathode surface. The

emitted secondary electrons are important in sustaining the generated plasma by colliding with the working gas and causing ionisation events. Providing that each secondary electron accelerated away from the cathode produces a sufficient number of ions to cause the release of further secondary electrons at the cathode, the glow discharge plasma will be self-sustaining. The proportion of produced secondary electrons is dependent upon the operating voltage of the cathode, the average energy required for producing ions in the working gas and the ion collection efficiency of the cathode. The proportion of secondary electrons emitted per incident ion,  $\Gamma_1$ , is termed the secondary electron yield. Typically for a pure metal cathode with argon as the working gas and a -500 V cathode potential,  $\Gamma_1$ , will be approximately 10 %.

### 2.2.3 Triode Sputtering

An advancement on the diode sputtering method is triode sputtering which results in an enhanced ionisation. The generated discharge is now no longer dependent solely on the secondary electron production at the cathode in order to sustain the plasma. The third electrode is typically a thermionic electron emitter as shown in fig. 2.7.

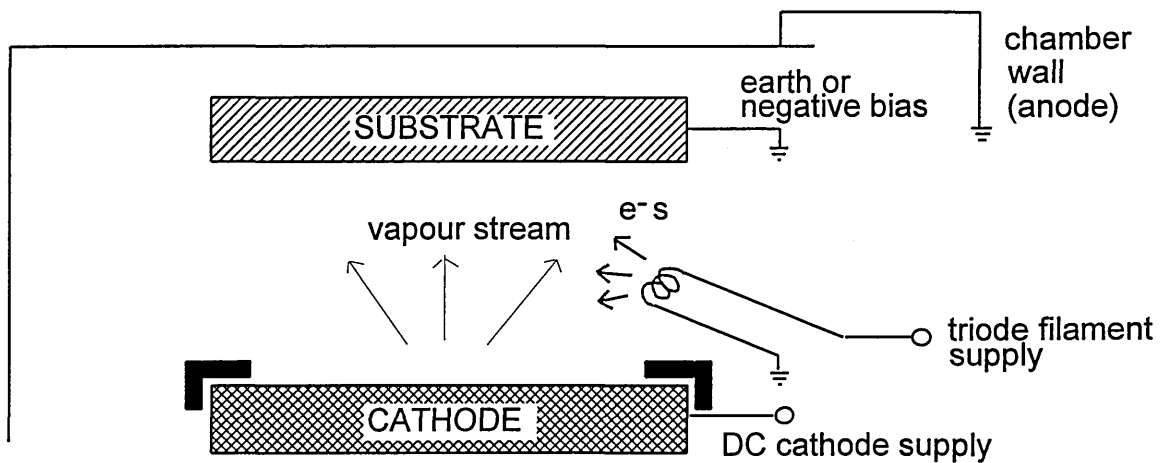


Fig. 2.7 Schematic representation of triode sputtering.

With this electron source, it becomes possible to vary the discharge current independently of the discharge voltage, making high ion densities at the cathode and

substrate possible. Such a triode arrangement is used in the commercial apparatus BAI 640 R Balzers coating unit [20]. A modification to this apparatus has been successfully used to combine the usual process with in-situ plasma nitriding by Dingremont *et al.* [21, 22].

All triode arrangements enable lower discharge voltage and operating pressures to be used, and leads to higher deposition rates and independent control of the plasma density. However, disadvantages of triode sputtering do exist. These include contamination from the thermionic source and substrate overheating due to direct electron bombardment or indirect heating from chamber walls.

#### 2.2.4 Glow Discharge Plasma

In sputtering processes used in PVD techniques, the type of dc discharge is known as an “abnormal glow discharge”. The discharge can be separated into several distinct regions. In front of the cathode is the “cathode glow region” which is luminous due to neutralisation at the cathode surface. Between this region and the cathode exists a “dark space” in which most of the applied potential is dropped, providing the acceleration for the impinging working gas ions and the emitted secondary electrons. The impinging working gas ions generate collisions in the dark space resulting in high kinetic energy neutrals that also impinge on the cathode surface thereby resulting in sputtering from the cathode by both ion bombardment and fast moving atom bombardment. The next region is the “negative glow” which usually fills the whole of the remaining coating chamber. This negative glow is often referred to as the plasma, and the accelerating electrons lose most of their energy in this region by creating ions and excited atoms. The regions present in a glow discharge plasma are shown in fig. 2.8.

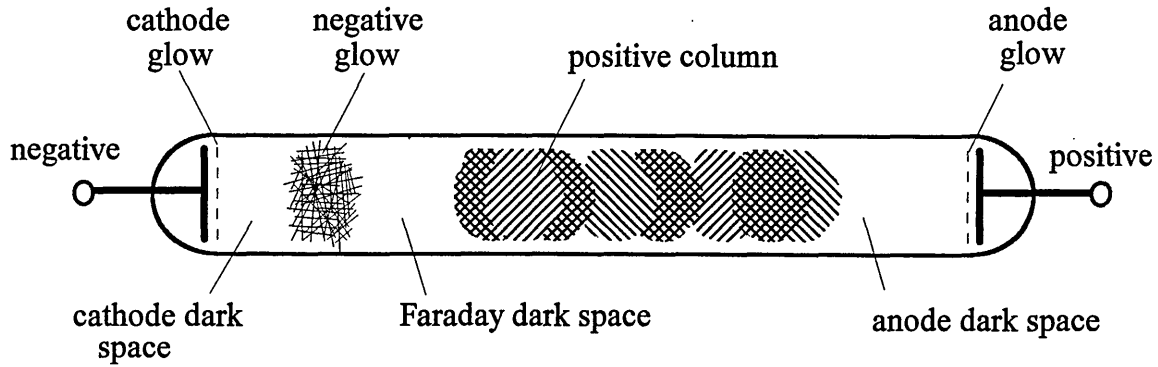


Fig. 2.8 Schematic of a glow discharge plasma.

Relaxation of the excited gas atoms in the plasma results in a characteristic colour glow by way of photon emission. The characteristic colour and intensity depends on the working gas, the cathode material, pressure and excitation. Beyond the negative glow and approaching the anode, exist several other regions. These are the “Faraday dark space”, the “positive column” and the “anode dark space”. However, these regions are not observed in the pressure ranges used in PVD processes.

### 2.2.5 Magnetron Sputtering

In a conventional glow discharge the produced secondary electrons are quickly lost by recombination at the anode. To minimise this loss and increase ionisation, a magnetic field can be used to confine the electrons [23]. The “magnetron” uses magnets behind the cathode which produce a magnetic field penetrating into the dark space, but since the field used is relatively weak, only electrons and not the more massive ions are affected. The principle behind the magnetron is that secondary electrons emitted from the cathode are acted upon by the Lorentz force due the crossed electric and magnetic fields. This causes the electrons to follow an orbital path, describing a semicircle of radius  $r$ , given by:

$$r = m_e V \cdot \sin\theta / Be$$

where  $m_e$  is the electron mass,  $V \cdot \sin\theta$  is the component of the velocity perpendicular to the magnetic field,  $\mathbf{B}$ , and  $e$  is the electron charge. Providing no collisions occur, the electrons will describe a helical path before returning to the cathode surface. In practice, this is achieved by arranging permanent magnets into a toroidal type tunnel, like a racetrack. The electrons become trapped in this tunnel and the plasma density increases in the magnetically confined region. Therefore by using a magnetron, a higher ion density typically 10 - 100 times higher than that in the glow discharge can be obtained. The higher current densities obtained make it possible to increase the deposition rate of films. Similarly, the deposition rate per unit power supplied to the cathode increases resulting in more efficient energy usage. A schematic of a magnetron is shown in fig. 2.9, along with the associated trace of electron energy motion.

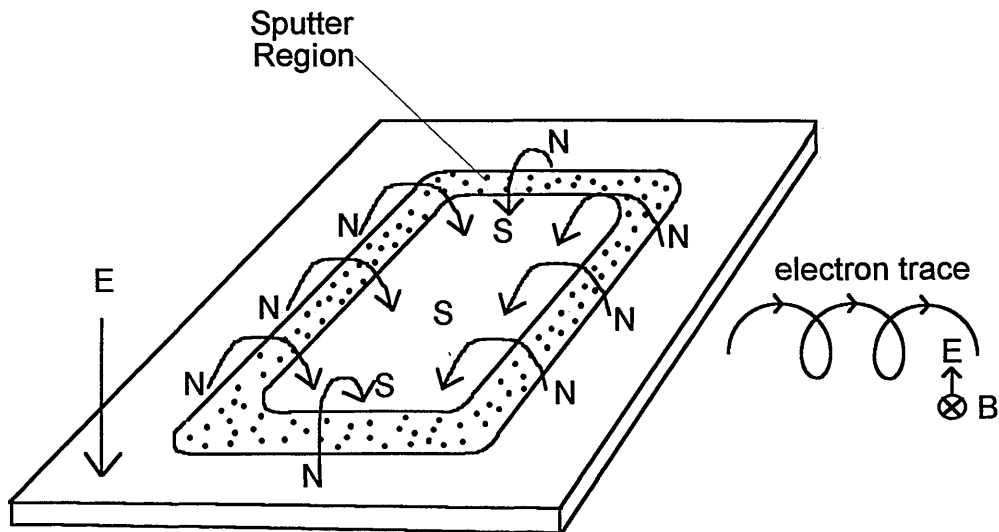


Fig. 2.9 Schematic of a planar magnetron.

Since the 1970's the principle of crossed electric and magnetic fields has been effectively applied to sputtering systems. Through this development several magnetron designs have emerged. These include cylindrical, circular and planar magnetrons. This work is concerned with the planar magnetron design since this is the most applicable to large scale PVD coating systems such as ABS<sup>TM</sup>.

The central and outer magnetic pole arrangement resulting in the racetrack makes a stable line source with substrate rotation necessary for achieving uniform coating deposition. However, this localised erosion in the racetrack area can lead to problems [24] such as variation in the deposition rate with operating time which necessitates frequent cathode replacement.

#### 2.2.6 Unbalanced Magnetron

A problem associated with the conventional magnetron is the poor “throwing distance” of the generated plasma and hence depositing species. However, a simple modification to the magnetic arrangement of the magnetron results in an “unbalanced magnetron” which has proved to be an extremely versatile source in PVD processes [25-27]. In the conventional magnetron, the strengths of both the inner and outer magnets behind the cathode are equal. By strengthening one set of magnets either with additional magnets or by using an electromagnetic coil, the magnetron becomes magnetically unbalanced. Unbalancing can be achieved by strengthening either the inner or outer poles resulting in different magnetic characteristics. Strengthening the inner poles has no obvious advantage since the increased secondary electron confinement draws the glow region into the surface of the cathode. However, if the outer pole is strengthened, then the magnetic field lines loop onto the cathode surface and curve away on all sides as shown in fig. 2.10. Since a number of secondary electrons follow these lines, the plasma glow is no longer confined solely to the cathode surface, but is also expanded out towards the substrate(s) to be coated. This results in increased ion bombardment on the substrate and since the ion energy and flux can be varied almost independently of one another, a further controllable process parameter.

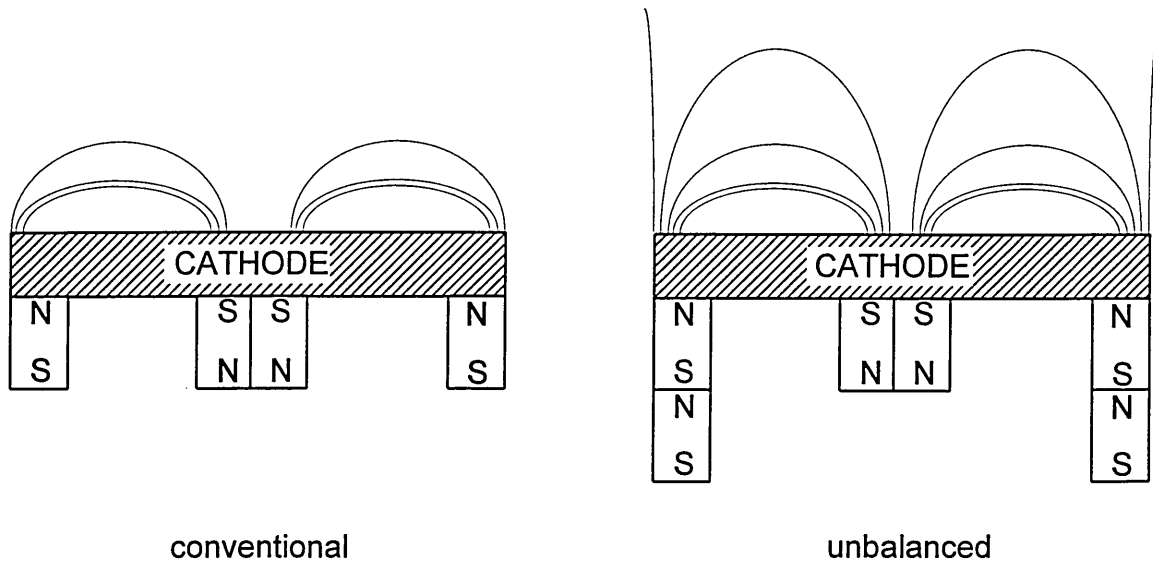
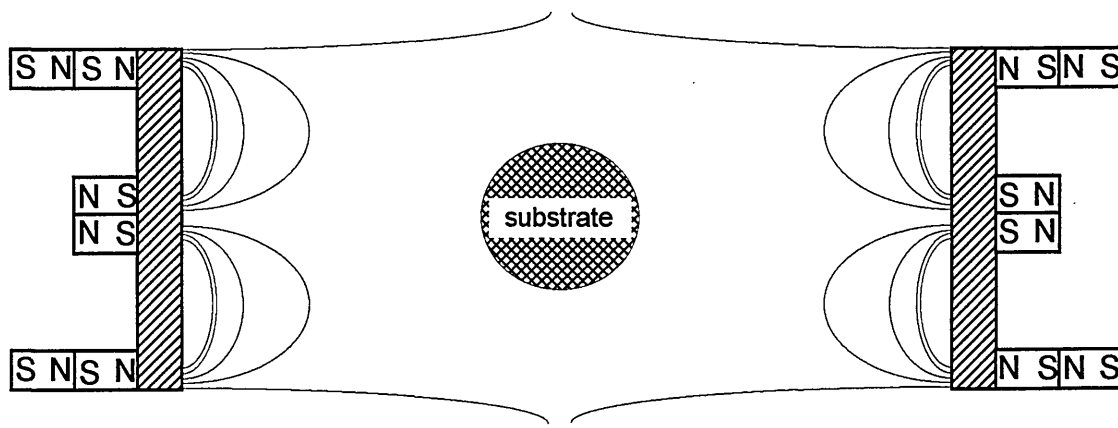


Fig. 2.10 Unbalanced and conventional magnetrons.

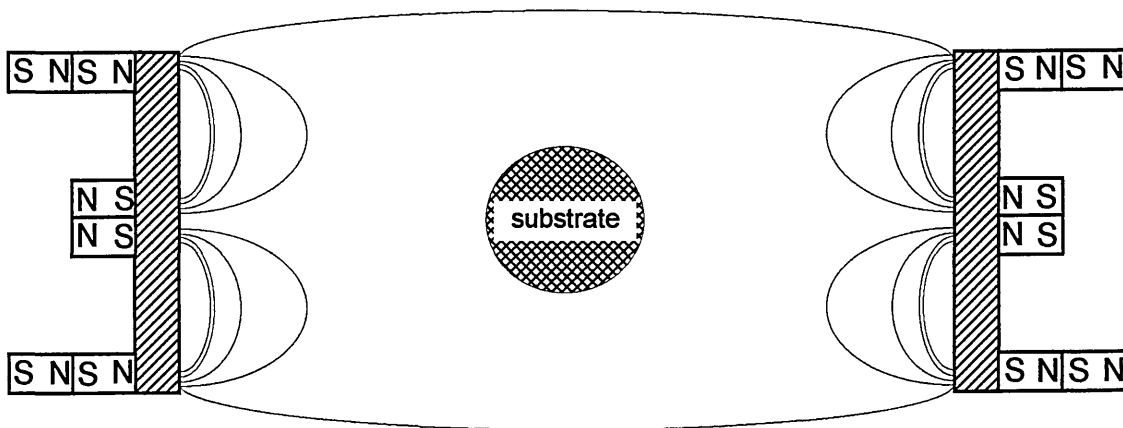
### 2.2.7 Magnetron Magnetic Arrangements

By using two or more unbalanced magnetron cathodes in the same system it is possible to generate various magnetic field geometries [28, 29]. Such multi-cathode systems typically have only two distinct configurations. These are the “mirrored” and “opposed” arrangements as shown in fig. 2.11.

In the mirrored arrangement the outer magnetic poles of the cathodes are alike whereas in the opposed arrangement each alternative cathode has like outer poles but the adjacent poles are opposite. In all these arrangements only an even number of cathodes may be used without upsetting the repeating pattern due to the bi-polar nature of magnets. The opposed magnetic arrangement results in magnetic field linking between north and south outer poles of adjacent cathodes which serves to reconfine the escaped secondary electrons and hence distribute the plasma intensity evenly around the multi-cathode system. The principle of plasma confinement using such magnetic field linking is used in the ABS<sup>TM</sup> system which consists of two pairs of opposing magnetron arrangements.



mirrored magnetron arrangement



opposed magnetron arrangement

Fig. 2.11 Magnetron field linking arrangements.

The opposed magnetic field linking used in PVD systems has the overall effect of increasing the travelling distance of the secondary electrons between cathodes, creating more ionisation events and increased sputtering. A further advantage of the closed magnetic field is the confinement of the plasma to the substrate region causing an enhancement of the deposition conditions [30, 31]. In contrast, the mirrored magnetic arrangement suffers from reducing the unbalancing efficiency by restricting the reach of the uncontained field lines to half the distance between the opposing cathodes.

### 2.3 Arc Bond Sputtering (ABS<sup>TM</sup>)

The previously described PVD methods are all in commercial use today, as entirely distinct techniques. The development of electron beam methods using ion enhancement, random and steered arc methods, and cathode sputtering methods all have widespread application in the field of hard coatings. However, the practical results of hard coatings produced by different methods often show distinct physical and chemical differences when studied using a range of high resolution analytical techniques. In particular, coatings produced by a variety of methods have been shown to differ in terms of morphology, microstructure, colour, lattice spacing, crystallographic orientation and adhesion [32].

In the studies of coatings produced by either steered or random arc methods, a penetration of Ti ions into the steel substrates has been found, in association with a change of the microstructure in this region. This may explain the improved adhesion for arc deposited TiN coatings compared with non-arc deposited coatings. Therefore, the idea behind the ABS<sup>TM</sup> method [33] is to combine the excellent adhesion properties associated with arc technology with the versatility of cathode material selection offered by magnetron sputtering. Also the method has the advantage of producing dense coatings which are virtually macroparticle free, particularly in cases involving cathodes composed of high and low melting point materials e.g. TiAl. The method is realised by integrating the functions of an arc source with an unbalanced magnetron in one single cathode unit as shown in fig. 2.12.

Magnetic discharge is achieved with a magnetic field positioned behind the target. The UBM effect is produced by reinforcement of the outer pole arrangement by the addition of electromagnets which allows adjustment of the unbalancing effect. The cathode arrangement allows for deposition of coatings at various temperatures without having to make changes in the sputtering power and associated coating rate. Bias current density and thus temperature of the substrates can be altered by adjusting the coil current.

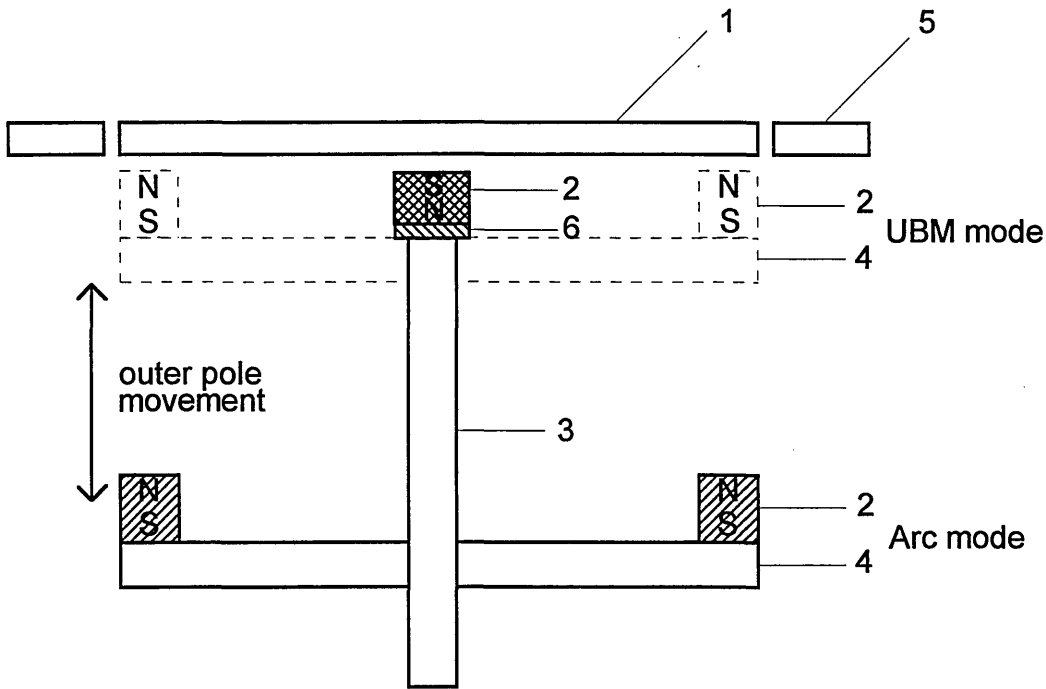


Fig. 2.12 Arrangement of single cathode unit used by the ABS™ method. 1, target; 2, permanent magnets; 3, centre pole fixturing; 4, magnetic yoke; 5, recipient; 6, magnetic neutral spacer.

Conversion from UBM to arc mode is by a simple movement of the outer poles controlled by a hydraulic arrangement. In the steered arc mode the central pole is kept up against the back of the target, whilst the outer poles are drawn back from the target far enough to produce a negligible magnetic field at the front of the target. The electromagnetic coils are used during the steered arc mode, by varying the coil current with time making it possible to produce a sweeping effect on the arc track. This arc movement allows for a droplet reduced etching process compared with random arc.

In practice even numbers of these single unit cathodes are used in the coating system to provide an enclosed magnetic field linking system to enhance plasma density in the substrate region and reduce electron drift to the chamber wall thereby reducing unwanted resputtering events. In this study a Hauzer Techno Coating 1000-4 ABS™ system has been used which comprises of four such cathode units. The coating chamber is described in further detail in chapter 4.

## 2.4 Plasma and Surface Interactions

### 2.4.1 Nucleation and Coating Growth

Nucleation and coating growth takes place on a substrate surface, often of a material different to that of the coating. Since the surface of the substrate comprises of only the top few atomic layers of the solid, it is likely to possess different properties to that of the bulk material [34]. This is because the characteristics of a bulk material depends on electronic properties which in turn, depend on the 3 dimensional potentials within the lattice. Any loss in this bulk periodicity due to the existence of a surface will result in changes in the electronic states and hence, the properties both near and at the surface. Similarly, the lack of adjacent neighbours at the surface, exposes “dangling bonds” which are readily available for chemical reactions. Therefore, the surface of a substrate is likely to affect the nucleation and initial deposition of the coating. These stages of nucleation and early growth in any PVD process are critical, since the nucleation can strongly affect grain size, crystallographic orientation and adhesion. This will have a resulting effect on the overall properties of the deposited coating.

The possible nucleation sites on a surface are significantly increased by the presence of any defects within the outermost atomic layers. At the atomic level both monocrystalline and polycrystalline solid surfaces exhibit “steps” [35]. A polycrystalline solid surface, such as a steel, consists of many individual grains of different crystallographic orientations. Modelling at a simplistic level, within each grain exist steps which have been formed from new atomic layers building on preceding layers. Existing between each step is a flat region termed a “terrace”. These terrace faces and steps may contain further defects such as vacancies and dislocations along with adsorption atoms. A schematic of surface defects is shown in fig. 2.13.

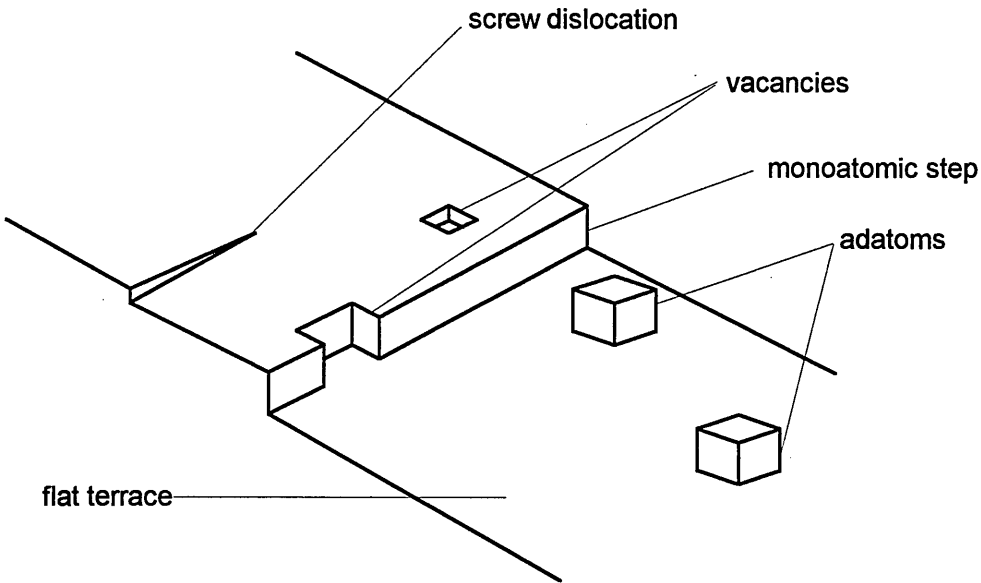


Fig. 2.13 Schematic of a surface at an atomic level.

At temperatures above absolute zero, all atoms vibrate in an individual potential well. However, if an atom receives sufficient energy, it may overcome the potential energy barrier and leave its initial site and become an adatom in a neighbouring position at a minimum potential energy [36]. This process is called “surface diffusion” and gives rise to “adatom mobility”. The time that a surface atom remains at one site is known as the “residence time” and depends on the bond strength, the depth of the potential well and the remaining thermal energy of the adatom. In surface diffusion, the atoms jump from one adsorption site to another. Generally, the adsorption is much stronger at steps or defects compared with the flat terraces. Therefore the residence time is longer, and diffusing adatoms tend to coalesce at these points and form primary nucleation sites for coating growth. Consequently a surface containing a high number of surface defects will have a higher nucleation density. Subsequent coating deposition will result in a greater deposition rate and possibly improved adhesion due to greater mechanical keying and a finer grain structure. This defect and step structure is fundamental to coating growth since during the deposition process, the growing film will have its own surface layer consisting of similar steps, defects and related adsorption sites, all of which contribute to the final quality and properties of the deposited coating.

After nucleation sites have been established the depositing coating will condense from the vapour phase about these sites as “islands”. The islands expand across the surface to the fronts of adjacent islands as shown in fig. 2.14.

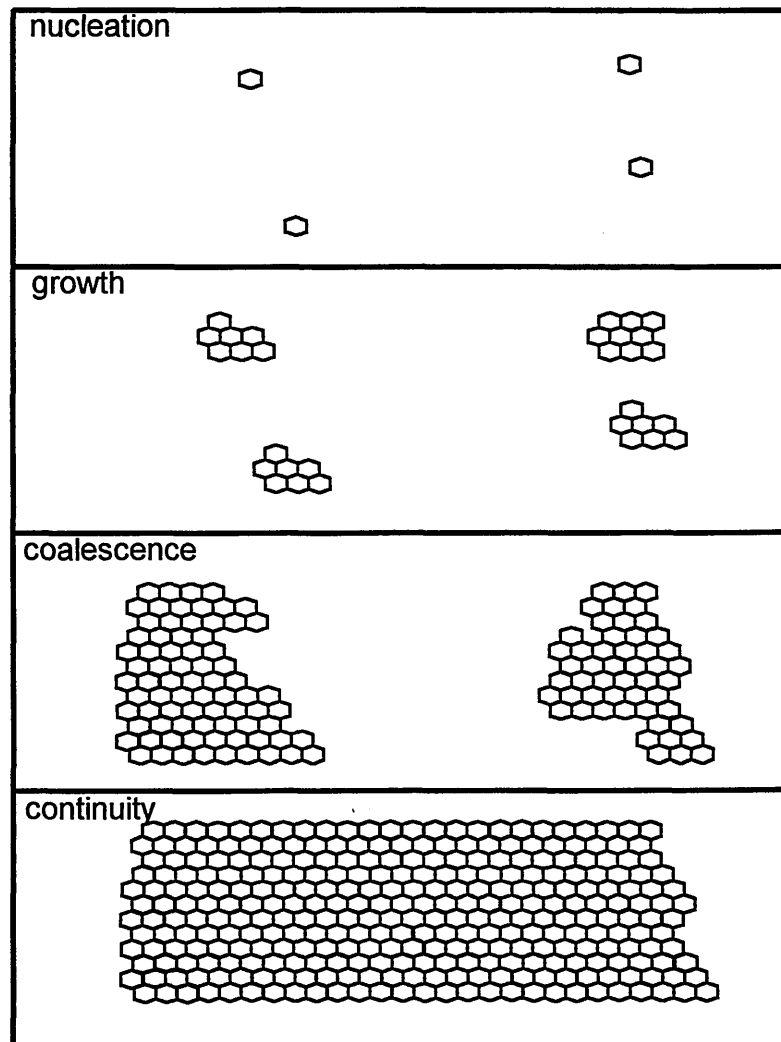


Fig. 2.14 The process of coating growth.

As the islands expand and the growth fronts meet, grain boundary defects are generated and further growth can only continue upwards. Subsequent growing layers attempt to match the grain orientation of the previous underlayer, and so initially all possible orientations are present on the surface. However, during coating deposition a preferred orientation is favoured for a particular set of process parameters. This results in “competitive growth”, where those grains with the favoured orientation flourish,

growing upwards and across the surface at the expense of grains orientated differently. The deposited coating comprises of columns clustered together into large features having a dominant orientation, resulting in the commonly observed columnar structure [37].

#### 2.4.2 Sputter Etching

A greater density of surface defects and hence the resulting improved coating growth can be achieved by either orientating the substrate to expose the largest number of surface steps or by an ion bombardment process. A method to achieve the latter, is to apply a high negative bias voltage (e.g. -1200 V) across the substrate which will result in the acceleration of positive ion species towards the substrate. The impinging ions rapidly lose their kinetic energy by momentum transfer to the surface atoms, which in turn generate a collision cascade in the near surface region of the substrate. The resulting cascade may travel deep into the substrate dissipating the associated energy as heat, or by recoiling and causing sputtering of surface atoms. The overall effect is the removal of surface atoms of the substrate along with any contaminants. This “sputter cleaning” process is widely used in PVD processes to provide a clean surface prior to coating deposition [38]. Such a cleaning process is a vital feature of the ABS<sup>TM</sup> method, by using both the argon working gas ions and multi-ionised metal ions during an etching pre-treatment process. However, one of the effects of sputtering is a roughening of the substrate surface and the possible introduction of lattice defects. This may be due to preferential sputtering of particular species or along grain boundaries and the angular dependence of sputter yields. Such surface roughening is detrimental to the overall surface finish of applied coatings used for decorative applications and thus, this sputtering step is minimised. However, for engineering applications, this form of enhanced cleaning provides a number of advantages. In particular, a high density of possible nucleation sites are created, as well as a “mechanical keying” effect which has been shown to improve adhesion [39].

Another possible effect of sputter cleaning is a small amount of ion implantation providing the cathodes are powered sufficiently and generate a number of metal ion species within the plasma. This implantation can be enhanced by a surface diffusion process, due to the heat energy created by the ion bombardment. Also part of the substrate may be sputtered and subsequently redeposited along with incident metal ions from the cathode producing a mixed layer e.g. FeTi. Therefore the substrate will contain a proportion of the depositing metal along with the mixed layer which is thought to improve coating adhesion [40].

The outlined sputtering effects can be modelled at a simplistic level by Monte Carlo simulation techniques. The widely available program TRIM (TRansport of Ions in Matter) can be used to predict collision cascades within the near surface region after ion bombardment for a given substrate material and incident ion energy. The program follows the incident ions and recoil atoms throughout the slowing down process until the remaining energy falls below a predetermined level governed by the incident ion and surface binding energies. Hence, by recording the atoms that reach the surface with sufficient energy to be sputtered, the sputter yield can be calculated. Comparisons of TRIM program output results with experimental data have shown good agreement [41]. However, it should be noted that TRIM only considers single ion-atom collisions at one time, and the continual intense ion bombardment occurring within a PVD process is much more complex.

#### 2.4.3 Structure Zone Models

It has generally been understood that the microstructures of thin films can be classified into several zones. To describe these zones, structure zone models (SZMs) were introduced first for evaporated metallic films by Movachan and Demichischin [42] and generalised for sputtered films by Thornton [43]. These SZMs describe microstructures as a function of substrate temperature over melting point ( $T/T_m$ ) as shown in fig. 2.15; according to Messier *et al.* [44].

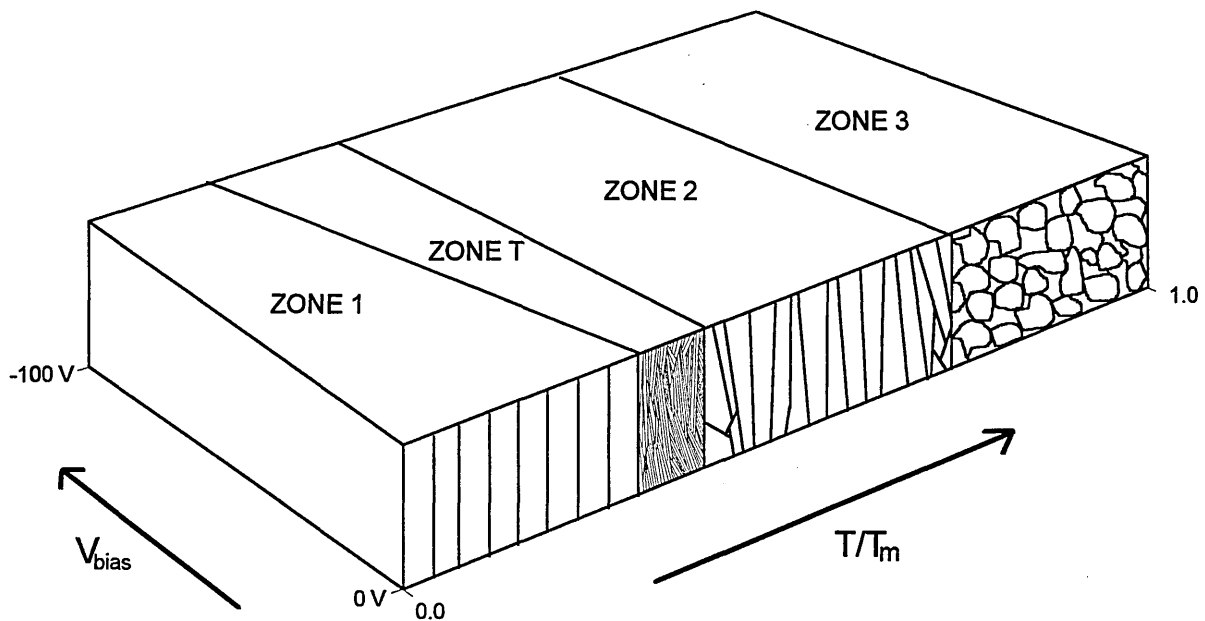


Fig. 2.15 Typical Structure Zone Model.

The low-temperature zone 1 structure corresponds to low adatom mobility and consists of widely spaced columns having domed or angular tops. The mid-temperature range zone 2 consists of densely packed columns with a smooth surface corresponding to significant diffusion processes. For the high temperature zone 3 microstructure, bulk diffusion dominates and the result is a recrystallized equiaxed structure. Work by Thornton [43] demonstrated the presence of a working gas such as argon could produce a further region called the transition or zone T. This zone exists between zones 1 and 2, and consists of densely packed but poorly defined fibrous grains. The zone is skewed relative to bias voltage such that at high bias, the fibrous structure can be obtained at a lower temperature than otherwise possible. Thus, zone 1 may be obtained by subjecting the growing film to ion bombardment as an alternative to increased substrate temperature. This can be achieved by applying a voltage bias to the substrate of -250 V approx. During coating growth resulting in the film being subjected to low-energy irradiation [45]. The deposition technique is then known as “ion plating” and the ion bombardment increases adatom mobility and the generation of point defects. The overall result is a densification of the depositing film, similar to the effect of raising process temperature, or lowering pressure such that fewer energy collisions occur. Therefore the deposited film has a higher packing density and smaller grain size [46].

#### 2.4.4 Interfaces

A solid interface consists of a small number of atomic layers that separate two solids in intimate contact with one another. The properties of the interface differ significantly from those of the bulk material it separates. For example, in surface engineering, a deposited hard coating is thus separated by a substrate-coating interface from the bulk substrate. In terms of atomic structure, the interface can belong to two important categories. Firstly, the interface may consist of either a crystalline or amorphous overlayer deposited on a crystalline substrate; such interfaces are termed “abrupt”. Secondly and more common in PVD processes, the interface can be considered to be “non-abrupt” on an atomic scale due to a diffusion between the coating and bulk substrate or the formation of a new chemical compound. These combinations are shown in fig. 2.16.

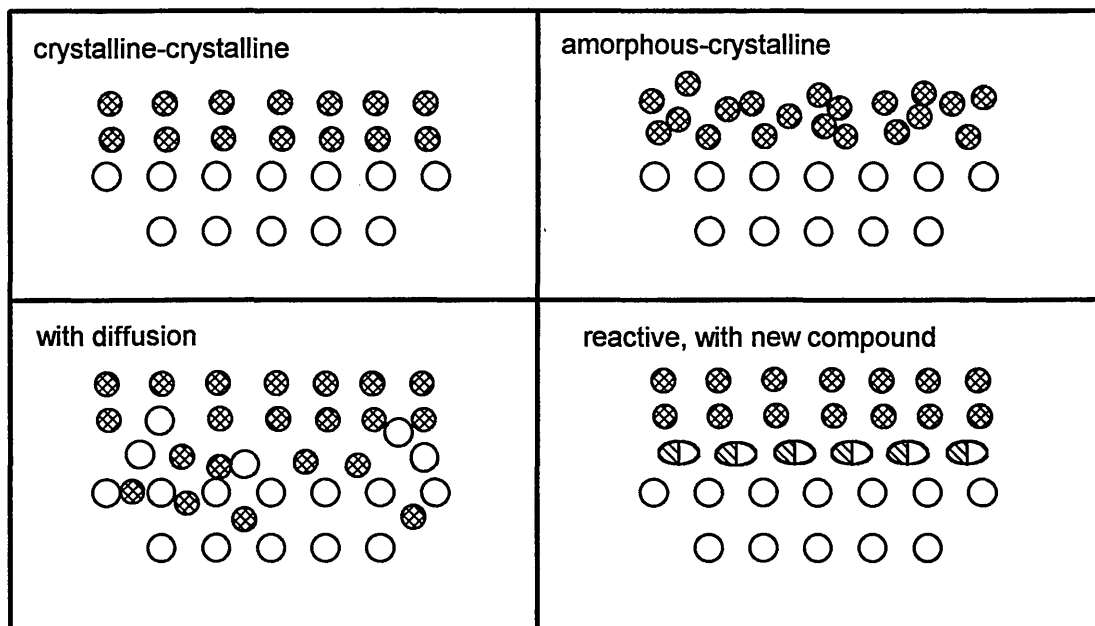


Fig. 2.16 Schematic of possible interfaces.

Interfaces generated by PVD techniques tend to be of the latter type since this produces a stable thermal equilibrium between the coating and the bulk substrate by reducing the acute step difference in material properties at the interface. Another type of interface

generated by PVD processes utilises a metal intermediate layer where the metal is one of the components of the deposited coating e.g. Ti. This method has been used where surface roughening by sputtering is not acceptable and has been shown to improve coating-substrate adhesion [47, 48]. This improvement may result from several factors. These include chemical gettering effects, where Ti reacts with and dissolves weak oxide layers at the interface, and mechanical effects, where the Ti acts as a soft layer reducing shear stresses across the interface thus hindering crack propagation. Therefore, it is of considerable importance that stress relaxation within the interface layer exists, as to support thick films without spallation, than would normally be possible [49].

Essentially in most systems the driving force for the formation of a metal-coating interface is the decrease in free energy that occurs when intimate contact is established between the two materials. This energy change per unit area of interface formed,  $\Delta G$ , is given by the Dupre equation [50 and references therein]:

$$\Delta G = \gamma_m + \gamma_c + \gamma_{mc} \quad (2.1)$$

where  $\gamma_m$  and  $\gamma_c$  are the surface energies of the metal and the coating, respectively and  $\gamma_{mc}$  is the metal-coating interfacial energy. In the simplest case where only chemical bonding is present at the interface, the energy change  $\Delta G$ , is identical to the work of adhesion,  $W_{ad}$ , which is defined as the work required to separate a unit area of interface into the two original surfaces.  $W_{ad}$  may be substituted into equation (2.1) and rearranged to give:

$$-\gamma_{mc} = \gamma_m + \gamma_c - W_{ad} \quad (2.2)$$

It becomes clear from equation (2.2) that the interfacial energy decreases as the work of adhesion increases. Therefore, improving the chemical bonding between the coating and the substrate results in an interfacial energy decrease. This type of relationship has been studied extensively for metal-ceramic systems with particular emphasis on  $Al_2O_3$  and SiC ceramics. However, it should be noted that interfacial regions generated by PVD processes, are in reality more complicated typically involving a combination of new chemical compounds at the interface along with interdiffusion between the coating and substrate as observed by Q. Q. Yang *et al.* [51]. In this study AES, TEM and microdiffraction techniques were used to investigate the interface between Ti-B-N films

deposited on HSS by using N ion bombardment on an electron beam deposited TiB film. The results show FeTi, Fe<sub>2</sub>Ti and Ti<sub>2</sub>N existing within a 150 nm wide interfacial diffusion zone. Several other studies report similar interfacial zones; see chapter 1. Some of these studies also report on the effects of strain energy on the preferred orientation of deposited films.

#### 2.4.5 Residual Stress

One of the subjects which has been extensively studied in TiN coatings is the residual or internal stress existing in the coatings. The magnitude of internal stress present in a coating is important since the stress relates to adhesion. This internal stress has been shown to attain values of several GPa in TiN films by Rickerby *et al.* [52] and is comprised of intrinsic and thermal stresses. The creation of these stresses is attributed to either thermal expansion mismatch between the substrate and coating, or to growth induced stress occurring during the deposition process.

Thermal stress occurs due to any expansion mismatch when the lattice of the substrate material contracts or expands by a different amount to the coating, when subjected to a temperature change. This temperature change may occur as a result of several factors. These include significant fluctuation in deposition temperature, sample cooling after deposition, or heat as a result of friction during use. Hence, if minimum residual stress is required during use, such as a cutting operation, then the deposition temperature should remain constant and match the working cutting operation temperature.

Growth induced stresses are a function of both the microstructure of the coating and the ion bombardment process. For example, a dense coating with close packed columns tends to have high compressive stresses as the column boundaries press against each other. Conversely, a less dense coating tends to have a much lower growth stress due to relaxation by the expansion of columns into existing voids.

Ion bombardment often generates compressive stresses by the “ion-peening” mechanism, in which the surface region of the depositing film undergoes plastic deformation to accommodate the generation of defects. The impacting ions, such as Ar, can also cause an expansion in the surface region by being forced into the depositing coating and become trapped. This forced expansion can result in a state of compressive stress within the coating and should be kept to a minimum.

A study by Oh and Jung Ho Je [53] has studied the effects of strain energy on the preferred orientation of TiN thin films. In their study, coatings were deposited on Si wafers by rf sputtering and XRD analysis showed that the preferred orientation of the TiN film was decided by the competition between surface energy and strain energy. The results show two competitive orientations; the (111) and (200) planes. The (200) dominates below a critical coating thickness, since the surface energy is dominant below this thickness and the overall energy of the (200) plane is lower than that of the (111) plane. However, as the strain energy begins to dominate above the critical thickness, the (111) plane has lower overall energy. Since the driving force is to minimise the overall energy of the growing film, the (200) preferred orientation is developed below the critical thickness, while the (111) plane is developed above this thickness.

## **2.5 The Fe-Ti System**

The element Ti exists in 2 allotropic forms: an  $\alpha$ -phase (hcp) below 885 °C and a bcc  $\beta$ -phase above the transition temperature. Stabilising of the  $\alpha$ -phase can be achieved by alloying with Al, Sn, O, N, or H resulting in a compound possessing good toughness, ductility and formability. Alloying with Mo, V, Cr, Mn or Fe stabilises the  $\beta$ -phase allowing the phase to be retained at room temperature. This stabilisation is the basis of commercial  $\alpha+\beta$  Ti alloys which combine high strength with moderate toughness and ductility. The metallurgy of the  $\alpha+\beta$  Ti alloys is complicated since along with the equilibrium phases a number of metastable phases exist. However, the characteristics of the Fe-Ti system are of considerable importance since the system can serve as a model

for  $\alpha+\beta$  Ti alloys. In this study, knowledge of the Fe-Ti binary system is required for the understanding of possible phase formations during the Ti ion etch pre-treatment process used in the ABS<sup>TM</sup> method.

The Fe-Ti system has been fairly well characterised over the years by a variety of analytical techniques. In particular, both X-ray diffraction techniques and thin foil electron microscopy have identified phases and studied phase transitions in Ti alloys [54,55]. However, both these techniques have disadvantages which may lead to ambiguous results. In the case of electron microscopy, uncertain interpretation may arise due to the overlapping of diffraction spots and difficulties caused by thin foil artefacts. Similarly, for XRD techniques ambiguity may arise due to submicroscopic particle size along with detectable threshold limits in the order of a few percent. Such low detection limits are not a significant problem in Mössbauer spectroscopy which has been shown to be sensitive in phase determination in the Fe-Ti system [56].

### 2.5.1 The Fe-Ti phase diagram

The equilibrium solid phases in the binary Fe-Ti system are shown in the phase diagram of fig. 2.17. In particular, the intermetallic compound FeTi has attracted considerable interest due to the hydrogen storage properties of the material [57-61]. Table 2.1 summarises the main phases, reaction types and structures associated with the system [62]. It should be noted that table 2.1 only briefly describes the main reactions occurring within the Fe-Ti system. However, the phase diagram may be characterised simply by 2 congruently melting intermetallic compounds FeTi and Fe<sub>2</sub>Ti and limited solubility solid solutions of Fe and Ti.

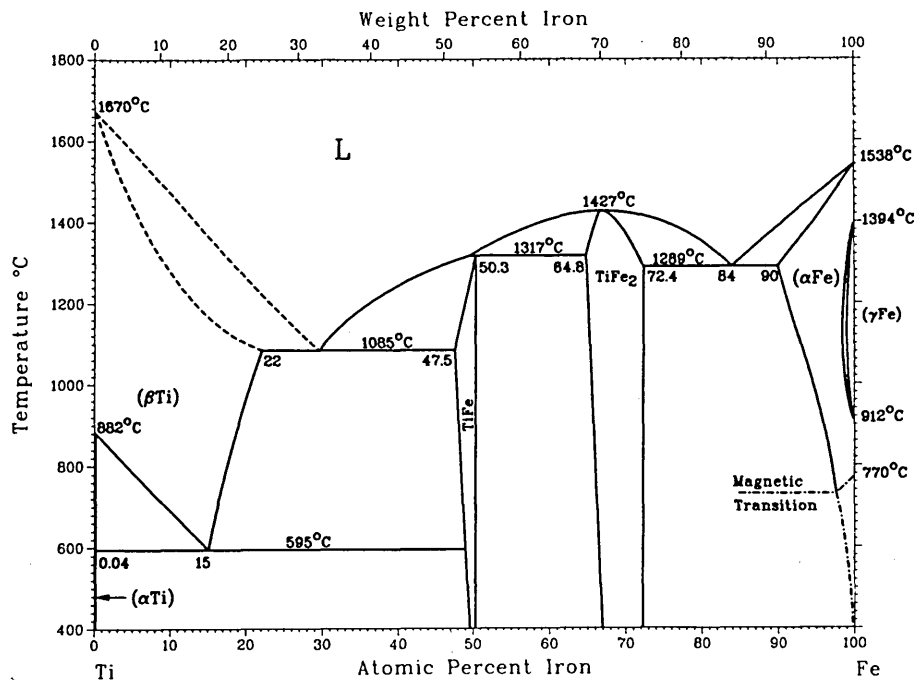


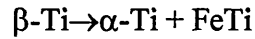
Fig. 2.17 The Fe-Ti phase diagram [62].

Phase	Reaction	Reaction Type	Temp (°C)	Composition (wt % Fe)	Structure Type
$\alpha$ -Ti	$\beta$ -Ti $\leftrightarrow$ $\alpha$ -Ti	allotropic transformation	882	0 to 0.047	hcp
$\beta$ -Ti	$\alpha$ -Ti $\leftrightarrow$ $\beta$ -Ti	allotropic transformation	882	0 to 24.7	bcc
FeTi	L + Fe <sub>2</sub> Ti $\leftrightarrow$ FeTi	peritectic	1317	51.3 to 54.1	CsCl
Fe <sub>2</sub> Ti	L $\leftrightarrow$ Fe <sub>2</sub> Ti	congruent	1427	68.2 to 75.4	MgZn <sub>2</sub>
$\alpha$ -Fe	$\gamma$ -Fe $\leftrightarrow$ $\alpha$ -Fe	allotropic transformation	1392	91.3 to 100	bcc
$\gamma$ -Fe	$\alpha$ -Fe $\leftrightarrow$ $\gamma$ -Fe	allotropic transformation	911	99.5 to 100	fcc

Table 2.1 Main characteristics of the Fe-Ti phase diagram.

The formation of FeTi and Fe<sub>2</sub>Ti can occur by several reactions not listed in the table. In particular,  $\beta$ -Ti solid solution can dissolve upto 25 wt % Fe at 1100 °C and for  $\beta$ -Ti

containing less than 6 wt % Fe the formation of FeTi can occur by the following eutectic reaction:



This reaction has been reported to occur in the temperature range between 585 - 615 °C [63]. The same workers also reported a more complex reaction for iron concentrations higher than 6 wt % involving retained  $\beta$ -Ti as a metastable phase at room temperature on slow cooling. Mössbauer measurements have shown the decomposition of this metastable  $\alpha$ -Ti phase to the  $\omega$ -metastable phase during various ageing processes [64]. A similar study by the same workers have reported other previously unknown metastable phases using Mössbauer spectroscopy [56]. The structure and composition of these metastable phases are not well understood. However, this study is primarily concerned with the phase formation of the intermetallic FeTi and the amorphous counterpart during Ti ion etch processes using the ABS<sup>TM</sup> method. The structure and composition of this intermetallic are well known and will be discussed in the next section along with the identification and analysis of the other significant phases in the Fe-Ti system.

### 2.5.2 Identification and Analysis of Fe-Ti phases

There has been considerable effort devoted to characterise the effects of structural disorder on the solid state properties of amorphous solids. Of particular interest is the Fe-Ti system, since the properties of both the crystalline compound and the amorphous analogue can be studied. In this system only two intermetallic compounds exist, Fe<sub>2</sub>Ti and FeTi. A study by Chien *et al.* [65] has compared FeTi and Fe<sub>2</sub>Ti properties in the amorphous and crystalline states by XRD, conductivity and Mössbauer measurements. In that study amorphous films having a thickness between 10 -24  $\mu\text{m}$  were prepared by magnetron sputtering onto liquid nitrogen cooled substrates. Crystalline samples of FeTi and Fe<sub>2</sub>Ti were produced by an arc furnace operated in a purified argon atmosphere followed by re-melting and rolling to ensure homogeneity. Both the sputtering targets and pellets for arc melting were made from homogeneous mixtures of 99.9 % purity Fe and 99.8 % purity Ti. The reported diffraction patterns of the crystalline states of FeTi and Fe<sub>2</sub>Ti are consistent with CsCl and MgZn<sub>2</sub> structures respectively as reported by

other workers [66]. The diffraction patterns of the intermetallics in the amorphous states are similar. However, comparison with the respective crystalline states suggest little evidence of a strong correlation between the crystalline and amorphous states of the same composition. Also pronounced differences in the electrical resistivity between the amorphous and crystalline states of the same composition do exist. In particular, high resistivities ( $100 \mu\Omega\text{cm}$ ) of the amorphous solids are dominated by defect scattering and show only a weak temperature dependence of resistivity. In contrast, for the crystalline states the resistivity varies approximately linearly, increasing with increasing temperature due to electron-phonon scattering mechanisms. In all cases the resistivity of the crystalline states are lower than that of the amorphous counterpart but at high temperatures (700-800 K) the resistivities for both states are comparable. Despite such clear experimental differences in the resistivity of the amorphous and crystalline solids, a satisfactory theory of the temperature dependence in the amorphous case has not been produced.

Transmission Mössbauer measurements of amorphous and crystalline FeTi and Fe<sub>2</sub>Ti show the two extremes of ordering in solids. This can be clearly seen in fig. 2.18 which shows the Mössbauer spectra at 300 K for the two states of both FeTi and Fe<sub>2</sub>Ti [65].

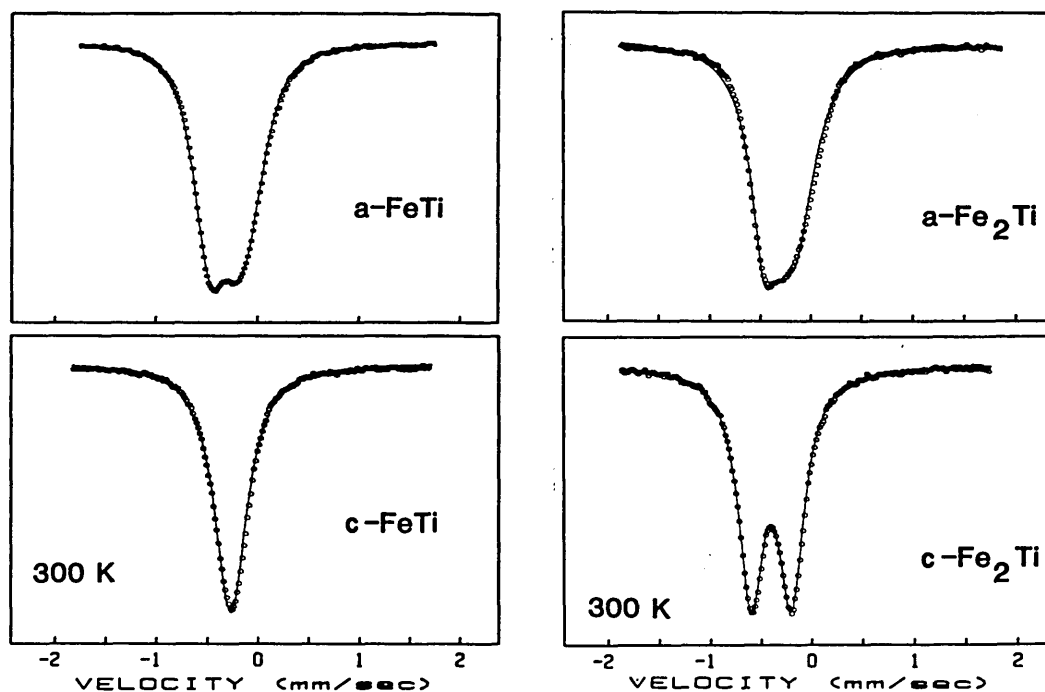


Fig. 2.18 Mössbauer spectra of crystalline(c) and amorphous(a), FeTi and Fe<sub>2</sub>Ti.

In the case of crystalline FeTi, the CsCl cubic structure shows a Mössbauer spectrum of a single line with no quadrupole splitting. In contrast, a sizeable quadrupole splitting of  $0.32 \text{ mm s}^{-1}$  has been observed for amorphous FeTi, indicating lower local symmetries of the Fe sites for the amorphous state. This is consistent with the model of amorphous solids proposed by Lines [67] which suggests a minimal and nearly zero probability of finding sites with cubic symmetry. For crystalline Fe<sub>2</sub>Ti the low symmetry results in a large quadrupole splitting of  $0.40 \text{ mm s}^{-1}$  in good agreement with other workers [68,69]. A smaller quadrupole splitting is observed for the amorphous Fe<sub>2</sub>Ti compound. The study by Chien also examined the isomer shift and quadrupole changes of the amorphous alloy Fe<sub>x</sub>Ti<sub>100-x</sub> ( $30 \leq x \leq 80$ ). The isomer shift relative to  $\alpha$ -Fe was found to increase from  $-0.22 \text{ mm s}^{-1}$  for  $x = 30$  to  $-0.14 \text{ mm s}^{-1}$  for  $x = 80$ . Also the quadrupole splitting was found to decrease from  $0.36 \text{ mm s}^{-1}$  for  $x = 30$  to a minimum of  $0.29 \text{ mm s}^{-1}$  for  $x = 70$ . The authors interpret these results as consistent with a random atomic arrangement of the amorphous state and any inherent short range order bears no resemblance to that of the crystalline state. Similar studies have been performed by other workers [70].

Further phase identification in the Fe-Ti system using Mössbauer spectroscopy has been undertaken by Stupel *et al.* [56,64]. In particular, the metastable phases which appear after quenching from  $1000 \text{ }^\circ\text{C}$  or by ageing at  $320 \text{ }^\circ\text{C}$  for 1 hour. Also during many of these processes the formation of a small quantity of crystalline FeTi occurs which is beyond the detection limits of XRD. However, this minute quantity of FeTi is particularly useful for analysis of the room temperature Mössbauer data. In general, the Fe concentration present within the Ti rich phase under study was calculated by considering the spectral area  $A_i$  corresponding to the  $i$ th phase is proportional to the product  $f_i x_i C_i$  where the  $f_i$  is the recoil free fraction,  $x_i$  is the weight fraction and  $C_i$  corresponds to the iron concentration. Therefore the iron concentration within the Ti rich phase, in equilibrium with FeTi, is obtained from the following relationship [71]:

$$\frac{A_{\text{FeTi}}}{A_{\text{Ti rich}}} = \frac{f_{\text{FeTi}} X_{\text{FeTi}} C_{\text{FeTi}}}{f_{\text{Ti rich}} X_{\text{Ti rich}} C_{\text{Ti rich}}}$$

However, f-factor data for the relevant phases are scarce and further analysis assumes equal f-factors. Such studies highlight the need for further investigation into the FeTi

phase, in particular, variable temperature Mössbauer studies are required for f-factor evaluation. Using the above analysis method Stupel determined the solubility of iron in  $\alpha$ -Ti in the temperature range 360 - 580 °C. The Fe solubility was found to increase from 0.009 wt % at a temperature of 360 °C to 0.053 wt % at 580 °C. Similar studies for the Fe rich part of the Fe-Ti phase diagram have been undertaken by Wertheim *et al.* and references therein [72]. In these studies the maximum solubility of Ti in bcc  $\alpha$ -Fe was found to be approximately 10 % occurring at 1290 °C.

An early study [72] on the intermetallic FeTi using Mössbauer spectroscopy showed the characteristic singlet spectrum of FeTi at 4.2 K. At present no variable temperature Mössbauer studies have been performed yielding data regarding the recoil free fraction or Debye temperature of the compound. However, a study by Wang *et al.* [73] has provided an estimate for the Debye temperature from differential scanning calorimetry measurements. In this study heat capacities of FeTi and Fe<sub>2</sub>Ti were measured through the temperature range 120-700 K. These measurements were used to determine the Néel temperature of the magnetic transition of Fe<sub>2</sub>Ti. Similarly the Debye temperature for both FeTi and Fe<sub>2</sub>Ti were determined by a method considering the enthalpy of formation. Generally, the stability of an intermetallic compound is given by the Gibbs free energy of formation which is almost the same as the enthalpy of formation at low temperatures. Both enthalpies of formation for Fe<sub>2</sub>Ti and FeTi are negative, and Fe<sub>2</sub>Ti has a more negative value. Therefore the intermetallic compound Fe<sub>2</sub>Ti must be more stable than FeTi. Calculations using the heat capacity data yielded Debye temperatures of  $\theta_D = 505.5$  K and  $\theta_D = 361.0$  K for FeTi and Fe<sub>2</sub>Ti respectively. The Debye temperature of 505.5 K for FeTi agrees well with the value of 540 K reported by other workers [74] from heat capacity measurements.

### 2.5.3 Single Crystals of FeTi

The growth and properties of single crystal FeTi have been studied by Liebertz *et al.* [75]. In this study, single crystals with a diameter of 34 mm and a length of 48 mm were grown from the melt with an excess of 1 % Ti employing the Bridgman technique [76].

These workers found that the only crucible material resistant to contamination is electrographite. Other workers have encountered similar contamination problems during the preparation of FeTi due to ceramic based crucible materials reacting with the melt. In the study by Liebertz, early attempts to produce single crystals employing the Czochralski technique carried out under an argon atmosphere were not successful. Analysis showed FeTi grains with inclusions of other phases due to impurities floating on the melt. These impurities induced a steady nucleation at the growth interface. However, this is not a problem with the Bridgman technique since crystallisation starts from the bottom of the crucible and reaches the upper surface only at the end of the process. By using the technique, the whole crucible with an inner diameter of 34 mm was moved downwards at 10 mm per hour and solidified completely into a single crystal. XRD showed both Fe<sub>2</sub>Ti and FeTi phases present at crystal pieces cleaved close to the crucible. Further analysis showed single phase FeTi for cleaved crystals from the core of the crucible. Determination of the lattice constant yielded the value  $a = 2.978 \pm 0.002 \text{ \AA}$  for 293 K Bragg reflection measurements. This represents a lattice mismatch with  $\alpha$ -Fe of only about 4 %. By using a buoyancy method, the density of a single crystal piece weighing approximately 43 g was found to be  $\rho = 6.465 \text{ g cm}^{-3}$ . This is only about 1 % smaller than the value calculated from the lattice constant for stoichiometric composition.

Felter *et al.* [77] have studied the (100) and (111) planes of crystalline FeTi using LEED. In this study single crystals of FeTi were isolated from a bulk melt. Subsequent cleaning by argon bombardment and heating to at least 1200 K, produced well ordered surfaces on the crystals as determined by AES. The measured lattice parameter using LEED was found to be  $a_0 = 4.3 \pm 0.2 \text{ \AA}$  for the (111) plane of FeTi. This is in agreement with the nearest neighbour distance in the (111) plane which is simply  $\sqrt{2}$  times the accepted lattice constant measured by XRD of  $a = 2.98 \text{ nm}$  [75].

Amorphous and nanocrystalline FeTi has been produced using a ball milling technique by Zaluski *et al.* [78]. In this study, FeTi was produced by ball milling using tungsten

carbide balls and a mixture of Fe and Ti powders under a purified argon atmosphere. XRD showed the formation of FeTi to depend strongly on the level of oxygen during the ball milling process. TEM examination showed equiaxed grains of nanocrystalline grains of FeTi about 7 nm in size for samples having a final oxygen content lower than 3 at %. Amorphous FeTi, confirmed by TEM, was found only to occur for oxygen content greater than 3 %. They conclude that oxygen contamination is responsible for the formation of amorphous phases in mechanical alloying of Ti and Fe powders. A similar observation has been made for NiZr films [79].

It should be noted that studies using XRD data regarding FeTi can lead to ambiguity and even misinterpretation since Fe and Ti have similar X-ray scattering factors and the superlattice lines of polycrystalline FeTi have a very low intensity. In fact, the intensity of the strongest superlattice line (001) is only about 2 % of the strongest line (011) line in the structure. This is particularly important when studying thin films comprising of FeTi.

#### 2.5.4 Predicted Isomer Shifts in Amorphous Fe Based Alloys

A study by van der Kraan *et al.* [80] has investigated the concentration dependence of the  $^{57}\text{Fe}$  Mössbauer isomer shift (IS) in various  $\text{Fe}_x\text{A}_{1-x}$  alloys, where the A component is a non-magnetic material. In this study amorphous alloys for A = Ti, B, Hf and Nb were prepared by means of source evaporation of the elements onto aluminium substrates. The base pressure of the high vacuum system was about  $5 \times 10^{-8}$  torr and the thickness of the deposited amorphous films were measured by Talystep techniques. The investigation has proved successful in determining the unstrained dilute limit of IS for a variety of amorphous systems. These values were obtained and analysed in terms of a model for the isomer shift of  $^{197}\text{Au}$  containing alloys first proposed by Miedema *et al.* [81]. In this model, the heat of formation,  $\Delta H$  of an intermetallic compound is described by two contributions:

$$\Delta H = F(x) \left[ P(\Delta\phi)^2 + Q(\Delta n_{WS}^{1/3})^2 \right]$$

where  $F(x)$  is a function of concentration, while  $P$  and  $Q$  are constants for a given group of metal combinations. The first term  $\Delta\phi$  is the electronegativity difference between the two metals i.e.  $\Delta\phi = \phi_A - \phi_{Fe}$ . This term makes a negative contribution to the heat of formation. The term takes into account the fact that electrons have a preference for one of the two metals during alloying. The second term originates from the discontinuity in electron density at the interface between dissimilar Fe and A atoms. This difference at the Weigner-Seitz atomic cell boundaries is given by  $\Delta n_{WS} = n_{WS}^A - n_{WS}^{Fe}$ . This term makes a positive contribution to the heat of formation. The work of van der Kraan *et al.* and Miedema *et al.* combine to give an expression for the unstrained dilute limit of the isomer shift  $\delta(IS)_{MAX}$ , in terms of electronegativity and electron densities at the atomic cell boundaries for a dilute system where each iron atom is only surrounded by A atoms:

$$\delta(IS)_{MAX} = P'(\phi_A - \phi_{Fe}) + Q' \frac{(n_{WS}^A - n_{WS}^{Fe})}{n_{WS}^{Fe}} \quad (2.3)$$

where  $P'$  and  $Q'$  are constants for given materials and for the same Mössbauer isotope. The term  $\phi_A - \phi_{Fe}$  implies a linear relationship to exist between the change in the number of electrons per iron atom and the increase in the s-electron density at the Fe nucleus. It is also assumed that the charge transfer relative to pure iron for an Fe atom which is completely surrounded by A neighbours is proportional to  $\phi_A - \phi_{Fe}$ , where the electronegativity,  $\phi_{Fe} = 4.93$  V.

It should be noted here that amorphous alloys are free from the difficulties associated with any atomic volume mismatches contributing to IS. In dilute crystalline alloys, this mismatch is of a consequence of the Fe atoms occupying sites of the host metal A atoms which differ in size. However in amorphous alloys and intermetallics all the component atoms are free to choose their own volume. For this reason amorphous and intermetallic states are expected to behave in an analogous way.

Experimental values of  $\delta(\text{IS})_{\text{MAX}}$  can be obtained for a given alloy series  $\text{Fe}_x\text{A}_{1-x}$  by extrapolation after plotting the measured IS values as a function of contact surface concentration defined by:

$$C_A^s = \frac{(1-x)V_A^{2/3}}{xV_{\text{Fe}}^{2/3} + (1-x)V_A^{2/3}}$$

where  $V_A$  and  $V_{\text{Fe}}$  are the atomic volumes of the A and Fe atoms respectively. The experimental values of  $\delta(\text{IS})_{\text{MAX}}$  have been calculated by van der Kraan *et al.* [80]. This can be achieved easily since  $\phi$  and  $n_{\text{WS}}$  values have been tabulated for all metals [82]. Therefore, in accordance with equation (2.3), by plotting the experimental values of  $\delta(\text{IS})_{\text{MAX}} / \Delta\phi$  for the alloys where A = Nb, Ti, Hf, Th, Zr and Y against the corresponding values of  $(\Delta n/n)\Delta\phi$  yields a straight line. From the intercept on the y-axis and from the gradient of the line, the values of P' and Q' are 0.75 and -1.65 respectively. Thus, equation (2.3) may be re-written as:

$$\delta(\text{IS})_{\text{MAX}}^{\text{calc}} = 0.75\Delta\phi - 1.65 \frac{\Delta n_{\text{WS}}}{n_{\text{WS}}^{\text{Fe}}}$$

For a finite concentration  $x$ , the isomer shift is expected to vary linearly with the area of contact for a given Fe atom with A neighbours. This fractional area of contact can be estimated by weighting the actual atomic fraction with the cross sectional areas of Fe and the alloying element. For amorphous alloys the co-ordination of the Fe atoms can be described as a statistical distribution,  $x$  having a mean  $\bar{x}$  of A and Fe atoms in the nearest neighbours to the Fe atoms. The corresponding concentrations are given by:

$$\bar{x} = \frac{xV_{\text{Fe}}^{2/3}}{xV_{\text{Fe}}^{2/3} + (1-x)V_A^{2/3}} \quad (2.4)$$

In this expression the cross-sectional areas of the Fe and A atoms have been taken to be proportional to  $V^{2/3}$ , where  $V$  is the atomic volume i.e. the atomic weight divided by the density. The concentration dependence of  $\delta(\text{IS})_{\text{MAX}}$  is then given as:

$$\delta IS = (1 - \bar{x})\delta(IS)_{MAX} \quad (2.5)$$

Experimental values of  $\delta(IS)_{MAX}$  compare well with the corresponding calculated values for amorphous  $Fe_xA_{1-x}$  alloys where A is a transition metal. Table 2.2 shows this comparison for a selection of elements.

	Nb	Hf	Ti	Th	Zr	Y
calculated $\delta(IS)_{MAX}$ (mm s <sup>-1</sup> )	-0.32	-0.25	-0.27	-0.20	-0.31	-0.18
experimental $\delta(IS)_{MAX}$ (mm s <sup>-1</sup> )	-0.30	-0.32	-0.26	-0.21	-0.35	-0.20

Table 2.2 Experimental and calculated  $\delta(IS)_{MAX}$  values relative to  $\alpha$ -Fe for various A components in amorphous  $Fe_xA_{1-x}$  alloys .

It can be seen from table 2 that good agreement exists between the calculated and experimental values of the unstrained dilute limit of IS. This is of particular importance, since by using the appropriate  $\delta(IS)_{MAX}$  and equations (2.4) and (2.5) it is possible to estimate the Fe concentration of  $Fe_xA_{1-x}$  alloys from the measured IS value.

The same empirical approach has been used by van der Kraan *et al.* [83] with application to intermetallic compounds. The method leads to different values of the constants P' and Q' leading to an expression for the unstrained dilute limit  $\delta(IS)_{MAX}$  as:

$$\delta(IS)_{MAX}^{calc} = 1.08\Delta\phi - 2.51 \frac{\Delta n_{WS}}{n_{WS}^{Fe}}$$

For the intermetallic FeTi, the experimental and calculated unstrained dilute limit values of the isomer shift are -0.28 and -0.33 mm s<sup>-1</sup>, respectively. The difference between the two values is due partly to ambiguity in the experimental value. This ambiguity arises

since only two intermetallics, FeTi and Fe<sub>2</sub>Ti exist in the Fe-Ti system, thereby making accurate graph extrapolation difficult.

It is clear from the different values of P' and Q' associated with amorphous and intermetallic states that the constants depend on the nature of the Fe environment. In particular, the Q' term is a measure of the intra-atomic redistribution of the s- and d-electrons around the Fe atom. This quantity is sensitive to the local symmetry of the Fe nucleus environment. This symmetry is low in amorphous and crystalline alloys but is high in intermetallic compounds. This may explain the reported differences in P' and Q' constant values reported by Dubiel *et al.* [84]. However, the outlined model predicts the isomer shift accurately for the amorphous compounds of the type Fe<sub>x</sub>A<sub>1-x</sub> where A is a transition metal. The model is less accurate for the intermetallics, but does correctly predict that the isomer shift is negative when Fe is combined with transition metals and is positive when combined with s and p metals or metalloids e.g. Sn, Al, Ga, Si etc.

#### 2.5.5 Amorphous alloy Fe<sub>1-x</sub>Ti<sub>x</sub>

Amorphous alloys of the type Fe<sub>1-x</sub>Ti<sub>x</sub> (0.25 ≤ x ≤ 0.75) have been prepared using a sputtering technique by Sumiyama *et al.* [70]. In this study, a facing target type sputtering system was used to prepare alloy films 50 μm in thickness on water cooled substrates. The alloy concentration was adjusted by changing the ratio of the surface area of Fe and Ti targets. XRD analysis showed amorphous Fe<sub>1-x</sub>Ti<sub>x</sub> alloys produced for x = 0.25 to x = 0.74. Also α-Fe, α-Ti and β-Ti phases formed for varying deposited Ti concentrations in accordance with the Fe-Ti phase diagram. The study used transmission Mössbauer spectroscopy at 4.2 K and room temperature to study the magnetic behaviour of Fe<sub>1-x</sub>Ti<sub>x</sub> as a function of x. The Mössbauer measurements showed a ferromagnetic sextet at 4.2 K for x = 0.34 indicating a distribution of the magnetic hyperfine field. The

same workers also showed the formation of the amorphous and crystalline alloy using a different sputtering technique. This indicates that the formation of the amorphous phase is insensitive to the sputtering method and that the  $\text{Fe}_{1-x}\text{Ti}_x$  alloy is stable against the competing crystalline phase. An earlier study by Liou *et al.* [85] investigated the magnetic properties of sputtered  $\text{Fe}_x\text{Ti}_{1-x}$  alloys for  $30 \leq x \leq 80$ . In this study, transmission Mössbauer spectroscopy at room temperature showed the characteristic quadrupole splitting for all the amorphous alloys. However, at 4.2 K the effective magnetic hyperfine field,  $H_{\text{eff}}$  was found to change as a function of  $x$ . The value of  $H_{\text{eff}}$  was found to be 200 kOe at  $x = 80$  and decreased monotonically as the Fe concentration is reduced, and reaches a zero value at approximately the magnetic threshold at  $x = 0.43$ . Both these studies show distinct differences in the hyperfine parameters between the crystalline FeTi and  $\text{Fe}_2\text{Ti}$  phases with all compositions of  $\text{Fe}_x\text{Ti}_{1-x}$ . Such differences in the isomer shift and quadrupole splittings provide evidence against any similar local short range order in the amorphous and crystalline states.

The average isomer shift and average quadrupole splittings of amorphous  $\text{Fe}_{1-x}\text{Ti}_x$  depends greatly on the concentration,  $x$ . A summary of this dependence, from the work of Sumiyama *et al.* [70] and Liou *et al.* [85] are shown in figs. 2.18 and 2.19. The negative isomer shift compared with  $\alpha$ -Fe is due to electron donations from Ti to Fe sites. The overall decrease in the isomer shift for increasing  $x$  concentration corresponds to a decrease in the s-electron density at the Fe nucleus arising from the expansion of the s-electron wavefunction by adding successive Ti atoms. The range of the average quadrupole splitting shown in fig. 2.19, indicates a wide variety of number, angle and spacing distributions of near neighbours around Fe atoms.

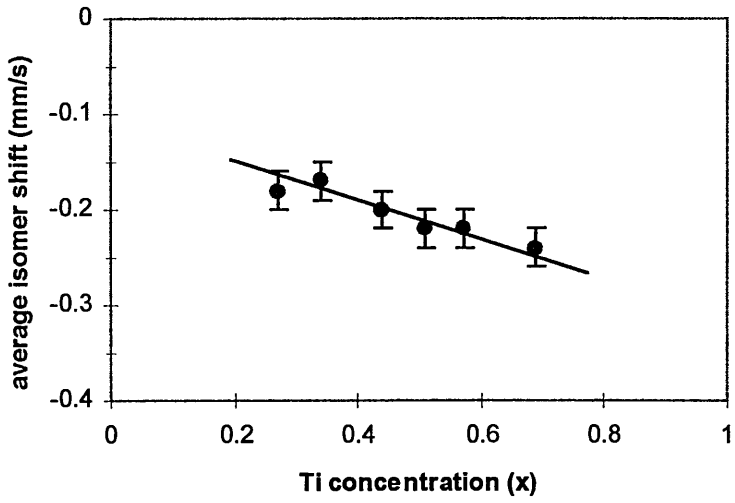


Fig. 2.18 Isomer shift dependence on x for amorphous  $\text{Fe}_{1-x}\text{Ti}_x$  alloy [70, 85].

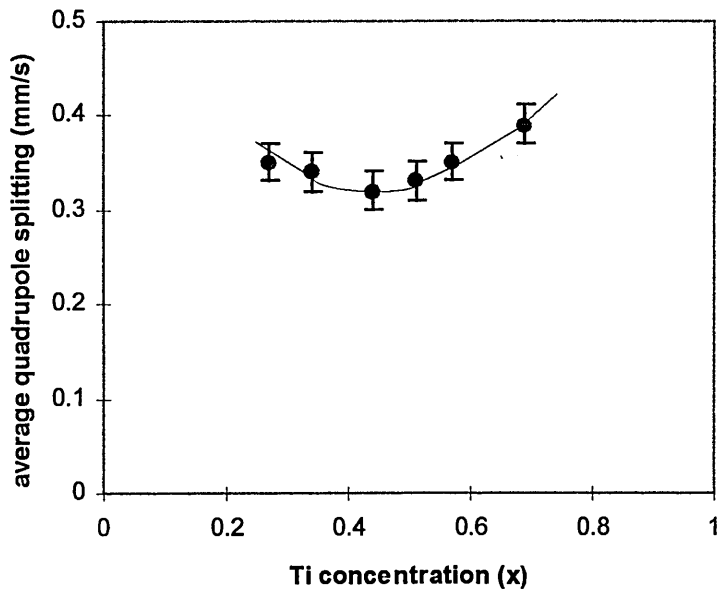


Fig. 2.19 Quadrupole splitting dependence on x for amorphous  $\text{Fe}_{1-x}\text{Ti}_x$  alloy [70, 85].

The thermal stability of amorphous  $\text{Fe}_{1-x}\text{Ti}_x$  alloys prepared by rf sputtering has been studied by Sumiyama *et al.* [86]. In this study 2  $\mu\text{m}$  thick films of the amorphous alloy for  $x = 0.2$  to  $0.75$  were deposited on substrates of polyamide and silicon wafers. Electron probe microanalysis determined the composition of the sputtered alloys. Both XRD and transmission Mössbauer spectroscopy showed amorphous  $\text{Fe}_{1-x}\text{Ti}_x$  for  $x = 0.3 - 0.4$  to be thermally stable up to 770 K. However after annealing for several hours, the amorphous phase transformed to crystalline  $\text{Fe}_2\text{Ti}$  at a temperature of 870 K. Further experiments showed the amorphous phase to transform after annealing at 670 K to  $\alpha\text{-Fe}$  for  $x < 0.3$ , to crystalline  $\text{FeTi}$  for  $0.45 < x < 0.63$ , to  $\text{Fe}_2\text{Ti}$  for  $0.65 < x < 0.7$ . Also for  $x = 0.7 - 0.75$  after annealing under the same conditions, the amorphous phase transformed to  $\text{Fe}_2\text{Ti}$  and bcc  $\beta\text{-Ti}$  solid solution. For all compositions of the amorphous alloy the Mössbauer spectra showed a slightly asymmetric quadrupole splitting. It has been suggested that this is due to a distribution of electric field gradients over the random ionic co-ordinations of amorphous solids [87].

Another study by Harada *et al.* [88] has investigated the thermal stability of Ti films deposited on Fe substrates (Ti/Fe) and Fe films evaporated on Ti substrates (Fe/Ti) by Mössbauer spectroscopy. In this study the evaporated layers were deposited at room temperature and the thickness of both the Fe layers and substrates were 10  $\mu\text{m}$ , while those of the Ti layers and substrates were 30 and 50  $\mu\text{m}$  respectively. After evaporation the samples were annealed for 1 hr between the temperature range of 700 - 1000  $^\circ\text{C}$ . Immediately after evaporation, transmission Mössbauer spectroscopy on the Ti/Fe films showed spectra similar to that of an Fe foil. No significant change in the spectrum was observed after heat treatment below 600  $^\circ\text{C}$ . After annealing, increasing spectral areas associated with both a singlet and doublet were observed for increasing temperatures from 700 - 1000  $^\circ\text{C}$ . Since no change in the isomer shift occurred over temperature range, the singlet was attributed to crystalline  $\text{FeTi}$  formed at the Ti/Fe interface, in accordance with the parameters of Chien *et al.* [65]. However, changes in the isomer shift and quadrupole splitting due to the doublet at temperatures upto 800  $^\circ\text{C}$  indicated the formation of  $\text{Fe}_x\text{Ti}_{1-x}$  at the interface. At annealing temperatures above 800  $^\circ\text{C}$  no

such change in the quadrupole splitting was observed and the hyperfine parameters agree well with those of  $\text{Fe}_2\text{Ti}$ . The relative amounts of  $\text{FeTi}$  and  $\text{Fe}_2\text{Ti}$  (or  $\text{Fe}_x\text{Ti}_{1-x}$ ) were estimated from the respective areas of the singlet and doublet. These relative amounts were found to increase from a few percent at  $700\text{ }^\circ\text{C}$  to almost 20 % at  $1000\text{ }^\circ\text{C}$ . Below  $800\text{ }^\circ\text{C}$ , the amount of  $\text{Fe}_x\text{Ti}_{1-x}$  is greater than that of  $\text{FeTi}$ . However, at temperatures above  $900\text{ }^\circ\text{C}$  the amount of  $\text{Fe}_2\text{Ti}$  and  $\text{FeTi}$  are almost the same. The changes in the relative amounts with temperature can be explained as follows.  $\text{Fe}_2\text{Ti}$  is formed in a relatively Fe rich layer and  $\text{FeTi}$  is formed in a relatively rich Ti layer. Since  $\text{Fe}_x\text{Ti}_{1-x}$  is formed during annealing below  $800\text{ }^\circ\text{C}$ , Ti atoms must diffuse into the Fe substrate more easily than Fe atoms diffuse out into the Ti layer. In contrast, at temperatures above  $800\text{ }^\circ\text{C}$ , both  $\text{FeTi}$  and  $\text{Fe}_2\text{Ti}$  are formed indicating more significant diffusion of the Fe atoms into the Ti layer. For the Fe/Ti films similar Mössbauer spectra were observed for the same annealing conditions. However, the relative amount of  $\text{FeTi}$  is significantly larger than that of  $\text{Fe}_2\text{Ti}$  above  $800\text{ }^\circ\text{C}$  and increases to approximately 45 % at  $1000\text{ }^\circ\text{C}$  compared with a few percent associated with  $\text{Fe}_2\text{Ti}$  at the same temperature. This suggests the diffusion of Fe atoms into the Ti substrate through lattice defects occurs much more readily than the diffusion of Ti atoms into the Fe film.

## References

- [1] L. Holland, in "Vacuum Deposition of Thin Films" (Chapman and Hall, London, 1966).
- [2] A. Matthews, *Surf. Eng.* **1(2)** (1985) 93.
- [3] S. Schiller, U. Heisig, M. Neumann and G. Beister, *Vak. Tech.* **35** (1986) 35.
- [4] H. K. Pulker, in "Coatings on Glass", (Elsevier, Amsterdam, 1984).
- [5] A. A. Snapper, USP 3625848/1971.
- [6] A. A. Snapper, USP 3836451/1974.
- [7] L. P. Sablev, USP 3793179/1974.
- [8] J. Vyskocil and J. Musil, *J. Vac. Sci. Technol. A* **10(4)** (1992) 1740.
- [9] R. L. Boxman and S. Goldsmith, *Surf. Coat. Technol.* **52** (1992) 39.
- [10] J. E. Dalder, *J. Phys. D: Appl. Phys.* (1976) **9** 2379.
- [11] C. N. Tai, E. S. Koh and K. Akari, *Surf. Coat. Technol.* **43/44** (1990) 324.
- [12] H. D. Steffens, M. Mack, K. Moehwald and K. Reichel, *Surf. Coat. Technol.* **46** (1991) 65.
- [13] P. J. Martin, R. P. Netterfield, A. Bendavid and T. J. Kinder, *Surf. Coat. Technol.* **54/55** (1992) 136.
- [14] D. M. Sanders, *J. Vac. Sci. Technol. A.* **6** (1988) 1929.
- [15] J. Vyskocil and J. Musil, *Surf. Coat. Technol.* **43/44** (1990) 299.
- [16] A. E. Robson and A. Von Engel, *Phys. Rev.* **93** (1954) 1121.
- [17] V. A. Nemchinskii, *Sov. Phys.-Tech. Phys.* **24(7)** (1979) 767.
- [18] D. Y. Fang, *J. Phys. D: Appl. Phys.* **15** (1982)
- [19] P. A. Dearnley, *Proc. of ASM Conf. Ion Plating and Implantation* (1986) 31.
- [20] E. Bergmann, *Surf. Coat. Technol.* **57** (1993) 133.
- [21] N. Dingremont, E. Bergmann and P. Collignon, *Surf. Coat. Technol.* **72** (1995) 157.
- [22] N. Dingremont, E. Bergmann, M. Hans and P. Collignon, *Surf. Coat. Technol.* **76/77** (1995) 218.
- [23] J. A. Thornton, *J. Vac. Sci. Technol.* **15(2)** (1978) 171.
- [24] W. Yao, S. Tung, W. Sai and Z. Qi, *Plasma Surf. Eng.* **1** (1989) 633.
- [25] S. Kadlec and J. Musil, *Surf. Coat. Technol.* **39/40** (1990) 39/40 487.
- [26] S. Kadlec, J. Musil, V. Valdova, W. -D. Münz, H. Petersein and J. Schroeder, *Vacuum* **41** (1990) 2233.
- [27] D. Monaghan and R. D. Arnell, *Vacuum* **43** (1992) 77.
- [28] M. S. Wong, W. D. Sproul and S. L. Rohde, *Surf. Coat. Technol.* **49** (1991) 121.
- [29] S. L. Rohde, I. Petrov, W. D. Sproul, S. A. Barnett, P. J. Rudwik and M. E. Graham, *Thin Solid Films* **193/194** (1990) 117.
- [30] W. D. Sproul, *Surf. Coat. Technol.* **49** (1991) 284.
- [31] I. Efeoglu, R. D. Arnell, S. F. Tinston and D. G. Teer, *Surf. Coat. Technol.* **57** (1993) 61.
- [32] G. Häkansson, L. Hultman, J. -E. Sundgren, J. E. Greene and W. -D. Münz *Surf. Coat. Technol.* **48** (1991) 51.
- [33] W. -D. Münz, D. Schulze and F. J. M. Hauzer, *Surf. Coat. Technol.* **50** (1992) 169.

- [34] A. H. Cottrell, in "An Introduction to Metallurgy", (Edward Arnold, London, 1967).
- [35] A. Zangwill, in "Physics at Surfaces", (Cambridge University Press, Cambridge, 1988).
- [36] P. G. Shewmon, in "Diffusion in Solids", (McGraw-Hill, New York, 1963).
- [37] P. Ding, Z. Ni, S. Zhou and F. Pan, *Surf. Coat. Technol.* **49** (1991) 203.
- [38] G. Kuznetsov and V. Delian, *Surf. Coat. Technol.* **54/55** (1992) 96.
- [39] J. A. Thornton, *Metal Finishing* **5** (1979) 83.
- [40] P. C. Johnson, *Physics of Thin Films* **14** (1989) 129.
- [41] J. P. Biersack and W. Eckstein, *Appl. Phys. A* **34** (1984) 73.
- [42] B. A. Movchan and A. V. Demchishin, *Fiz. Met. Metalloved* **28** (1969) 653.
- [44] R. Messier, A. P. Giri and R. A. Roy, *J. Vac. Sci. Technol. A* **2** (1984) 500.
- [45] R. P. Howson, H. A. Jafer and A. G. Spencer  
*Thin Solid Films* **193/194** (1990) 127.
- [46] W. -D. M Münz, *Surf. Coat. Technol.* **48** (1991) 81.
- [47] S. Vuorinew, E. Niemi and A. S. Korhonen  
*J. Vac. Sci. Technol. A* **3** (1985) 2445.
- [48] D. S. Rickerby and R. Newbury, *Vacuum* **38** (1988) 161.
- [49] O. Knotek, R. Elsing, G. Kramer and F. Jungblut  
*Surf. Coat. Technol.* **46** (1991) 265.
- [50] J. M. Howe, *Int. Mat. Rev.* **38(5)** (1993) 233.
- [51] Q. Q. Yang, L. H. Zhao, H. Q. Du and L. S. Wen  
*Surf. Coat. Technol.* **81** (1996) 287.
- [52] D. S. Rickerby, A. M. Jones and B. A. Bellamy  
*Surf. Coat. Technol.* **37** (1989) 4375
- [53] U. C. Oh and Jung Ho Je, *J. Appl. Phys.* **74(3)** (1993) 1692.
- [54] J. C. Williams (1973) "Titanium Science and Technology" ed. by R. I. Jaffe and H. M. Burke p1433, Plenum Press, New York.
- [55] J. C. Williams, D. De Fontaine and N. E. Paton, *Metall. Trans.* **4** (1973) 2701.
- [56] M. M. Stupel, M. Ron and B. Z. Weiss, *J. Appl. Phys.* **47** (1976) 6.
- [57] F. Stuki, *J. Appl. Phys.* **53(3)** (1982) 2643.
- [58] T. Matsumoto and M. Amano *Scripta Metall.* **15** (1981) 879.
- [59] D. Khatamian, F. D. Manchester and J. M. Daniels, *J. Less-Common Met.* **130** (1987) 511.
- [60] D. Khatamian and F. D. Manchester, *Surf. Sci.* **186** (1987) 309.
- [61] J. H. Sanders and B. J. Tatarchuk, *Thin Solid Films* **166** (1988) 225.
- [62] J. L. Murray (1987) "Phase Diagrams of Binary Titanium Alloys" ed. by J. L. Murray p99 ASM International, Ohio, USA.
- [63] A. K. Molchanova (1965) "Phase Diagrams of Ti Alloys" p82 Israel Program for Scientific Translations.
- [64] M. M. Stupel, B. Z. Weiss and M. Ron, *Acta Metall.* **25** (1977) 667.
- [65] C. L. Chien and S. H. Liou, *Phys. Rev. B* **31(12)** (1985) 8238.
- [66] W. Bruckner, R. Perthel, K. Kleinstuck and G. E. R. Schultze  
*Phys Status Solidi* **29** (1968) 211.
- [67] M. E. Lines, *Phys. Rev. B* **20** (1979) 3729.
- [68] G. K. Wertheim, J. H. Wernick and R. C. Sherwood  
*Solid State Comm.* **7** (1969) 1339.

- [69] J. Pelloth, R. A. Brand and W. Keune  
*J Magn and Magn Mat* **140-144** (1995) 59.
- [70] K. Sumiyama, H. Yasuda and Y. Nakamura,  
*J. Phys. Cond. Matt.* **2** (1990) 3595.
- [71] M. M. Stupel, M. Bamberger and M. Ron, *J. Less-Comm. Met.* **123** (1986) 1.
- [72] G. K. Wertheim and J. H. Wernick, *Acta Metall.* **15** (1967) 297.
- [73] H. Wang R. Lück and B Predel, *Z. Metallkunde* **84** (1993) 4.
- [74] R. Kuentzler and R. M. Waterstrat, *J. Less-Comm. Met.* **125** (1986) 261.
- [75] J. Liebertz, S. Stäher and S. Haussühl, *Kristall und Technik* **15(11)** (1980) 1257.
- [76] C. Batur, A. Srinivasan, W. M. B. Duval and N. B. Singh,  
*Prog. Crys. Grow. Char. Mat.* **30(4)** (1995) 217..
- [77] T. E. Felter, S. A. Steward and F. S. Uribe, *Surf. Sci.* **122** (1982) 69.
- [78] L. Zuluski, S. Hosatte, P. Tessier, D. H. Ryan, J. O. Ström-Olsen, M. L. Trudeau  
and R. Schulze, *Zeit Für Physik Chemie BD* **183(5)** (1994) 1067.
- [79] J. J. Hauser, *Phys. Rev. B* **32** (1985) 2287.
- [80] A. M. Van der Kraan and K. H. J. Buschow *Phys Rev B* **27(5)** (1983) 2693.
- [81] A. R. Miedema and F. Van der Woude, *Physica* **100B** (1980) 145.
- [82] A. K. Niessen, F. R. De Boer, R. Boom, P. F. Châtel, W. C. M. Mattens  
A. R. Miedema, *Calphad* **7** (1983) 51.
- [83] A. M. Van der Kraan and K. H. J. Buschow, *Physica* **138** (1986) 55.
- [84] S. M. Dubiel and W. Zinn, *Phys. Rev. B* **29** (1984) 2279.
- [85] S. H. Liou and C. L. Chien, *J. Appl. Phys.* **55(6)** (1984) 1820.
- [86] K. Sumiyama, H. Ezawa and Y. Nakamura, *Acta Metal.* **35** (1987) 1221.
- [87] G. Czjzek, J. Finki, F. Götz, H. Schmidt, J. M. D. Coey, J. P. Rebouillat  
and A. Lienard, *Phys. Rev. B* **23(6)** (1981) 2513.
- [88] H. Harada, S. Ishibe, R. Konishi and H. Saskura  
*Jap. J. Appl. Phys.* **24(9)** (1985) 1141.

## CHAPTER 3

# THE MÖSSBAUER EFFECT AND MÖSSBAUER SPECTROSCOPY

### 3.1 Theoretical linewidth of the Emitted 14.4 keV $\gamma$ -Ray

The well known effect of recoilless resonance fluorescence within a nuclear system was first reported in 1958 by R. L. Mössbauer [1]. Since then, over 50 isotopes have been shown to exhibit the Mössbauer effect and more than 20 isotopes can give useful information without any extreme experimental difficulty. However, the majority of Mössbauer spectroscopy applications have concentrated on the isotopes  $^{57}\text{Fe}$  and  $^{119}\text{Sn}$ . The utilisation of the Mössbauer effect as a form of high energy resolution spectroscopy, makes use of nuclear  $\gamma$ -rays with energies in the range of 10 -100 keV. The associated lifetimes of nuclear excited states producing such  $\gamma$ -rays are typically  $10^{-10}$  s to  $10^{-6}$  s. This results in a typical natural linewidth of the order  $10^{-8}$  eV. This represents a much higher intrinsic resolution than that of any other spectroscopy.

Radioactive  $^{57}\text{Fe}$  is produced by the electron capture decay of  $^{57}\text{Co}$  as shown in fig. 3.1. The decay scheme of  $^{57}\text{Co}$  results in the emission of essentially three  $\gamma$ -rays of energies of 14.4, 122, and 136 keV.

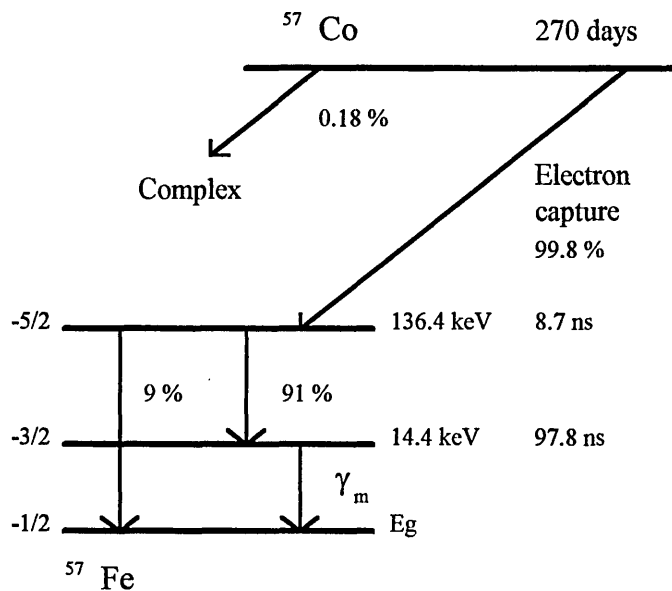


Fig. 3.1 Decay scheme for  $^{57}\text{Co}$ .

The emitted Mössbauer  $\gamma$ -ray,  $\gamma_m$  has a Lorentzian energy distribution centred on a mean energy,  $E_0$  and having a natural linewidth at half height,  $\Gamma$  shown in fig. 3.2.

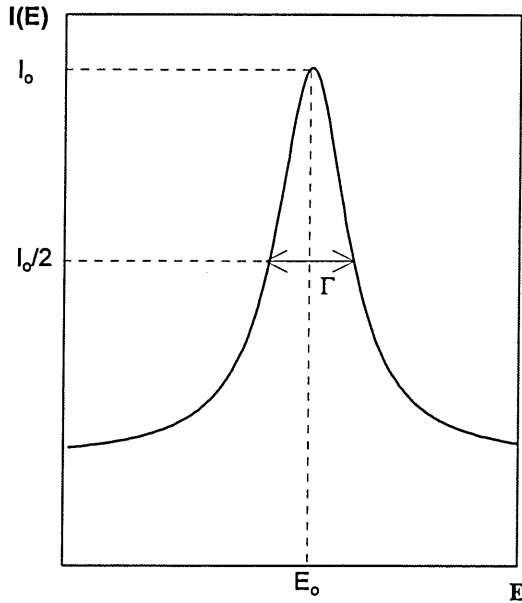


Fig. 3.2 The Lorentzian distribution of the emitted  $\gamma$ -ray.

The energy distribution of the  $\gamma$ -rays is defined by the Breit-Wigner equation [2]. The process of recoilless nuclear resonance fluorescence occurs by the superposition of the emission and absorption energy profiles associated with both the source and the absorber. Therefore, the theoretical Mössbauer natural linewidth,  $\Gamma_H = 2\Gamma$  and is controlled by the Heisenberg uncertainty principle such that:

$$\Delta E \cdot \Delta t \geq \hbar \text{ or } \Gamma_H \cdot \tau = \hbar$$

where  $\hbar = h / 2\pi = h / 2\pi$  ( $h = \text{Planck's constant} = 6.626 \times 10^{-34} \text{ J s}$ )

and  $\tau$  is the mean lifetime, related to the half-life,  $t_{1/2}$  by the relationship:

$$\tau = \frac{t_{1/2}}{\ln 2}$$

Hence

$$\Gamma_H = \frac{\hbar \ln 2}{t_{1/2}} \quad (3.1)$$

The 14.4 keV excited state of the  $^{57}\text{Fe}$  nucleus has a half-life of 97.8 ns [3]. Substituting numerical values into equation (3.1) and remembering that  $1\text{eV} = 1.602 \times 10^{-19} \text{ J}$ , the theoretical linewidth,  $\Gamma_{\text{H}} = 4.6 \times 10^{-9} \text{ eV}$ . This gives a theoretical resolution of:

$$\frac{\Gamma_{\text{H}}}{E} = \frac{4.6 \times 10^{-9}}{14.4 \times 10^{-3}} \approx \frac{1}{10^{12}}$$

i.e. approximately 1 part in  $10^{12}$ .

### 3.2 Mechanism of the Mössbauer Effect

Special experimental procedures are required in order to observe the energy transitions associated with the Mössbauer effect. Firstly, Doppler broadening increases the effective linewidth, and secondly, the recoil of the emitting nucleus displaces the emission line from the absorption line, making observation of the resonance absorption impossible. However, the crucial discovery by Mössbauer was that when the emitting nucleus is within a solid matrix at low temperature, there is a high probability that the recoil momentum of the emitted  $\gamma$ -ray will be taken up by the crystal lattice as a whole, rather than by a single nucleus. The mechanism may be described by considering a photon emitted from a nucleus of mass,  $m$ , moving with an initial velocity,  $V_{\text{T}}$ , due to thermal motion. The total energy above the ground state of the nucleus at rest is  $E_{\text{e}} + \frac{1}{2}mV_{\text{T}}^2$ . After emission, the  $\gamma$ -ray will have an energy  $E_{\gamma}$  and the nucleus a new velocity  $(V_{\text{T}} + v)$  due to recoil, where  $v$  is a vector in the opposite direction to  $V_{\text{T}}$ . Therefore, by conservation energy:

$$E_{\text{e}} + \frac{1}{2}mV_{\text{T}}^2 = E_{\text{g}} + E_{\gamma} + \frac{1}{2}m(V_{\text{T}} + v)^2$$

since the transition energy,  $E_{\text{t}} = E_{\text{e}} - E_{\text{g}}$

$$\begin{aligned} E_{\text{t}} &= \frac{1}{2}m v^2 + mV_{\text{T}} \cdot v + E_{\gamma} \\ E_{\text{t}} - E_{\gamma} &= \frac{1}{2}mv^2 + mV_{\text{T}}v \end{aligned} \quad (3.2)$$

This may be written as :

$$\delta E = E_{\text{R}} + E_{\text{D}} \quad (3.3)$$

From the description of the simple mechanism, it can be seen that the  $\gamma$ -ray energy differs from the nuclear energy level separation by an amount which depends on the recoil kinetic energy,  $E_R$ , and by  $E_D$  which is proportional to the atom velocity,  $V_T$  and is a Doppler effect energy. Therefore, emission of the  $\gamma$ -ray from the source results in an energy shift of the emission profile,  $E_\gamma = E_t - E_R$ . Similarly for resonant absorption, a  $\gamma$ -ray energy shift of  $E_\gamma = E_t + E_R$  occurs in the absorption profile. This effect of  $E_R$  on both the emission and absorption energy distribution is shown in fig. 3.3.

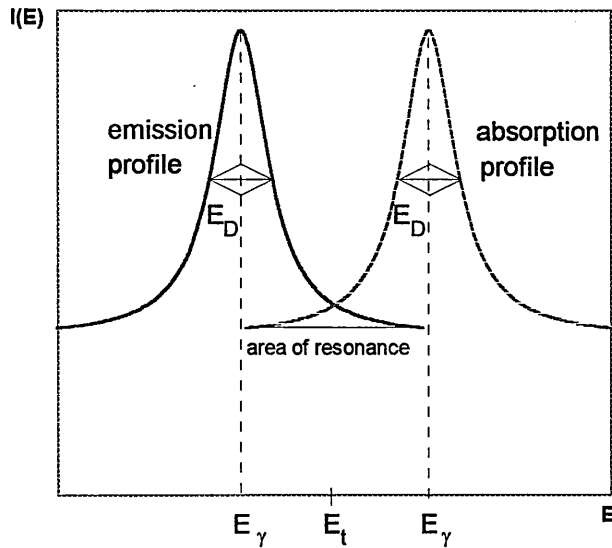


Fig. 3.3 Energy distribution profiles showing the effect of recoil and thermal Doppler broadening.

Fig. 3.3 also shows the effect of Doppler broadening,  $E_D$ , due to the random thermal velocities within the source and absorber. The magnitude of Doppler broadening can be considered for the one dimensional case, by relating the random thermal energy resulting from nuclei velocities  $v_T$ , to the absolute temperature,  $T$ :

$$\frac{1}{2} m \bar{v}_T^2 = \frac{1}{2} kT \quad : \text{ mean kinetic energy}$$

$$(\bar{v}_T^2)^{\frac{1}{2}} = \sqrt{\frac{kT}{m}}$$

From equations (3.2) and (3.3),  $E_D = mV_T v$

$$\therefore E_D = m v \sqrt{\frac{kT}{m}}$$

$$E_D = \sqrt{kT m v^2}$$

But  $E_R = \frac{1}{2}mv^2$

$$\therefore E_D = \sqrt{2kTE_R} \quad (3.4)$$

Therefore, it can be seen that the probability that resonance will occur depends on the magnitude of  $E_R$ . For transition energies of the order  $10^4$  eV, the value of  $E_R$  is significant and overlap of emission and absorption energy distributions is poor. It can also be seen from (3.4) that for thermal broadening to be zero, and hence theoretical resolution achievable, recoil must be eliminated. This condition is achieved for some nuclear transitions due to the quantised nature of the lattice.

### 3.3 The Quantised Lattice

Mössbauer discovered that for certain conditions, nuclei embedded in lattices at low temperatures were effectively “frozen” in the lattice and hence unable to recoil and experience the Doppler broadening of the associated emission and absorption lines. This effect of “freezing” arises due to the quantised nature of lattice vibrations described by Einstein.

The classical description of the behaviour of vibrating atoms within a solid, suggests that vibrating atoms on equilibrium positions occurs with an energy that varies continuously with temperature. However, Einstein realised that a solid is a quantum mechanical system and therefore its energy should be quantised and only certain allowable transitions could occur through phonon interactions. The Einstein energy  $E_E$ , is the minimum energy required to excite the lattice and corresponds to a single phonon transition of the lowest allowed energy  $E_E$ . The vibrational energy of a nucleus can be taken up either by the whole crystal or transferred to the lattice through phonon interactions. If the recoil energy,  $E_R$  is less than  $E_E$ , then a zero phonon interaction occurs and the recoil is taken up by the whole crystal. However, if  $E_R \gg E_E$ , many phonon interactions are involved and the energy is transferred to the vibrational energy of the lattice. Therefore, the emitted  $\gamma$ -ray suffers energy recoil and Doppler line broadening occurs.

### 3.4 Observation of the Mössbauer Effect

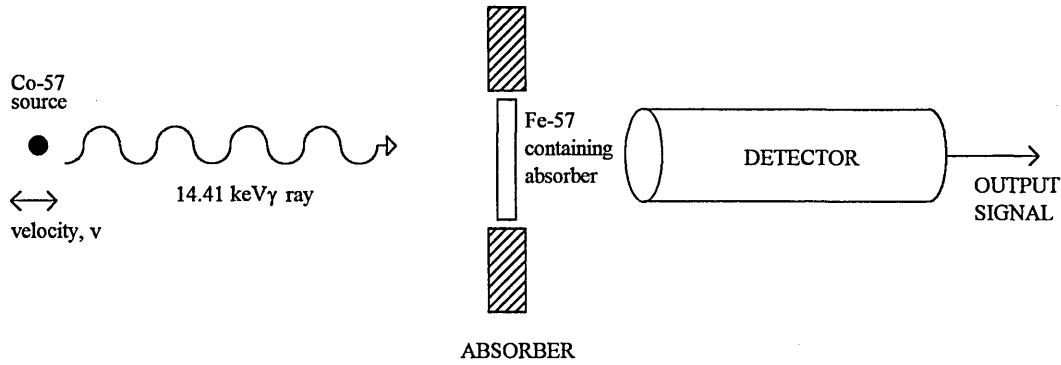


Fig. 3.4 Schematic representation of a Mössbauer experiment.

Fig. 3.4 considers the emission of the 14.41 keV Mössbauer  $\gamma$ -ray emitted by a  $^{57}\text{Co}$  source and an absorber containing  $^{57}\text{Fe}$  in an identical lattice. The detector is used to observe the intensity of the radiation which passes through the absorber. This intensity will be less than expected due to resonant absorption and subsequent re-emission over a  $4\pi$  solid angle. In order to observe the resonance, a Doppler velocity,  $v$  is applied to the source with respect to the absorber thereby producing an energy shift of the source spectral line. The energy of the  $\gamma$ -ray,  $E_\gamma$  is modified by the Doppler relationship:-

$$E_\gamma = E_0 \pm \frac{E_0 v}{c}$$

Therefore, by scanning a range of velocities, at a particular velocity and hence energy, when both the emission and absorption profiles are exactly coincident, resonance absorption will be observed. Thus a Mössbauer spectrum is a plot of absorption against a series of Doppler velocities between the source and absorber. Similarly, the modification of the emitted  $\gamma$ -ray energy by the Doppler effect can be used to achieve resonance when the transition energies of the source and absorber are different. Such differences in the nuclear energy levels are directly related to both the electronic and magnetic environment of the absorbing nuclei. Therefore, by utilising these differences in the nuclear energy levels, Mössbauer spectroscopy is a powerful tool for investigating the chemical and physical environment of the nucleus.

### 3.5 Hyperfine Interactions

The most important consequence of the Mössbauer effect is that it makes possible the analysis of the hyperfine structure of nuclear transitions. This is made possible by exploiting the precise energy resolution associated with the Mössbauer effect. The theoretical energy resolution provided by the Mössbauer effect for the  $^{57}\text{Fe}$  system has previously been shown to be approximately 1 part in  $10^{12}$ . The associated observed linewidths are comparable with or less than the interaction energies between the nuclei and the extra-nuclear electric and magnetic fields. These interactions between the nucleus and the surrounding environment are known as the Hyperfine Interactions.

The hyperfine interactions of an absorber containing a stable Mössbauer isotope are usually studied using a single line source. This radioactive source is mounted on a velocity transducer and the absorber is fixed in a suitable manner. Mössbauer absorption will take place within the absorber at a number of different Doppler energies due to the splitting of the nuclear energy levels by the hyperfine interactions. This is registered as a detected change in count rate when the Doppler velocity applied to the source brings the emitted  $\gamma$ -ray into coincidence with the absorption energy.

Three types of hyperfine interactions exist, the isomer shift,  $\delta$ , the quadrupole splitting,  $\Delta E_Q$  and the magnetic Zeeman splitting,  $H$ . Several review articles [3,4] describe the hyperfine interactions in detail. All the interactions can be expressed as a product of a nuclear term, which is a constant for any given Mössbauer  $\gamma$ -ray transition and an electronic term which is related to the absorber under study. A schematic representation of the hyperfine interactions is given in table 3.1.

Solid State Factor	Magnetic Field	Electronic Field Gradient	Electron Density at Nuclear site
	↓	↓	↓
Interaction	$\Delta E = \mu H$	$+ QVE$	$+ \text{const} \langle R^2 \rangle \rho(0)$
	↑	↑	↑
Nuclear Interaction	Nuclear Magnetic Moment	Nuclear Quadrupole Moment	Mean Square Nuclear Charge Radius
	Magnetic Hyperfine interaction	Electric Quadrupole Interaction	Chemical Isomer Shift

Table 3.1 Schematic representation of the hyperfine interactions.

### 3.5.1 Isomer Shift

For many purposes, a simple description of the nucleus as a point charge which influences the extranuclear electrons via the coulomb potential is adequate. However, since the nucleus has a finite volume, it is necessary to consider the nucleus-electron interaction more carefully for the purpose of understanding the nature of the isomer shift,  $\delta$ .

Essentially, the nucleus is surrounded and penetrated by electronic charge with which it interacts electrostatically. The term isomer shift refers to the difference in electrostatic interaction as a result of the difference in the nuclear radii of the ground and excited states. This change arises since the s-electron density wavefunction implies a non-zero electron charge density within the nuclear volume. The resulting change in the coulomb interaction produces a shift in the nuclear energy levels as shown in fig. 3.5.

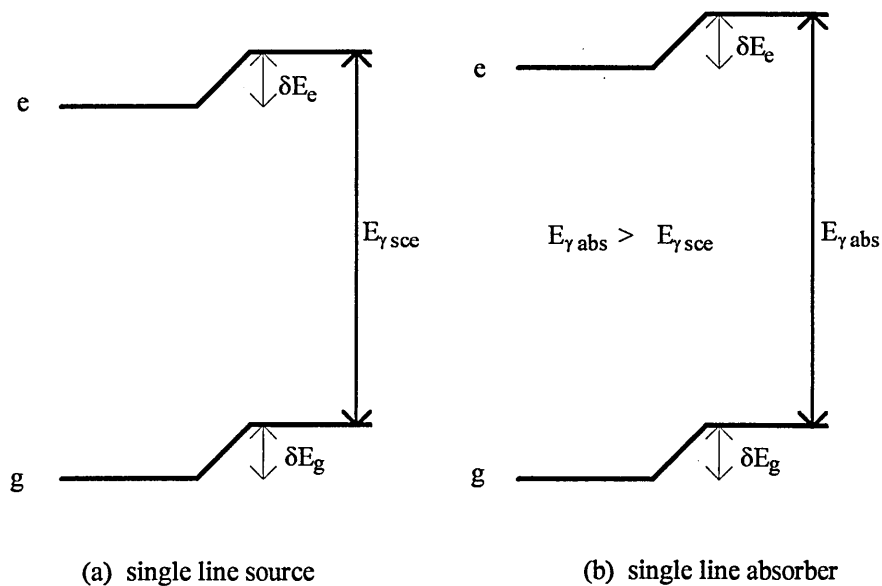


Fig 3.5 Isomer shift of the nuclear energy levels;  
 (a) single line source and (b) single line absorber.

It is not possible to measure the change in the coulomb interaction directly since the change is only a small fraction of the total coulomb interaction. However it is possible to compare the change by means of a suitable reference i.e. the  $\gamma$ -ray emitted from the Mössbauer source. The observed chemical isomer shifts give information regarding any change in the s-electron density which may arise from a change in valency.

An expression for the isomer shift can be derived by considering the nucleus as a uniformly charged sphere of radius,  $R$  and a constant s-electron density throughout the nucleus as  $|\Psi(0)|^2$ . By considering the difference between the electrostatic interaction of a point nucleus and of a nucleus having a radius,  $R$  the interaction energies can be estimated. This energy difference,  $\delta E$  is given by

$$\delta E = k|\Psi(0)|^2 R^2 \quad (3.5)$$

where  $k$  is a nuclear constant. However, the nuclear radius,  $R$  is generally different for the ground and excited states,  $\delta E_g$  and  $\delta E_e$  respectively. Therefore equation (3.5) becomes:

$$\delta E_e - \delta E_g = k|\Psi(0)|^2 (R_e^2 - R_g^2)$$

The  $R$  values are nuclear constants, but  $|\Psi(0)|^2$  varies from compound to compound. The energy difference is measurable in a Mössbauer experiment by comparing the source nuclear transition energy  $E_{\gamma_{scc}}$  with the absorber nuclear transition energy  $E_{\gamma_{abs}}$ . This transition energy difference can be expressed as:

$$\delta = k(R_e^2 - R_g^2) \left\{ |\Psi(0)|_{abs}^2 - |\Psi(0)|_{scc}^2 \right\} \quad (3.6)$$

Since the change in the radius  $R_e - R_g$  is very small, the normalised radius difference,  $\delta R/R$  allows equation (3.6) to be re-written as:

$$\delta = 2kR^2 \frac{\delta R}{R} \left\{ |\Psi(0)|_{abs}^2 - c \right\}$$

where  $\delta R = R_e - R_g$  and  $c$  is a constant characteristic of the radioactive source used. For a given nuclide both  $|\Psi(0)|_{scc}^2$  and  $\delta R/R$  are constant, and the isomer shift can be related to  $|\Psi(0)|_{abs}^2$  once the sign of  $\delta R/R$  is known. For the  $^{57}\text{Fe}$  system  $\delta R/R$  is less than zero and the isomer shift decreases as  $|\Psi(0)|_{abs}^2$  increases. Hence an increase in the isomer shift implies a decrease in s-electron density.

Although changes in isomer shifts are due to s-electron density variation at the nucleus, differences in isomer shifts are observed on addition or removal of p-, d- and f-electrons. These electrons do not interact directly with the nuclear charge density but provide a screening effect which effectively decreases the s-electron density at the nucleus. For example a  $3d^6 4s^1$  outer electronic configuration will have a higher s-electron density at the nucleus than a  $3d^7 4s^1$  electronic configuration. From this it can be clearly seen that observation of the isomer shift provides information relating to covalency and bond formation i.e. the chemical bonding of the atom.

### 3.5.2 Nuclear Quadrupole Interaction

The nuclear quadrupole interaction,  $\Delta E_Q$ , arises from the interaction of the nuclear quadrupole moment with the local electric field gradient. The theory of the quadrupole interaction essentially considers nuclei with a spin quantum number greater than  $I=1/2$ , having a non-spherical charge distribution. The non-spherical charge distribution results in the nucleus assuming either a prolate or oblate shape. The nuclear quadrupole moment,  $Q$ , reflects the deviation of the nucleus from spherical symmetry as shown in fig. 3.6.

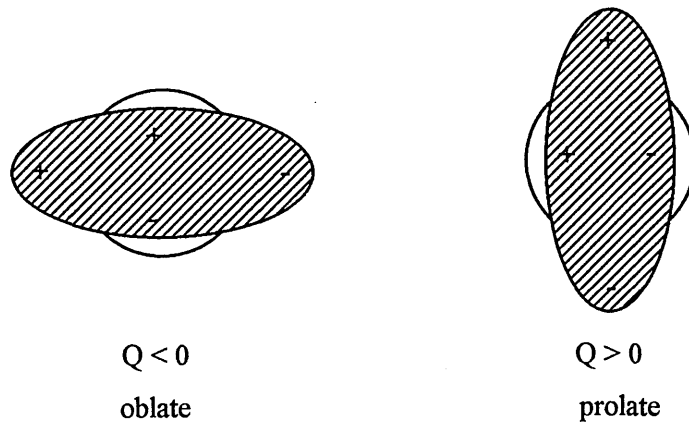
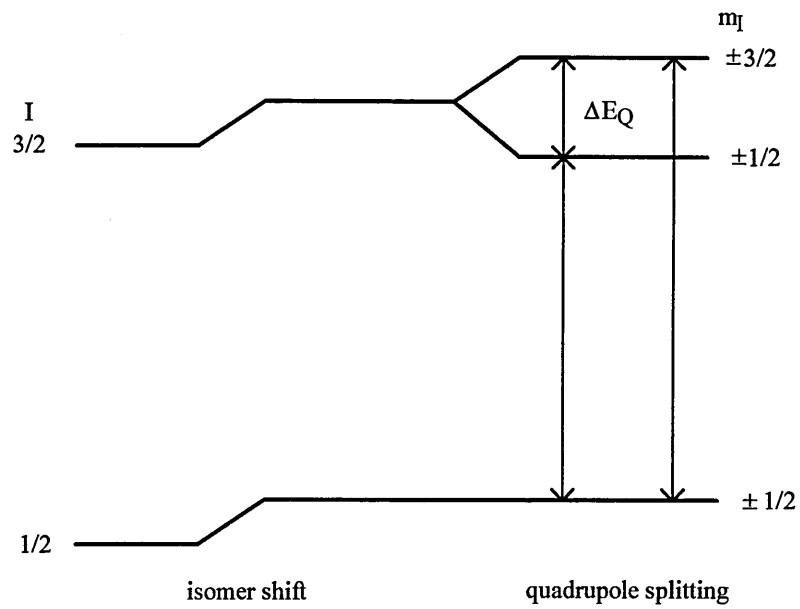
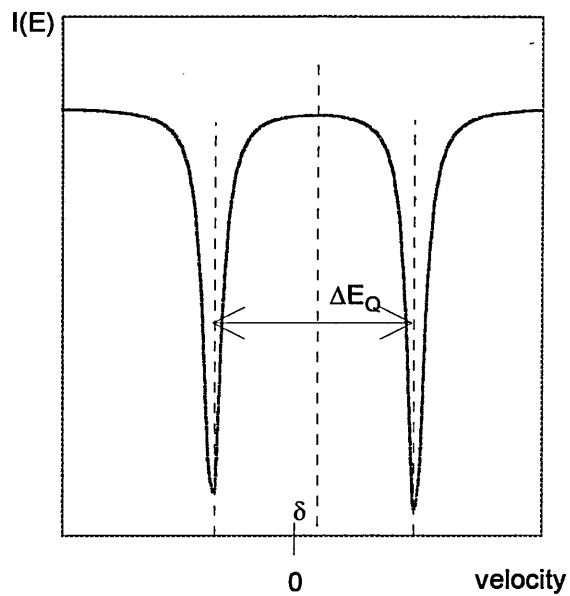


Fig. 3.6 Deviation of nucleus from spherical symmetry.

The quadrupole interaction results in a splitting of the nuclear energy levels. For the  $^{57}\text{Fe}$  system  $I_e=3/2$  and  $I_g=1/2$ , the  $I_e=3/2$  level splits into two  $m_i=\pm 3/2$  and  $m_i=\pm 1/2$  levels. The  $I_g=1/2$  level does not exhibit a quadrupole interaction and remains degenerate. Both the possible transitions are allowed with equal probability and a characteristic two line Mössbauer spectrum is observed. The separation of the two peaks is the quadrupole splitting,  $\Delta E_Q$ , and by convention is quoted in units of  $\text{mm s}^{-1}$ . Fig. 3.7 shows the quadrupole splitting of the nuclear energy levels combined with the isomer shift and the resulting Mössbauer spectrum.



(a) Energy level scheme



(b) Resultant Mössbauer spectrum

Fig. 3.7 Quadrupole splitting of the nuclear energy levels combined with the isomer shift for the  $^{57}\text{Fe}$  system; (a) energy level scheme and (b) resultant Mössbauer spectrum.

The quadrupole interaction results in an energy change,  $\Delta E_Q$  which is given by the following expression [3]:

$$\Delta E_Q = \frac{e^2 q Q}{4I(2I-1)} \left[ 3m_I^2 - I(I+1) \right] \left( 1 + \frac{\eta^2}{3} \right)^{\frac{1}{2}}$$

where  $Q$  = nuclear quadrupole moment  
 $\eta$  = asymmetry factor  
 $m_I$  = magnetic quantum number  
 $e$  = electronic charge  
 $eq$  = maximum value of the field gradient

The magnitude of the quadrupole interaction is a product of two factors,  $eQ$  is a nuclear constant for a particular isotope and  $eq$  is a function of the chemical environment due to the nature of the electric field gradient (EFG).

The EFG is usually expressed by three components  $V_{zz}$ ,  $V_{yy}$  and  $V_{xx}$ . These components do not exist independently and are related by the Laplace equation [5] to produce a co-ordinate system such that:

$$V_{xx} + V_{yy} + V_{zz} = 0$$

and the asymmetry parameter defined as:

$$\eta = \frac{|V_{xx} - V_{yy}|}{V_{zz}}$$

Using the convention  $|V_{xx}| \leq |V_{yy}| \leq |V_{zz}|$  ensures that  $0 \leq \eta \leq 1$ . Evaluation of  $\eta$  from a Mössbauer spectrum is straightforward. However, relating  $\eta$  to the electronic structure of the compound under study is more difficult. This is due to the observed sign of  $e^2qQ$  being an important factor in deciding the origin of the EFG. The simplest approach to overcome this problem is by considering a point charge model of the EFG for computing the relative magnitude of the EFG [6,7].

The source of the EFG is a combination from both the valence electrons of the atom and from the surrounding ions. The valence contribution,  $q_{val}$  arises from a total value of  $V_{zz} \neq 0$  due to the electron orbital population being non-spherical. The second source of the EFG is termed the lattice contribution,  $q_{lat}$  resulting from associated Ligands. Both  $q_{val}$  and  $q_{lat}$  are not independent components due to shielding effects and by assuming an

inverse cubic dependence on distance, the magnitude of  $q_{\text{val}}$  will be much greater than  $q_{\text{lat}}$ . Due to the two sources contributing to the EFG, the observed quadrupole splitting of a Mössbauer spectrum is particularly useful for providing information regarding the spin state and the distribution geometry of the compound under study.

### 3.5.3 Magnetic Hyperfine Interaction

The magnetic hyperfine interaction,  $H$  arises from the interaction between the nuclear dipole moment,  $\mu$  with the hyperfine field,  $H$  existing at the nucleus. As a result of this interaction the energy levels are shifted by a quantity,  $E_m$ .

$$E_m = -\mu H \frac{m_I}{I} = \mu_N g_N H m_I \quad (3.7)$$

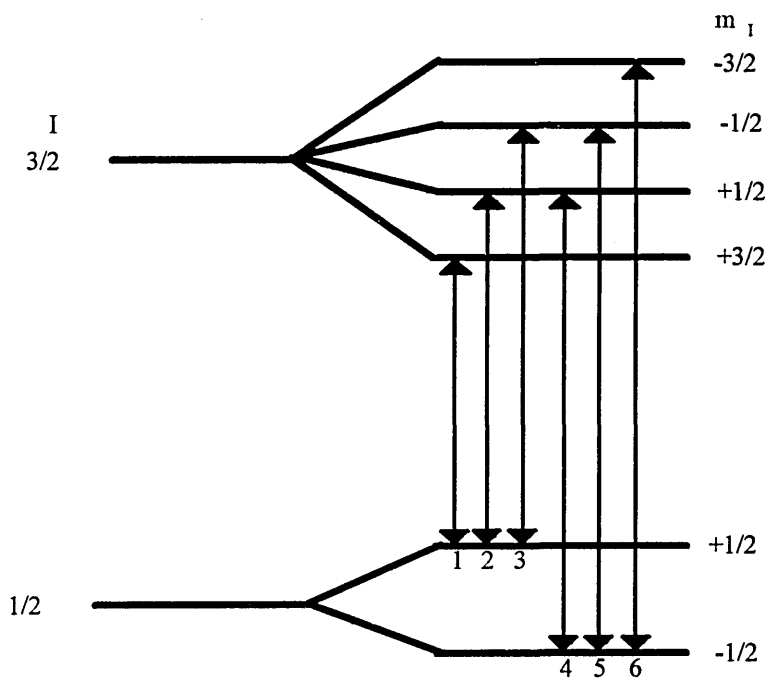
where  $I$  = nuclear spin  
 $g_N$  = nuclear g-factor ( $\mu/I\mu_N$ )  
 $\mu_N$  = nuclear Bohr magneton

The interaction completely removes the degeneracy of the nuclear spin,  $I$ , splitting each level into  $(2I+1)$  sub-levels. For the  $^{57}\text{Fe}$  system  $g_N$  differs in sign for the ground and excited states. The selection rule ( $\Delta m = 0$  or  $\pm 1$ ) describing the allowed Mössbauer transitions gives rise to a characteristic Mössbauer spectrum as shown in fig. 3.8.

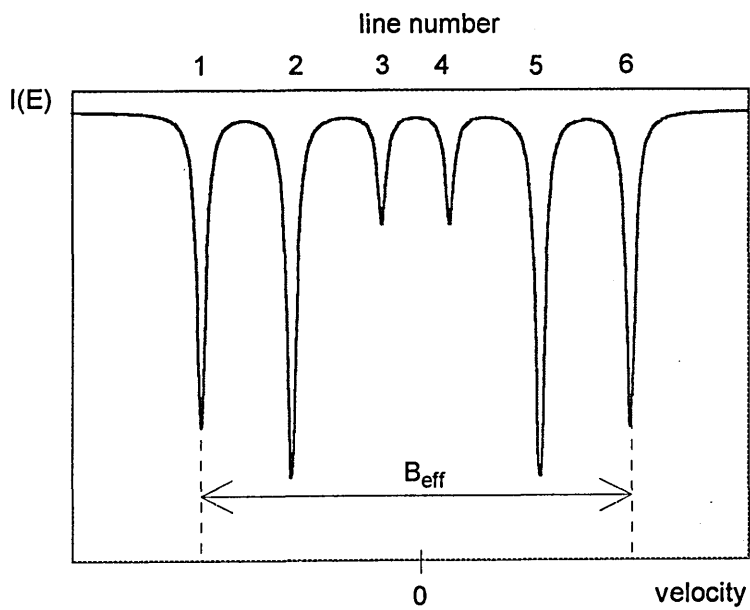
The magnetic hyperfine interaction is the product of a nuclear term which is a constant for a given isotope, and a magnetic field which is dependent on the electronic structure of the compound under study. The observed magnetic field or effective field,  $H_{\text{eff}}$  (or  $B_{\text{eff}}$ ) may originate from the material itself or be due to an external source:

$$H_{\text{eff}} = H_{\text{internal}} + H_{\text{external}}$$

$H_{\text{internal}}$  originates from a number of factors arising from the motion of the electrons within the material [8]. These factors can produce field strengths at the nucleus of  $H_{\text{internal}} = 10\text{-}100$  kG.



(a) Nuclear energy scheme



(b) Resultant Mössbauer spectrum

Fig. 3.8 Magnetic splitting of the  $^{57}\text{Fe}$  system; (a) energy level scheme and (b) resultant Mössbauer spectrum.

Since the internal magnetic field of a magnetically ordered compound is usually proportional to the magnetisation, the temperature dependence of the magnetic splitting will follow a Brillouin function which approaches zero at the Curie or Néel temperature [3]. Observation of the magnetic splitting depends on the relaxation time of electronic spins compared with the Mössbauer event time. In equation (3.7),  $H$  is a vector product which occurs over a time scale in the order of  $10^{-8}$  s. The electronic pairs which generate  $H$  undergo spin relaxation due to changes of direction. In paramagnetic compounds, this spin relaxation is rapid and results in  $H$  having a time average of zero and hence no magnetic splitting is observed. However, in ferromagnetic or antiferromagnetic compounds, the spin relaxation rate is slower and magnetic splitting is observed. Similarly, intermediate conditions regarding spin relaxation exist where the time scale is comparable with that of the Larmor frequency. Such systems include both ordered materials with unusually fast spin relaxation and also paramagnetic compounds with slow spin relaxation. These conditions result in the observation of complex Mössbauer spectra [9, 10].

In compounds where two or more distinct magnetic lattices are present, the Mössbauer spectra will reveal the internal field at each individual site. Hence, observation of the magnetic splitting is particularly useful for confirming the presence of any magnetic ordering within the compound under study.

### 3.6 Backscatter Mössbauer Spectroscopy

Mössbauer spectroscopy is usually performed in a transmission geometry and involves the detection of  $\gamma$ -ray radiation transmitted through a thin absorber. In such an experiment a wealth of data relating to the bulk properties of the solid may be obtained. However, such an experimental arrangement rarely provides information relating to the surface properties of the solid except for special cases. Examples are solids with high internal surface areas e.g. zeolites or clay minerals and stacking arrangements of very thin absorbers. To overcome these problems and allow the study of the surface and near surface regions of solids, it is necessary to utilise backscattering techniques based on the detection of conversion electrons and/or fluorescent X-rays emitted from the surface generated by resonant events within the sample under study. Since the electrons are rapidly attenuated within solids, only those electrons produced in the near surface region have sufficient energy to escape from the surface and contribute to the resulting Mössbauer spectrum. Thus the Mössbauer spectrum is weighted towards the near surface region of the solid under study.

The principle of Conversion Electron Mössbauer Spectroscopy (CEMS) may be applied to many Mössbauer isotopes, but like transmission Mössbauer spectroscopy the majority of studies have concentrated on the isotopes  $^{57}\text{Fe}$  and  $^{119}\text{Sn}$ . The main advantages of CEMS may be summarised as:

- (i) non-destructive technique
- (ii) high surface sensitivity - monolayer detection
- (iii) depth selectivity, associated with the short electron penetration range
- (iv) no line broadening due to absorber thickness.

This study uses CEMS to gain an understanding of the role of the metal ion etch pre-treatment used in ABS<sup>TM</sup>, by detecting the total backscattered electrons using a He/CH<sub>4</sub> gas flow detector, for  $^{57}\text{Fe}$  enriched substrates. Such an approach is referred to as integral CEMS and depends upon the resonant absorption of  $\gamma$ -rays followed by de-excitation via internal electron conversion.

### 3.7 Principles of CEMS

#### 3.7.1 Overview

The process of internal conversion during the decay of the  $I=3/2$  excited spin state of the  $^{57}\text{Fe}$  nucleus is shown in fig. 3.9.

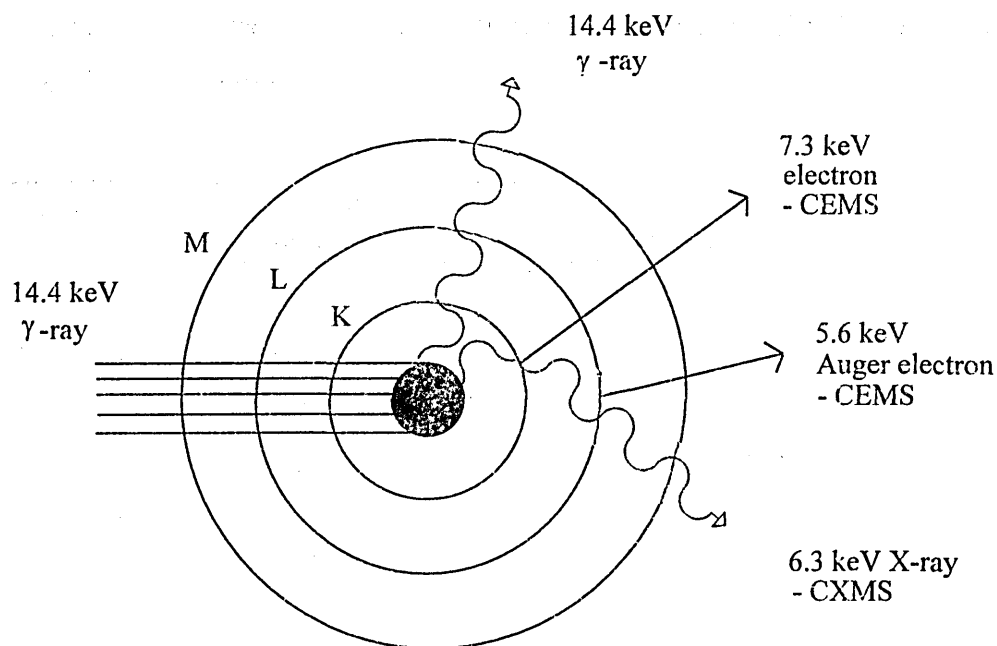


Fig. 3.9 De-excitation scheme of the  $^{57}\text{Fe}$  nucleus.

The internal conversion coefficient,  $\alpha$ , for the  $I=3/2 \rightarrow I=1/2$  decay transition is large, and only 10 % of the decay events occur by the emission of a 14.4 keV  $\gamma$ -photon. Table 3.2 summarises the main radiation characteristics and associated decay probabilities for the  $^{57}\text{Fe}$  de-excitation.

Type	Probability per de-excitation	Energy (keV)	Bethe range in iron (nm)
K-conversion	0.8	7.3	320
L, M-conversion	0.1	13.6	910
K Auger	0.53	5.6	210
K X-rays	0.27	6.3	-
$\gamma$ -ray	0.1	14.4	-

Table 3.2 Summary of the main radiation characteristics for the  $^{57}\text{Fe}$  de-excitation.

It can be seen from table 3.2 that the probing depth of integral CEMS is in the order of 300 nm, although experiments have shown that 66 % of the detected electrons in a He/CH<sub>4</sub> counter are generated within a surface depth of 54 nm for natural Fe foils [11]. The table also shows that the combined effect of detecting the generated conversion electrons and Auger electrons, is such that resonant effects in the order of 1000 % for 100 nm <sup>57</sup>Fe deposited films can be achieved using a 30 mCi <sup>57</sup>CoRh source after only a few minutes [12]. This high level of resonance also makes high surface sensitivity possible, and it has been demonstrated that about 10 nm of a new surface phase can be detected [13]. The same study showed the detection of an <sup>57</sup>Fe monolayer deposited on a Mössbauer inert substrate.

In parallel with the experimental areas of CEMS, several theories [14-16] have been published on the transmission and detection of the resonant electrons produced in the de-excitation process occurring in the absorber. The aim of the theories have been to obtain expressions for both the flux and associated energy distributions of the electrons reaching the absorber surface.

### 3.7.2 Electron Re-Emission and Transport in <sup>57</sup>Fe CEMS

The most comprehensive theory has been produced by Liljequist *et al.* [17, 18]. This theory is referred to as LEB and involves the Monte Carlo analysis of electron transport and energy loss for <sup>57</sup>Fe integral CEMS for the case of natural isotopic abundance (2.2 %) absorbers. LEB considers the total electron flux at the absorber surface from five contributions. These are (1) K-conversion electrons (KCE); (2) Auger electrons (AE); (3) L- and M-conversion electrons (LMCE); (4) photo electrons due to X-rays emitted following resonance absorption (XPE) and (5) photo electrons due to  $\gamma$ -rays emitted following resonance absorption (GPE).

The LEB obtains expressions for the relative contributions of these electrons to the total electron flux at the absorber surface. This is achieved by considering the associated weight function  $T(x)$  for each type of resonant electrons. For example, the weight function  $T^{\text{KCE}}(x)$  refers to the probability for a K-conversion electrons originating from a depth  $x$  to emerge from the surface of the absorber. The total weight function  $T(x)$  is the sum of weight functions:

$$T(x) = T^e(x) + \hat{T}(x) \quad (3.8)$$

where  $T^e(x)$  is the part due to electrons directly emitted from the de-excitation i.e. KCE, AE and LMCE, and  $\hat{T}(x)$  is the contribution due to electrons produced via photons. The LEB considers a duplex absorber having a uniform surface layer phase, S of thickness  $d$ , covering a bulk phase, B. The Mössbauer spectrum area is given by:

$$I_S = \int_0^d T^e(x) A_S(0) dx = C n_S \int_0^d T^e(x) dx \quad (3.9)$$

where  $A_S(x)$  is the number of de-excitations per unit depth associated with the S phase,  $C$  is a constant for a given measurement and  $n_S$  is the effective density of  $^{57}\text{Fe}$  in the S phase. The bulk phase Mössbauer spectrum area is given by:

$$I_B = C n_B \int_d^\infty T^e(x) dx + \int_d^\infty \hat{T}(x) A_B(x) dx \quad (3.10)$$

where  $A_B(x)$  is the number of de-excitations per unit depth associated with the B phase and  $n_B$  is the effective density of  $^{57}\text{Fe}$  in the B phase. Again, a trivial constant,  $C$  is associated with a given measurement, but this cancels when considering ratios of phase signals. Detailed calculations of all the associated weight functions are given elsewhere [18], and have been found applicable to arbitrary phases within a limited effective atomic number, provided that the depth is measured as a mass to area ratio. This allows for the use of the convenient unit  $\text{Fe}\text{\AA}$  (= mass thickness of 1  $\text{\AA}$  of iron) and provides a simple expression for the effective density of  $^{57}\text{Fe}$  which is proportional to the resonance absorption coefficient [3].

The program CEMSN2 [18][Appendix 1] calculates the associated weight functions for a duplex system and provides the ratio of Mössbauer spectral areas for the surface contribution to the total signal as a function of surface phase thickness. The flexible parameters required for the program are the effective densities of  $^{57}\text{Fe}$  in both the surface and bulk phases, the recoil free fraction in the bulk phase and the density ( $\text{g cm}^{-3}$ ) of the surface phase. Also required are the X-ray and  $\gamma$ -ray photon attenuation lengths within both the surface and bulk phases and the range of the XPE and GPE electrons in each phase. These variables are input using  $\text{Fe}\text{\AA}$  units and for the majority of duplex systems a set of default values can be used. Finally, the experimentally measured variables of line widths and line positions are required along with the efficiency of the detector. This efficiency parameter,  $\epsilon$  is defined as the probability that a single electron emerging from the absorber surface will give rise to an output pulse from the detector. However, it has been shown that varying the detector efficiency has only a small effect on the result. This effect can be seen in fig. 3.10 which also shows a comparison of CEMSN2 results with experimental data for a natural iron surface layer on stainless steel.

From fig. 3.10 it can be seen that the CEMSN2 program generates results in very good agreement with the experimental data and is a powerful tool for the prediction of surface layer thickness within a duplex system from integral CEMS measurements. This study uses the CEMSN2 program to quantify the etch rates associated with Ti ion etches for substrates held in 1 fold, 2 fold and 3 fold rotations during the metal ion etch step of the ABS<sup>TM</sup> process.

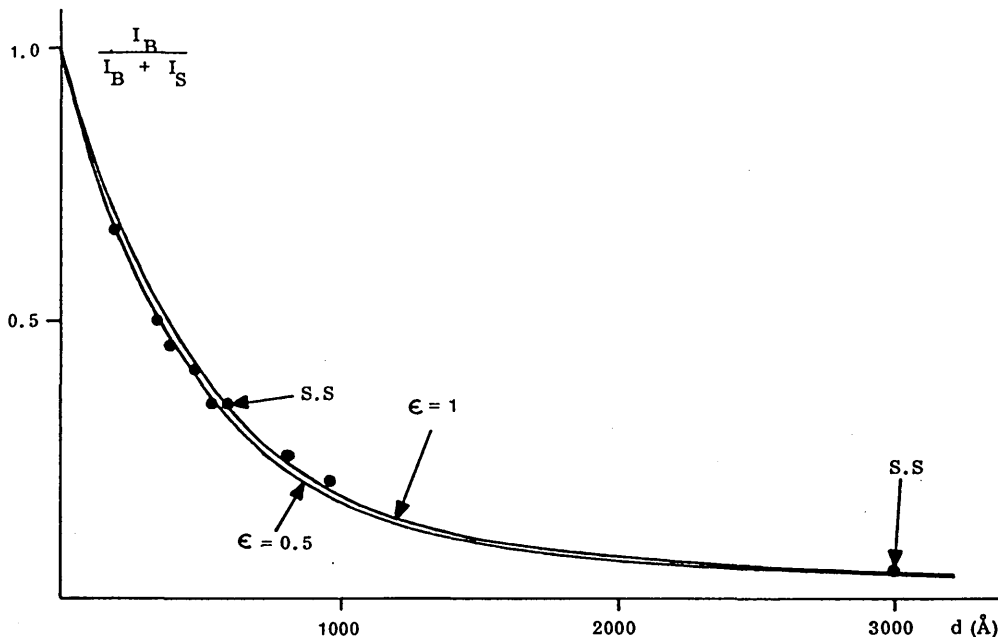


Fig. 3.10 Ratio of stainless steel to total signal as a function of thickness,  $d$  of a natural iron overlayer on a stainless steel substrate. Dots are experimental results due to Thomas *et al.* [19] except for those marked S.S. which are due to Swanson and Spijkerman [11]. Curves are calculated from LEB theory; cited from [18].

### 3.8 Applications of $^{57}\text{Fe}$ CEMS

In recent years the potential of  $^{57}\text{Fe}$  CEMS for solving problems connected with the properties of surfaces has been realised. The ability of the technique to probe surface and near surface regions of low area solids in a non-destructive manner has proved extremely useful in a range of areas. The more exotic areas include inorganic solids and minerals [20], lunar materials [21] and archaeological artefacts, in particular the study of ancient pottery ware [22]. Virtually all the studied areas use integral CEMS and major applications with regard to iron and steel surfaces are briefly summarised.

### 3.8.1 Characterization of the Surface Properties of Oxidised Steels

There have been many studies using CEMS of oxidised iron foils which identify the surface oxide products. One study by Simmons *et al.* [23] attempted to determine the oxide thickness as a function of oxidising temperature, time and oxygen pressure for  $^{57}\text{Fe}$  enriched substrates. This study observed the formation of non-stoichiometric magnetite ( $\text{Fe}_3\text{O}_4$ ) after 5 minutes at 225 °C in 1 atm of oxygen, while for the same length of time at 350 °C a duplex layer of  $\alpha\text{-Fe}_2\text{O}_3$  and  $\text{Fe}_3\text{O}_4$  was formed. After oxidation for 10 minutes at 450 °C the oxide was mainly stoichiometric  $\text{Fe}_3\text{O}_4$ . This study concluded that the oxidation rate depends upon the ion and electron conductivities through the oxide, and the absence of  $\alpha\text{-Fe}_2\text{O}_3$  at the higher temperature was attributed to the higher cation flux. Growth of  $\alpha\text{-Fe}_2\text{O}_3$  is not favoured until a sufficient thickness of  $\text{Fe}_3\text{O}_4$  has formed which reduces the cation flux through the oxide layer. The absence of  $\alpha\text{-Fe}_2\text{O}_3$  under similar conditions has also been shown by other workers [24]. However, oxidation of a pure iron sample at 500 °C for a few minutes at 10 torr of oxygen produced comparable amounts of both  $\alpha\text{-Fe}_2\text{O}_3$  and  $\text{Fe}_3\text{O}_4$ .

Similar studies by Swanson and Spijkerman [11] showed that the total oxide thickness obtained from relative spectral areas for samples oxidised at 500 °C was approximately proportional to the square root of the oxidation time. Other studies have independently determined the oxide thickness by measuring the oxygen uptake during oxidation. The main study of this type was by Graham *et al.* [25] in which iron substrates were oxidised at 240 °C in  $5 \times 10^{-3}$  torr of oxygen. Magnetite films with thicknesses between 26.5 and 425 nm were produced and the thickness of the oxide was related to the Mössbauer spectral area by:

$$d(\text{nm}) = -1.95 \times 10^2 \ln(1-0.01P) \quad (3.11)$$

where  $d$  is the oxide thickness and  $P$  is the relative spectral area due to the oxide. Good agreement was found between the data and theoretical predictions [14] except for the

oxide thickness of 425 nm. This was due to this oxide film having a rougher surface thereby effectively decreasing the associated electron attenuation coefficient. A similar study [26] has investigated the oxidation of  $^{57}\text{Fe}$  enriched substrates in pure oxygen at a pressure of 10 torr and temperatures of 150 and 500 °C.

The identification of corrosion products deposited on steel surfaces after immersion in aqueous solutions of various salts has been investigated by several workers. Ujihura and Nomura [27] found that the main corrosion product formed after immersion of polished mild steel in deionised water for several 10's of hrs was  $\gamma\text{-FeOOH}$ . This study also observed the formation of  $\text{Fe}_3\text{O}_4$  covered with brown coloured spots of  $\gamma\text{-FeOOH}$  for stainless steel samples immersed in 0.5 M  $\text{NaNO}_3$  solution. However, it must be noted that this type of aqueous corrosion is complex and may lead to a variety of products including  $\alpha\text{-FeOOH}$ ,  $\beta\text{-FeOOH}$  and  $\gamma\text{-FeOOH}$  along with  $\alpha\text{-Fe}_2\text{O}_3$  and  $\gamma\text{-Fe}_2\text{O}_3$ . Difficulties may arise in the identification of products that contain only quadrupole doublets, since these may arise from either  $\beta\text{-FeOOH}$  and  $\gamma\text{-FeOOH}$ . Confirmation of the identified products has been achieved by other workers performing a variable temperature CEMS study [28].

A study by Ensling *et al.* [29] has investigated the formation of protective oxide coatings on steam generator tubes in the presence of water at high temperatures and pressures. Magnetite was found to be the only oxide phase present on the surface of martensitic iron-chromium and austenitic iron-chromium-nickel steels. The time dependence of the growth was monitored and the oxide thickness was calculated using a method described by Thomas *et al.* [19].

### 3.8.2 Corrosion Studies of Steels in Aggressive Atmospheres

Several corrosion studies of steels in atmospheres containing HCl, SO<sub>2</sub> or H<sub>2</sub>S have been performed. A comprehensive study by Handa *et al.* [28] has investigated the corrosion products formed under HCl containing atmospheres by CEMS at room temperature and 80 K. The steel substrates were exposed to a moist atmosphere of HCl fumes for 8 minutes at room temperature and various partial pressures of HCl,  $\rho_{\text{HCL}}$ . CEMS identified the FeCl<sub>2</sub> · 2H<sub>2</sub>O formation at  $\rho_{\text{HCL}} = 40\text{-}70$  torr, whilst for  $\rho_{\text{HCL}} = 70\text{-}80$  torr the formation of FeCl<sub>2</sub> · 4H<sub>2</sub>O was observed. The thin white surface layer of FeCl<sub>2</sub> · xH<sub>2</sub>O (x = 2 or 4) was found to be stable in completely dry air for 7 days. However, exposure of the samples to slightly humid air, produced a transformation of the FeCl<sub>2</sub> · xH<sub>2</sub>O to a brownish yellow coloured surface layer, found to be β-FeOOH. Raising the air humidity up to 100 % produced an increase in the ratio of γ-FeOOH to β-FeOOH. Only γ-FeOOH was formed by the exposure of FeCl<sub>2</sub> · xH<sub>2</sub>O coated steel to water saturated air. Other workers have also reported the formation of FeCl<sub>2</sub> · 4H<sub>2</sub>O after similar exposures to HCl fumes [30]. A similar study [31] involving the exposure to atmospheres containing SO<sub>2</sub> has identified the formation of FeSO<sub>4</sub> · xH<sub>2</sub>O (x = 2 or 4) deposits on the steel surface as the initial corrosion product which subsequently transferred to Fe<sub>4</sub>SO<sub>4</sub>(OH)<sub>10</sub>. Treatment of the same steel in a gas mixture of H<sub>2</sub>S (0.86 vol. %) and nitrogen (bal.) at 25 °C for various periods initially produced paramagnetic FeS<sub>1-x</sub> (mackinawite) which subsequently transferred to Fe<sub>3</sub>S<sub>4</sub> (greigite) after further corrosion.

A study by Brooks and Thorpe [32] has investigated corrosion products beneath a protective layer after exposure to an SO<sub>2</sub> atmosphere. This study allowed the early stages of corrosion to be detected beneath a protective layer of varnish on mild steel substrates which had been enriched in the near surface region with <sup>57</sup>Fe by a diffusion technique. The adopted diffusion profile enabled improved surface sensitivity associated with the 6.3 keV fluorescent X-rays which are energetic enough to penetrate the protective layer. The results showed the formation of additional spectral lines corresponding to ferric and ferrous doublets after 3 hrs exposure to a SO<sub>2</sub> atmosphere.

After 18 hrs exposure, a black corrosion product was clearly visible through the transparent varnish coating and the two doublets associated with  $\text{Fe}^{2+}$  and  $\text{Fe}^{3+}$  ions became more intense. These doublets were due to either paramagnetic phases of corrosion products or the result of superparamagnetic phases of small particles.

### 3.8.3 Ion Implantation Studies

Ion implantation provides a method of introducing a controlled number of atoms of one species into a substrate. To achieve this atoms are ionised and accelerated to typically 50-200 keV before penetrating the target material. The implanted ions lose energy mainly in elastic collisions with the target atoms before coming to rest. If the transferred energy to a target atom is sufficient, then this atom becomes displaced and in turn produces further displacements thereby generating a collision history associated with each incident ion. This history will be different for each incident ion and there will be a spread of ranges generally assumed to be Gaussian in shape.

This implantation process creates lattice defects of interstitials and vacancies. These defects determine the final metallurgical state of the lattice. Several studies have used CEMS to analyse the lattice changes after ion implantation for a variety of probe and target atoms. A systematic approach of the Mössbauer parameters for variety of implants and a wide range of targets has been carried out by Sawicki and Sawacka [33]. In fact, almost a complete data set is available for all the elements in Fe, Ni and Co targets [34].

Mössbauer measurements on natural iron or steel samples implanted with various ions to improve the surface durability have been made. One study [35] has investigated implantation of nitrogen in natural iron foils and fig. 3.11 shows the CEM spectra associated with various ion dosage levels. The results indicate the presence of nitrides for dosage levels greater than  $1 \times 10^{17}$  ions  $\text{cm}^{-2}$ , the dose at which the maximum

improved wear resistance was observed. Mössbauer subspectra due to  $\gamma$ -Fe<sub>4</sub>N (sextet) and  $\epsilon$ -Fe<sub>3-x</sub>N (doublet) were observed. These nitrides were shown to be thermodynamically unstable and annealing at 257 °C was sufficient to allow the nitrogen to migrate. This observation is significant since this temperature could well be reached during the wear process at the surface of the treated steel. Similar CEM spectra showed the formation of the carbides,  $\theta$ -Fe<sub>3</sub>C and  $\chi$ -Fe<sub>5</sub>C<sub>2</sub> for carbon implanted iron foils. These carbides were found to decompose at 400 °C.

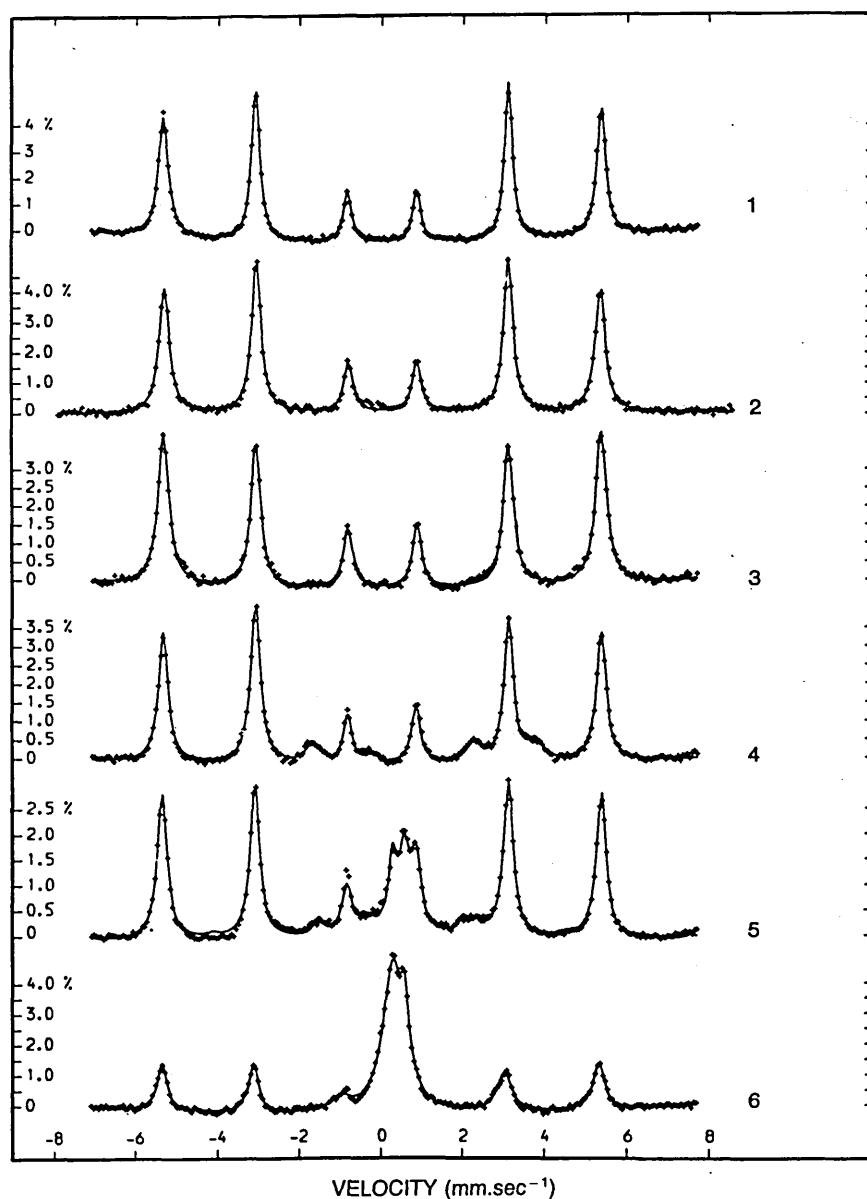


Fig. 3.11 CEM spectra showing the effects of ion implantation; (1) natural iron and (2) ion implanted with  $1 \times 10^{17}$  argon/cm<sup>2</sup>, (3)  $1 \times 10^{17}$  nitrogen/cm<sup>2</sup>, (4)  $2 \times 10^{17}$  nitrogen/cm<sup>2</sup>, (5)  $4 \times 10^{17}$  nitrogen/cm<sup>2</sup> and (6)  $6 \times 10^{17}$  nitrogen/cm<sup>2</sup>. Cited from [35].

#### 3.8.4 Analysis of Hardened Steel Surfaces

The solid phase reaction of steel and  $B_4C$  powder at  $900\text{ }^\circ\text{C}$  for 5 hrs has been studied by CEMS [36]. The borided steel surface was analysed after the removal of a desired thickness by SiC powder. The CEM spectra showed a decrease in the internal magnetic field compared with  $\alpha\text{-Fe}$ , for the uppermost surface of the steel. This was attributed to  $FeB_x$  ( $x > 1$ ). The CEM spectrum of the exposed layer after grinding  $5\text{ }\mu\text{m}$  off the top of the same sample, showed a second internal magnetic field identified as FeB. A second CEM spectrum after grinding to a depth of  $20\text{ }\mu\text{m}$  from the original top surface, suggested the presence of a superposition of both FeB and  $Fe_2B$ . A further layer removal at a depth of  $33\text{ }\mu\text{m}$  showed only the existence of  $Fe_2B$ . Increasing depths showed the presence of both  $Fe_2B$  and  $\alpha\text{-Fe}$ , with the  $Fe_2B$  to  $\alpha\text{-Fe}$  ratio decreasing to zero as the substrate material was reached at a depth greater than  $130\text{ }\mu\text{m}$ . A similar study [37] of the multilayer structure of borided Armco iron has showed the presence of FeB at  $5\text{ }\mu\text{m}$  and  $Fe_2B$  at  $15\text{ }\mu\text{m}$  depths.

The multilayered structures of hardened surfaces of nitrided steels have also been analysed by CEMS [38]. CEMS revealed the presence of 4 distinct layers for gas nitrided steels produced by the thermal decomposition of ammonia at  $520\text{ }^\circ\text{C}$  for 30 hrs. The top surface was identified as  $\epsilon\text{-Fe}_2\text{N}$ , estimated to be less than  $10\text{ }\mu\text{m}$  thick and other deeper layers were attributed to  $Fe_{3+x}\text{N}$  ( $0 \leq x \leq 1$ ) and  $\gamma\text{-Fe}_4\text{N}$ . The fourth layer was found to be distorted  $\alpha\text{-Fe}$  suggesting that this layer is disturbed by interaction with the  $\gamma\text{-Fe}_4\text{N}$  layer.

However, it should be noted that in virtually all the studies of hardened steels the statistical quality of the CEMS data has been poor and further confirmation of the phases present has been achieved by complementary techniques, in particular XRD. Such

statistical quality has been unavoidable since improvement by  $^{57}\text{Fe}$  enrichment over depths in the order of  $100\ \mu\text{m}$  is both costly and impractical.

### 3.8.5 Surface Stress and Orientation of the Magnetic Field of Iron and Steel Substrates

Measurement of surface stress levels by examining pressure induced changes in the Mössbauer parameters has been performed [39]. The observed changes are small, for example a hydrostatic stress of  $700\ \text{MN m}^{-2}$  will only shift an  $\alpha$ -iron spectrum by approx.  $6\ \mu\text{m s}^{-1}$ . Such small changes for an iron bar held in both compression and tension have been observed by Mercader and Cranshaw [40]. However, the technique needs further development for the measurement of lower magnitudes of stress with high accuracy.

The difference in the relative peak intensities among the sextet patterns for CEM and CXM spectra originates from the orientation difference of the magnetic axis of the iron grains between the surface and underlayers. The relative peak intensities for both CXM and transmission spectra of polycrystalline iron foils are 3:2:1:1:2:3. This similarity is due to the direction of the magnetic field of iron located in the surface layer of the range of the X-ray (about  $20\ \mu\text{m}$ ). However the observed intensities of 3:4:1:1:4:3 for a CEM spectrum suggests that the internal magnetic field of polycrystalline  $\alpha$ -iron is orientated parallel to the surface to a depth in the order of  $100\ \text{nm}$ . Table 3.3 shows the dependence of relative peak intensity as a function of the angle,  $\theta$  between the incident  $\gamma$ -ray and the internal magnetic field.

Transition	+3/2→+1/2	+1/2→+1/2	-1/2→+1/2	+1/2→+1/2	-1/2→-1/2	-3/2→-1/2
Peak	1	2	3	4	5	6
$\Delta m$	$\pm 1$	0	$\pm 1$	$\pm 1$	0	$\pm 1$
Intensity ratio	$\frac{3}{4}(1+\cos^2\theta)$	$\sin^2\theta$	$\frac{1}{4}(1+\cos^2\theta)$	$\frac{1}{4}(1+\cos^2\theta)$	$\sin^2\theta$	$\frac{3}{4}(1+\cos^2\theta)$
random	3	: 2	: 1	: 1	: 2	: 3
$\theta = 0^\circ$	3	: 0	: 1	: 1	: 0	: 3
$\theta = 45^\circ$	9	: 4	: 3	: 3	: 4	: 9
$\theta = 90^\circ$	3	: 4	: 1	: 1	: 4	: 3

Table 3.3 Relative peak intensities for the  $I = 3/2 \rightarrow 1/2$  transition.

### 3.8.6 Intermetallic Compounds Formed at the Interface of Metal Coated Substrates

The identification of interface structures for various coating-substrate systems have been performed using CEMS. One study by Clemens and Williamson [41] has identified amorphous phase formation within the Fe-Zr system. In this work, multilayers consisting of natural Fe and Zr were prepared by electron beam evaporation and sputter deposition techniques. Layer thicknesses were varied between 50 monolayers of each constituent down to 2 monolayers. CEMS data associated with both preparation techniques shows a transition from crystalline bcc  $\alpha$ -Fe to an amorphous paramagnetic Fe-Zr phase for decreasing multilayer thickness,  $n$ . However, the sputtered multilayers show less of the paramagnetic phase for the same  $n$ . The interface is suggested to be twice as large in the electron beam evaporated samples as in the sputter deposited samples, where it is about 2-4 atomic planes thick. The amorphous phase which is 50 at. % Zr, is suggested to grow during a solid state reaction between crystalline iron and zirconium. The evidence

suggests that the greater diffusion and poorer layering in the electron beam evaporated samples is due to the lower energy of the arriving species compared with the sputter deposition process. The variation of Fe-Zn intermetallic compounds produced at a zinc coated steel surface as a function of depth has been studied [42]. The intermetallic structures were observed after mechanically polishing a desired thickness off the top surface. CEMS confirmed a multilayer structure of the galvanised steel surface.

From the outlined studies of intermetallic phase formations it can be seen that CEMS is a very revealing and versatile technique. However, only a few studies have used CEMS or any other technique, to investigate the phase formation at the interface of ceramic type coatings on steel substrates deposited by PVD methods. These studies are discussed in chapter 1.

### **3.9 Mössbauer Spectroscopy Instrumentation**

A Mössbauer spectrum is a record of the rate of interactions occurring within the sample as a function of energy. The occurrence of the interactions can be detected by the absorption of  $\gamma$ -rays from the beam i.e. transmission Mössbauer spectroscopy, or by the detection of either conversion electrons or X-rays i.e. backscatter Mössbauer spectroscopy. The variation of  $\gamma$ -ray energy is obtained by introducing a relative motion between the source and the sample by changing the energy according to the Doppler effect,  $\delta E_\gamma = E_\gamma v/c$ . Therefore a spectrum can be collected by recording the backscatter rate for selected values of  $v$  in a “point by point” manner. This is called the constant velocity method. A more convenient method is to arrange a cyclic motion of either the source or sample, and to sweep through the range of velocities of interest. By spending equal times in equal velocity increments, the motion must have constant acceleration, and this is called the constant acceleration method.

In this study, the Mössbauer spectrometer was used in the constant acceleration mode and the radioactive source was a  $^{57}\text{CoRh}$  of an initial activity of 25 mCi. Early stages of the work used an experimental arrangement based around an Elsinct drive system. However for a major part of the work, experiments were performed using a more modern WissEl function generator/driver system. The experimental backscatter arrangement is shown in fig. 3.12.

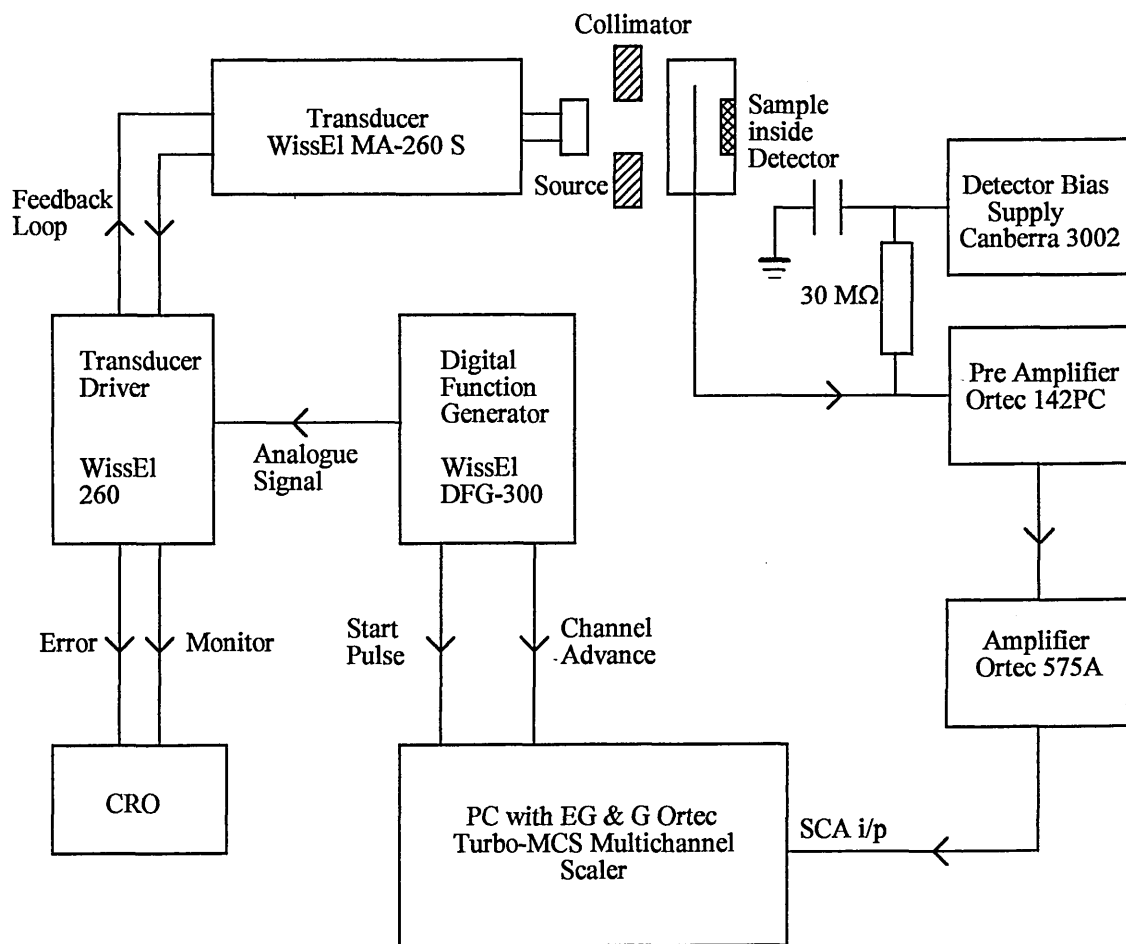


Fig. 3.12 Experimental arrangement used for backscatter Mössbauer spectroscopy.

### 3.9.1 Operation of the Spectrometer

The digital function generator DFG-500 provides a triangular reference signal for the Mössbauer driving system 260. This reference signal is generated digitally to ensure that the source motion during the Mössbauer experiment is absolutely synchronous to the channel sweep of the Multichannel Scaler. The synchronisation is achieved by sending a positive start pulse and a channel advance pulse when the analog triangular reference waveform has reached its positive maximum.

The frequency of this analog output is set at 23 Hz which is divided in to 512 channels and hence provides the range for the velocities of interest. This analog output is amplified by the driver unit 260 and provides the velocity transducer with precise motion of the Mössbauer source. To achieve this precise motion the driver unit and transducer form a feedback system which minimises the deviation of the actual source motion from the ideal waveform.

The velocity transducer MA-260 S is based upon the principle of two mechanically coupled loudspeakers or coils. The first coil causes the motion of the transducer elements and the second coil acts as a pickup to provide a signal proportional to the measured velocity back to the driver unit. This type of feedback set-up ensures an accuracy in the Mössbauer source motion to 0.15 % for a triangular waveform providing the source is rigidly mounted to the transducer and that the load is not greater than 400 g. This high accuracy of motion can be monitored by observing the monitor and error signals of the driver unit using the CRO.

Operating bias for the counter is provided through a filter and a large bias resistance of 30 M $\Omega$ . From there it is passed through the signal input cable to the counter as shown in fig. 3.12. This input is via a short length of 93  $\Omega$  impedance coaxial cable. This reduces

the input capacitance to a minimum and decreasing ground loops and radio frequency pickup, both of which are sources of noise for the preamplifier. The preamplifier is powered from the 575A amplifier.

The creation of ion pairs within the counter generates a quantity of charge delivered as a narrow current pulse to the preamplifier 142PC. This preamplifier is a charge sensitive device and integrates the input charge on a feedback capacitor generating an output voltage proportional to the charge. The voltage is input to the 575A amplifier which is powered by a NIM-standard bin unit providing  $\pm 6V$ ,  $\pm 12V$  and  $\pm 24V$ . The amplifier provides Gaussian pulse shaping and amplification to a suitable voltage level for further signal processing.

The gain of the amplifier is adjusted to give maximum output voltage pulses with a magnitude of 10V without saturation. The bipolar output pulses of the amplifier are then fed to the internal Single Channel Analyser (SCA) of the Turbo MCS Multichannel Scaler. The SCA generates an output pulse only for input voltages that rise above a lower level threshold without exceeding an upper level threshold. These thresholds or discriminator levels are independently selectable via the PC from 0 to +10V. However for CEMS, since the pulse height spectrum consists of a continual energy loss electron profile, it is only necessary to set an energy window which eliminates the counts associated with the amplifier noise. To achieve this typical lower and upper level discriminator settings are 0.2V and 10V respectively. Thus the SCA via a coincidence circuit allows for all pulses, except for those associated with amplifier noise, to be recorded by the Multichannel Scaler (MCS).

The MCS records the number of counts over 512 channels synchronised by the digital function generator and by repetitive scanning, multiple scans are summed to diminish the statistical scatter in the recorded spectrum. Since a symmetrical waveform is used to drive the velocity transducer, a mirror image of the spectrum is obtained. This is useful

as folding the data eliminates any curvature of the base line due to slightly different count rates detected at the extremes of the source motion. This symmetry also provides a useful check on the linearity of the system. Since any loss of linearity destroys the mirror symmetry.

### 3.9.2 Electron Detection

The photons generated from a  $^{57}\text{Co}$  source per parent nuclide decay consist of 14.4 keV  $\gamma$ -rays (8.4 %), 122 keV  $\gamma$ -rays (85 %), 136 keV  $\gamma$ -rays (11 %) and Fe K X-rays (52 %). A backscatter electron detector must therefore ensure high detection efficiency of both the resonantly produced conversion and Auger electrons generated by the 14.4 keV Mössbauer  $\gamma$ -rays, whilst rejecting the non-resonantly produced electrons associated with all incident radiations. These non-resonant electrons contribute only to the background signal and are generated by the photo-electric effect for interactions with high Z elements and Compton scattering for interactions with low Z elements.

In this study CEMS measurements were performed by mounting the sample in a gas flow proportional counter using He + 5 %  $\text{CH}_4$  as the gas mixture at a flow rate in the order of 10 ml per minute . The sample formed the cathode and application of a positive HT voltage to a single wire anode enabled the detection of the 7.3 keV conversion and 5.6 keV Auger electrons. The counter was based upon the MBSC200 design produced by the Harwell Mössbauer group. The cylindrical chamber measured 55 mm in diameter and the anode used was 25  $\mu\text{m}$  diameter stainless steel wire. Collimation of the incident  $\gamma$ -rays was provided by a 3 mm thick lead plate having a 6 mm diameter hole. This ensured accurate beam alignment and restricted the incident  $\gamma$ -rays to the central region of the sample. Such collimation provides improved signal to noise ratio by reducing the production of non-resonant photo and Compton electrons generated by beam

interactions with the counter walls [43]. Fig. 3.13 shows the layout of the gas flow proportional counter.

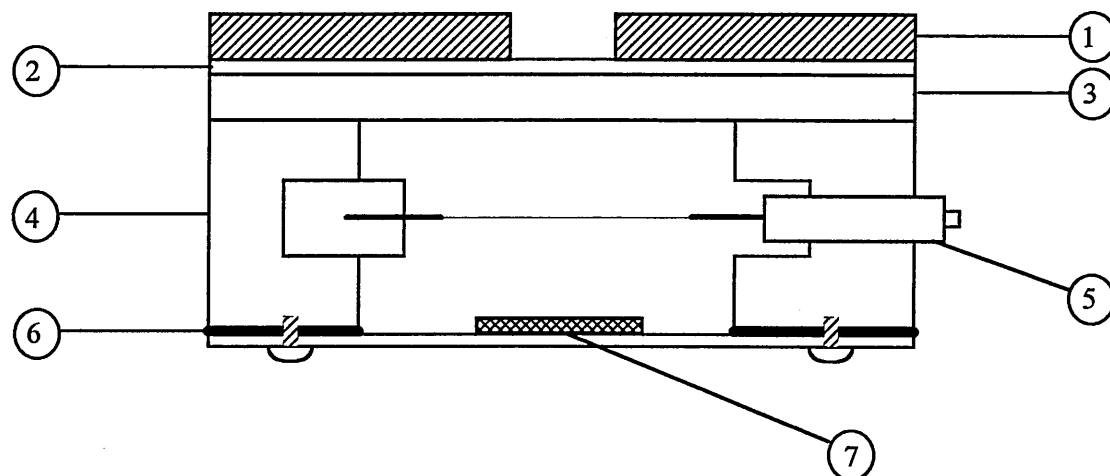


Fig. 3.13 Gas flow proportional counter; gas input and output pipes are not shown for clarity. 1: 3 mm of lead, 2: aluminised mylar, 3: perspex, 4: brass body, 5: HT connector, 6: vacuum seal and 7: sample.

From fig. 3.13 it can be seen that between the collimator and the main body of the counter exists a thin aluminised mylar layer and a 4 mm thick perspex layer. These layers absorb the Fe K X-rays from the incident beam without significantly absorbing the higher energy 14.4 keV Mössbauer  $\gamma$ -rays, thereby further suppressing the creation of non-resonant electrons.

For CEMS measurements the counter is operated at a HT voltage of +1500 V which ensures the formation of ion pairs in the gas mixture and that no appreciable recombination of positive and negative ions occur. A major advantage of this counter is that by operating at a HT voltage of +1350 V and using a Ar + 5% CH<sub>4</sub> gas mixture, the detection of the 6.3 keV fluorescent X-rays is made possible.

### 3.10 Computer Fitting of Mössbauer Spectra

The problem in analysing Mössbauer spectra is to determine the parameters of the curve that best fit the data points comprising the spectrum. Since this type of problem is complex, computer facilities are necessary for the determination of line positions, relative intensities and linewidths etc. in a Mössbauer spectrum. This work uses a Silicon Graphics Indy workstation and a FORTRAN program based on the work of Longworth and Cranshaw [44] used for data analysis. A typical fitting program considers the curve to be described by a function  $F(x_i)$ , where  $x_i$  are parameters, and is measured at  $n$  points. Therefore, the values  $F_i(i=1,n)$  of the function of these points differ from the measured values  $p_i$  due to statistical fluctuations. It assumes that each  $p_i$  is distributed normally about  $F_i$  with a standard deviation  $\sigma_i$ . In the least squares minimisation method the parameters are varied until the sum  $\sum_i (F_i - p_i)^2 / \sigma_i^2 = \chi^2$  reaches a minimum.

The constant acceleration spectrometer produces a Doppler velocity varying linearly from  $+V$  to  $0$  to  $-V$  and back through  $0$  to  $+V$  over a complete cycle of 512 channels. Since the two zero velocity positions are at the extremes of the source displacement, the resultant spectrum contains the mirror image of the data shown in the first 0-255 memory channels of the MCS and the memory channels 256-511.

#### 3.10.1 Data Folding

The first operation in the fitting process is to fold the data stored in channels 0-255 on to the data channels 256-511 and to average the counts stored in the corresponding channels. The determination of the zero velocity position is achieved by scanning 10 half channels each side of the expected folding position of channel 128.5 to find the best mirror axis. The scanning minimises the sum of the squared differences and allows for fluctuations in the signal levels of the driver system. Similarly the loss of high accuracy

disregarding a set of channels associated at the maximum and minimum velocities. The remaining 249 channels are stored as a folded data file and a listing file which contains details of the fold.

### 3.10.2 Data Fitting

In the simplest case in which both the source and absorber energy profiles are assumed to be Lorentzian, the resulting Mössbauer spectrum is also Lorentzian. However if the absorber line is split into a number of components by the hyperfine interactions, the spectrum can be considered to be a superposition of several Lorentzian lines.

The centres, widths and intensities of these Lorentzian lines are determined by the hyperfine parameters. The fitting is achieved by a least squares fitting routine to calculate an initial estimate of the spectrum from approximate starting parameters. The parameters are input via an array which is divided up into those parameters needed to fit a singlet, a quadrupole doublet and a magnetic sextet with a small quadrupole interaction. Each of these are regarded as a phase with a relative spectral area which is determined by the least squares analysis. The parameters for the phases are as follows:

each singlet	isomer shift, halfwidth,
each doublet	isomer shift, half quadrupole splitting, left halfwidth, right halfwidth,
each sextet	isomer shift, half magnetic splitting of lines 1 to 6, overall quadrupole splitting, intrinsic halfwidth, incremented halfwidth, relative intensities of lines 2 and 5, relative intensities of lines 1 and 6.

In the case of the sextet, the use of the two components for the linewidth allows for a narrow distribution of fields, for example fields associated with different atomic surroundings.

The quality of the fit to the experimental data can be inspected by considering the “goodness of fit” parameter,  $\chi^2$ . Therefore the  $\chi^2$  value is taken into account when deciding on a “good” fit; initial fitting of a folded data set yields output parameter values with an associated  $\chi^2$  of the fit. These output values are then used in a subsequent re-fit of the data as input parameters. This process of running the fitting program and using the output values as starting parameters for a further fit of the data, is repeated until  $\chi^2$  reaches a minimum.

### 3.11 Spectrometer Calibration

A spectrometer calibration is required to determine the velocity range associated with the helipot setting on the transducer driver. This is obtained by using the magnetically split six line spectrum of an  $^{57}\text{Fe}$  enriched iron calibration standard. The associated line positions are known to occur at the following Doppler velocities [45]:

$$\begin{aligned} \text{lines 1,6} &= \pm 5.312 \text{ mm s}^{-1} \\ \text{lines 2,5} &= \pm 3.076 \text{ mm s}^{-1} \\ \text{lines 3,4} &= \pm 0.840 \text{ mm s}^{-1} \end{aligned}$$

An inspection of the folded data set associated with a calibration yields initial estimates of the line positions. These are used as starting parameters for a calibration program which fits Lorentzian lines to the data. The calibration constant,  $c$  is determined for each line pair using the expression:

$$c = \frac{\text{splitting}}{2 \times \text{Doppler velocity}} \quad \text{channels / mm s}^{-1}$$

The final value of  $c$  is taken from the average of the three results obtained. A typical CEM spectrum calibration is shown in fig. 3.14.

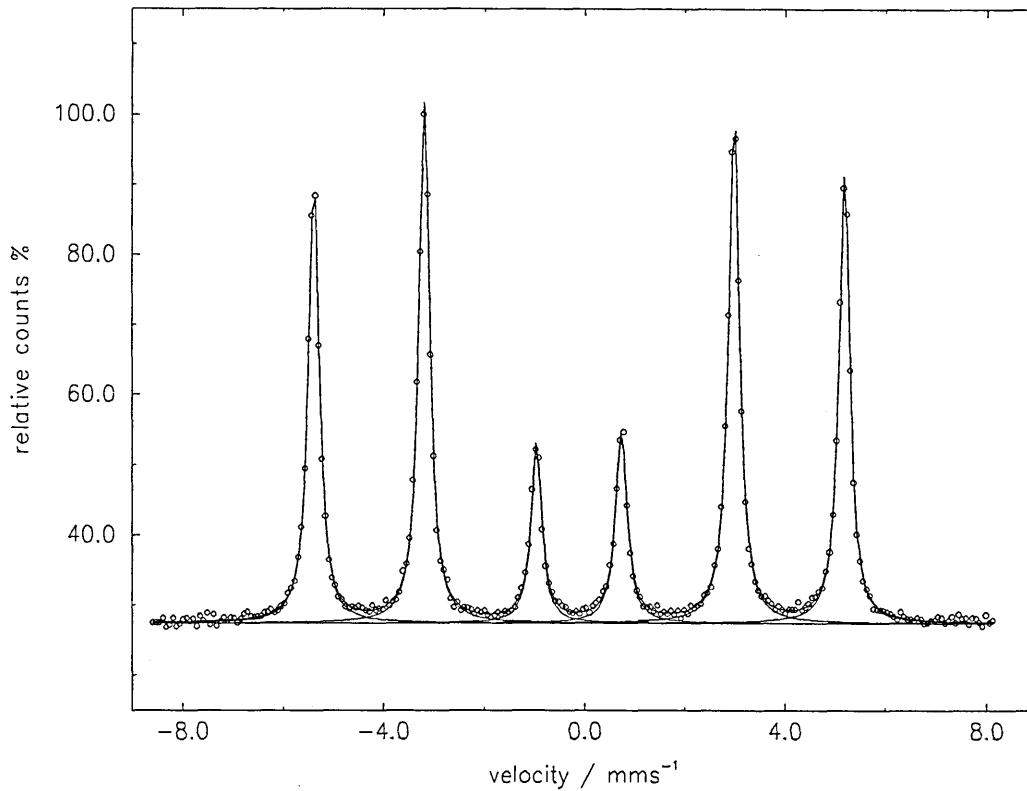


Fig. 3.14 Typical CEMS calibration from an  $^{57}\text{Fe}$  enriched iron foil.

The acquired calibration constant is then used to provide a velocity reference for the subsequent experiment. Also by performing a series of calibrations for a range of helipot settings it is possible to relate the velocity range to any helipot setting on the WissEl drive system, as shown in fig. 3.15. Thus, an approximate helipot setting for a particular velocity range can be obtained from the graph. This is useful, since in this study it has been necessary to perform calibrations for various velocity ranges depending on the spectral resolution required. From the graph it can be calculated that the drive velocity range is approximately 4.75 X the helipot setting.

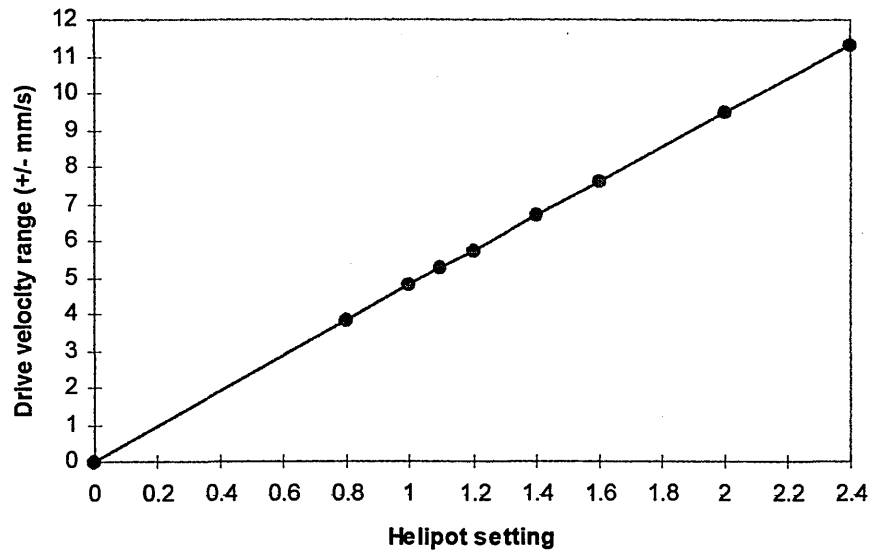


Fig. 3.15 Relationship between the helipot setting on the WissEl drive 260 and the drive velocity range.

## References

- [1] R. L. Mössbauer, *Z Physik* **151** (1958) 24.
- [2] G Breit, E. Wigner, *Phys Rev* **49** (1936) 519.
- [3] N. N. Greenwood, T. C. Gibb, "Mössbauer Spectroscopy", (Chapman and Hall, London, 1971).
- [4] H. Frauenfelder, "The Mössbauer Effect", (W. A. Benjamin, New York, 1962).
- [5] K. A. Stroud, "Further Engineering Mathematics", 2nd edition (Macmillan, London, 1990).
- [6] R. L. Collins, J. C. Travis, "Mössbauer Effect Methodolog", (Plenum Press, New York, 1967).
- [7] R. V. Parish, R. H. Platt, *Inorg. Chim. Acta.* **4** (1970) 65.
- [8] V. I. Goldanskii and R. H. Heber in "Chemical Applications of Mössbauer Spectroscopy" (Academic Press, 1968)
- [9] S. S. Hana, J. Heberle, G. J. Perlow, R. S. Preston, D. H. Vincent, *Phys Rev Letts* **4** (1960) 513.
- [10] G. J. Long, "Mössbauer Spectroscopy Applied to Inorganic Chemistry", Vol 1, (Plenum Press, New York, 1984).
- [11] K. R. Swanson and J. J. Spijkerman, *J. Appl. Phys.* **41** (1970) 3155.
- [12] J. A. Sawicki, *Mat. Sci. Eng.* **69** (1985) 501.
- [13] M. Petreva, U. Gonser, U. Hasmann, W. Keune and J. Lauer, *J. J. Physics (Paris) Colloq.* **C6** (1976) 295.
- [14] G. P. Huffman, *Nucl. Instr. Meth.* **137** (1976) 267.
- [15] J. Bainbridge, *Nucl. Instr. Meth.* **128** (1975) 531.
- [16] F. Salvat and J. Parellada, *Nucl. Instr. Meth.* **B1** (1984) 70.
- [17] D. Liljequist, T. Ekdahl and U. Bäverstam, *Nucl. Instr. Meth.* **155** (1978) 529.
- [18] D. Liljequist and T. Ekdahl, USIP Report 78-17, October, 1980.
- [19] J. M. Thomas, M. J. Tricker and A. P. Winterbottom, *J. Chem. Soc. Faraday 2* **71** (1975) 1708.
- [20] F. J. Berry, *J. Chem. Soc. Dalton Trans.* (1979) 1736.
- [21] D. W. Forester *Proc. Lunar. Sci. Conf. 4th* **3** (1973) 2697.
- [22] G. Longworth and M. S. Tite, *J. Physics (Paris) Colloq.* (1979) 460.
- [23] G. W. Simmons, E. Kellerman and H. Leidheisser, *Corrosion* **29** (1973) 227.
- [24] A. Sette Camara and W. Keune, *Corrosion Sci.* **15** (1975) 441.
- [25] M. J. Graham, D. F. Mitchell and D. A. Channing, *Oxid. Met.* **12** (1978) 247.
- [26] G. P. Huffman and H. H. Podgurski, *Oxid. Met.* **10** (1976) 377.
- [27] Y. Ujihira and K. Nomura, *Japan Analyst* **27** (1978) 782.
- [28] A. Handa, J. Kobayashi and Y. Ujihira, *Appl. Surf. Sci.* **20** (1985) 581.
- [29] J. Ensling, J. Fleisch, R. Grimm, J. Grüber and P. Gütlich, *Corrosion Sci.* **18** (1978) 797.
- [30] V. Ramshesh, K. Ravichandran and K. S. Venkateswarle, *Ind. J. Chem.* **20A** (1981) 867.
- [31] M. Fujinami and Y. Ujihira, *Appl. Surf. Sci.* **17** (1984) 265.
- [32] J. S. Brooks and S. C. Thorpe, *J. Hyper Int.* **47** (1989) 159.
- [33] B. D. Sawicka and J. A. Sawicki, *Nucleonika* **19** (1974) 811.
- [34] G. Langouche, *Solid State Phen.* **27** (1992) 181.

- [35] G. Longworth and N. E. W. Hartley, *Thin Solid Films* **48** (1978) 95.
- [36] A. Handa and Y. Ujihira, *J. Mat. Sci.* **18** (1983) 1751.
- [37] M. Carbucicchio, L. Barundi and G. Palumbarini, *J. Mat. Sci.* **15** (1980) 711.
- [38] Y. Ujihira and A Handa, *J. de Phys.* **40** (1979) C2-586.
- [39] G. Longworth, *Non-Destr. Test.* (1977) 242.
- [40] R. C. Mercader and T. E. Cranshaw, *J. Phys. F* **5** (1975) L124.
- [41] B. M. Clemens and D. L. Williamson,  
*Mat. Res. Soc. Symp. Proc.* **133** (1988) 159.
- [42] M. J. Graham, P. E. Beaubien and G. I. Sproule, *Thin Solid Films* **48** (1978) 95.
- [43] T. Fujii, R. Katano, S. Ito and Y. Isozumi, *Bull. Instr. Chem.  
Res. Kyoto Univ* **68(2)** (1990) 110.
- [44] G. Longworth, "Spectral Data Reduction and Refinement" in "Mössbauer  
Spectroscopy Applied to Inorganic Chemistry" ed. by G. J. Long (Plenum Press,  
1984) p.43.
- [45] *M.E.R.D.J.* **3** (1980) 99.

## CHAPTER 4

### EXPERIMENTAL TECHNIQUE

#### 4.1 Sample Preparation

Throughout this study, two substrate materials have been used; a type 304 stainless steel and a bright mild steel BS:1983:080A15. The composition of the mild steel was, C: 0.13-0.18 %, Mn: 0.70-0.90 %, Si: 0.10-0.40 %, P: 0.05 % max. and S: 0.05 % max. The mild steel substrates were polished to an average surface finish,  $R_a \approx 0.05 \mu\text{m}$  and measured  $40 \times 10 \times 3 \text{ mm}^2$ . All samples were cleaned using degreasing detergent and distilled water followed by ultrasonic cleaning in solutions of acetone and industrial methylated spirits prior to hot air drying to eliminate drying spots. After cleaning, all substrates were handled with either cotton gloves or metal tongs to prevent contamination with oils and salts from the skin.

##### 4.1.1 Evaporation

The deposition of a thin surface layer of the Mössbauer isotope  $^{57}\text{Fe}$  was achieved by vacuum evaporation from a tungsten filament using an Edwards E306 coating unit. Due to the very high cost of  $^{57}\text{Fe}$  (£6 per mg) as many samples as possible were coated in a single evaporation. This was achieved by attaching approximately 30 samples to a hemispherical grid arrangement of radius 8 cm. Each sample was attached through two 2 mm dia. holes by narrow gauge stainless steel wire. The vacuum level achieved was better than  $2 \times 10^{-7}$  torr and care was taken during the evaporation to minimise alloying between the  $^{57}\text{Fe}$  and the tungsten filament. The thickness of the deposited layer was estimated by considering the density of  $^{57}\text{Fe}$ , the mass of  $^{57}\text{Fe}$  evaporated and the source target-distance. For an evaporated mass of 17 mg the estimated thickness of the deposited layer was determined to be  $25 \pm 5 \text{ nm}$ .

### 4.1.2 Annealing Conditions

Initially, several attempts of producing annealed samples using a technique involving sealing the enriched substrates in fused silica tubing under argon, resulted in the formation of significant surface iron oxides identified by CEMS. Fig. 4.1 shows the CEM spectra obtained from a typical failed annealed sample and table 4.1 shows the associated Mössbauer parameters. The presence of  $\text{Fe}^{2+}$  ions (doublet in spectrum) can be deduced from the room temperature data obtained. However, to specifically identify the oxidation product as e.g. oxide, hydroxide or oxyhydroxide, it would be necessary to perform variable temperature backscatter Mössbauer spectroscopy.

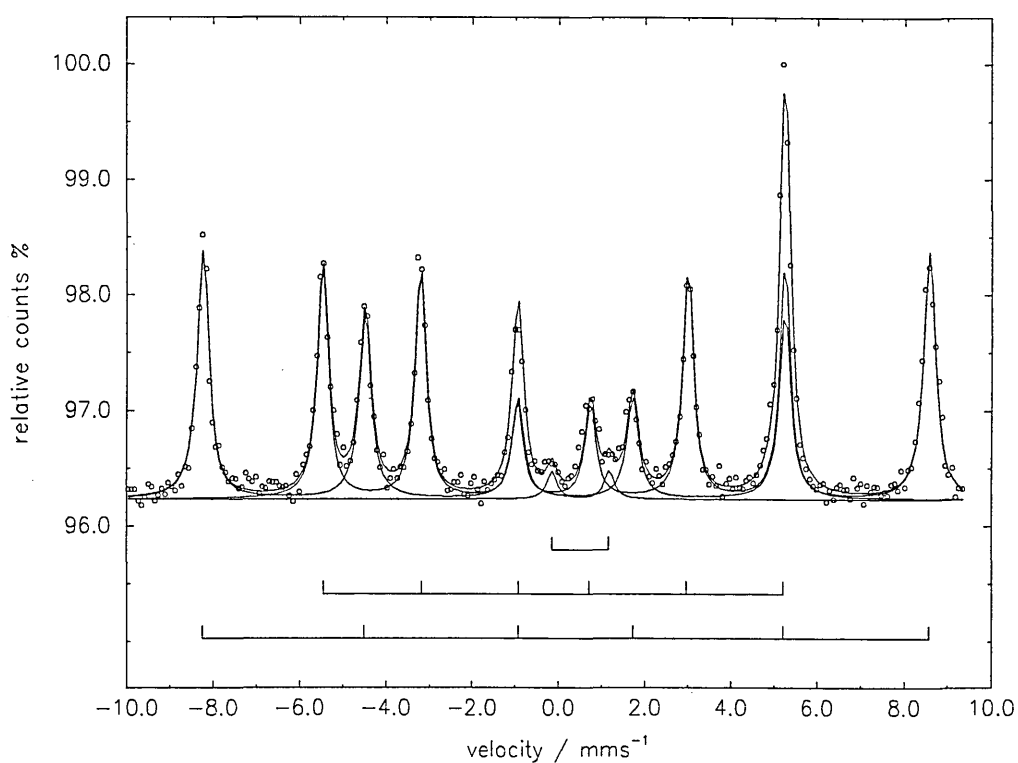


Fig. 4.1 Mild steel with an estimated 25 nm surface layer of  $^{57}\text{Fe}$  followed by annealing at 900 K for 90 minutes (failed sample).

Phase	$\delta(\text{Fe}) / \text{mm s}^{-1} \pm 0.02$	$\Delta / \text{mm s}^{-1} \pm 0.02$	$H_{\text{int}} / \text{kG} \pm 5$
$\text{Fe}^{2+}$	0.62	1.34	-
$\alpha\text{-Fe}$	0.00	-	330
$\text{Fe}_2\text{O}_3$	0.38	0.00	521

Table 4.1 Mössbauer parameters associated with an unsuccessfully annealed sample.

After initial attempts of producing annealed samples as shown in fig. 4.2, a successful annealing technique was achieved. This consisted of sealing the enriched substrates after careful cleaning of all the sample edges including the reverse side, in fused silica tubing under argon with 2 pieces of freshly polished titanium.

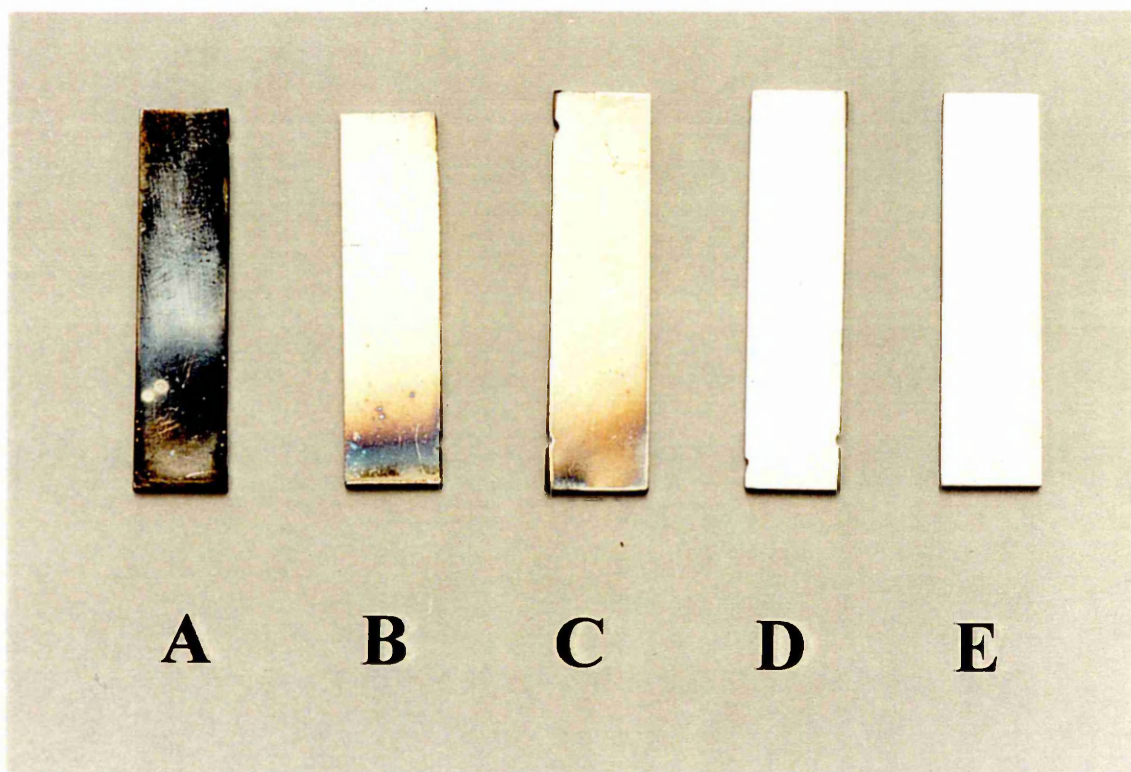


Fig. 4.2 Samples annealed at 900 K for 90 minutes at various argon pressures at room temperature in sealed fused silica tubing; A, 80 Torr, B 150 Torr, C 760 Torr, D and E, 760 Torr after careful cleaning of the edges and reverse sides.

The titanium acted as an oxygen scavenger and preferentially oxidised. The sealed substrates were annealed at 900 K for 90 minutes. The successful annealing technique involved using an argon pressure of 1 atm and the substrates had clean edges and reverse sides. The arrangement used is shown in fig. 4.3.

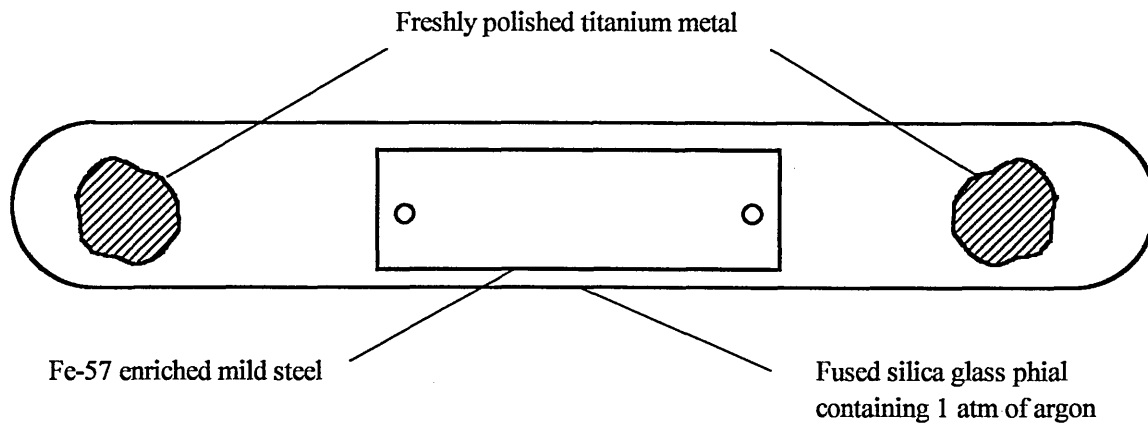


Fig. 4.3 Arrangement used for annealing substrates.

## 4.2 Diffusion Model

A simple diffusion model [1] enables the depth profile of the  $^{57}\text{Fe}$  to be predicted as a function of annealing conditions. This model assumes that a uniform layer of  $^{57}\text{Fe}$  is deposited and that the annealing takes place in an oxygen free environment. The diffusion equation may be written as:

$$\nabla^2 F = \frac{1}{D} \frac{\delta F}{\delta t} \quad (4.1)$$

F = Fractional concentration of  $^{57}\text{Fe}$   
(F = 1 corresponds to 100 %  $^{57}\text{Fe}$ )  
D = Diffusion rate

D can be expressed as:

$$D = D_0 \exp\left\{\frac{-Q}{RT}\right\}$$

Q = Activation energy  
 R = Molar gas constant  
 T = Absolute temperature

Equation (4.1) may be rewritten for the 1 dimensional case as:

$$\frac{\delta^2 F}{\delta x^2} = \frac{1}{D} \frac{\delta F}{\delta t}$$

This can be reduced to a dimensionless equation by using the following substitutions:

$$x = Ld \quad \text{and} \quad \tau = \frac{Dt}{d^2}$$

Hence,

$$\frac{\delta^2 F}{\delta L^2} = \frac{1}{D} \frac{\delta F}{\delta \tau}$$

This differential equation may be solved numerically by a standard iterative net method subject to the following boundary conditions as shown in fig. 4.4.

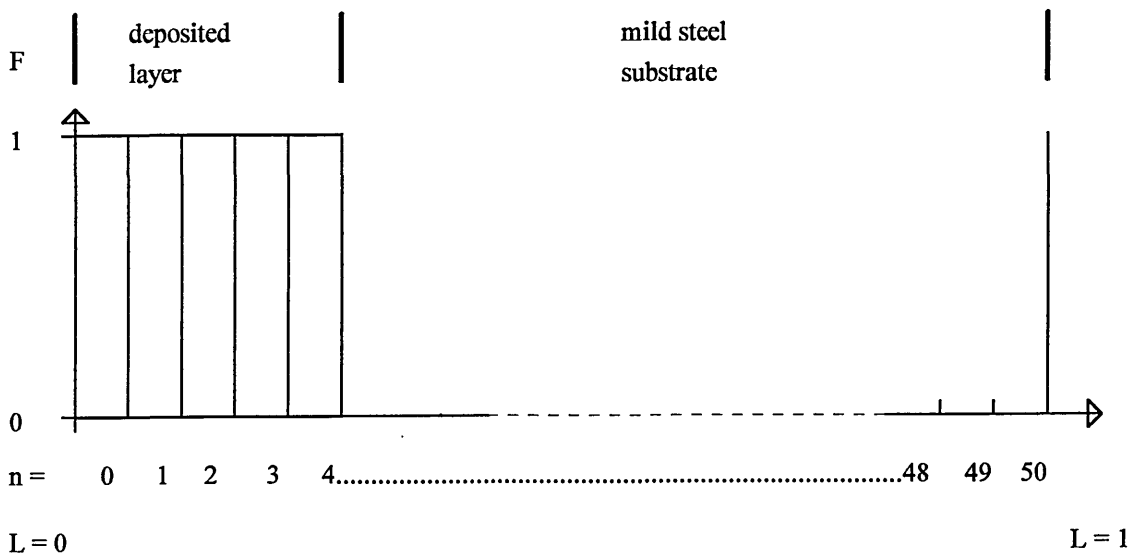


Fig. 4.4 Boundary conditions for numerical model.

By defining the concentration at time  $\tau$  to be  $F_0 - F_n$  and evaluating at time  $\tau + \Delta\tau$  as  $G_0 - G_n$  the standard iterative net approach leads to:

$$G_i = \frac{\Delta\tau}{(\Delta L)^2} \{ F_{(i+1)} - 2F_i + F_{(i-1)} \} + F_i$$

For stability, it is necessary for  $\Delta\tau/(\Delta L)^2 < 1/2$  e.g.

$$\frac{\Delta\tau}{(\Delta L)^2} = n^2 \Delta\tau = 0.25 \quad \text{selecting } \Delta\tau = 1 \times 10^{-4}$$

A computer program written in FORTRAN (see Appendix 3) allows the above numerical method to solve the differential equation for a given number of points. It was decided that an adequate solution would be generated by considering 50 net points.

#### 4.2.1 Lattice Self Diffusion in Iron

Mild steel can be considered to have similar properties to the bcc phase of iron. Okwa [2] has reviewed the lattice self diffusion in iron. For the paramagnetic region ( $1043 \text{ K} < T < 1809 \text{ K}$ ), the diffusion rate can be written as:

$$D_{\alpha p} = D_{\alpha\alpha p} \exp\left\{\frac{-Q}{RT}\right\} \quad 1043 \text{ K} < T < 1809 \text{ K}$$

$$D_{\alpha\alpha p} = 2.00 \times 10^{-4} \text{ m}^2 \text{ s}^{-1}$$

$$Q = 2.41 \times 10^5 \text{ J mol}^{-1}$$

However, for most practical purposes, annealing takes place at temperatures lower than  $1043 \text{ K}$ ; the ferromagnetic region. The diffusion rate for the ferromagnetic region can be written as:

$$D_{\alpha p} = D_{\alpha\alpha p} \exp\left\{\frac{-Q(1 + 0.22S^2)}{RT}\right\} \quad T < 1043 \text{ K}$$

$$S = \frac{I_s(T)}{I_s(0)} \quad I_s = \text{saturation magnetization}$$

The previously described diffusion model evaluates the fractional concentration  $F$  at each net point per iteration of unit time  $\Delta\tau$ . This is related to real time by the expression:

$$\Delta\tau = \frac{D\Delta t}{d^2}$$

Therefore, for an estimated 25 nm layer of  $^{57}\text{Fe}$  equated to 5 net points, then the total number of 50 net points defines a thickness of 250 nm. This yields the following real time values:

Temperature / K	$S^2$	$D_{\text{af}} / \text{m}^2 \text{s}^{-1}$	$\Delta t / \text{sec per iteration}$
900	0.49	$7.3 \times 10^{-20}$	55

At 900 K, each iteration requires 55 s, thus 100 iterations take 5500 s; approximately 90 minutes. Fig. 4.5 shows the predicted diffusion for the associated thin  $^{57}\text{Fe}$  surface layer, annealed at 900 K for various times. It can be seen that after approximately 90 minutes, the surface fractional concentration has reduced to almost 0.5 and the diffused  $^{57}\text{Fe}$  penetrates to a depth of almost 100 nm at a fractional concentration higher than the  $^{57}\text{Fe}$  natural abundance level.

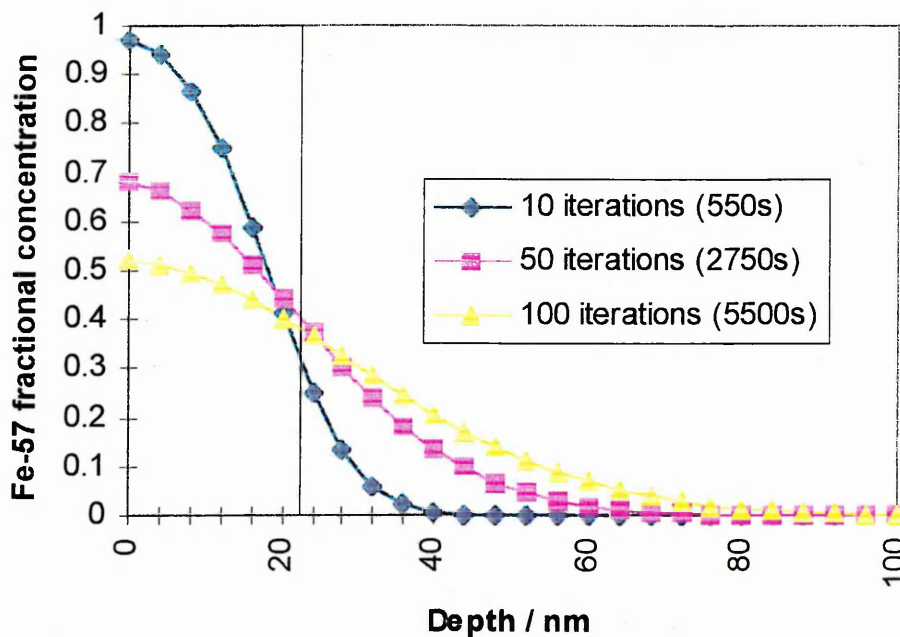


Fig. 4.5 Predicted fractional concentration of  $^{57}\text{Fe}$  as a function of depth for a mild steel annealed at 900 K.

### 4.3 ABS™ Experimental Arrangement

The vacuum chamber design of the Hauzer HTC 1000-4 coating system comprises of 25 mm thick stainless steel chamber which has an octagonal cross section. This allows for maximum accessibility to the interior of the chamber, targets and substrates. Access can be from two sides of the chamber, thereby allowing the system to be 'see through' as shown in fig. 4.6.

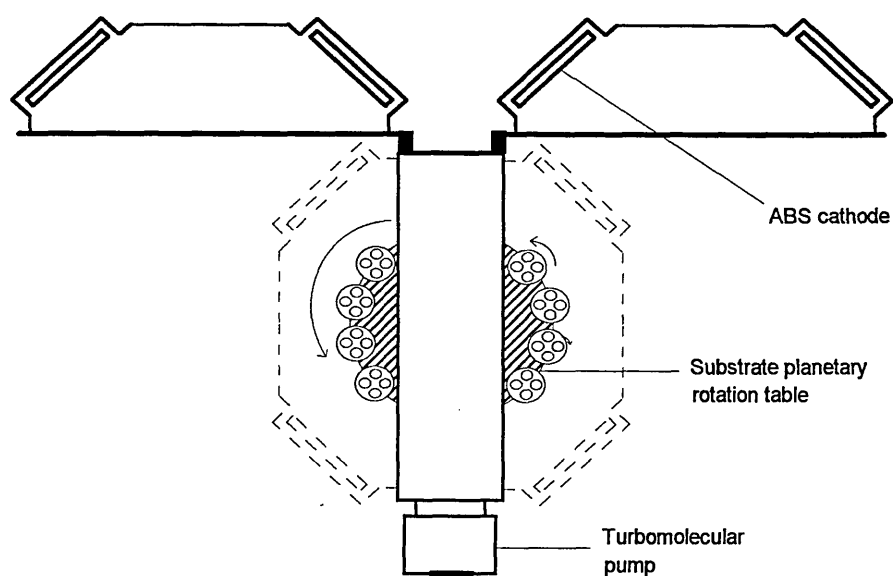


Fig. 4.6 Schematic of the Hauzer HTC 1000-4 coating chamber.

The 4 targets can be up to 600 mm long x 190 mm wide. The chamber is equipped with two view ports along with openings for the necessary pumping arrangement. This pumping arrangement consists of 2 Balzers TPH 2200 turbomolecular pumps, to provide an oil free vacuum within the chamber, combined with a roots pump and a rotary vane pump.

Movable shutters operate between the targets and substrate holder which makes it possible to cover the cathodes during pre-sputter to stabilise the operation of the cathodes before the etching process. The substrate holder can be kept stationary or, more usually used to provide triple planetary rotation which is rotated on a vertical axis

during the coating process. For the coating of small components, each component is rotated, which in turn is mounted on opposite rotating satellite modules. During the coating process the satellites are moved through the chamber rotating in a vertical orientation, opposing their own rotation. This method is typically used for the coating of drill bits and is termed “3-fold rotation”. The turntable can also provide single and 2-fold rotations by attaching pieces directly to the turntable or to the satellite axis, respectively. A side view of the substrate holder showing the triple planetary rotation is shown in fig. 4.7.

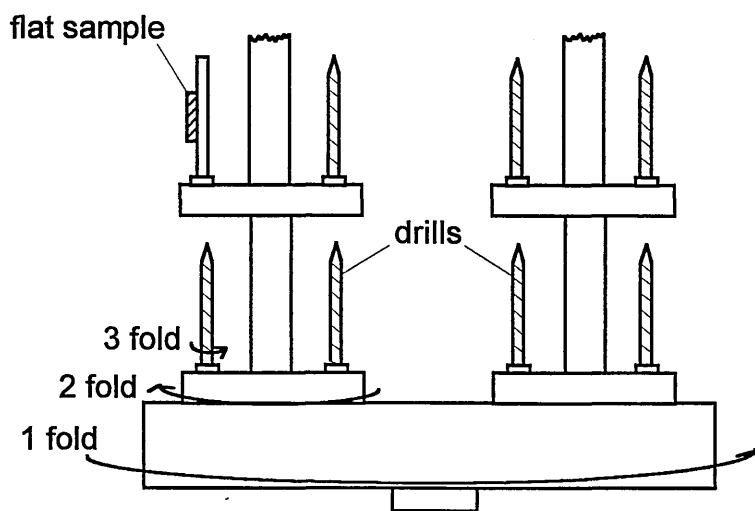


Fig. 4.7 Substrate holder showing the modes of rotation.

The water cooled cathodes were fabricated from 99.98 % purity titanium and could be operated in steered arc or magnetron mode with variable electromagnetic unbalancing in a linked or closed field configuration. Each cathode was connected to an individual power supply capable of delivering 80 V @ 100 A max. in the arc mode and 750 V @ 40 A max. in the magnetron mode. During experiments the substrate temperature was monitored by two thermocouples positioned in the centre of the chamber. Before loading the samples into the chamber any surface dust was removed using an air jet. A typical process sequence would be as follows:

- 1) Pump down with samples positioned in the vacuum chamber to approximately  $1 \times 10^{-5}$  mbar. This would typically take 2 hours. A residual gas analyser was used to ensure that the water vapour to nitrogen ratio was better than 1:10.
- 2) Heat the substrates to approximately 350 °C for approximately 30 minutes.
- 3) Clean the cathode(s) with Ar ions in unbalanced magnetron glow discharge mode for approximately 10 minutes using shutters over the cathode(s) to collect sputtered contaminants. This step was usually carried out at  $2 \times 10^{-3}$  mbar Ar pressure, bias voltage 0 V and a cathode discharge power of 5 kW.
- 4) Ti ion pre-treatment of substrates using the steered arc mode at Ar pressures between  $3 \times 10^{-3}$  to  $7 \times 10^{-4}$  mbar, at a bias voltage of -1200 V and a maximum cathode discharge current 100 A. Due to the rapid heating this step generates, ion bombardment was confined to a maximum of 1 minute intervals to reach a temperature of 450 °C, followed by cooling to 400 °C. Longer pre-treatment times were achieved by repeating the ion bombardment followed by a cooling cycle.
- 5) Ti coating deposition (if required) at an Ar pressure of  $5 \times 10^{-3}$  mbar and a substrate bias voltage of -80 V. The discharge power per cathode was typically 2 kW and the deposition was carried out for 30 s. to deposit a thin Ti layer.
- 6) Cool down to below 200 °C by increased Ar flow for typically 2-3 hours before removing samples.

## 4.4 Complementary Techniques

During this study, several analytical techniques have been used. These techniques did not require any significant sample preparation other than a quick surface clean with an air jet. Such preparation, unlike mechanical sectioning, polishing etc., ensures that no distortion, damaging or contamination of the sample to be examined occurs.

### 4.4.1 Scanning Electron Microscopy

Scanning Electron Microscopy (SEM) depends on the interaction of an electron beam with a sample [3,4]. The incident electrons are in the form of a very fine probe having energies typically between 20 - 40 keV and are focused across in a pattern of parallel lines or "raster". At the surface of the sample a number of phenomena occur in the region of electron impact. Most importantly, these include the emission of secondary electrons with energies a few tens of eV and the re-emission or reflection of higher energy backscattered electrons from the primary beam. The intensity of emission of both secondary and backscattered electrons is sensitive to the angle at which the primary beam strikes the surface of the sample and hence provides topographical information. The emitted electron current may be detected by a photomultiplier detector and after amplification, a variation in the resulting signal strength over the raster produces a similar brightness variation of a trace on a cathode ray tube (CRT) by scanning in synchronisation with the probe. Therefore, a direct position correspondence exists between the scanning electron beam across the sample and the fluorescent image on the CRT. The produced magnification is the ratio between the dimensions of the final image display and the raster on the sample. This magnification is realised by passing an electron beam produced by an electron gun, through several electromagnetic lenses which determine the final fine probe size. Changes in the magnification are brought about by altering the extent of the sample scan whilst keeping the display size constant. In practice, this is achieved by varying the angle the electron beam is deflected which is dependent on the working distance of the sample from the final lens. For a typical working distance of 15 mm, this may result in a magnification range between x10 to

x100,000. In addition to secondary and backscattered electrons, the interaction of the primary beam with the sample produces characteristic X-rays. This occurs since during electron emission by the inelastic collision with the primary beam, the resultant ion undergoes relaxation from the excited state by dropping an outer shell electron into the vacancy in the inner shell. Subsequently, energy is emitted during this transition in the form of an X-ray photon, characteristic of the element from which it came. Therefore, this phenomenon can be utilised for elemental compositional spectrometry, with either a Wavelength Dispersive or Energy Dispersive detector for the purpose of EDS or WDS respectively. This study used a Philips XL40 ASEM equipped with EDS.

#### 4.4.2 Glow Discharge Optical Emission Spectroscopy

Glow Discharge Optical Emission Spectroscopy (GDOES) utilises the principle of excitation followed by relaxation of atoms originating from the sample under study. The excitation process occurs if sufficient energy is transferred to an atom causing an increase in the energy of an electron such that it is promoted to a higher energy level or orbital. This unstable state subsequently undergoes relaxation by dropping the electron to a vacant lower energy level. This is energetically more favourable and results in the dissipation of excess energy by photon emission whose wavelength,  $\lambda$  corresponds to the energy, E emitted:

$$E = hc/\lambda$$

where h is Planck's constant and c is the speed of light. The energy transition process of an electron between two quantised energy levels corresponds to the absorption or emission of energy as electromagnetic radiation. Since each elemental atom comprises of different electron orbital energy levels, then the allowed possible electron transitions will also differ. Hence excitation for each elemental atoms gives rise to the emission of characteristic spectral lines by which each individual element may be identified. However, it should be noted that if more than a certain threshold or binding energy is supplied to an outer orbital electron of an atom, then the electron will be completely freed and the atom becomes ionised. The produced ion cannot spontaneously undergo

relaxation without external interaction and so does not contribute to photon emission directly, but the free electron or ion itself can cause excitation in other atoms.

The intensities of the produced spectral lines are proportional to the number of emitted quanta, and hence to the elemental contribution. For spectral lines to be produced by the method described, the atoms must be in the form of a low pressure gas, since an excited solid will produce a continuum of energy emission due to thermal radiation and lattice vibrations. Therefore, the solid must be volatilised into an evacuated chamber. GDOES uses a glow discharge plasma for this process. The technique requires little or no sample preparation for bulk solids and is capable of providing compositional depth profiling.

The analysis chamber used in this technique is based upon a glow discharge lamp design by Grimm [5] as shown in fig. 4.8. The arrangement consists of a small vacuum chamber with a hollow cylindrical anode typically 4 or 8 mm in diameter with the sample under study forming the cathode at one end. The outside of the anode cylinder is vacuum pumped and contains argon as the working gas. The other end of the cylinder is sealed with a photon transparent window. The transmitted photons are detected and analysed via a polychromator. Typical operating conditions are 500 to 1500 V at 20 to 200 mA, yielding a sputter rate in the range 10 to 100 nm per second.

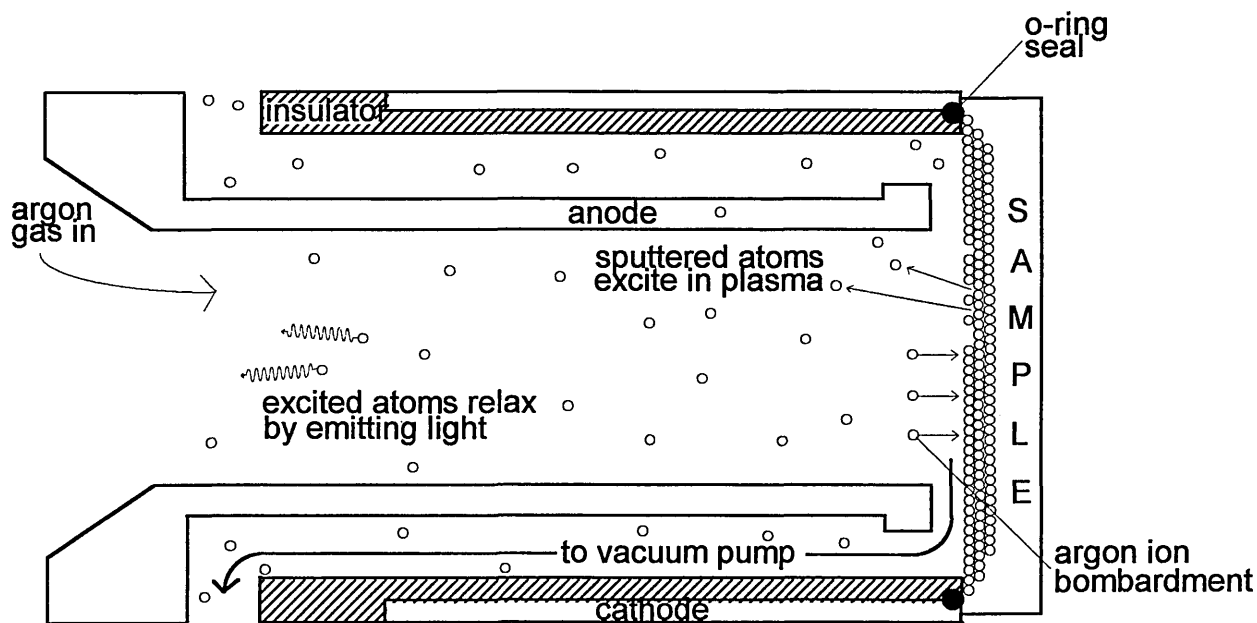


Fig. 4.8 Schematic of sputtering in a glow discharge lamp.

The glow discharge process is generated by applying a suitable voltage across the anode and cathode, that causes a breakdown of the argon gas and the produced ions are accelerated across the dark space towards the cathode. On impact, kinetic energy is transferred and causes sputtering of neutral cathode atoms along with secondary electrons. The secondary electrons accelerate rapidly towards the anode and upon collision with the working gas atoms, cause ionisation which sustains the discharge. The sputtered cathode atoms diffuse across the dark space into the negative glow region and undergo excitation or ionisation by collisions with secondary electrons or argon ions. These excited cathode atoms emit characteristic line spectra after relaxation, as described previously. Similarly spectral line emission is generated from the excited argon atoms. The emitted photons pass through the window at the end of the discharge chamber and are detected by a polychromator arrangement.

The basic polychromator arrangement contains an entrance slit that provides a narrow optical image. Parallel light rays of the emitted photons are focused and pass through this entrance slit and a concave reflective diffraction grating is used to disperse the incident light. Exit slits at appropriate locations forming a Rowland circle [6] are used to isolate particular spectral wavelengths. A total of 44 photomultiplier tubes placed behind the exit slits are used to detect, amplify and convert the light into an electrical signal suitable for processing. The quantification allows for the determination of the sputtered depth, from the sputter times and sputter etch rates of individual elements along with the chemical content from the emission line intensities.

The monitored emission line intensities are dependent on the voltage, current and sputter rates, along with the chemical composition. By operating in either constant current or voltage mode the intensity dependence on a variable parameter can be found, leading to an empirical formulae relating all the parameters. This intensity calibration is performed routinely using certified reference materials of known chemical composition.

GDOES has proved to be of considerable importance for the analysis of PVD coatings [7]. The technique has been shown to provide information about coating thickness,

elemental distribution and stoichiometry [8]. However, the technique cannot provide substantial chemical information regarding the constituents of interfaces in the order of nanometers in thickness.

#### 4.4.3 Secondary Ion Mass Spectrometry

Secondary Ion Mass Spectrometry (SIMS) is a powerful surface analysis technique for investigating the chemical nature of solid surfaces [9]. The technique consists of the mass analysis of ejected particles from a solid surface during bombardment with an energetic ion beam. The incident primary beam usually consists of noble gas ions e.g.  $\text{Ar}^+$  ions in order to minimise any chemical modification of the sample under study. The sputtered secondary particles consist of both atomic and molecular species and exist as positive and negative ions as well as electrically neutral particles. The ejected particles are analysed as a function of mass/charge to produce a mass/charge spectrum of the sputtered ions in a similar way to mass spectrometry. By having a sufficiently good mass resolution providing perfect mass separation, it is possible to detect all elemental and poly-atomic ions. Hence, SIMS allows for the detection of all elements and associated isotopes. However, a major disadvantage of SIMS is that often only a minute fraction of sputtered particles leave the surface in a charged state resulting in low detection efficiency. Techniques related to SIMS have been developed which attempt to overcome this problem by post-ionisation of the ejected neutrals prior to detection - Secondary Neutral Mass Spectrometry (SNMS) [10].

Essentially the SIMS technique can be characterised by the gun type used and the analysis instrumentation, giving rise to 3 distinct operating modes. Firstly by using a low primary beam current  $\sim 1 \text{ nA/cm}^2$ , the sample surface suffers little disturbance and the resultant SIMS spectrum gives information about the top few monolayers of the material; this is known as “Static SIMS”. Secondly by using a liquid metal gun generating a beam resolution of  $\sim 100 \text{ nm}$ , it is possible to build up a secondary ion map of the sample surface by rastering the primary beam; this is known as “Imaging SIMS”. Finally, in “Dynamic SIMS” a higher flux of primary ions is used and the sample is rapidly eroded

layer by layer using a rastering technique which results in a compositional/depth profiling technique. Using this method, sampling depths of 10 monolayers can be achieved with a sensitivity in the order of <1 p.p.m. The Dynamic SIMS technique has been used for interface analysis [9 references therein]. In particular, the technique has been used to study the interface region of various nitride coatings deposited by magnetron devices [11-13] However, it should be noted that sputter depth profiling is a destructive technique which can result in interfacial mixing making quantitative analysis at the interface difficult.

## References

- [1] J. S. Brooks and S. C. Thorpe, *J. Hyp. Int.* **47** (1989) 159.
- [2] H. Oikawa, *Technology Reports, Tohoku Univ.* **47** (1982) 67.
- [3] D. K. Bowen and C. R. Hall, "*Microscopy of Materials*", (Macmillan Press, London, 1975).
- [4] I. M. Watt, "*The Principles and Practice of Electron Microscopy*", (Cambridge University Press, Cambridge, 1989).
- [5] W. Grimm, *Spectrochimica Acta B* **23** (1968) 443.
- [6] J. F. James and R. S. Steraberg, "*The Design of Optical Spectrometers*", (Chapman and Hall, London, 1969).
- [7] V. Hoffman, *Fres. J. Analytical Chem.* **346(1-3)** (1993) 165.
- [8] M. Ives PhD thesis, "*Fundamental Studies of the PVD Technique*", Sheffield Hallam University, 1994.
- [9] D. Briggs and M. P. Seah, "*Practical Surface Analysis, 2nd edition. Vol. 2 Ion and Neutral Spectroscopy*", (John Wiley and Sons, Chichester, 1992)
- [10] A. M. Spool, *IBM J. Res. Develop.* **38** (1994) 391.
- [11] S. Lopez, H. M. Dunlop, M. Benmalk, G. Tourillon, M. S. Wong and W. D. Sproul, *Surf. Int. Analysis* **25(5)** (1997) 315.
- [12] G. S. Foxrabinouich, A. I. Kovalev and D. L. Wainstein, *J. Elec. Spec. Rel. Phen.* **85(1-2)** (1997) 65.
- [13] K. Koski, J. Holsa, J. Ernoult and A. Rouzand, *Surf. Coat. Technol.* **80(1-2)** (1996) 195.

## CHAPTER 5

# PRELIMINARY MÖSSBAUER STUDIES AND SURFACE INTERACTIONS IN A PVD PROCESS

### 5.1 Surface Sensitivity of CEMS

The deposition of Aluminium films onto type 304 stainless steel was performed using a resistive heating evaporation method from a tungsten filament at a pressure of  $2 \times 10^{-7}$  torr. The deposited thickness,  $t$  was estimated using the relationship:

$$t = \frac{m}{4\pi r^2 \rho} \quad (5.1)$$

where  $m$  is the evaporated mass,  $\rho$  is the density of the evaporant and  $r$  is the source-substrate distance. For aluminium,  $\rho = 2700 \text{ kg m}^{-3}$  and in this case,  $r$  was set at  $r = 5 \times 10^{-2} \text{ m}$ . During the evaporation of the thicker films, a small piece of Si wafer was placed adjacent to the stainless steel substrate. This was later used for a verification of the estimated thickness by GDOES. Fig. 5.1 shows the GDOES depth profile for an estimated  $106 \pm 6 \text{ nm}$  of Al deposited on a Si wafer. It can be clearly seen from the depth profile that a small surface Si oxide layer is present, and more importantly, the cross-over of Al and Si occurs at approximately 102 nm. This verifies the initial estimate and validates the relationship relating the deposited thickness with the evaporated mass, density and source-substrate distance.

The produced Al overlayers ranged from 25-130 nm and the obtained CEM spectra for the deposited Al layers on stainless steel, along with a stainless steel substrate prior to coating are shown in fig. 5.2. In all cases, the measured isomer shift relative to  $\alpha$ -Fe was  $-0.09 \pm 0.02 \text{ mm s}^{-1}$  and  $\Gamma/2 = 0.17 \pm 0.01 \text{ mm s}^{-1}$ . The observed spectra provide an indication of the maximum permissible thickness of deposited coating allowed, for a CEM spectrum to be recorded having adequate statistical quality. Table 5.1 shows the measured percent effect and S/N values of the CEM spectra for various Al thickness overlayers.

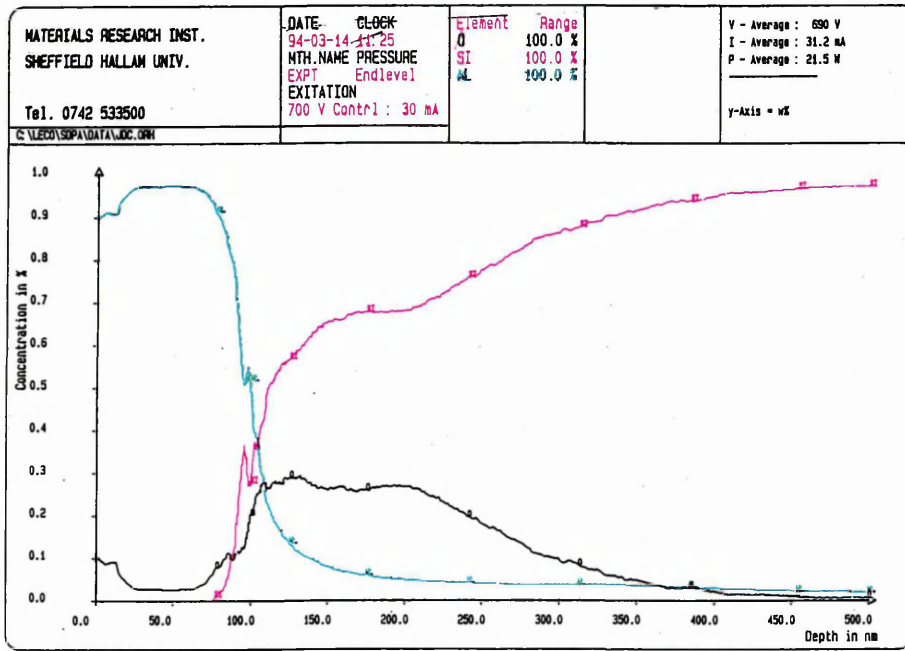


Fig 5.1 GDOES depth profile of an estimated  $106 \pm 6$  nm thickness of aluminium deposited on a silicon wafer.

Al mass (mg) / $\pm 0.5$	Al thickness (nm) / $\pm 6$	Percent effect (%)	S/N
-	0	5.2	0.53
2.0	25	8.1	0.84
4.5	53	7.7	0.75
6.5	77	6.4	0.59
9.0	106	3.8	0.34
11.0	130	1.7	0.15

Table 5.1 Percent effect and S/N values associated with the CEM spectra for various aluminium thickness overlayers on type 304 stainless steel.

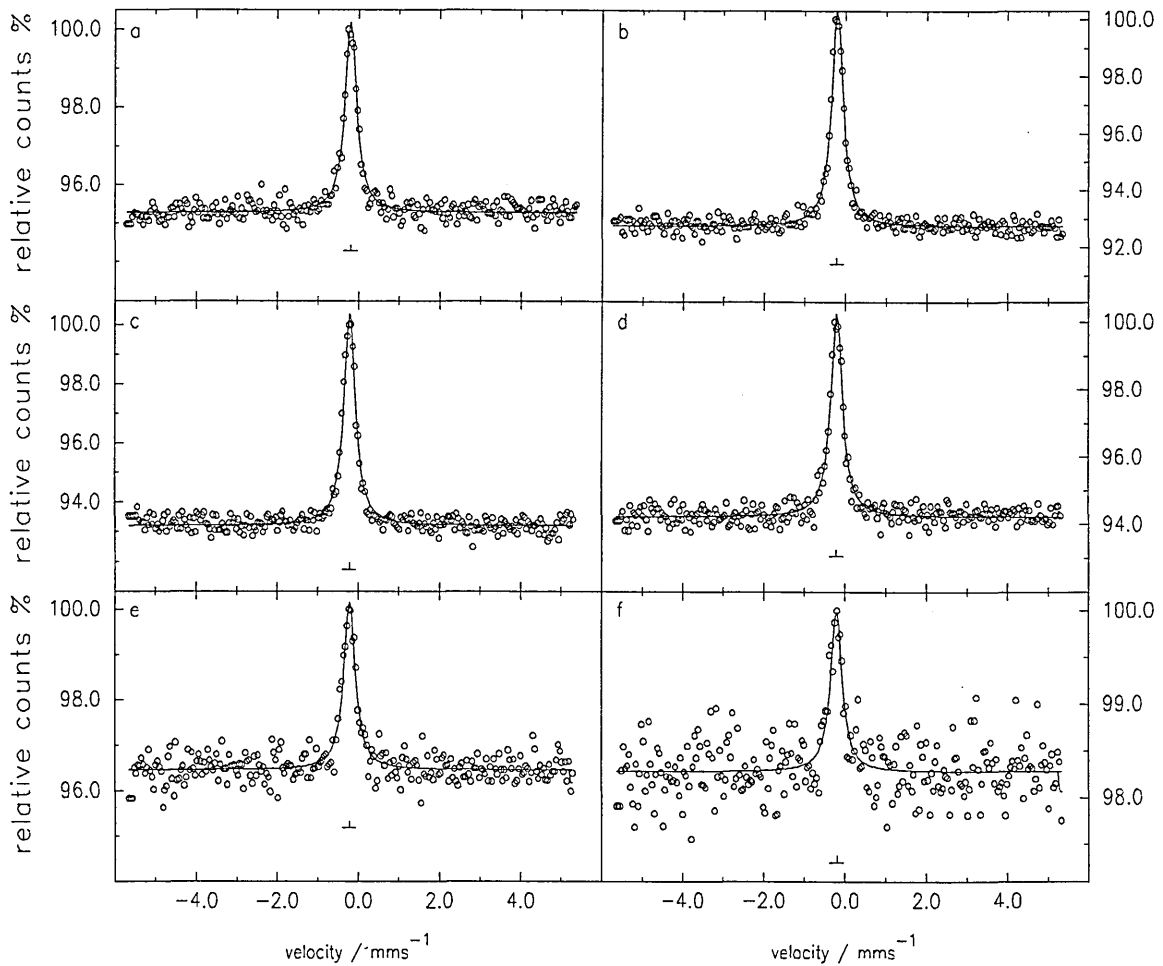


Fig.5.2 CEM spectra of stainless steel (a) and various Al overlayers on stainless steel; (b) 25, (c) 53, (d) 77, (e) 106, and (f) 130 nm.

The variation of the percent effect and S/N as a function of deposited Al thickness on stainless steel are shown in figs. 5.3 and 5.4. In both cases an initial increase in the percent effect and S/N can be seen for the 25 nm deposited Al layer on stainless steel sample, compared with a sample prior to deposition. This can be explained by considering the fate of incident  $\gamma$ -rays on a sample. A proportion of  $\gamma$ -rays are absorbed resonantly within the sample and approximately 30 % of the excited  $^{57}\text{Fe}$  nuclei emit K X-rays. These X-rays are only weakly absorbed within the sample, unlike the produced conversion and Auger electrons, and therefore a generated flux of X-rays reach the

surface of the sample. If a Mössbauer inert surface overlayer e.g. Al is present, then the fluorescent X-rays will produce photo-electrons in the surface layer which may be detected in the counter. Such a mechanism has been shown by Tricker *et al.* [1] to alter the ratio of Fe on stainless steel substrates with an inert Mössbauer surface layer in an unexpected way. In their study, the stainless steel substrate intensity was found to increase compared with the  $\alpha$ -Fe overlayer with the addition of successive layers of Al or Au due to the described effect.

For the addition of increased thickness of deposited Al layers from 60 - 130 nm on stainless steel, figs. 5.3 and 5.4 show a linear decrease in both the percent effect and the S/N. This is due to the dominant phenomenon now present being the absorption of electrons in matter and the effect of X-ray production generating electrons in the surface layers becoming less important.

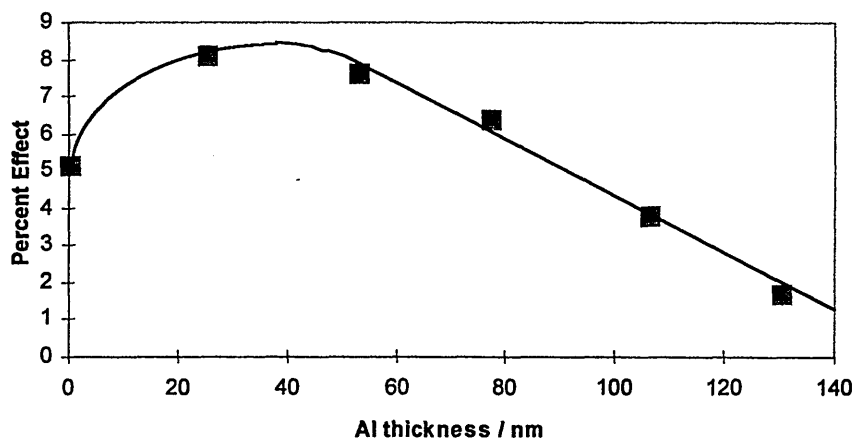


Fig. 5.3 Variation of Percent effect as a function of deposited Al thickness.

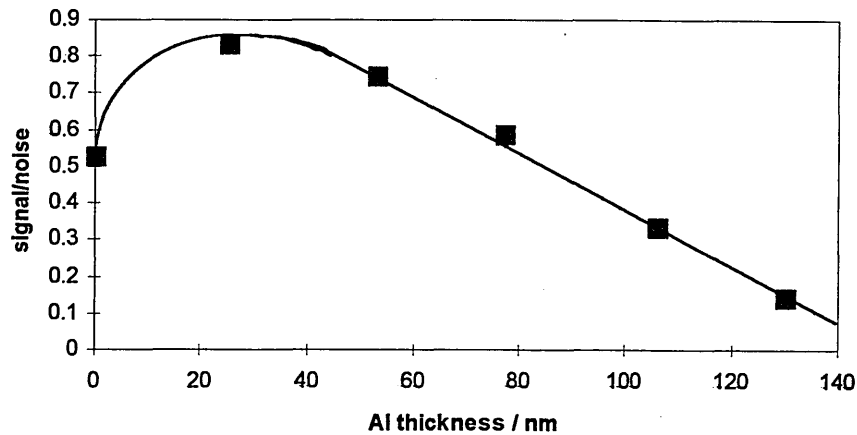


Fig. 5.4 Variation of S/N as a function of deposited Al thickness.

## 5.2 Determination of Ion Etch Rates in the ABS<sup>TM</sup> Process

The Ti ion pre-treatment process used in the ABS<sup>TM</sup> method has been shown to result in the ejection of a small quantities of macroparticles from the cathode arc source ranging in size upto several microns [2]. Therefore the determination of etch rates using weight loss measurements or depth cratering techniques are not suitable due to the existence of macroparticles on the pre-treated substrate surface.

The program CEMSN2 (Chapter 3 and Appendix 1) determines the thickness of a surface overlayer from the relative spectral areas of a measured CEM spectrum for a duplex system. In this study, the CEMSN2 proram has been used to determine the thickness of a natural Fe overlayer on stainless steel substrates before and after Ti ion etching and thereby quantifies the associated etch rates for various pre-treatment processes over a short period of time.

Two batches of type 304 stainless steel substrates were ultrasonically cleaned in both industrial methylated spirits and acetone prior to the deposition of a thin overlayer of iron of natural <sup>57</sup>Fe abundance, by evaporation under vacuum at  $2 \times 10^{-7}$  torr . Two separate experiments were performed using the Hauzer (HTC) 1000-4 ABS<sup>TM</sup> PVD system. The first experiment studied Ti ion etching effects for two samples placed

directly in front of one cathode operating in the steered arc mode with the substrate holder remaining stationary. In this "static" experiment the two cathode-sample distances used were 250 and 350 mm respectively. The second experiment used two horizontally opposed cathodes operating simultaneously and studied the Ti ion etching effects for four samples while rotating the substrate holder at a velocity typically used in a conventional industrial pre-treatment/coating process. In this experiment, two samples were subjected to 2 fold and 3 fold rotations and a further two samples were subjected to 1 fold rotation at minimum cathode-sample distances of 250 and 350 mm. In both the static and substrate rotation experiments, the substrate bias voltage was -1200 V and the pre-treatment processes were performed for 30 s at an argon pressure of  $3 \times 10^{-3}$  mbar and the maximum substrate temperature was 450 °C.

The CEM spectra of the as deposited natural Fe on stainless steel and the samples subjected to the static Ti ion etch pre-treatment are shown in fig. 5.5. For the as deposited sample an estimate of the thickness of the Fe overlayer was provided from the measured mass gain after deposition. This gain was measured to be  $210 \pm 10 \mu\text{g}$  over a sample area of  $15 \times 30.5 \text{ mm}^2$ . This corresponds to a thickness of  $58 \pm 3 \text{ nm}$ . This thickness differs from the 51 nm predicted by the CEMSN2 program since the real sample surface area is greater than the measured area due to surface roughness.

The measured spectra show a singlet resulting from the paramagnetic Fe sites of the stainless steel and an additional sextet pattern due to the natural Fe overlayer. In all cases the measured halfwidths of the spectral lines was found to be  $0.16 \pm 0.02 \text{ mm s}^{-1}$  and no changes in the magnetic field of the  $\alpha$ -Fe prior to and after the pre-treatment process was observed as shown in table 5.2.

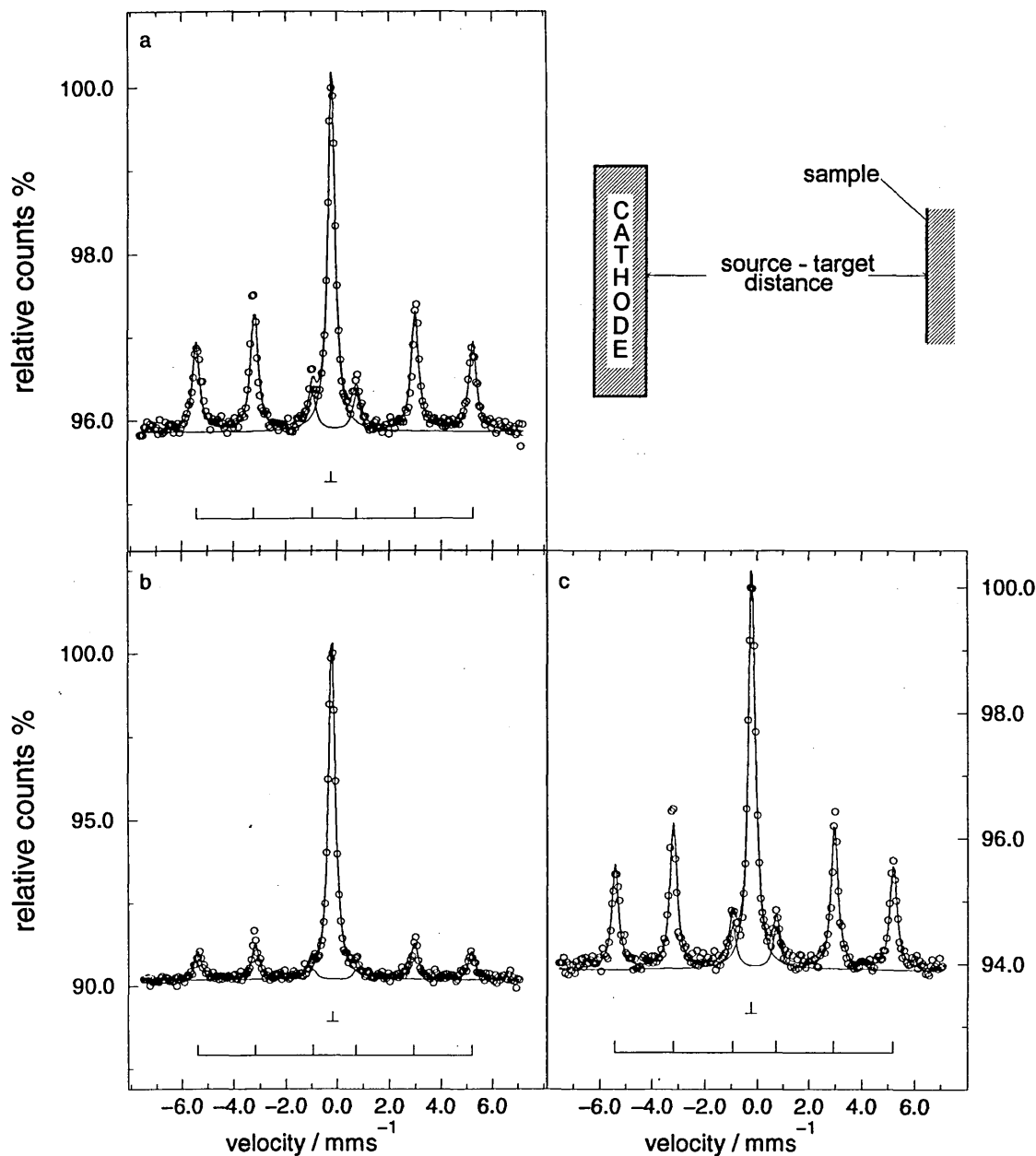


Fig 5.5 CEM Spectra of natural iron on stainless steel before and after a Ti ion pre-treatment for 30 s using one cathode source at different sample-cathode distances; (a) as deposited, (b) 250 mm and (c) 350 mm.

The measured isomer shift relative to  $\alpha$ -Fe for the stainless steel substrate was  $0.10 \pm 0.02 \text{ mm s}^{-1}$  before and after the etching process. This indicates no s-electron density change of the Mössbauer isotope within the substrate material due to any detectable Ti ion implantation or chemical alloying effects. This is consistent with TRIM (TRANSPORT of Ions in Matter) Monte Carlo simulation [3] which yields an ion implantation depth of

2 nm for Ti ions of energies associated with the applied bias voltage. However, this depth can only be considered to be a crude estimate since TRIM only considers non-interacting bombarding ions and the implantation also depends on the substrate temperature and ion flux density.

Sample	Phase	$\delta$ / mm s <sup>-1</sup> ±0.02	$\Gamma/2$ / mm s <sup>-1</sup> ±0.02	H <sub>eff</sub> / kG ±5	Relative Area / %
as deposited	st. st.	-0.11	0.17	-	42
	$\alpha$ -Fe	0.00	0.17	331	58
d = 250 mm	st. st.	-0.09	0.15	-	68
	$\alpha$ -Fe	0.00	0.16	329	32
d = 350 mm	st. st.	-0.11	0.17	-	42
	$\alpha$ -Fe	0.00	0.17	331	58

Table 5.2 Hyperfine parameters for natural Fe on stainless steel substrates before and after a Ti ion etch for 30 seconds, using no rotation and 1 target.

Sample	Rel. Area of st.st. / %	Rel. Area of $\alpha$ -Fe / %	LEB Thickness / nm	Average Etch rate / nm min <sup>-1</sup>
as deposited	42	58	51	-
d = 250 mm	68	32	21	60
d = 350 mm	42	58	51	not effective

Table 5.3 LEB Thickness calculated from the relative spectral areas of stainless steel and the remaining natural Fe overlayer after a Ti ion etch for 30 seconds.

Table 5.3 shows the relative spectral areas due to the natural Fe overlayer for the CEM spectra before and after the Ti static ion pre-treatment. The table also shows the calculated thickness of the natural Fe overlayer according to the LEB theory of CEMS using the CEMSN2 program. It can be clearly seen that 30 nm of the natural Fe overlayer has been removed from the sample positioned at a cathode-sample distance of 250 mm during the 30 s pre-treatment process. However, for the sample positioned at the greater cathode-sample, distance no detectable reduction in the natural Fe overlayer was observed by CEMS. This indicates a rapid decrease in the Ti ion bombardment and

hence plasma current density over a distance of 100 mm. However, an inspection of the samples with the naked eye showed that natural Fe removal at the sample edges had occurred since the Fe overlayer presents itself as a dull surface finish unlike the more reflective stainless steel substrate. This subtle optical effect is difficult to observe from a photograph but is shown schematically in fig. 5.6.

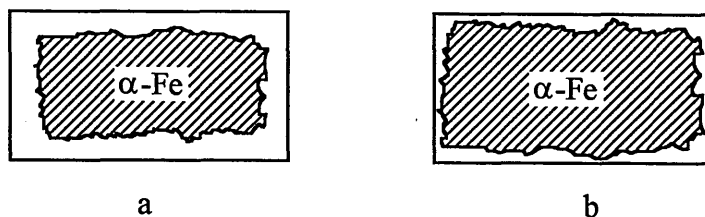


Fig. 5.6 Schematic of Fe overlayer surface remaining on stainless steel substrates after a 30 s static Ti ion pre-treatment process for different cathode-substrate distances; (a) 250 mm and (b) 350 mm.

It can be seen that the edge effect is greater for the sample at the closer cathode-sample distance, where the exposed substrate perimeter was in the order of 2 mm for a sample measuring 12 x 30 mm<sup>2</sup>. A similar, but less significant effect, was observed for the sample positioned at a cathode-sample distance of 350 mm. In both cases the effect is due to higher ion bombardment occurring at the edges compared with the central region of the samples. This is known as the bias edge effect [4] and occurs since the substrate behaves as a cathode in the plasma, generating a dark space region around the sample, which most of the applied bias potential is dropped. At the edges or corners, the ratio of dark space surface area to substrate surface area increases, causing a localised increase in ion current density at the substrate as shown in fig. 5.7.

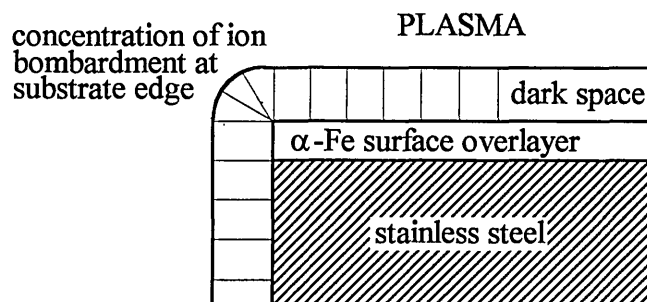


Fig. 5.7 Cross section of a pre-treated sample showing the effect of edge biasing.

This greater ion bombardment is responsible for an increase in surface etching and hence the observed optical effect. However, such an effect does not influence the measured CEM spectra with regard to relative spectral areas. This is because the observed spectra yield information over a central region of the sample of approximately 5 mm dia. due to the collimation of the incident  $\gamma$ -rays provided by the detection system. In the calculations that follow, the etch rate has been used to determine the average bias current density over this region for the sample positioned at the closest cathode-sample distance ie 30 s Ti ion etch using one cathode source and a bias voltage of -1200V:

Comparison of the Mössbauer spectral areas before and after the etch process using the LEB theory of CEMS (see Chapter 3) yielded a natural Fe loss equivalent to a thickness of 30 nm:

Atomic diameter of Fe = 0.24 nm.

Number of atomic layers removed

after 30 seconds -  $30/0.24 = 125$  atomic layers.

Density of Fe =  $7870 \text{ kg m}^{-3}$  : Atomic  $N^{\circ} = 55.85 \text{ g mol}^{-1}$

Therefore  $\rho_{\text{Fe}} = 140913 \text{ mols m}^{-3}$ .

$N^{\circ}$  of atoms per mol,  $N_A = 6.022 \times 10^{23} \text{ atoms mol}^{-1}$ .

$\therefore$  Fe atoms per cubic meter =  $8.5 \times 10^{28} \text{ atoms m}^{-3}$ .

$\therefore$  Fe atoms in a single layer =  $2 \times 10^{19} \text{ atoms m}^{-2}$ .

$N^{\circ}$  of removed atoms during etch =  $2 \times 10^{19} \text{ atoms m}^{-2} \times 125$  atomic layers  $\Rightarrow 2.5 \times 10^{21} \text{ atoms m}^{-2}$ .

From TRIM the sputter yield  $\approx 2$  Fe atoms per incident Ti ion.

$$\therefore N^{\circ} \text{ of Incident ions for 30 seconds} = 1.25 \times 10^{21} \text{ ions m}^{-2}.$$

$$\therefore N^{\circ} \text{ of Incident ions per second} = 4.17 \times 10^{19} \text{ ions m}^{-2} \text{ s}^{-1}.$$

(Amps x Coulombs)

$$\therefore \underline{\text{Current Density} \approx 6.68 \text{ Amps m}^{-2}}.$$

The etch rate,  $E$  can also be calculated by using the well known equation [5] relating  $E$  to the bias current density,  $j_+$ , target mass,  $m$ , sputter yield,  $Y$ , and target density,  $\rho$ :-

$$E = 62.3 j_+ Y \left( \frac{m}{\rho} \right) \quad (5.2)$$

where  $E$  is given in  $\text{\AA} \text{ min}^{-1}$  and  $j_+$  in  $\text{mA min}^{-1}$ . Substituting  $Y = 2$ ,  $m = 55.85 \text{ g mol}^{-1}$ ,  $\rho = 7.87 \text{ g cm}^{-3}$  and  $j_+ = 0.67 \text{ mA min}^{-1}$  gives:-

$$E = 62.3 \times 2 \times 0.67 \frac{55.85}{7.87}$$

$$= 592 \text{ \AA min}^{-1}$$

ie approximately 60 nm min<sup>-1</sup>.

The CEM spectra of natural Fe on stainless steel prior to and after the Ti ion pre-treatment using substrate holder rotation and operating two cathode sources are shown in fig. 5.8. Similar isomer shifts, magnetic field splittings and half linewidths to the samples pre-treated without substrate rotation were observed in all cases. Similar but less significant edge biasing effects were also observed.

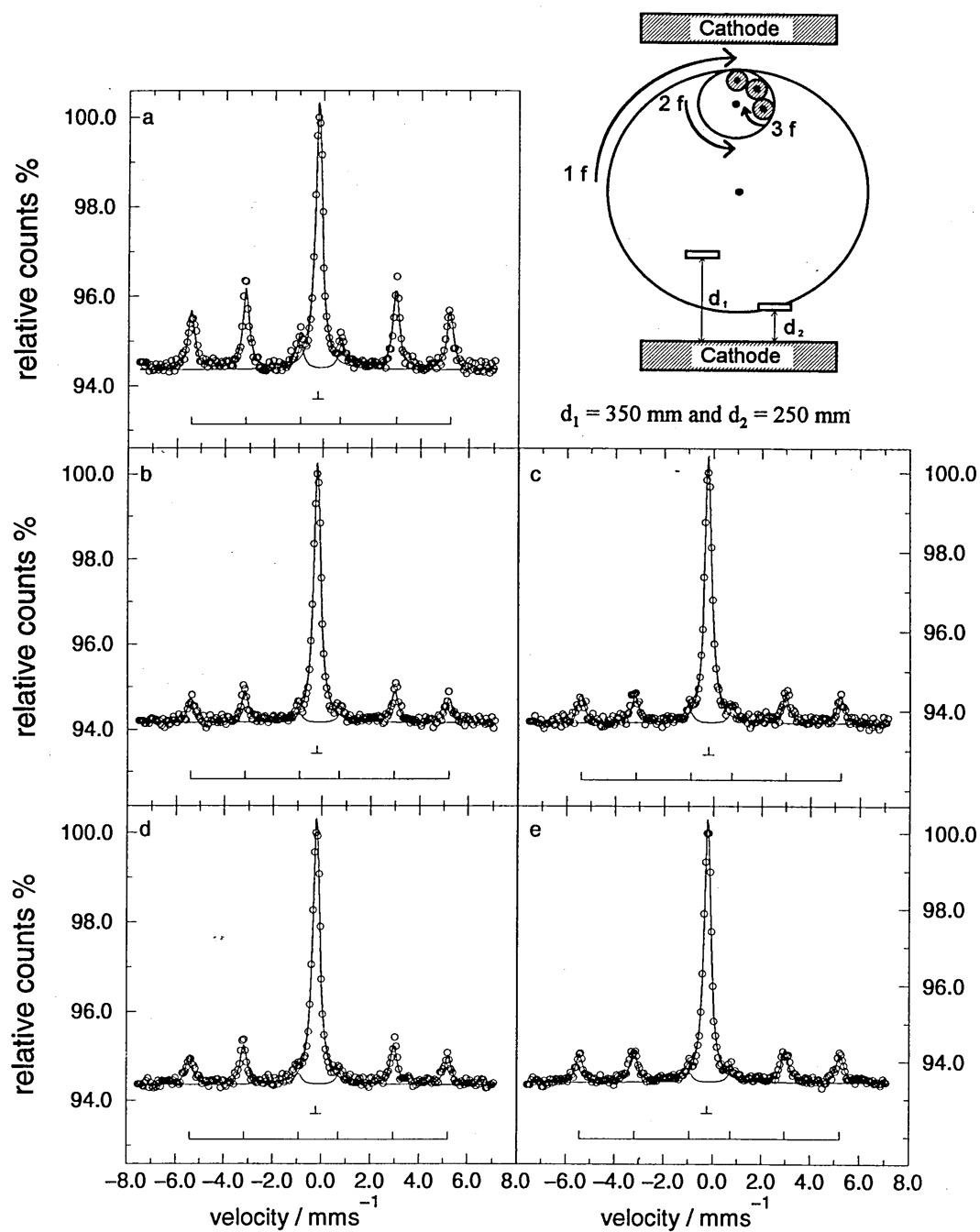


Fig. 5.8 CEM spectra of natural iron on stainless steel before and after a Ti ion pre-treatment; (a) as deposited, (b) 1 fold (250 mm), (c) 1 fold (350), (d) 2 fold and (e) 3 fold.

Table 5.4 shows the relative CEM spectral areas due to the natural Fe overlayer for samples before and after the Ti ion pre-treatment using substrate rotation and two operating cathodes.

Sample	Phase	$\delta / \text{mm s}^{-1}$ $\pm 0.02$	$\Gamma/2 / \text{mm s}^{-1}$ $\pm 0.02$	$H_{\text{eff}} / \text{kG}$ $\pm 5$	Relative Area / %
as deposited	st. st.	-0.10	0.16	-	46
	$\alpha$ -Fe	0.00	0.16	330	54
1 fold: 250 mm	st. st.	-0.11	0.17	-	67
	$\alpha$ -Fe	0.00	0.16	330	33
1 fold: 350 mm	st. st.	-0.10	0.17	-	66
	$\alpha$ -Fe	0.00	0.17	330	34
2 fold	st. st.	-0.11	0.17	-	63
	$\alpha$ -Fe	0.00	0.17	330	37
3 fold	st. st.	-0.10	0.16	-	62
	$\alpha$ -Fe	0.00	0.18	330	34

Table 5.4 Hyperfine parameters for natural Fe on stainless steel substrates before and after a Ti ion etch for 30 s, using 1 fold, 2 fold and 3 fold rotations.

Sample	Rel. Area of st.st. / %	Rel. Area of $\alpha$ -Fe / %	LEB Thickness / nm	Average Etch rate / $\text{nm min}^{-1}$
as deposited	46	54	45	-
1 fold: 250 mm	67	33	23	
1 fold: 350 mm	66	34	24	43
2 fold	63	37	27	
3 fold	62	38	28	35

Table 5.5 LEB Thickness calculated from the relative spectral areas of stainless steel and the remaining natural Fe overlayer after a Ti ion etch for 30 seconds.

From the calculated LEB thickness of the natural Fe overlayer, shown in table 5.5, it can be seen that all the pre-treated samples have suffered a net loss of the Fe overlayer compared with the as deposited sample. For the sample positioned at an initial and

perpendicular near cathode-sample distance of 350 mm an etch rate of  $43 \text{ nm min}^{-1}$  has been calculated. This is in contrast with the undetectable etch rate for the sample pre-treated for the same length of time at a constant perpendicular sample-cathode distance of 350 mm for the static process using only one cathode. This can be explained by the angular dependence of sputter yield [5] which maximises between  $60^\circ$  and  $80^\circ$  from the incident ion bombardment to the plane of the target and falls rapidly for larger angles. Such incident angles will be encountered during the rotation of the substrate holder and hence the increased etch rate. However, it should be noted that angular shifts between the sample and cathodes will lead to considerable variations in the time dependent flux conditions.

The small calculated differences in the average etch rates between the 1 fold and both the 2 fold and 3 fold rotated samples are significant; many workers have shown the measured thickness of Fe overlayers on stainless steel to agree with the LEB theory predictions within  $\pm 3 \text{ nm}$ , as shown in chapter 3 (section 3.7.2). The approximate 20 % difference in etch rates for these samples is due to greater surface shadowing associated with the 2 fold and 3 fold rotated samples compared with the 1 fold rotation. Thus the length of time an Fe overlayer surface is presented to a cathode source for the 2 and 3 fold rotated samples is less than for a 1 fold rotated sample, resulting in less ion bombardment and subsequently a lower etch rate.

For the 1 fold rotated sample, the bias current density can be calculated using equation (5.2) and substituting the etch rate of  $430 \text{ \AA min}^{-1}$ . This gives a bias current density of  $0.49 \text{ cm}^{-3}$ . This is lower than for the static pre-treatment process using one cathode for the same time, as expected but can only be considered to be a crude estimate since no account of the angular dependence of  $Y$  has been considered.

Such etch rate calculations derived from the described method using CEMS and the CEMSN2 program prove advantageous over weight loss and depth cratering measurement methods, usually used for the determination of etch rates. This advantage can be clearly understood by considering the presence of macroparticles as shown in fig. 5.9.



Fig. 5.9 SEM image of a mild steel substrate followed by a Ti ion pre-treatment at 1200 V<sub>bias</sub> for 10 minutes ( 3 fold rotation).

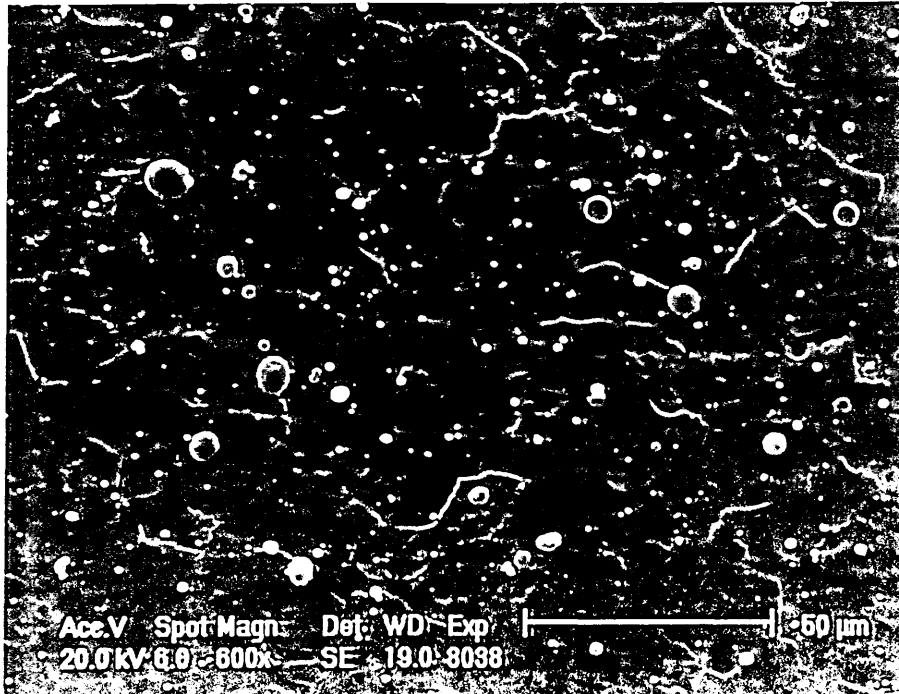


Fig. 5.10 SEM image of a mild steel substrate followed by a Ti ion pre-treatment at 1200 V<sub>bias</sub> for 30 minutes ( 3 fold rotation).

The large size (upto several microns) of the formed macroparticles would severely hinder any attempt of gaining meaningful results from depth profiling e.g. SIMS and hence the determination of etch rates in the order of  $\text{nm min}^{-1}$ . The severity of the etching process, for a mild steel sample subjected to a Ti ion pre-treatment at -1200 V bias for a total time of 30 minutes can be clearly seen in fig. 5.10, which shows significant exposure of grain boundaries.

### 5.3 $^{57}\text{Fe}$ Enrichment

In the previous section, samples pre-treated using the steered arc of the ABS<sup>TM</sup> method, contained only the natural abundance level of  $^{57}\text{Fe}$ . As a consequence any small quantities of Fe containing phases formed due to chemical alloying effects remain undetected. However, further improvement of the surface sensitivity of the CEMS technique can be provided by  $^{57}\text{Fe}$  enrichment of substrates. The enrichment process, if sufficient, will provide greater surface sensitivity and increase the probability of observing subtle chemical alloying effects occurring as a result of a Ti ion pre-treatment process. Two  $^{57}\text{Fe}$  enrichment procedures have been investigated (i) ion implantation and (ii) evaporation followed by diffusion.

#### 5.3.1 Ion Implantation

Two stainless steel (type 304) samples were ion implanted over a  $1 \text{ cm}^2$  region by the Division of Applied Physics at the University of Hull. The dosage levels of the ion implantation were as follows:

Batch #1	$1.0 \times 10^{15}$ of $^{57}\text{Fe}^+$ ions $\text{cm}^{-2}$ @ 50 keV
Batch #1	$2.6 \times 10^{15}$ of $^{57}\text{Fe}^+$ ions $\text{cm}^{-2}$ @ 50 keV

The CEM spectra shown in figs. 5.11 and 5.12 show the effect of the ion implantation for non-implanted and ion implanted regions of the samples for both dosage levels.

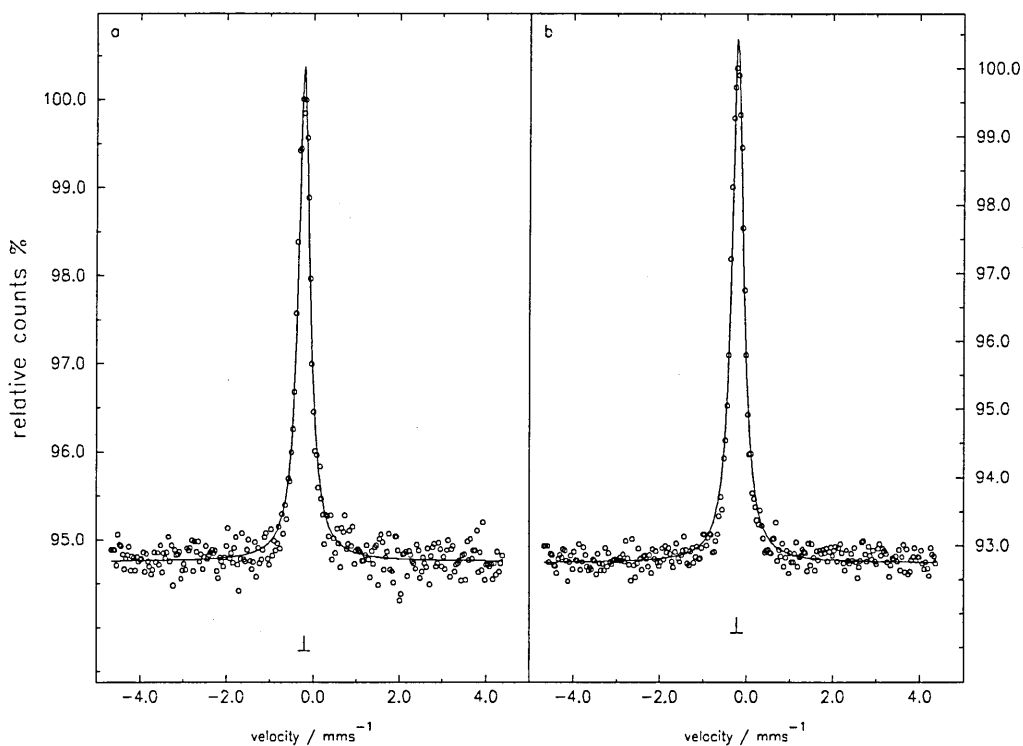


Fig. 5.11 CEM spectra of (a) type 304 stainless and (b) implanted region with  $1.0 \times 10^{15}$  ions  $\text{cm}^{-2}$  of  $^{57}\text{Fe}^+$  @ 50 keV.

Both dosages of ion implantation have shown a significant increase in the percent effect, signal/noise and the spectral areas compared with the non-implanted regions as shown in tables 5.6 and 5.7. This can be simply understood by considering an implanted region to have a greater density of  $^{57}\text{Fe}$  nuclei and hence greater emission of 7.3 keV conversion electrons takes place resulting from the decay of the  $^{57}\text{Fe}$  nuclei. This increase in 7.3 keV conversion electron emission causes an increase in the probability of detection within the gas flow proportional counter. The results show no significant change in the isomer shift indicating no change in the s-electron density at the nucleus between a non-implanted and an implanted sample.

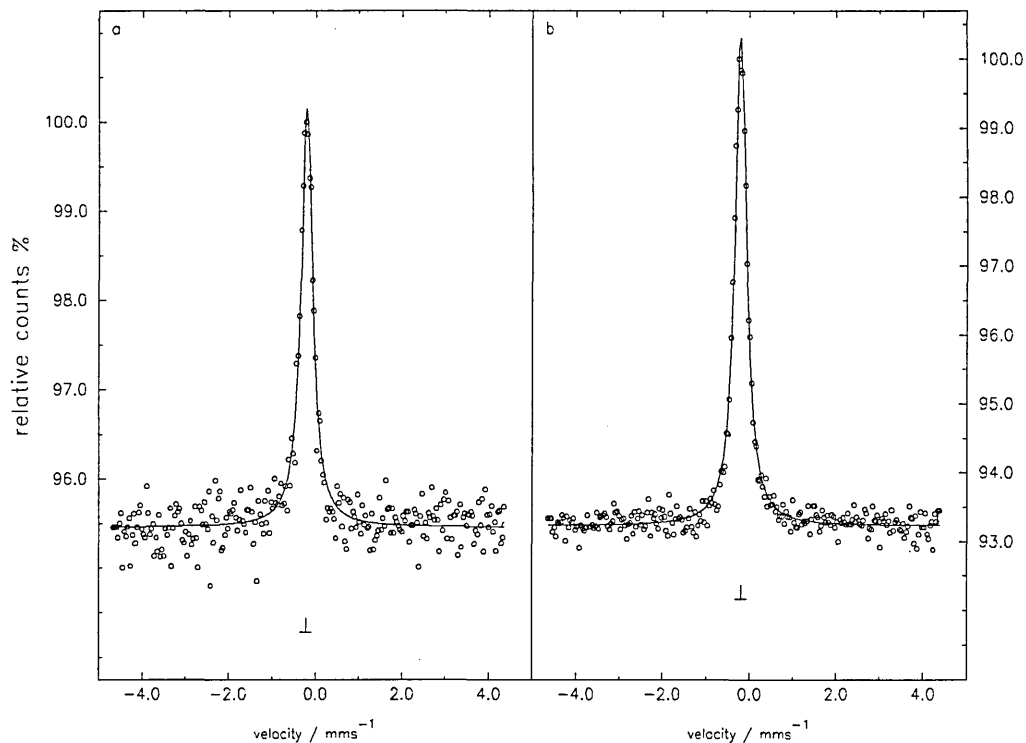


Fig. 5.12 CEM spectra of (a) type 304 stainless and (b) implanted region with  $2.6 \times 10^{15}$  ions  $\text{cm}^{-2}$  of  $^{57}\text{Fe}^+$  @ 50 keV.

	Non-implanted region	Implanted region	Percent change
$\Gamma/2$ ( $\text{mm s}^{-1}$ )	$0.16 \pm 0.02$	$0.16 \pm 0.02$	-
$\delta$ ( $\text{mm s}^{-1}$ )	$-0.10 \pm 0.02$	$-0.10 \pm 0.02$	-
percent effect (%)	6	8	38 %
signal/noise	1.08	1.55	44 %
area	-0.00159	-0.00221	40 %

Table 5.6 Mössbauer results for an  $^{57}\text{Fe}$  ion implantation of  $1.0 \times 10^{15}$  ions  $\text{cm}^{-2}$  at 50 keV.

	Non-implanted region	Implanted region	Percent change
$\Gamma/2$ ( $\text{mm s}^{-1}$ )	$0.16 \pm 0.02$	$0.16 \pm 0.02$	-
$\delta$ ( $\text{mm s}^{-1}$ )	$-0.09 \pm 0.02$	$-0.09 \pm 0.02$	-
percent effect (%)	5	8	56 %
signal/noise	0.62	1.47	137 %
area	-0.00131	-0.00204	56 %

Table 5.7 Mössbauer results for an  $^{57}\text{Fe}$  ion implantation of  $2.6 \times 10^{15}$  ions  $\text{cm}^{-2}$  at 50 keV.

A comparison of the Mössbauer signal parameters between non-implanted and  $^{57}\text{Fe}$  ion implanted regions for the two dosage levels indicate that the ion implantation has been successful. The bar chart shown in fig. 5.13 shows the change in Mössbauer signal parameters between non-implanted and  $^{57}\text{Fe}$  ion implanted regions for the two dosage levels studied.

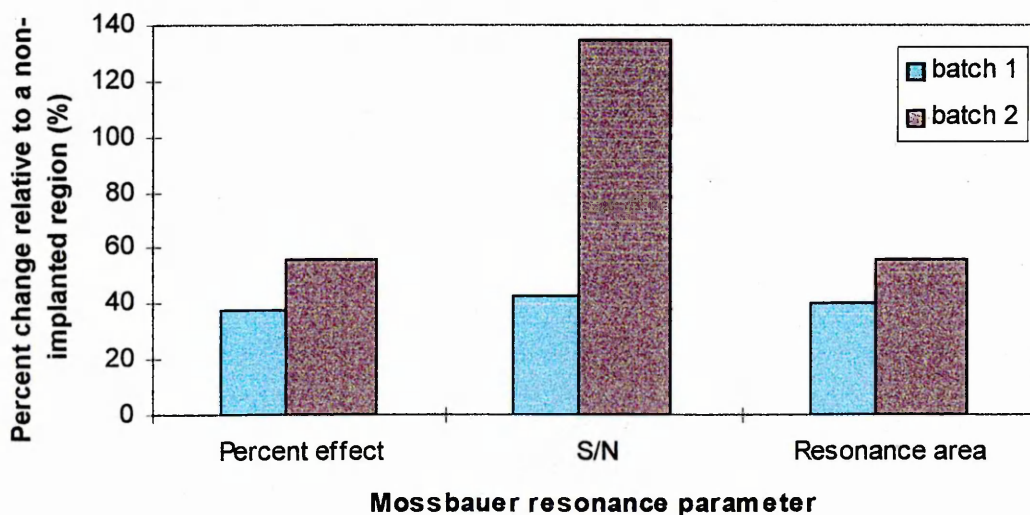


Fig. 5.13 Bar chart showing the relative changes in the Mössbauer resonance parameters for  $^{57}\text{Fe}$  ion implanted samples at 50 keV for two dosage levels; batch 1,  $1.0 \times 10^{15}$  ions  $\text{cm}^{-2}$  and batch 2,  $2.6 \times 10^{15}$  ions  $\text{cm}^{-2}$ .

An estimation of the  $^{57}\text{Fe}$  concentration provided by the ion implantation is as follows:

The stainless steel examined had an FCC structure and a unit cell length,  $a$ , where  $a$  is approximately  $3.5 \times 10^{-10}$  m [6].

$$\begin{aligned} \text{unit cell volume, } a^3 &= (3.5 \times 10^{-10})^3 = 4.3 \times 10^{-29} \text{ m}^3 \\ \text{unit cells per cm}^3 &= (1 \times 10^{-6} \text{ m}^3) / (4.3 \times 10^{-29} \text{ m}^3) = 2.3 \times 10^{22} \text{ unit cells cm}^{-3} \\ \text{FCC has 4 atoms per unit cell, therefore atoms per cm}^3 &:- \\ 4 \times 2.3 \times 10^{22} &= 9.2 \times 10^{22} \text{ atoms cm}^{-3} \end{aligned}$$

The TRIM software estimated the mean range of 50 keV  $^{57}\text{Fe}^+$  ions (approximately a Gaussian distribution) to be 220 Angstroms with a straggle (spread) of 90 Angstroms.

For the lower ion dosage level:

for bombardment with  $1 \times 10^{15}$  atoms  $\text{cm}^{-2}$  at a depth of  $2.2 \times 10^{-6}$  cm (TRIM)  
N<sup>o</sup> of atoms per  $\text{cm}^3$  of  $^{57}\text{Fe} = 1 \times 10^{15} / 2.2 \times 10^{-6} \text{ cm}^3 = 4.5 \times 10^{20}$  atoms  $\text{cm}^{-3}$   
2.2 % natural abundance of  $^{57}\text{Fe} = (9.2 \times 10^{22} \times 0.022) = 2.0 \times 10^{21}$  atoms  $\text{cm}^{-3}$   
percentage increase in  $^{57}\text{Fe} = ((4.5 \times 10^{20}) / (2.0 \times 10^{21})) \times 100 = 22.5 \%$

giving a total concentration of  $^{57}\text{Fe} = 2.2 + (2.2 \times 0.225) = 2.7 \%$

For the higher ion dosage level:

for bombardment with  $2.6 \times 10^{15}$  atoms  $\text{cm}^{-2}$  at a depth of  $2.2 \times 10^{-6}$  cm  
N<sup>o</sup> of atoms  $\text{cm}^{-3}$  of  $^{57}\text{Fe} = 2.6 \times 10^{15} / 2.2 \times 10^{-6} \text{ cm}^3 = 1.2 \times 10^{21}$  atoms  $\text{cm}^{-3}$   
percentage increase in  $^{57}\text{Fe} = ((1.2 \times 10^{21}) / (2.0 \times 10^{21})) \times 100 = 60 \%$

giving a total concentration of  $^{57}\text{Fe} = 2.2 + (2.2 \times 0.60) = 3.5 \%$

The calculated actual  $^{57}\text{Fe}$  concentration levels indicates that the  $^{57}\text{Fe}$  enrichment is relatively low compared with the natural 2.2 % abundance level of  $^{57}\text{Fe}$ . The higher dosage level only provided a concentration of  $^{57}\text{Fe}$  of 3.2 % to depth of a few nm (estimated by TRIM). This ion implantation method was not regarded as a suitable enrichment technique capable of detecting subtle phase formations generated by the ABST<sup>TM</sup> method for two reasons. Firstly, the increased  $^{57}\text{Fe}$  concentration extends only to a depth of a few nanometers and subsequent Ti ion etching would quickly cause a removal of this enrichment and hence a loss of improved surface sensitivity. Secondly, the  $^{57}\text{Fe}$  enrichment concentration levels do not achieve the necessary increases in surface sensitivity of the CEMS technique. Therefore a more suitable enrichment method was adopted which could provide a higher  $^{57}\text{Fe}$  concentration level extending down to a greater depth - evaporation followed by diffusion.

### 5.3.2 Evaporation Followed by Diffusion

Fig. 5.14 shows the CEM spectra obtained from stainless steel samples having a natural Fe overlayer deposited by a single evaporation, as a function of angular dependence for samples positioned on a hemispherical grid. Inspection of the relative areas due to the  $\alpha$ -Fe and stainless steel subspectra show only a slight decrease of  $\alpha$ -Fe relative area for increasing  $\theta$ , as shown in table 5.8.

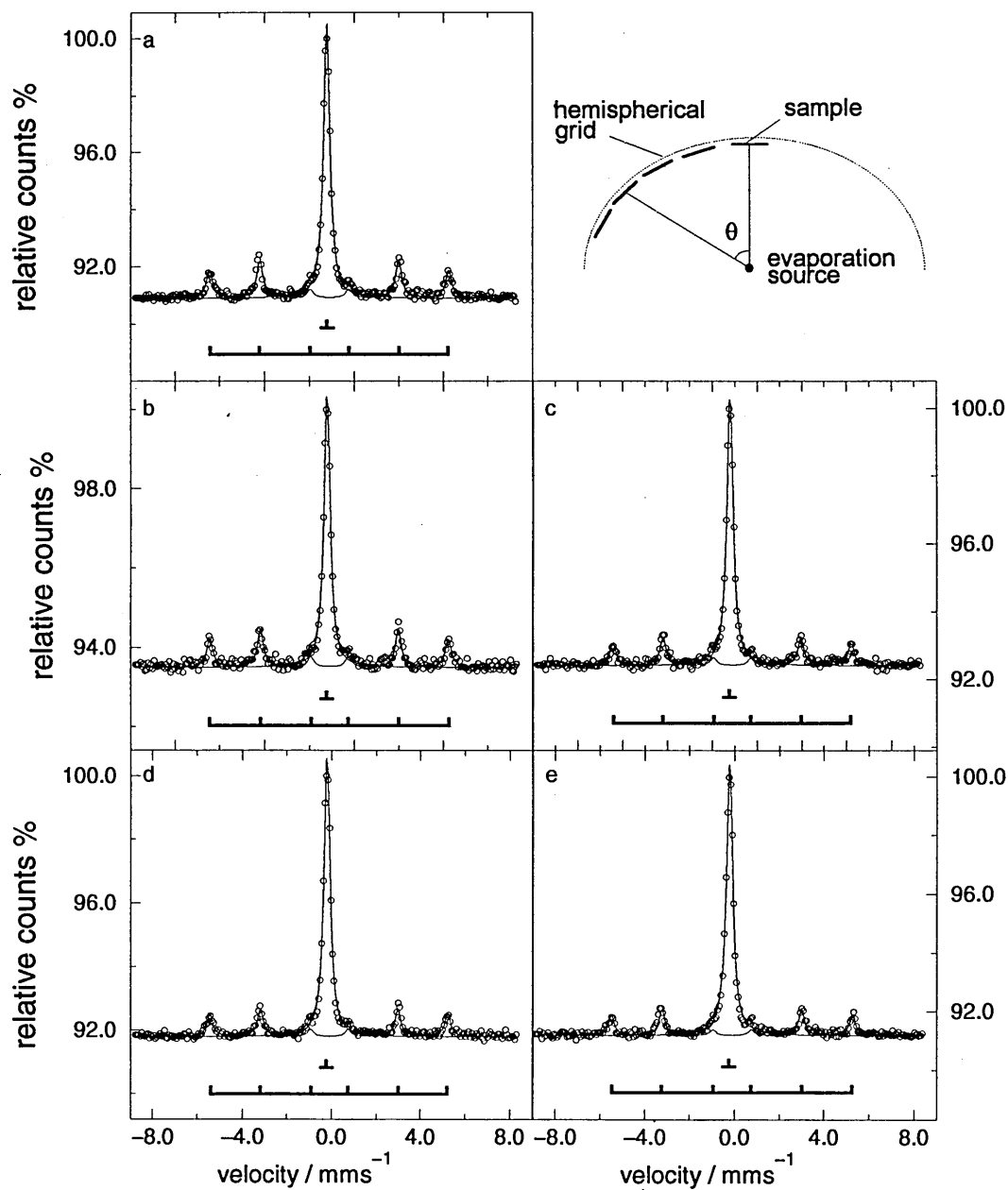


Fig. 5.14 CEM spectra showing natural iron on stainless steel as a function of angular dependence,  $\theta$  for samples positioned on a hemispherical grid; (a)  $0^\circ$ , (b)  $20^\circ$ , (c)  $40^\circ$ , (d)  $60^\circ$  and (e)  $80^\circ$ .

Sample Position / $\theta$	Rel. Area of $\alpha$ -Fe / %
0°	34.6
20°	34.5
40°	29.5
60°	29.1
80°	27.7

Table 5.8 Relative spectral area as a function of sample position on hemispherical grid.

Thus the deposited thickness of natural Fe can be considered to depend on the sample position on the hemispherical grid. However, the sharp decrease of the thickness of natural Fe only occurs for the highest of position angles. Therefore, the evaporation can be considered to confirm an approximate thin coating uniformity from sample to sample providing such large angles are avoided. This uniformity was necessary since for the actual  $^{57}\text{Fe}$  deposition approximately 30 samples were coated during a single evaporation due to the high cost of  $^{57}\text{Fe}$ .

The  $^{57}\text{Fe}$  enrichment by evaporation produced an estimated  $25 \pm 5$  nm deposited overlayer on mild steel substrates. The change from stainless steel to mild steel substrates offered two major advantages. Firstly, the Mössbauer peaks associated with Fe-Ti phases occur between peaks 3 and 4 of the  $\alpha$ -Fe CEM spectrum ie in the velocity region of the peak position for paramagnetic stainless steel. Secondly, mild steel can be polished to a higher surface finish than stainless steel and hence can be cleaned to a higher degree. This improves the likelihood of successful annealing after  $^{57}\text{Fe}$  deposition ie without the formation of oxides or other Fe containing surface species. Such contamination would severely hinder the discrimination of small quantities of Fe-Ti phases, formed as a result of a Ti ion pre-treatment, from the CEM spectrum.

From the CEM spectrum shown in fig. 5.15, it can be clearly seen that the deposition of a thin  $^{57}\text{Fe}$  surface layer results in increased signal intensity compared with an ordinary mild steel. More importantly, the CEM spectrum shown in fig. 5.16 indicates that the annealing process has not altered the physical properties of the original mild steel ie no iron oxide formation. It can be seen that the annealing has had the effect of reducing the

S/N of the CEM spectrum compared with the as deposited sample. This is consistent with the diffusion of  $^{57}\text{Fe}$  to produce a near surface region rich in  $^{57}\text{Fe}$  to a predicted depth of 100 nm, taking into account that 66 % of the detected electrons in the counter arise from within the first 54 nm of the substrate [7,8].

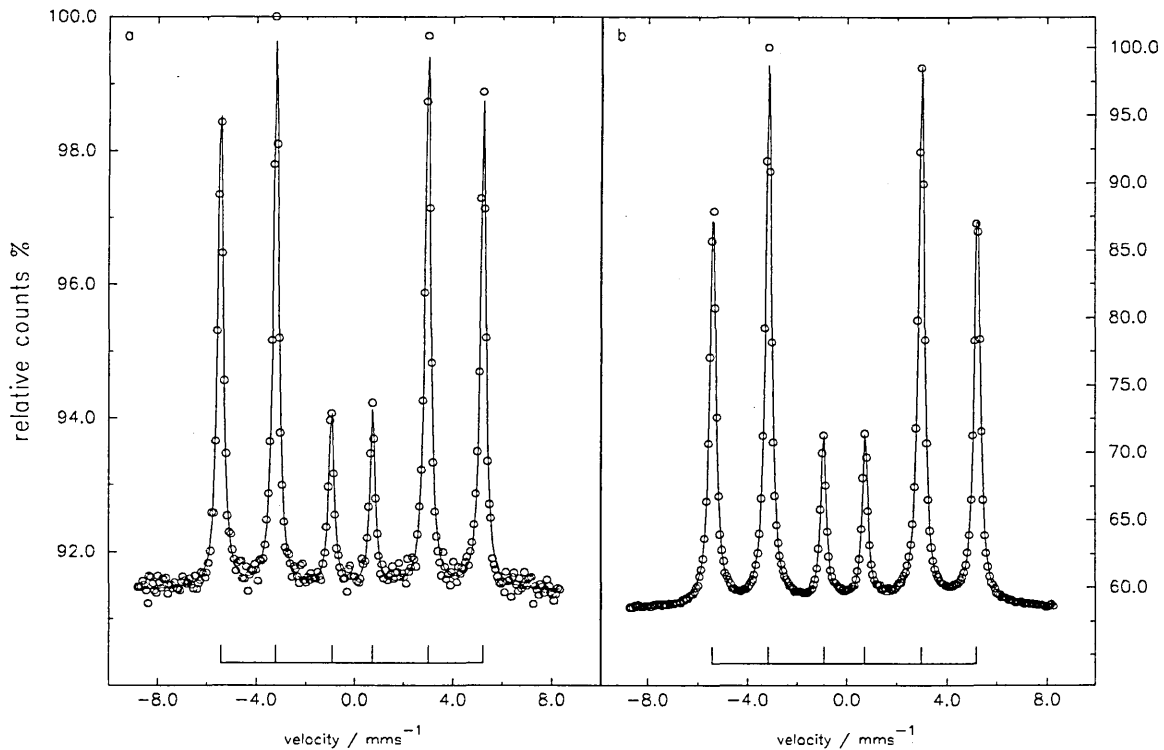


Fig. 5.15 CEM spectra of (a) mild steel and (b) mild steel with an estimated 25 nm surface layer of  $^{57}\text{Fe}$ .

Figs. 5.17 and 5.18 show dynamic SIMS profiles of an estimated  $25 \pm 5$  nm  $^{57}\text{Fe}$  layer on mild steel and the same sample after annealing for 90 minutes at 900 K, respectively. The depth profile for the annealed sample used twice the probe current as for the as deposited sample and consequently probed deeper into the bulk. The return of the  $^{57}\text{Fe}$  to the normal isotopic abundance level can be clearly seen, along with significant back diffusion of  $^{56}\text{Fe}$  from the bulk to the surface.

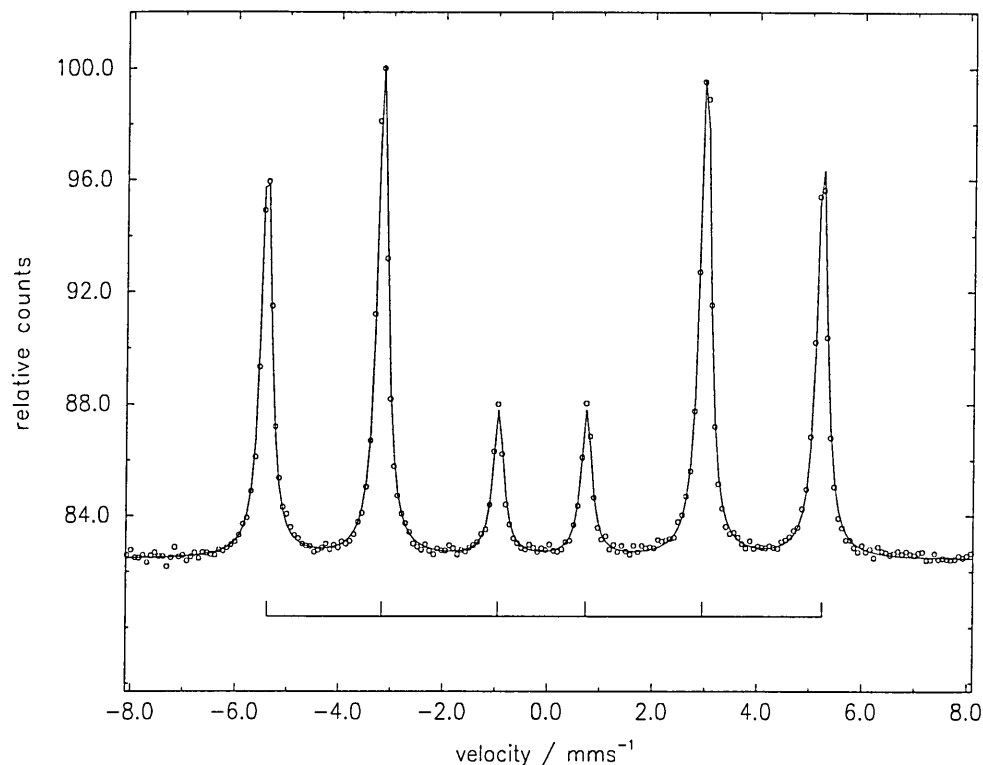
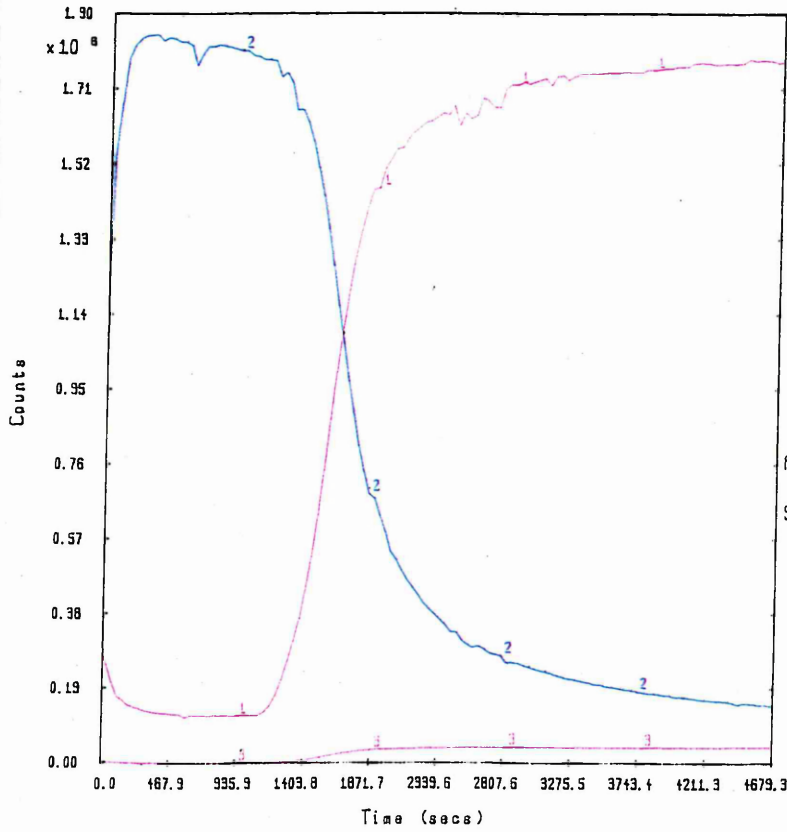


Fig. 5.16 CEM spectrum of a mild steel with an estimated 25 nm surface layer of  $^{57}\text{Fe}$  followed by annealing at 900 K for 90 minutes.

Figs. 5.19 and 5.20 show SNMS depth profiles for as deposited and annealed samples. From a Sloan Dektak depth cratering measurement for the as deposited  $^{57}\text{Fe}$  enriched sample, the final sputter time of 1671.2 s corresponds to a depth of approximately 60 nm. Therefore the  $^{57}\text{Fe}$  and  $^{56}\text{Fe}$  crossover occurs at a depth of approximately 25 nm, as estimated. For the annealed sample, by considering the count level of  $^{57}\text{Fe}$  at the natural isotopic abundance level, a maximum enrichment factor 4.8 x can be estimated. This represents a maximum  $^{57}\text{Fe}$  concentration level of 11.6 % over an extended depth compared with the maximum 3.2 % concentration level provided by the ion implantation technique down to only a few nm. However, a meaningful depth crater measurement for this sample could not be obtained. This was due to excessive surface roughening at the bottom of the crater as a result of the primary beam  $\text{Ar}^+$  bombardment. This surface roughening made an accurate depth measurement difficult to achieve, and can be clearly seen in the micrograph of fig. 5.23.

:5657E001 VG SCIENTIFIC 19/ 7/1996



Positive SIMS Depth Profiles

No	Name	Mass	Target Bias (V)	Time (secs)
1	FES6	56.0	-1.5	13.1
2	FES7	57.0	-1.5	13.1
3	MN	55.0	-1.5	13.1

AR Primary Beam 4keV 200nA

S1 S7 DEP ON SURFACE

Fig. 5.17 SIMS depth profile of an estimated  $25 \pm 5$  nm surface layer of  $^{57}\text{Fe}$  deposited on a mild steel substrate.

:5657D001 VG SCIENTIFIC 9/ 8/1996

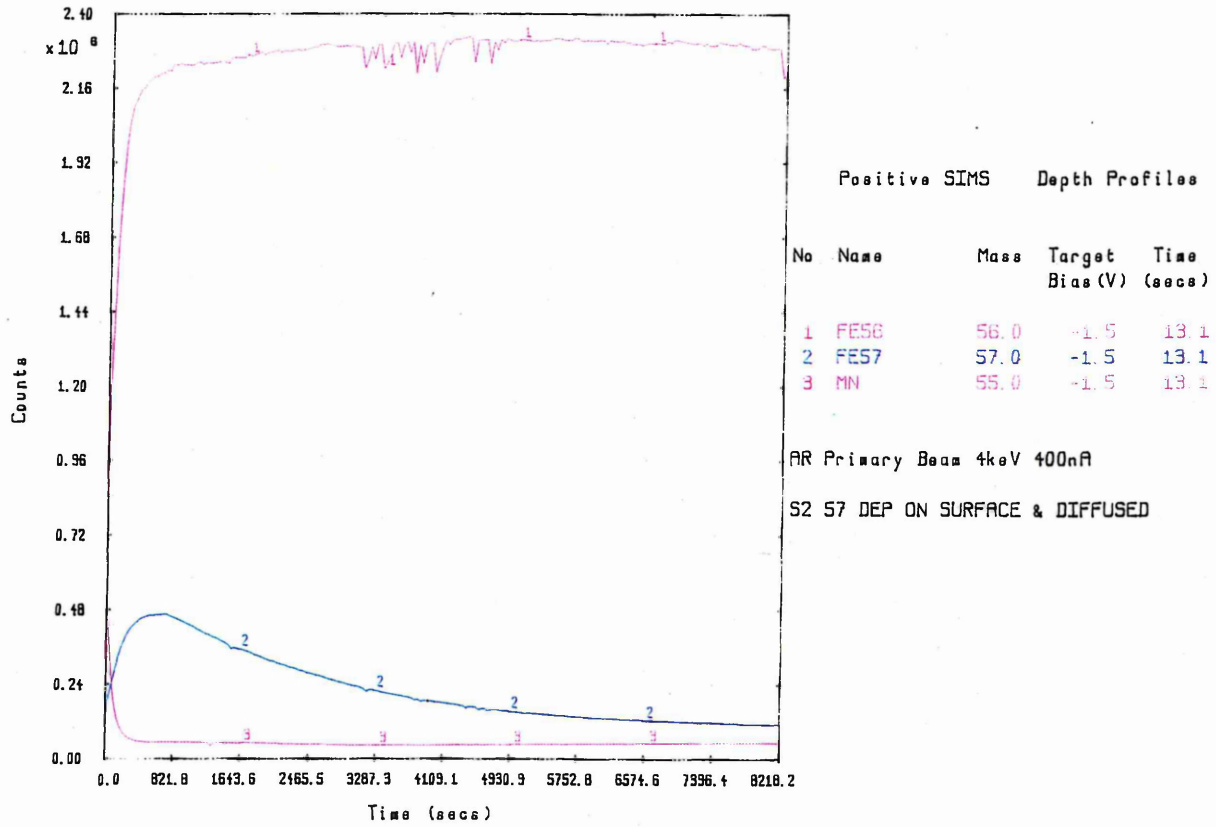


Fig. 5.18 SIMS depth profile of an estimated  $25 \pm 5$  nm surface layer of  $^{57}\text{Fe}$  deposited on a mild steel substrate followed by annealing at 900 K for 90 minutes.

:hal1001 VG SCIENTIFIC 8/ 2/1996

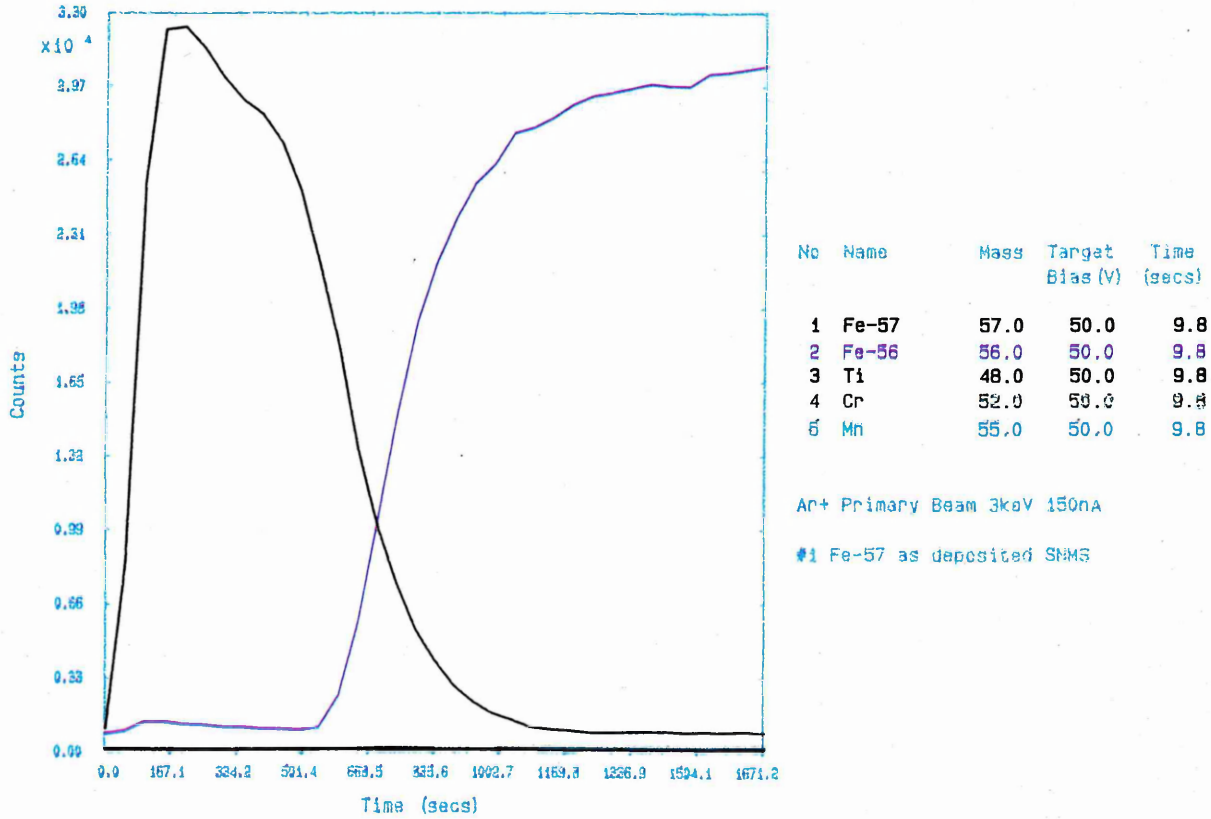
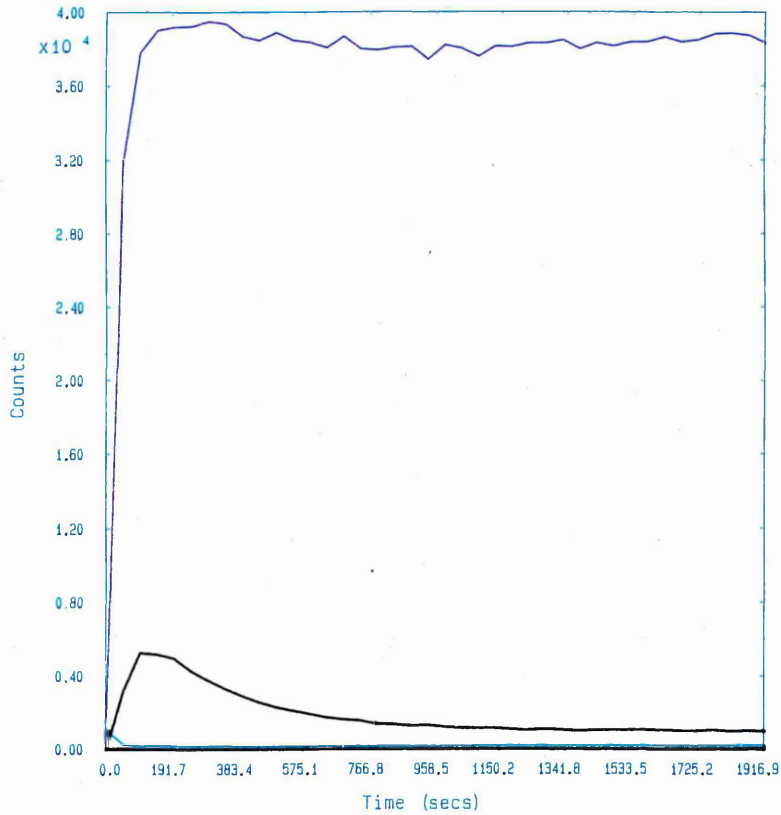


Fig. 5.19 SNMS depth profile of an estimated  $25 \pm 5$  nm surface layer of  $^{57}\text{Fe}$  deposited on a mild steel substrate.

:hal2001 VG SCIENTIFIC 8/ 2/1996



No	Name	Mass	Target Bias (V)	Time (secs)
1	Fe-57	57.0	50.0	9.8
2	Fe-56	56.0	50.0	9.8
3	Ti	48.0	50.0	9.8
4	Cr	52.0	50.0	9.8
5	Mn	55.0	50.0	9.8

Ar+ Primary Beam 3keV 150nA

#2 Fe-57 enriched after anneal SNMS

Fig. 5.20 SNMS depth profile of an estimated  $25 \pm 5$  nm surface layer of  $^{57}\text{Fe}$  deposited on a mild steel substrate followed by annealing at 900 K for 90 minutes.

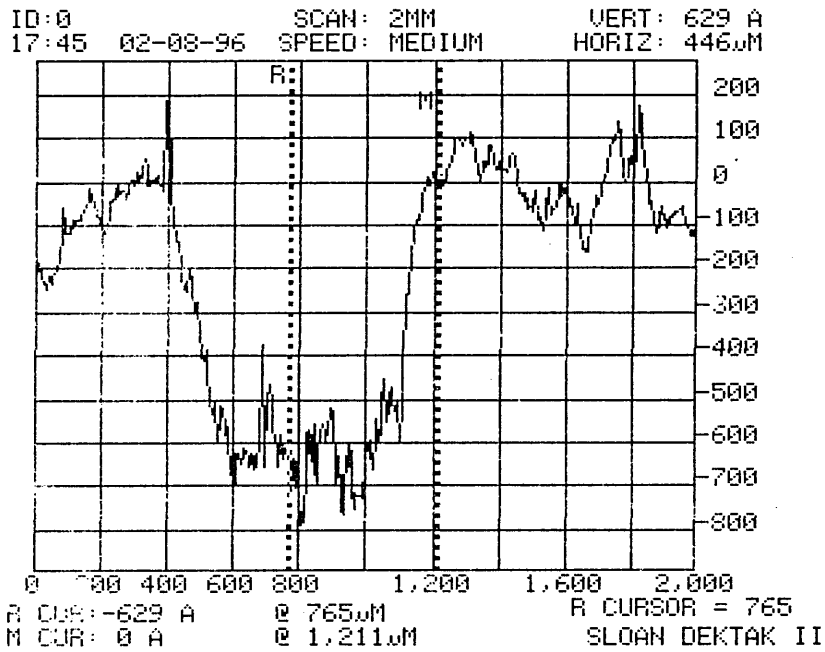


Fig. 5.21 Depth crater from the sample consisting of  $^{57}\text{Fe}$  as deposited on a mild steel substrate, after SNMS analysis.

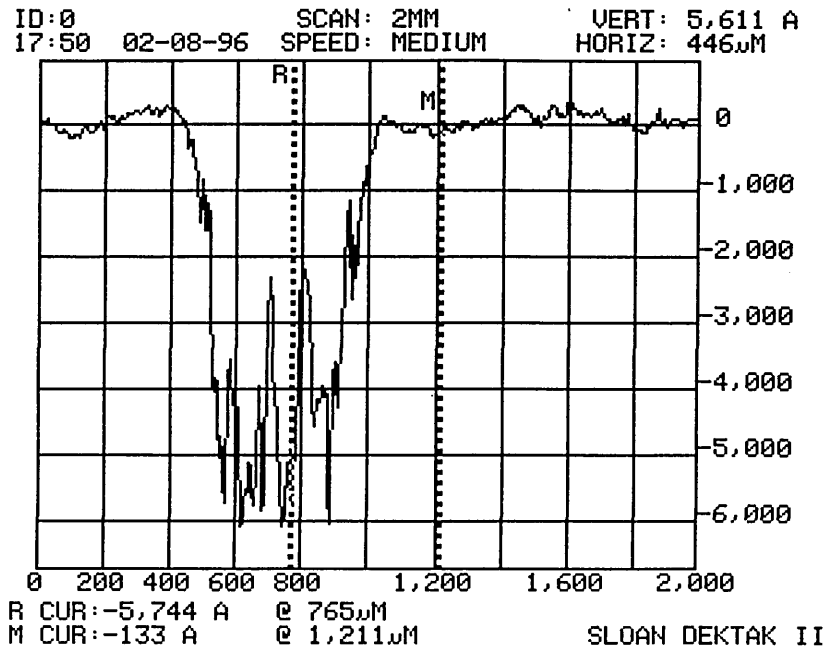


Fig. 5.22 Depth crater from the sample consisting of  $^{57}\text{Fe}$  deposited on a mild steel substrate followed by annealing at 900 K for 90 minutes, after SNMS analysis.



Fig 5.23 SEM image of the crater bottom produced by SNMS for the annealed sample.

## References

- [1] M. J. Tricker, L. A. Ash and T. E. Cranshaw, *Nucl. Instr. and Meth.* **143** (1977) 307.
- [2] W. -D. Münz, D. B. Lewis, S. Creasey, T. Hurkmans, T. Trinh and W. V. Ijzendorf, *Vacuum* **46(4)** (1994) 325.
- [3] Transport of Ions in Matter, TRIM95, available from J. Ziegler, IBM Research, Yorktown Heights, NY 1010598, USA.
- [4] M. Ives PhD Thesis: "*Fundamental Studies of the PVD Technique*", Sheffield Hallam University, 1994.
- [5] H. H. Anderson and H. L. Bay: "Sputter Yield Measurements", in *Sputtering by Particle Bombardment 1* ed. By R. Behrisch, Topics in Applied Physics, Vol. 47 (Springer-Verlag Berlin Heidelberg 1981) p.145.
- [6] B. D. Cullity, *Elements of X-ray Diffraction*, 2nd ed. Addison-Wesley Pub. Co., 1978.
- [7] K. R. Swanson and J. J. Spijkerman, *J. Appl. Phys.* **41** (1970) 3155.
- [8] M. J. Thomas, M. J. Triker, A. P. Winterbottom, *J. Chem. Soc. Faraday 2.* **71** (1975) 1708.

## CHAPTER 6

### INTERFACES IN PVD PROCESSES

#### 6.1 Interfaces Generated by Ti ions in a Steered Arc Discharge

Good substrate-coating adhesion is the most fundamental requirement for an applied surface coating since, if the interfacial adhesion is poor, coating detachment will occur before any of the advantageous properties of the coating can be realised. In Chemical Vapour Deposition (CVD) methods, the high temperatures involved lead to the removal of surface contaminants by reaction prior to deposition, in addition to elemental diffusion/intermixing processes. Both these effects lead to improved substrate-coating adhesion. However, such interdiffusion does not readily occur at the lower temperatures associated with PVD processes. Therefore in a PVD process, additional adhesion enhancing techniques have to be employed, such as ion etching used to sputter clean the substrate and to generate local heating effects thereby promoting limited diffusion and/or ion implantation. Also the formation of a new substrate surface phase(s) may result by ion etching with metal ions at sufficiently high ion energies and flux during a pre-treatment process prior to coating deposition. Thus the sputter cleaned surface forms the basis of the interface region between the deposited coating and the substrate material, and therefore an investigation of the pre-treated surface is of considerable importance. The results presented in this section are typical of various Ti ion pre-treatments performed using a commercial PVD ABS<sup>TM</sup> coating system.

To study the differences between a typical 10 minute industrial Ar and Ti ion etch, two samples were <sup>57</sup>Fe enriched followed by annealing, as described previously, pre-treated using a steered arc process using two cathode sources. Without diffusion, the enriched <sup>57</sup>Fe would be fully removed by the surface sputtering process. The first sample was ion etched in an Ar<sup>+</sup> plasma at -150 V and the second was Ti ion etched at a substrate bias voltage of -1200 V. In both experiments a thin Ti layer was deposited at a bias voltage of -80 V for 2 minutes. Three-fold rotation was used throughout and the maximum temperature was 450 °C.

Fig. 6.1 shows a GDOES depth profile through the Ti coating for the Ar ion etched sample. From the depth profile, it can be seen that the thickness of the applied coating is of the order of 25 nm. This thickness of coating will not hinder the statistical quality of a collected CEM spectrum and therefore the coating conditions used to deposit this thin coating were used in subsequent coating processes. From the depth profile a small carbon content is observed at the interface. This carbon may be due to diffusion from the bulk of the mild steel into the interface or is a consequence of remaining surface contamination. Although carbon diffusion in mild steel occurs readily at low temperatures, the more likely explanation is remaining surface contamination. Such surface contamination is usually completely removed after a Ti ion etch for the same length of time due to the greater severity of ion etching with multi-ionised metal ions compared with lower energy Ar<sup>+</sup> ions.

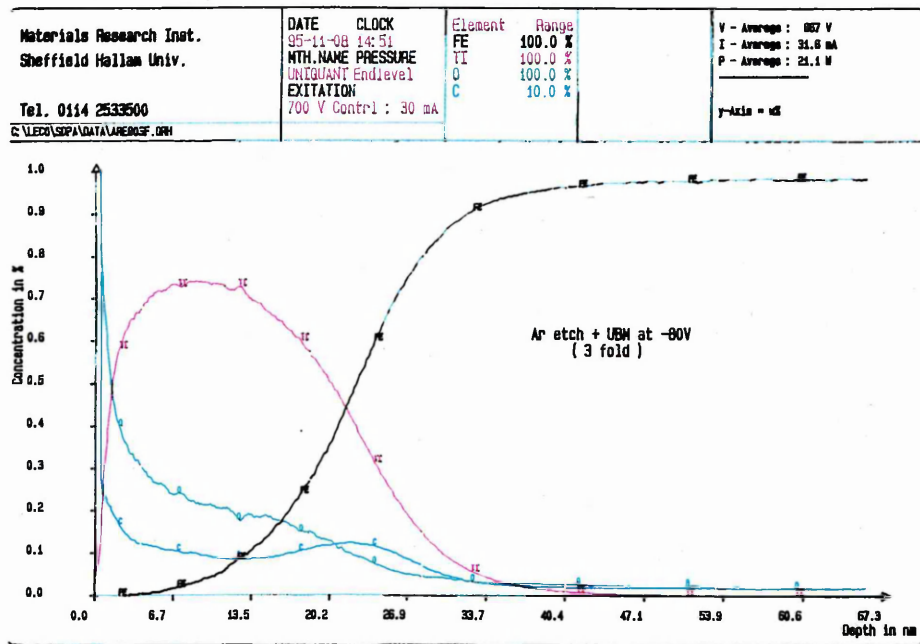


Fig. 6.1 GDOES depth profile of a sample pre-treated with an Ar ion etch for 10 minutes followed by the deposition of a Ti layer for 2 minutes, using two cathode sources and 3 fold rotation.

From the CEM spectra of fig. 6.2, an intense magnetically ordered  $\alpha$ -Fe sextet of the substrate is observed, but no oxides are present after either pre-treatment process. However, for the Ti ion etched sample, small quantities of FeTi amorphous and crystalline phases can be seen shown in the spectrum as a doublet and singlet, respectively. Further evidence of the crystalline phase can be seen from a typical XRD trace using Cu K $\alpha$  radiation, as seen in fig. 6.3. A further CEM spectra shown in fig. 6.4 of the same Ti ion etched sample was obtained at a lower velocity range in order to improve the resolution the region of interest. The low intensities of the amorphous and crystalline phases are due to the small quantity of phase formation.

The measured Mössbauer hyperfine parameters associated with the Ti ion etch pre-treatment for 10 minutes are given in table 6.1. There is good agreement with the measurements of Chien and Liou [1] and the work of Stupel *et al.* [2]. In the case of the amorphous phase Fe $_x$ Ti $_{1-x}$  the Mössbauer hyperfine parameters depend greatly on the concentration, x. For both the crystalline and amorphous phases, the negative isomer shift compared with  $\alpha$ -Fe is due to electron donations from Ti to Fe sites.

Phase	$\delta / \text{mm s}^{-1}$ $\pm 0.02$	$\Gamma/2 / \text{mm s}^{-1}$ $\pm 0.02$	$\Delta Q / \text{mm s}^{-1}$ $\pm 0.02$	$H_{\text{eff}} / \text{kG}$ $\pm 5$	Rel. Area / %
FeTi - c	-0.14	0.18	-	-	0.2
FeTi - a	-0.20	0.19	0.36	-	1.0
$\alpha$ -Fe	0.00	0.12	-	330	98.8
FeTi - c <sup>a</sup>	-0.15	-	-	-	-
Fe $_x$ Ti $_{1-x}$ ( $0.3 \leq x \leq 0.8$ ) <sup>b</sup>	-0.14 to -0.22	-	0.29 to 0.36	-	-

<sup>a</sup>From M. M. Stupel *et al.* [2].

<sup>b</sup>From S. H. Liou and C. L. Chien [4].

Table 6.1 Hyperfine parameters relative to  $\alpha$ -Fe of the phases present after a Ti ion pre-treatment followed by the deposition of a thin titanium layer.

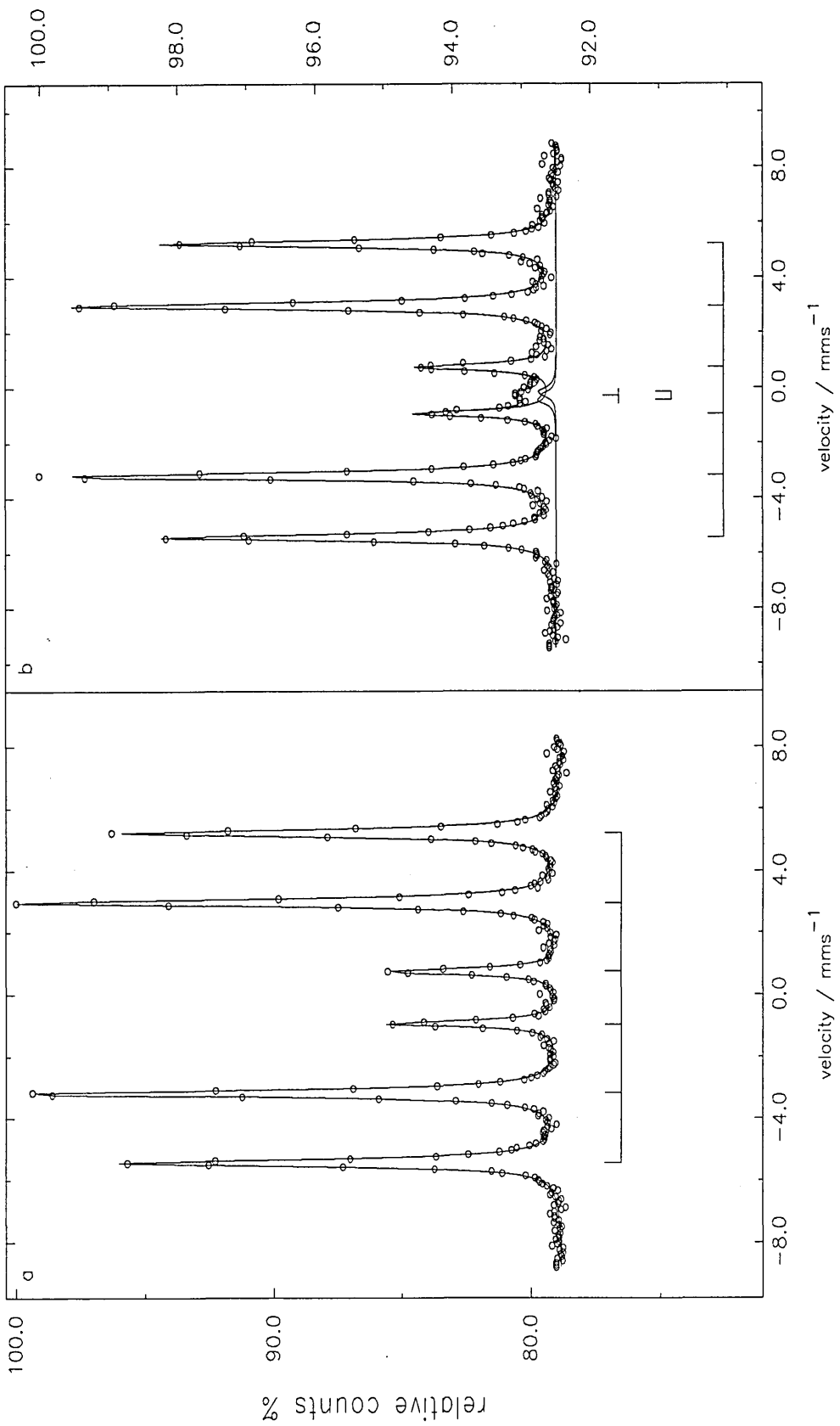


Fig. 6.2 CEM spectra of (a) 10 minute Ar ion pre-treatment followed by the deposition of a thin Ti layer and (b) Ti ion pre-treatment at -1200 V bias followed by the deposition of a thin Ti layer under the same conditions as in (a).

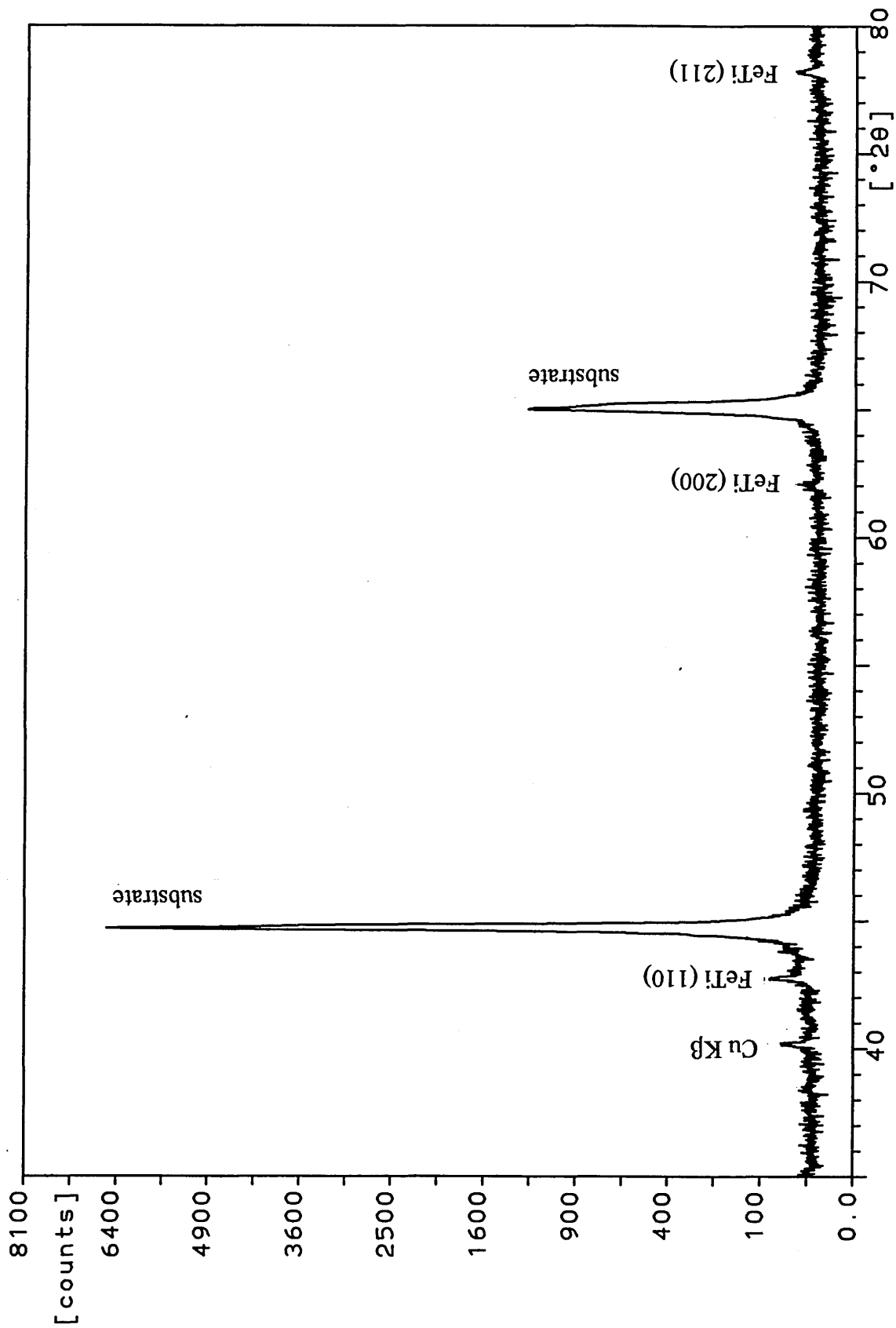


Fig. 6.3 Typical XRD trace using Cu  $k\alpha$  radiation of a sample after a Ti ion pre-treatment for 10 minutes using two cathode sources and 3 fold rotation.

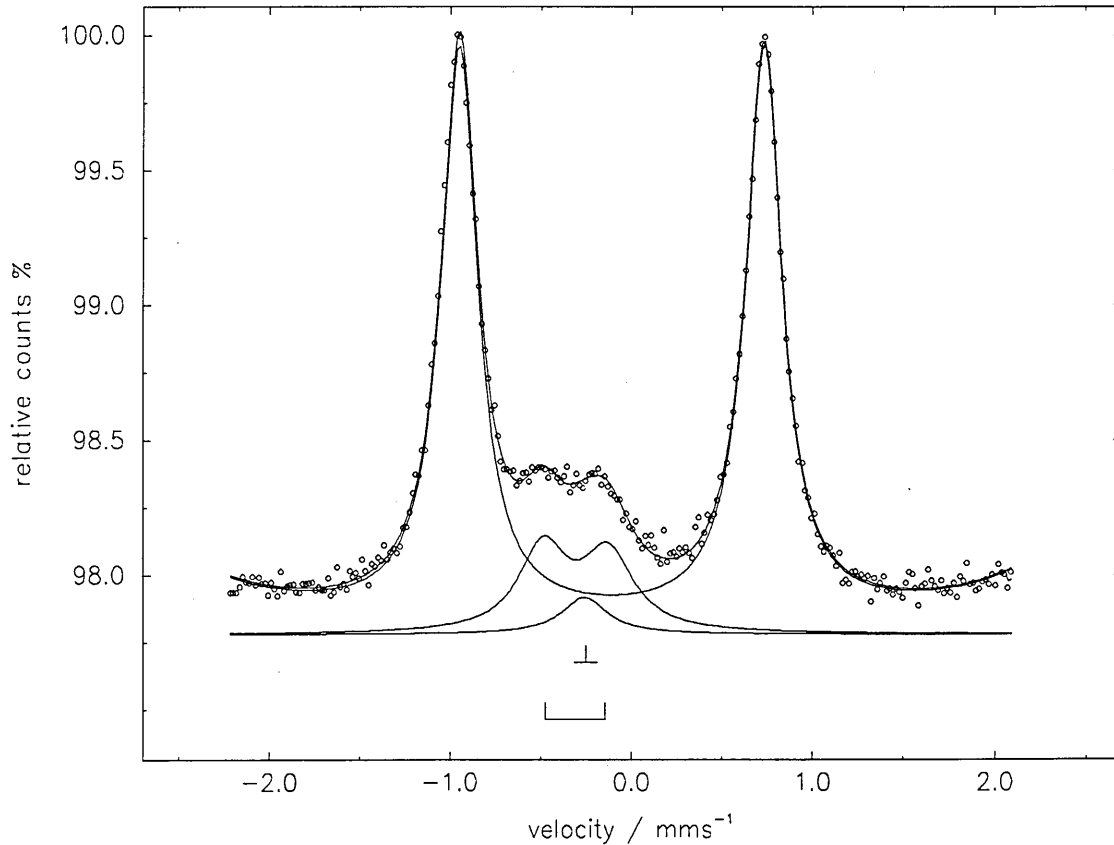


Fig. 6.4 CEM spectrum performed over a narrow velocity range of a sample after a Ti ion pre-treatment for 10 mins followed by the deposition of a thin titanium coating.

The dependence of the concentration  $x$ , has been investigated experimentally by Sumiyama *et al.* [3] and by Liou *et al.* [4] for amorphous alloys prepared by rf sputtering using Fe and Ti targets simultaneously. Also the concentration dependence has been predicted in a range of amorphous alloys with varying  $x$  concentration by van der Kraan [5]. Using their prediction model and the measured isomer shift from this study, for the amorphous phase the concentration  $x$  can be determined

### 6.1.1 Calculation of x in the Fe<sub>x</sub>Ti<sub>1-x</sub> Alloy

By considering the model proposed by van der Kraan investigating the <sup>57</sup>Fe isomer shift in amorphous based alloys as described in chapter 2 (section 2.5.4), it is possible to calculate x for Fe<sub>x</sub>Ti<sub>1-x</sub>.

For Fe<sub>x</sub>Ti<sub>1-x</sub>:  $\delta IS_{MAX} = -0.27 \text{ mm s}^{-1}$  [van der Kraan]

$$\delta IS = (1 - \bar{x})\delta IS_{MAX}$$

Using the measured isomer shift,  $\delta = -0.20 \text{ mm s}^{-1}$  and quadrupole splitting,  $\Delta Q = 0.36 \text{ mm s}^{-1}$  for the detected Fe<sub>x</sub>Ti<sub>1-x</sub> phase:

$$\bar{x} = \frac{-0.20 + 0.27}{0.27}$$

$$\bar{x} = 0.259$$

and,

$$\begin{aligned} V_{Fe}^{2/3} x &= \bar{x}xV_{Fe}^{2/3} + \bar{x}V_{Ti}^{2/3} - \bar{x}xV_{Ti}^{2/3} \\ V_{Fe}^{2/3} x &= 0.259xV_{Fe}^{2/3} + 0.259V_{Ti}^{2/3} - 0.259xV_{Ti}^{2/3} \end{aligned} \quad (6.2)$$

where V is the atomic volume i.e. atomic weight/density:

$$V_{Fe} = \frac{55.85}{7.87} = 7.10 \text{ cm}^3 \text{ mol}^{-1}$$

$$V_{Ti} = \frac{47.88}{4.50} = 10.64 \text{ cm}^3 \text{ mol}^{-1}$$

substituting  $V_{Fe}$  and  $V_{Ti}$  into equation (6.2) gives:

$$3.69x = 0.96x + 1.25 - 1.25x$$

$$x = \frac{1.25}{3.69 - 0.96 + 1.25} = 0.31$$

Therefore the formulae for the amorphous phase is approximately:-



By considering the measured isomer shift to have an associated error of  $\pm 0.02 \text{ mm s}^{-1}$ , the corresponding calculated error in  $x = 0.08$ . The calculation of  $x = 0.3$  also obtains a value for the contact surface concentration,  $c_{\text{Ti}}$ , yielding  $c_{\text{Ti}} = 0.75$ . This surface concentration can be regarded as a measure of the fractional area of contact of the Fe atomic cells with the Ti atomic cells. This represents a high level of titanium in the near surface region and subsequent Fe-Ti interaction. Such a high level of Ti present in this region is unlikely to be as a consequence of ion implantation alone. This may be explained by atomic intermixing due to the ion bombardment increasing adatom mobility by diffusion effects. However, Ti interdiffusion in steel does not occur significantly at temperatures less than  $600 \text{ }^\circ\text{C}$  [6], a temperature significantly higher than the recorded process temperature of  $450 \text{ }^\circ\text{C}$ . Weber *et al.* [7] has proposed that local heating effects of the substrate due to the impinging ions may approach  $600 \text{ }^\circ\text{C}$  for bias current densities of  $22 \text{ mA cm}^{-2}$ . Such heating effects are likely to occur in the studied pre-treatment process of the ABS<sup>TM</sup> method, where this study has shown for a single cathode and no substrate rotation, the calculated bias current density is  $67 \text{ mA cm}^{-2}$ . Taking into account that the conventional pre-treatment process uses two cathodes simultaneously with 3 fold rotation, the received bias current density is likely to be sufficiently high to generate local heating effects in excess of  $600 \text{ }^\circ\text{C}$ , thereby generating diffusion effects and explaining the high level of Ti present in the amorphous  $\text{Fe}_x\text{Ti}_{1-x}$  phase. The diffusion of Cr, present in the mild steel, into the thin Ti overlayer for a sample Ti ion pre-treated for 10 minutes, can be seen in the SNMS depth profile shown in fig 6.5. This depth profile emphasises the advantages of the CEMS technique, since no information from the depth profile regarding any Fe-Ti chemical interaction can be discerned.

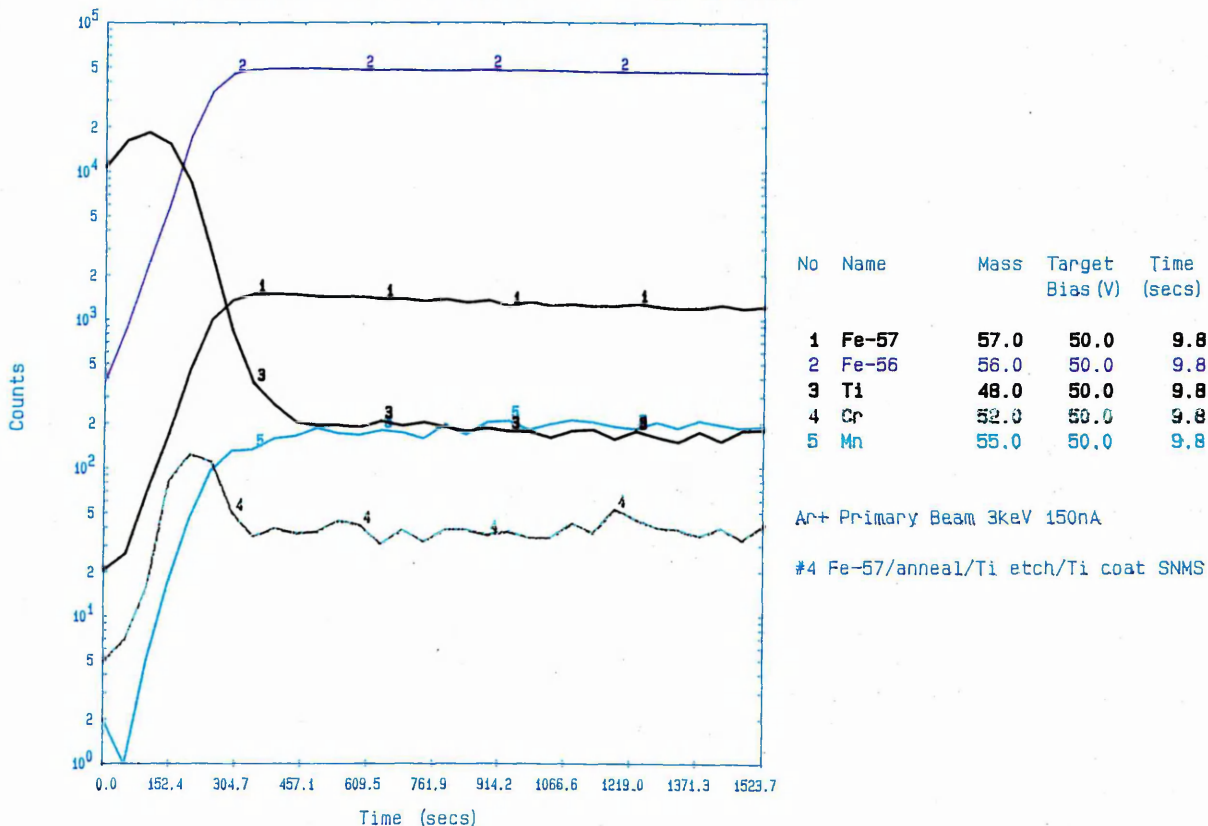


Fig. 6.5 SNMS depth profile of a sample after a Ti ion pre-treatment for 10 minutes at -1200 V bias followed by the deposition of a thin titanium layer, using two cathode sources and three-fold rotation.

### 6.1.2 Further Experiments using a Steered Arc Discharge

In further experiments, samples were used with an estimated 25 nm of  $^{57}\text{Fe}$  deposited on the surface without any subsequent annealing. Samples were enriched in this way to study the effects occurring over shorter lengths of time, and consequently  $^{57}\text{Fe}$  removal is not as severe compared with the 10 minute pre-treatment process. These samples were Ti ion pre-treated at the same bias voltage of -1200 V at an Ar pressure of  $7 \times 10^{-4}$  mbar for different lengths of time, 25 s and 300 s using 3 fold substrate rotation. Similarly prepared samples were pre-treated at different Ar pressures at a substrate bias voltage of -1200 V. These experiments were performed for 45 s with no substrate rotation, and in order to sustain the cathode arc at the lower gas pressure it was necessary to have the target shutter only half open. In all the these pre-treatment processes the maximum recorded temperature was 450 °C.

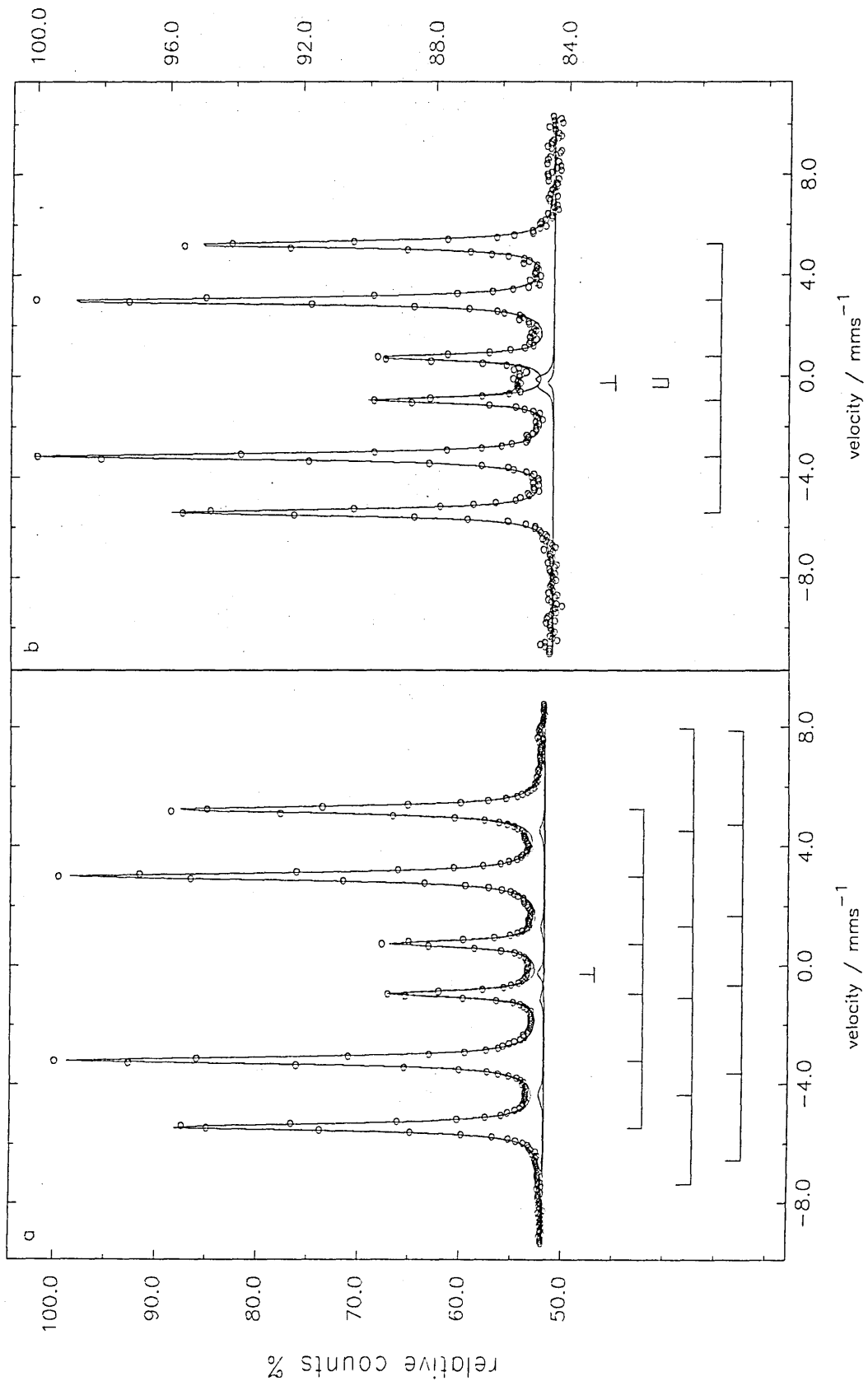


Fig. 6.6 Comparison of Ti ion pre-treatments for different lengths of time using 2 cathodes and 3 fold rotation (a) 25 s and (b) 300 s.

Phase	$\delta / \text{mm s}^{-1}$ $\pm 0.02$	$\Gamma/2 / \text{mm s}^{-1}$ $\pm 0.02$	$\Delta Q / \text{mm s}^{-1}$ $\pm 0.02$	$H_{\text{eff}} / \text{kG}$ $\pm 5$	Rel. Area / %
FeTi - c	-0.15	0.18	-	-	0.5
$\alpha$ -Fe	0.00	0.14	-	330	96.4
Fe <sub>3</sub> O <sub>4</sub> (A-site)	0.30	0.28	0.22	478	2.5
Fe <sub>3</sub> O <sub>4</sub> (B-site)	0.69	0.24	0.14	442	0.6

Table 6.2 Hyperfine parameters relative to  $\alpha$ -Fe of the phases present after a Ti ion etch performed for 25 s.

The CEM spectra of the two samples Ti ion pre-treated for different lengths of time are shown in fig. 6.6 and the associated hyperfine parameters for the shorter etch process are given in table 6.2. For the 25 s pre-treatment the presence of magnetite, Fe<sub>3</sub>O<sub>4</sub> and a low level of crystalline FeTi can be seen. The A site sextet pattern with the larger magnetic splitting is due to Fe<sup>3+</sup> ions in tetrahedral (A) sites and the B sites are due to both Fe<sup>2+</sup> and Fe<sup>3+</sup> in octahedral sites. Inspection of the relative intensities for I<sub>B</sub> and I<sub>A</sub>, yields I<sub>B</sub>/I<sub>A</sub> = 0.24 which is significantly lower than the value of 1.88 for stoichiometric magnetite reported by Sawatzky *et al.* [8]. Further inspection of the relative line intensities indicates that the magnetite has formed with a random magnetization. The observed non-stoichiometric magnetite can be explained by atomic intermixing during the Ti bombardment processes causing re-arrangement of the Fe<sup>2+</sup> and Fe<sup>3+</sup> sites. Graham *et al.* [9] have used CEMS to study magnetite films grown on electropolished natural Fe substrates. Their study found a relationship for the percentage, P of the total spectrum area contributed by the oxide thickness, d. It was found that d upto 300 nm could be expressed, to an accuracy of 5 % by:

$$d(\text{\AA}) = -1.95 \times 10^3 \ln(1-0.01P)$$

Using the above expression a total relative spectral measured area of 3 % for the 25 s pre-treatment process, corresponds to an oxide layer thickness of 6 nm. However, the Ti pre-treated sample consisted of an initial 25 nm <sup>57</sup>Fe overlayer on a mild steel substrate, in contrast to the natural Fe substrates used by Graham *et al.* Since the remaining <sup>57</sup>Fe overlayer after the pre-treatment has resulted in an increased surface sensitivity compared with a natural Fe foil, the detected oxide thickness can be

considered to be less than 6 nm. Such a thin oxide layer can be explained by oxide sputtering from the chamber walls and substrate holder followed by subsequent redeposition on the sample.

For the longer 300 s Ti ion pre-treatment process the removal of the magnetite phase and a more significant formation of both amorphous and crystalline FeTi phases can be clearly seen. The measured hyperfine parameters are given in table 6.3. By comparison of the relative spectral areas, the Fe-Ti phases have increased by a factor of 4, from the 25 s to 300 s pre-treatment processes. This indicates an increase in the Ti concentration in the near surface region with increasing time over 275 s. Since crystalline FeTi only exists for Ti concentrations between approximately 48 - 51 at. % Ti, the observation of amorphous  $\text{Fe}_{0.3}\text{Ti}_{0.7}$  containing significantly more Ti, after 300 s is consistent with the Ti diffusion/intermixing effects due to local heating effects described previously.

Phase	$\delta / \text{mm s}^{-1}$ $\pm 0.02$	$\Gamma/2 / \text{mm s}^{-1}$ $\pm 0.02$	$\Delta Q / \text{mm s}^{-1}$ $\pm 0.02$	$H_{\text{eff}} / \text{kG}$ $\pm 5$	Rel. Area / %
FeTi - c	-0.15	0.16	-	-	0.3
FeTi - a	-0.19	0.19	0.36	-	1.7
$\alpha$ -Fe	0.00	0.14	-	330	98.0

Table 6.3 Hyperfine parameters relative to  $\alpha$ -Fe of the phases present after a Ti ion etch performed for 300 s.

The CEM spectra showing the comparison of the Ti ion pre-treatment under differing Ar gas pressures, fig 6.7, show the formation of iron carbonitride and low levels of magnetite. The formation of these phases is due to the sputtering of surface debris from the shutter, and subsequent re-deposition on to the samples. Relative line intensities of the carbonitride phase, indicates a magnetization parallel to the substrate surface, unlike the random magnetization of the magnetite. Typical measured hyperfine parameters for the detected iron carbonitride phase are as follows:

Phase	$\delta / \text{mm s}^{-1}$	$\Gamma/2 / \text{mm s}^{-1}$	$\Delta Q / \text{mm s}^{-1}$	$H_{\text{eff}} / \text{kG}$	Rel. Area / %
Fe-C,N	$-0.17 \pm 0.02$	$0.28 \pm 0.02$	$0.06 \pm 0.02$	$214 \pm 5$	4.5

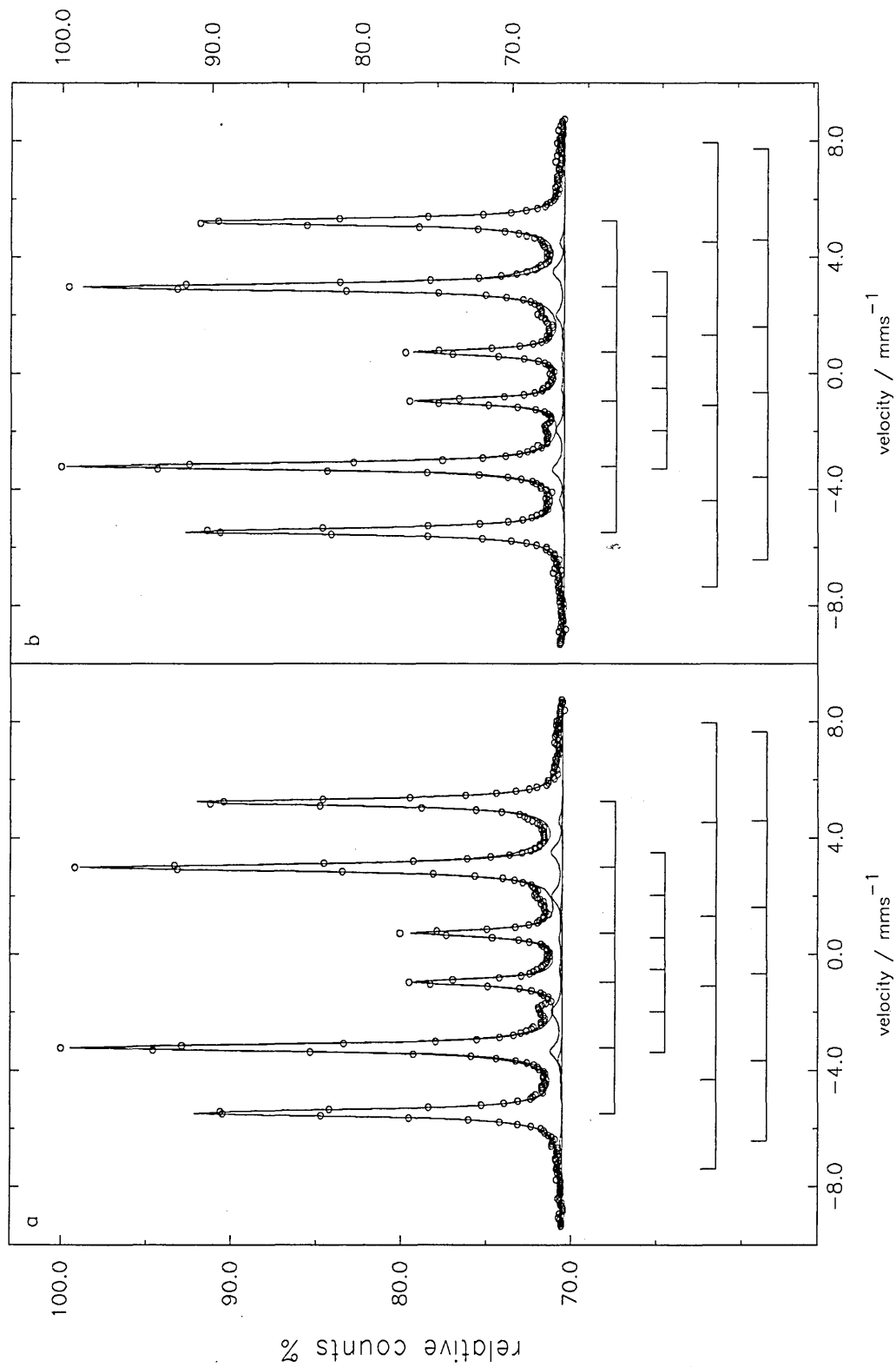


Fig. 6.7 Comparison of Ti ion pre-treatment performed under different Ar pressures - (a)  $6 \times 10^{-5}$  and (b)  $3 \times 10^{-3}$  mbar.

The observed broadened linewidth associated with the iron carbonitride is due to either metastable phases or lattice relaxation caused by strains, which are inherently present in the Fe-C-N system [10 and references therein]. Similar broad linewidths and  $H_{\text{eff}}$  values for carbonitrides have been observed by Hanzel *et al.* [11] for interfaces generated by a Balzers sputron device [12].

It should be noted that in order to sustain the arc at the lower gas pressure it was necessary to have the shutter covering half the target, to generate a well defined positive electrode with respect to the cathode source. This positioning of the shutter is not usual in the ABS<sup>TM</sup> process, but was necessary for just these two arrangements. Comparison of the percent effect of the CEM spectra, indicates that more  $^{57}\text{Fe}$  has been removed from the surface when a lower gas pressure is used, showing the greater effect of the Ti ion etch under these conditions. For both these CEM spectra the S/N and percent effects are high, indicating a significant quantity of the  $^{57}\text{Fe}$  as deposited 25 nm layer still remains after 45 s. This is in sharp contrast with the calculated  $60 \text{ nm min}^{-1}$  etch rate for natural Fe on stainless steel for the same cathode-sample distance (see chapter 5, section 5.5.2). However, this can be explained by the reduced Ti ion bombardment as a consequence of covering half the cathode source with the shutter and hence less significant  $^{57}\text{Fe}$  removal.

## 6.2 Comparison with the ABS<sup>TM</sup> Process

For a comparison with the ABS<sup>TM</sup> process, a sample was treated using a modified BAI 640R Balzers coating unit [13]. The method used combined triode ion plating with in situ plasma Ar and N nitriding to improve the wear characteristics of metal injection moulding dies [14]. The process relies on plasma nitriding [15,16] a region to a depth in the order of 10's of microns. The nitriding process improves the wear characteristics of the steel and a further improvement against wear can be achieved by the addition of compound layers of iron nitrides or carbonitrides. By the addition of a final ion plated coating such as TiN over the nitrided substrate, a further improvement in both the friction and wear characteristics of the component can be achieved. This method is

known as an "integrated duplex process". The process has been described in detail elsewhere [13,14] and has been shown to produce  $\epsilon$ -Fe<sub>2-3</sub>(CN) and  $\gamma$ -Fe<sub>4</sub>N compound layers [17,18].

A sample was treated in such a way to produce a compound layer followed by the deposition of a Ti layer. This sample was a mild steel substrate with an estimated 40 nm of <sup>57</sup>Fe surface layer followed by annealing at 900 K for 45 minutes. The predicted diffusion profile of the <sup>57</sup>Fe is shown in fig. 6.8 and was felt to be appropriate for a typical Ar etch process, preventing excessive removal of the Mössbauer isotope and hence maintaining surface sensitivity. From the predicted profile it can be seen that the diffused <sup>57</sup>Fe penetrates a depth of almost 100 nm at a fractional concentration higher than the <sup>57</sup>Fe natural abundance level. However, the fractional concentration of <sup>57</sup>Fe decreases more rapidly compared with the previously discussed samples, comprising of an initial 25 nm of <sup>57</sup>Fe followed by annealing at the same temperature but for twice the length of time.

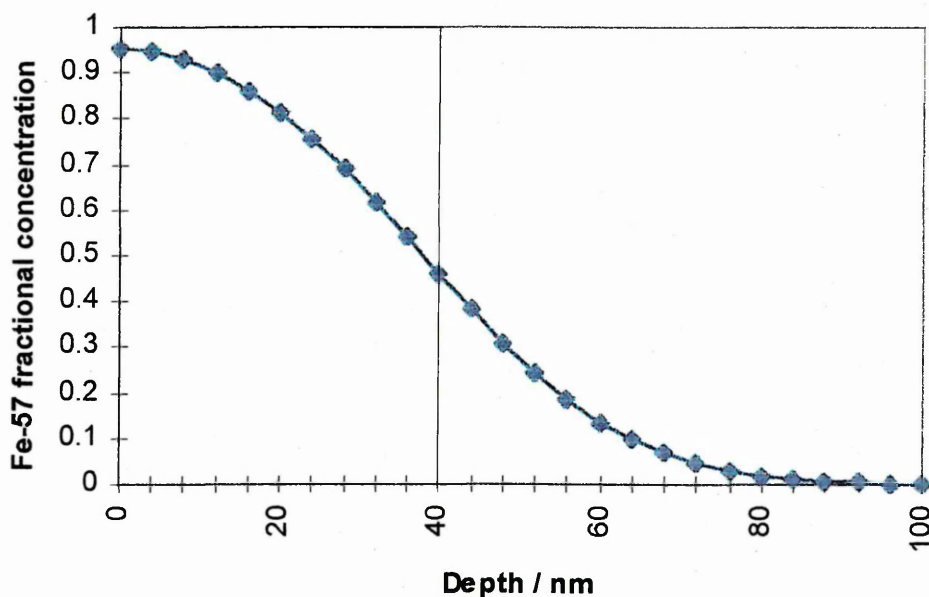


Fig. 6.8 Predicted fractional concentration of <sup>57</sup>Fe as a function of depth for a mild steel annealed at 900 K.

The <sup>57</sup>Fe enriched sample was heated to 600 K prior to Ar etching for 3 minutes at a substrate bias voltage of -200 V. This was followed by the deposition of a thin Ti layer at a bias voltage of -100 V at an Ar pressure of  $1.2 \times 10^{-3}$  mbar. The emission current

of the electron beam gun was held constant at 0.4 A and plasma enhancement was obtained using the high current plasma beam at 80 A.

The CEM spectrum from the  $^{57}\text{Fe}$  enriched sample treated by the modified Balzers coating unit is shown in fig. 6.9(a). This spectrum clearly shows an additional sextet pattern attributed to the early growth stages of the compound layer,  $\epsilon\text{-Fe}_{2-3}(\text{CN})$ . The measured hyperfine parameters of these phases are shown in table 6.4. From the relative intensities of the spectral lines within the sextet, it follows that the compound layer grows on the substrate with a magnetization parallel to the sample surface. A further CEM spectrum shown in fig. 6.9(b) of the same sample, recorded at a lower velocity range shows the formation of a small quantity of the amorphous phase,  $\text{Fe}_x\text{Ti}_{1-x}$ .

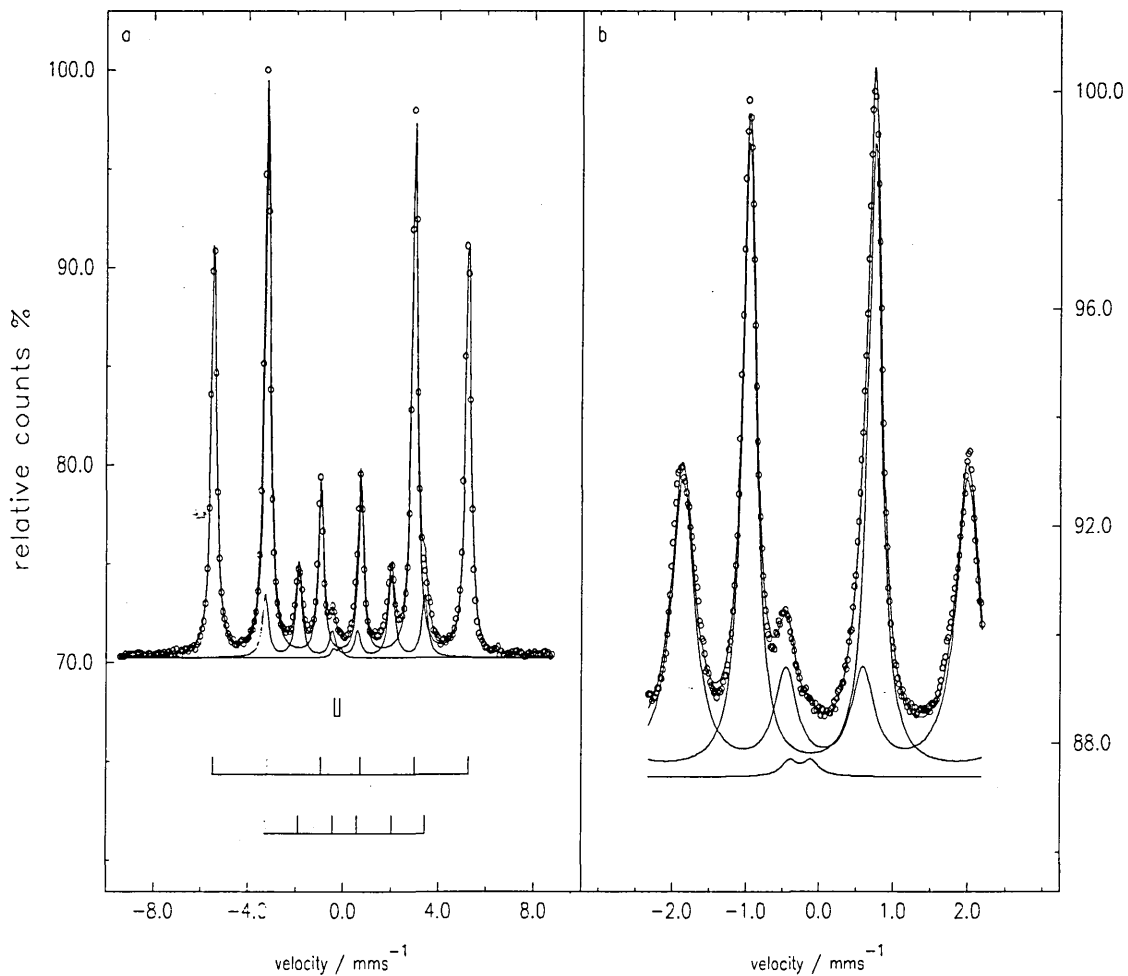


Fig. 6.9 CEM spectra of (a) 3 minute Ar ion etch followed by a 40 s deposition of Ti at a bias voltage of 100 V using the Balzers BAI 640R coating unit and (b) lower velocity range.

Phase	$\delta / \text{mm s}^{-1}$ $\pm 0.02$	$\Gamma/2 / \text{mm s}^{-1}$ $\pm 0.02$	$\Delta Q / \text{mm s}^{-1}$ $\pm 0.02$	$H_{\text{eff}} / \text{kG}$ $\pm 5$
FeTi - a	-0.15	0.13	0.30	-
$\alpha$ -Fe	0.00	0.13	0.00	330
$\epsilon$ -Fe <sub>2-3</sub> (CN)	-0.18	0.19	0.00	214

Table 6.4 Hyperfine parameters relative to  $\alpha$ -Fe of the phases present after a 3 minute Ar etch followed by the deposition of a thin Ti layer at 100 V bias by the Balzers process.

The measured isomer shift for the detected amorphous phase of  $-0.15 \text{ mm s}^{-1}$  is in contrast with the measured value of  $-0.20 \text{ mm s}^{-1}$  for the more evident  $\text{Fe}_x\text{Ti}_{1-x}$  formation in the ABS<sup>TM</sup> method. This increase in the isomer shift for the sample treated by the Balzers process, corresponds to an increase in the s-electron density at the Fe nucleus by fewer interacting Ti atoms compared with the  $\text{Fe}_x\text{Ti}_{1-x}$  phase formed in the ABS<sup>TM</sup> method. The observation is consistent with greater Ti surface intermixing occurring in the steered arc mode of the ABS<sup>TM</sup> method compared with the Balzers process. This is due to the greater surface interaction of higher energy multiply charged Ti ions at a bias voltage of  $-1200 \text{ V}$ , compared with the much lower energy Ti ions in the Balzers process during deposition at a bias voltage of  $-100 \text{ V}$ . However, it should be noted that an accurate isomer shift measurement for such a small phase formation is difficult. Similarly, a true comparison of the  $\text{Fe}_x\text{Ti}_{1-x}$  formed between the two coating methods is difficult due to differences in the detected CEMS signal as a consequence of the nature of the produced conversion electrons in the sample under study. Most significantly the number of resonantly produced electrons by the Mössbauer effect depends on the remaining  $^{57}\text{Fe}$  enrichment level at the depth of interest. This level will differ as a result of the severity of the etching with either low energy Ar or higher energy multi-ionised Ti. This may cause observed differences in the magnitude of the relative spectral areas arising from each detected component in the CEM spectrum. Also different spectral area contribution effects of the relative phase components may arise due to the deposited Ti layer generating detectable secondary electrons by a method described by Tricker *et al.* [19]. This is significant, since the thickness of the deposited Ti layer by each process may be different and hence will contribute differently to the relative phase components of the measured CEM spectra.

## References

- [1] C. L. Chien and S. H. Liou, *Phys. Rev. B* **31(12)** 1985 8238.
- [2] M. M. Stupel, M. Ron and B. Z. Weiss, *J. Appl. Phys.* **47** (1976) 6.
- [3] K. Sumiyama, H. Yasuda and Y. Nakamura, *J. Phys. Cond. Matt.* **2** (1990) 3595.
- [4] S. H. Liou and C. L. Chien, *J. Appl. Phys.* **55(6)** (1984) 1820.
- [5] A. M. Van der Kraan and K. H. J. Buschow, *Phys. Rev. B* **27(5)** (1983) 2693.
- [6] T. Weber, J. Verhoeven, R. Schlatmann, A. Keppel and S. Bultman, *Appl. Phys. Lett.* **68(21)** (1996) 2948.
- [7] T. Weber, J. Verhoeven, F. W. Saris, T. Osipowicz and W. -D. Münz, *Nucl. Instr. Meth. B* **106(1-4)** (1995) 159.
- [8] G. A. Sawatzky, F. van der Woude and A. H. Morrish, *Phys. Rev.* **183** (1969) 383.
- [9] M. J. Graham, D. F. Mitchell and D. A. Channing, *Oxid. Met.* **12(3)** (1978) 247.
- [10] M. Ron, in “*Applications of Mössbauer Spectroscopy*” ed. by R. L. Cohen, Vol. 2 (Academic, New York, 1980) p.329.
- [11] D. Hanzel, W. Meisel, D. Hanzel, P. Griesbach, B. Navinsek, P. Panjan and P. Gütlich, *J. Vac. Sci. Technol. A* **11(6)** (1993) 3034.
- [12] B. Navinsek and J. Fine, *Vacuum* **36** (1986) 711.
- [13] E. Bergmann, *Surf. Coat. Technol.* **57** (1993) 133.
- [14] N. Dingremont, E. Bergmann and P. Collignon, *Surf. Coat. Technol.* **72** (1995) 157.
- [15] R. F. Bunshah: “Overview of Deposition Technologies with Emphasis on Vapor Deposition Techniques”, in *Industrial Materials Science and Engineering*, ed. by L. E. Murr, Manufacturing Engineering and Materials Processing Vol. 13 ( Marcel Dekker, Inc. New York 1984) p. 393.
- [16] A. Mathews *et al*: “Developments in Plasma-assisted PVD Processing” in *Process Technology and Surface Analysis*, ed. by P. K. Datta and J. S. Gray, Surface Engineering Vol. 3 (Royal Society of Chemistry 1993) p. 99.
- [17] N. Dingremont, E. Bergmann, M. Hans and P. Collignon, *Surf. Coat. Technol.* **76/77** (1995) 218.
- [18] N. Dingremont, E. Bergmann, P. Collignon and H. Michel, *Surf. Coat. Technol.* **72** (1995) 163.
- [19] M. J. Tricker, L. A. Ash and T. E. Cranshaw, *Nucl. Instr. and Meth.* **143** (1977) 307.

## CHAPTER 7

### CONCLUSIONS AND FUTURE WORK

The initial stages of this research program concentrated on developing a method to enrich the near surface region of substrates with the Mössbauer isotope  $^{57}\text{Fe}$ . The enrichment process was necessary to successfully characterise by CEMS the Fe/Ti interface region generated by PVD process. CEMS has shown that Mössbauer signal parameters can be improved by both ion implantation and evaporation of  $^{57}\text{Fe}$  followed by diffusion. However more significant improvement in sensitivity can be achieved by the evaporation followed by diffusion technique. CEMS has shown a successful annealing technique for  $^{57}\text{Fe}$  enriched substrates has been achieved without the formation of iron oxides. This area of research work was found to be both time consuming and initially technically difficult to achieve. However once the  $^{57}\text{Fe}$  evaporation followed by diffusion technique was successfully mastered, the adopted enrichment procedure was found to routinely produce starting samples with an exceptionally high success rate greater than 90 %. The distribution of  $^{57}\text{Fe}$  within the near surface region due to the annealing was predicted by a diffusion model. Due to the high cost of  $^{57}\text{Fe}$ , the majority of the initial annealing attempts were performed using as deposited natural iron overlayers. Although using this method, CEMS cannot yield adequate information regarding a thin surface oxide formation, the method does give a visual indication of the success/failure of the annealing. This approach should be used by future workers in the interest of saving time and costly  $^{57}\text{Fe}$  metal, until confidence in the sample preparation has been gained. Dynamic SIMS and SNMS verified the estimated thickness of the as deposited  $^{57}\text{Fe}$  prior to annealing. Similarly, GDOES also confirmed the validity of the method used to estimate the thickness of a thicker Al coating on a Si wafer.

The CEMSN2 analysis of natural iron on stainless steel substrates has proved particularly useful in determining the etch rate for a static Ti ion pre-treatment. This estimated an etch rate of 1nm per second for a sample positioned at a cathode-sample distance of 250 mm during a 30 second pre-treatment process. The non-measurable natural iron removal

at the greater sample-cathode distance of 350 mm indicated a rapid decrease in Ti ion bombardment over a distance of 100 mm. This is of considerable practical importance since utilisation of the beneficial aspects of the ion pre-treatment requires uniform sputter cleaning of the substrates. Differences in the average etch rates between 1 fold and 2 fold/3 fold rotated samples were also observed. Future work should consider mathematical modelling of the angular shifts between the sample and the cathodes as a function of pre-treatment time and sample starting position. This is of significant importance for 3 fold rotated samples which may undergo shadowing from the cathodes during the pre-treatment process and hence receive a variation of ion bombardment compared with other modes of rotation.

CEMS has been shown to be of considerable importance in detecting phase formations in the Fe-Ti system for PVD interfaces generated using a steered arc discharge. Very few techniques are suitable to the study of detecting such a low level of interaction. For comparison with CEMS, the XRD trace of a Ti ion pre-treated sample emphasises this point. Future work could consider the use of cross-sectional TEM which is capable of resolving the interface region. However this technique is experimentally extremely difficult and does not readily yield the kind of chemical information provided by CEMS. Similarly, Glancing Angle XRD [1, 2] could be used for structure and crystallographic determination of the phases present at the interface.

CEMS has shown that sputter cleaning with multiply ionised Ti ions is more effective than using Ar ions for the same length of time, due to the greater mass and hence bombardment energy ( $\frac{1}{2}mv^2$ ). The sputter cleaning process has also been shown to be more effective at lower residual gas pressures. The development of the FeTi crystalline phase during the experiments, has been identified after a short pre-treatment of 25 s. During this time scale iron oxides and carbonitrides have also been identified by CEMS. The sources of the oxide formation is likely to be from water vapour contamination and surface debris present within the coating chamber. The water vapour is a consequence of the large size of the vacuum chamber and turntable assembly resulting in moist air entrapment during sample loading. Unfortunately this problem cannot be easily overcome, since the large chamber doors offer the advantage of straightforward sample

loading and removal. However after longer pre-treatments of 300 s, CEMS has shown the formation of the amorphous  $\text{Fe}_x\text{Ti}_{1-x}$  phase along with the crystalline phase but no iron oxides or carbonitrides were detected. This suggests successful sputter cleaning of substrates after a short period of time, followed by FeTi crystalline formation followed by  $\text{Fe}_x\text{Ti}_{1-x}$  formation where  $x$  has been calculated to be approximately 0.3. The formation of the amorphous phase after the crystalline phase is consistent with increased Ti intermixing in the near surface region occurring with increasing ion pre-treatment time. The difficulty in producing a bulk sample of single phase FeTi is discussed in the Annexe.

The compound  $\epsilon\text{-Fe}_{2-3}(\text{CN})$  layer produced by a Balzers process involving Ar ion bombardment followed by Ti ion deposition, has been confirmed by CEMS for a sample consisting of an initial 40 nm  $^{57}\text{Fe}$  layer followed by annealing at 900 K for 45 minutes. Similar processes studied by Hanzel *et al.* [3] showed carbonitrides of lower intensity in the CEM spectrum for samples consisting of an initial 25 nm  $^{57}\text{Fe}$  surface layer on low carbon steels. This emphasises the advantage of the enrichment using the adopted annealing technique which has resulted in an improvement of surface sensitivity in the near surface region, thereby enhancing the carbonitride phase. From the Balzers process, there is some evidence of a small quantity of  $\text{Fe}_x\text{Ti}_{1-x}$  phase formation. The small quantity of the detected amorphous phase is a result of the lower energy Ti ions depositing at a bias voltage of -100 V generating only a small amount of Fe/Ti mixing compared with the higher energies involved in the ABS<sup>TM</sup> process.

Future work could consider the study of the ion pre-treatment process using metal ion species other than titanium. In particular, chromium nitride coatings are being used as a replacement for electroplated hard chromium in various applications. This type of nitride coating has been deposited by the ABS<sup>TM</sup> method after chromium ion etching of the substrates [4]. CEMS could provide useful information regarding the associated etch rates with the Cr ion pre-treatment process by analysis with the CEMSN2 program. Improvements in the analysis of etch rate information could be achieved by using thicker deposited iron overlayers on stainless steel substrates and etching for longer periods of

time compared with the reported 30 second pre-treatments. Using this approach could lead to the detection of substantial differences in the observed etch rates for the various modes of rotation used in the ABS<sup>TM</sup> process. Explanation of these differences, primarily due to substrate shadowing effects, could be mathematically modelled as a function of geometrical and time dependent parameters. A mathematical approach studying the effects of various rotation frequencies has been shown to affect the flux and growth conditions for a typical multi-axial substrate holder used in PVD processes [5].

Also, regarding the Cr ion pre-treatment process, CEMS could be used to observe Fe-Cr interactions formed as a consequence of the pre-treatment for <sup>57</sup>Fe enriched substrates. However, it should be noted that the interpretation of Mössbauer spectra for the Fe-Cr system is far more complex compared with the Fe-Ti system. Several Mössbauer studies [6-8] have shown that Fe-Cr alloys exist over a wide composition range which can be fitted to several subspectra due to resultant magnetic interactions. Therefore, accurate interpretation of CEM spectra obtained from <sup>57</sup>Fe enriched samples subjected to Cr ion pre-treatments would be extremely difficult due to the nature of the Fe-Cr system. To aid accurate interpretation, future work could consider using Depth selective CEMS (DCEMS) [9, 10]. This technique allows for a semi-quantitative analysis of the observed backscatter spectra by considering the associated escape ranges of the detected conversion electrons. DCEMS measurements are usually performed using a channeltron [11, 12] in conjunction with a simple energy analyser for the selection of certain electron energies and therefore different sample depths. By using DCEMS, a significant improvement in distinguishing the Fe-Cr subspectra from the subspectra due to the substrate could be achieved, by recording several spectra of the same sample corresponding to different analysed depths. Hence improving the observed sensitivity with respect to the Fe-Cr interaction at the depth of interest. A similar approach would also prove extremely useful in providing information of the interaction depth for the Fe-Ti system, regarding the observed formation of FeTi crystalline and amorphous phases generated by the Ti ion pre-treatment process.

## References

- [1] C. Quaeqhaegens, L. M. Stals, M. Vanstappen and L. Deschepper, *Thin Solid Films* **197(1-2)** (1991) 37.
- [2] K. K. Kadyrzhanov, N. F. Yugai, Y. Z. Tuleushev and S. V. Mytnichenko, *Nucl. Instr. Meth. A* **308(1-2)** (1991) 308.
- [3] D. Hanzel, W. Meisel, D. Hanzel, P. Griesbach, B. Navinsek, P. Panjan and P. Gütlich, *J. Vac. Sci Technol. A* **11(6)** (1993) 3034.
- [4] T. Hurkmanns, D. B. Lewis, J. S. Brooks and W. -D. Münz, *Surf. Coat. Technol.* **87-8(1-3)** (1996) 192.
- [5] B. Rother, *Surf. Coat. Technol.* **64** (1994) 155.
- [6] R. Frattini, G. Longworth, P. Matteazzi, G. Principia and A. Tiziani, *Scripta Metallurgica* **15** (1981) 873.
- [7] L. H. Schwartz and D. Chandra, *Phys. Stat. Sol. B* **45** (1971) 201.
- [8] V. A. Peña Rodriguez, E. Baggio-Saitovitch, S. K. Xia, C. Larcia and J. C. De Lima, *Hyp. Int.* **69** (1991) 721.
- [9] Zs. Kajcsos, Ch. Sauer, A. Holzwarth, R. Kurz, W. Zinn, C. Ligtenberg and G. Van Aller, *Nucl. Instr. Meth. B* **34** (1988) 383.
- [10] B. Bodlund-Ringström, U. Bäverstam and C. Bohm, *J. Vac. Sci. Technol.* **16(4)** (1979) 1013.
- [11] J. A. Sawicki, T. Tyliczszak, B. D. Sawicka and J. Kowalski, *Phys. Lett. A* **91** (1982) 414.
- [12] H. M. Van Noort, F. J. Ferguson, C. J. G. Verwer, A. A. Van Gorkum, J. M. E. Van Laarhoven and C. J. M. Denisson, *Nucl. Instr. Meth. B* **34** (1988) 391.

## ACKNOWLEDGEMENTS

The author wishes to express sincere thanks and gratitude to a group of people whose efforts have made the writing of this thesis possible. Principally, Professor John Brooks who provided useful advice and encouragement along with Professor Dieter Münz for clarifying several aspects of surface engineering and the ABS process. Also, I wish to thank Dr Sue Forder for superbly fulfilling her supervisory role throughout the programme of research. In addition, I am thankful to all the people connected with the Mössbauer Lab., especially Jules Hamer for never failing to surprise and Andy Reeder for enlightening and entertaining dialogue.

During the course of my research work at SHU, I have called on the expertise of many technicians and support staff in several departments including Applied Physics, Chemistry, Engineering and Computer Services. Those warranting a special mention are Kevin Blake for the operation of the Microlab and Bob Grant for his skill and advice regarding the use of a very very hot oxy-acetylene torch necessary for sealing the fused silica tubing. Also concerning the sample preparation, I would like to thank the local department store for supplying the hemispherical grid arrangement which conveniently doubles as a useful kitchen sieve; a key component of the  $^{57}\text{Fe}$  deposition!

I wish to thank Dr David Liljequist of the Institute of Physics at the University of Stockholm, for kindly supplying the CEMSN2 program. Similarly, I am grateful to Dr Mats Larsson of the Department of Materials Science at the University of Uppsala, for performing the PVD processes using the modified Balzers coating unit.

I also wish to thank the staff of the Materials Research Institute at SHU. In particular Iain Smith and Dr Lee Donohue along with the other researchers and technicians working in the Surface Engineering Lab. for their patience and services regarding the PVD processes. Furthermore, many thanks to the people at Mats UK, Liverpool for obtaining revealing SNMS depth profiles very quickly indeed! Finally, I am indebted to my family and friends who have provided continual support (financial and otherwise) over the years of my research.

## COURSES AND CONFERENCES ATTENDED

*NOVAC '93 Training course in vacuum technology designed for graduate students commencing postgraduate work in October 1993, Dept. of Physics, University of York, 31 October - 2 November 1993.*

*Fourth Seeheim Workshop on Mössbauer Spectroscopy, Lufthansa Training Centre, Seeheim, Germany, 24-28 May 1994.\**

*Fifth Annual Northern Universities Meeting on Chemical Physics, School of Chemistry, University of Leeds, 6 July 1994.\**

*35 th Meeting of the Mössbauer Discussion Group, University of Nottingham, 19-20 September 1994.\**

*Sheffield ABS Days: An Annual Meeting, Holiday Inn Royal Victoria Hotel, Sheffield, 29-30 March 1995.*

*36 th Meeting of the Mössbauer Discussion Group, University of Nottingham, 7-8 September 1995.\*\**

*Plasma and Surface Coatings, Institute of Physics, 76 Portland place. London, 12 June 1996.*

*Fifth International Conference on Plasma Surface Engineering, Garmisch-Partenkirchen, Germany, 8-13 September 1996.\*\**

\* Poster presentation.

\*\* Oral presentation.

## ANNEXE

### PRODUCTION OF SINGLE PHASE FeTi

Variable temperature transmission Mössbauer analysis [1, 2 and references therein] of single phase crystalline FeTi could be used to yield significant information of the chemical and physical properties of the intermetallic compound. In particular, knowledge of the recoil free fraction,  $f$ , of the compound may be used to give an estimate of the phase formation thickness of FeTi during a steered arc Ti ion bombardment. Such a thickness determination relies upon an interpretation of electron re-emission and detection theories of CEMS e.g. Huffman [3], Bainbridge [4], Salvat [5], Liljequist [6] etc. using accurate data for the  $f$ -factor and an estimate for the electron attenuation length within FeTi. Simplified analysis for the thickness determination of a surface phase on a bulk material observed by CEMS, can be achieved by assuming approximately equal  $f$  factors for the two phases and considering a non-enriched absorber. However, for  $^{57}\text{Fe}$  enriched absorbers, a simplified analysis can be useful in determining the uppermost thickness of the observed layer by comparison of the relative spectral areas due to the surface and bulk phases in the CEM spectrum. This emphasises the crucial significance of  $f$ -factor determination of crystalline FeTi by variable temperature Mössbauer spectroscopy. However, this analysis technique requires bulk FeTi starting material in the order of mg compared with the significantly smaller amounts detected by CEMS of a thin surface layer. Therefore, preliminary studies have attempted to produce single phase crystalline FeTi and analysis of so called "single phase" FeTi from commercial suppliers.

Initial attempts of producing single phase FeTi, concentrated on an alloy pre-cursor of Fe/Ti 50/50 at. % obtained from Goodfellow Cambridge Ltd. The precursor was compacted under Ar using a 10 tonne hand press. The produced compact measured 10 mm in diameter and was heated to 1400 °C in an Ar flow furnace. The experimental arrangement is shown in fig. 8.1.

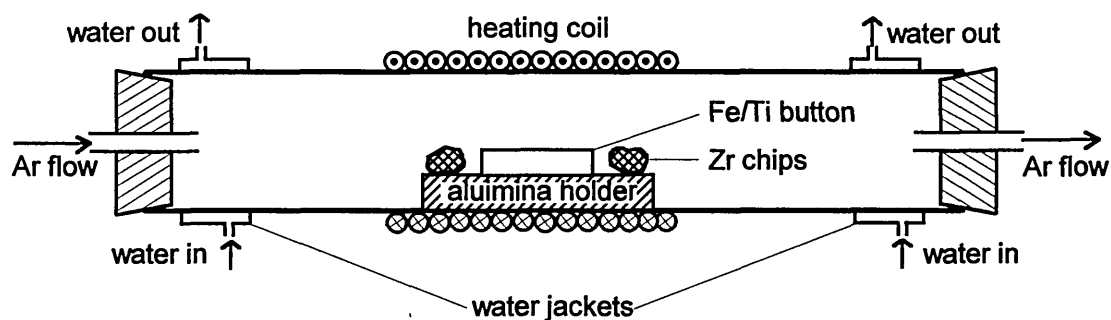


Fig. 8.1 Ar flow furnace arrangement.

The Zr chips acted as oxygen scavengers and in practice the Fe/Ti compact was placed on a quarter sectioned alumina pipe, thereby reducing contact area and allowing Ar flow underneath the sample. This minimises the source of contamination. Before heating, the ceramic tube of the flow furnace was flushed with Ar and the flow rate was maintained at  $1 \text{ l min}^{-1}$ . After heating for 30 minutes at  $1400 \text{ }^\circ\text{C}$ , the sample was allowed to cool overnight to room temperature before removal. On inspection, the sintered sample was found to be slightly tinged blue, indicating a surface layer of titanium containing oxides. After removing this layer by polishing a bright metallic surface was revealed and the subsequent CEM spectrum of this surface is shown in fig. 8.2. The measured hyperfine parameters from this spectrum are given in table 8.1.

Phase	$\delta / \text{mm s}^{-1}$ $\pm 0.02$	$\Gamma/2 / \text{mm s}^{-1}$ $\pm 0.02$	$\Delta Q / \text{mm s}^{-1}$ $\pm 0.02$	Rel. Area / %
crystalline FeTi	-0.16	0.17	-	63
Fe <sub>2</sub> TiO <sub>4</sub>	-0.18	0.14	0.30	37

Table 8.1 Hyperfine parameters relative to  $\alpha$ -Fe of a mixture of Fe/Ti sintered in an argon flow furnace.

From the CEM spectrum shown in fig. 8.2, it can be clearly seen that two phases are present; a singlet due to crystalline FeTi and a doublet identified as Fe<sub>2</sub>TiO<sub>4</sub> from the XRD trace shown in fig. 8.3.

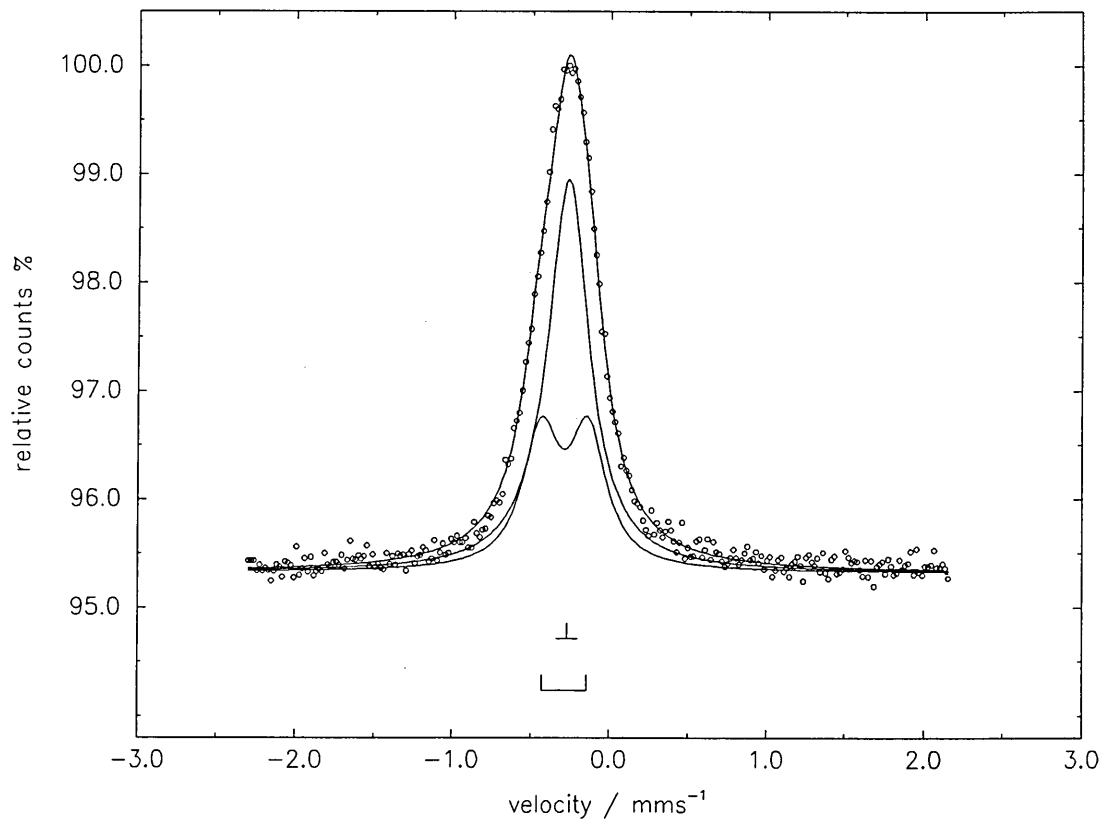


Fig. 8.2 CEM spectrum of the polished surface of a Fe/Ti mixture sintered in an argon flow furnace.

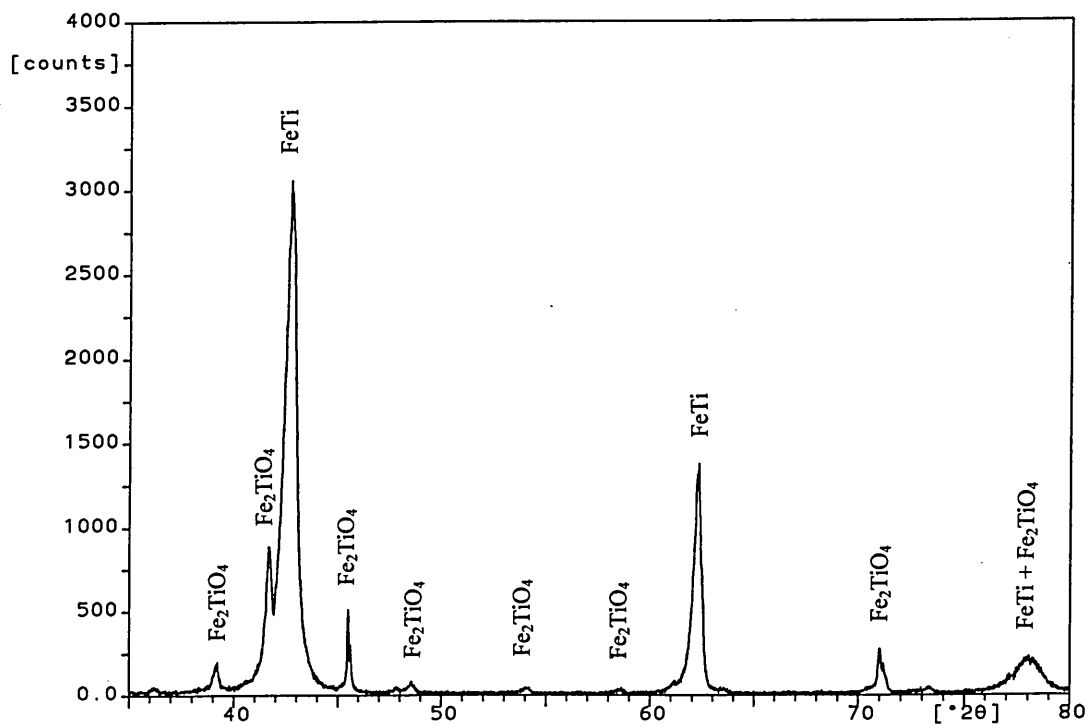


Fig. 8.3 XRD trace of a polished surface of a Fe/Ti mixture sintered at a maximum temperature of 1400 °C using an argon flow furnace.

Other attempts at producing single phase FeTi using the same furnace arrangement, but increasing the Ar flow rate yielded similar results. The difficulty in producing the single phase using this method can be explained by considering that FeTi only exists over a narrow  $\approx 2.8\%$  composition range as shown in the Fe-Ti phase diagram of chapter 2. If the prepared composition is only slightly deficient in Ti ( $< 49.7$  at. %) the two phase field of FeTi + Fe<sub>2</sub>Ti is entered. Since molten FeTi, like many Ti alloys, has a strong affinity for oxygen, any oxygen contamination will alter the original Fe/Ti ratio and subsequently other phases will form. In fact, oxygen solubility in liquid FeTi is in the order of 1-2 wt. %, whereas solid FeTi has almost zero solubility for oxygen [7]. Therefore oxygen contamination in the melt will be rejected during solidification by the formation of Fe-Ti oxides. In this study, the oxygen contamination is likely to have three sources; (i) trapped oxygen in the compacted button, (ii) oxygen outgassing from the ceramic tube of the flow furnace and (iii) contact with the alumina crucible. The most significant sources are likely to be the latter two, since the compacts were prepared under argon. Such contamination explains the formation of the observed Fe<sub>2</sub>TiO<sub>4</sub>.

Further experiments investigated commercially available “single phase” FeTi from two suppliers as shown below:

Sample	Description	Supplier
FeTi 89897	99+% purity < 325 mesh	Alfa, Johnson Mathey plc, UK
FeTi HY-STOR <sup>®</sup> 101	140 mesh	Ergenics Inc., New Jersey, USA

The supplied powders were compacted using a hand press to produce small buttons as previously described. The produced buttons were analysed by CEMS as shown in fig. 8.4 and the measured hyperfine parameters are shown in tables 8.2 and 8.3.

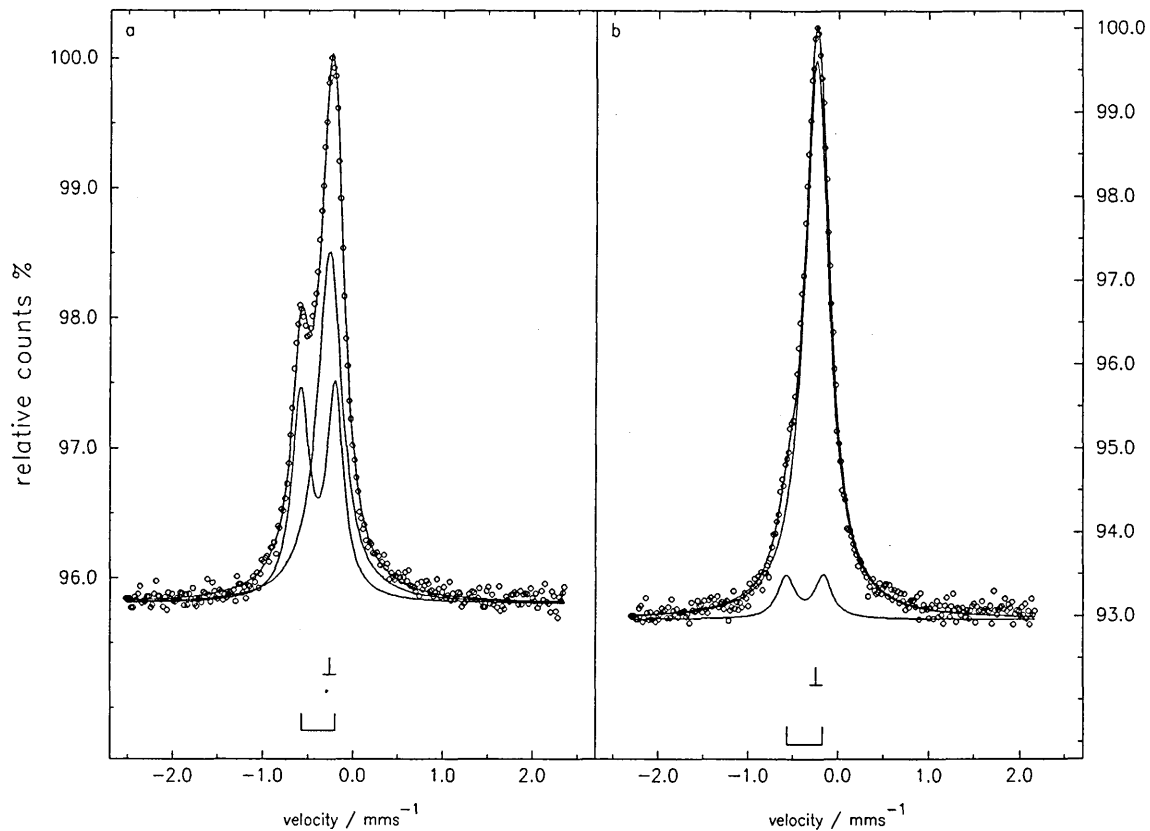


Fig. 8.4 CEM spectra of commercially supplied "single phase" FeTi from (a) Alfa Chemicals and (b) Ergenics Inc.

Phase	$\delta / \text{mm s}^{-1}$ $\pm 0.02$	$\Gamma/2 / \text{mm s}^{-1}$ $\pm 0.02$	$\Delta Q / \text{mm s}^{-1}$ $\pm 0.02$	Rel. Area / %
crystalline FeTi	-0.15	0.17	-	56
Fe <sub>2</sub> Ti	-0.28	0.12	0.38	44

Table 8.2 Hyperfine parameters relative to  $\alpha$ -Fe of "single phase" FeTi supplied by Alfa.

Phase	$\delta / \text{mm s}^{-1}$ $\pm 0.02$	$\Gamma/2 / \text{mm s}^{-1}$ $\pm 0.02$	$\Delta Q / \text{mm s}^{-1}$ $\pm 0.02$	Rel. Area / %
crystalline FeTi	-0.14	0.17	-	91
Fe <sub>2</sub> Ti	-0.26	0.12	0.40	9

Table 8.3 Hyperfine parameters relative to  $\alpha$ -Fe of "single phase" FeTi supplied by Ergenics.

From the CEM spectra of the commercially available “single phase” FeTi, it can be clearly seen that a second doublet phase of Fe<sub>2</sub>Ti is also present. The measured isomer shift and quadrupole splitting of  $0.27 \pm 0.02$  and  $0.39 \pm 0.02$  mm s<sup>-1</sup> agree well with the reported values of 0.29 and 0.40 respectively, by Wertheim *et al.* [8]. For both the analysed samples, it is assumed that during the production process, oxygen contamination has resulted in a change in the Fe/Ti ratio, thereby entering the FeTi + Fe<sub>2</sub>Ti phase field. Such contamination can occur readily when using conventional air or vacuum induction furnaces by reaction with the melt and the crucible. These furnaces are commonly used by commercial suppliers of alloys as opposed to the more expensive technique of inert electrode arc melting [9, 10]. This technique involves pressing finely divided components of the material to form the alloy, into an electrode which is arc melted under an argon atmosphere. This method has been applied to produce single phase FeTi by several workers, as described in section 2.5.1.

Unfortunately, the FeTi + Fe<sub>2</sub>Ti powdered mixtures from Alfa and Ergenics are not suitable for variable temperature transmission Mössbauer analysis to determine an accurate f-factor for FeTi. This is because the Fe<sub>2</sub>Ti phase has been shown to contain two distinct iron sites below the Néel temperature of 275 K [8, 11]. The two sites are a result of the properties of the hexagonal (MgZn<sub>2</sub>) type Laves structure of Fe<sub>2</sub>Ti. The resultant Mössbauer spectrum below 275 K consists of a magnetic six line subspectra due to iron in 6h sites and a doublet subspectra due to iron in 2a sites [12]. Such subspectra hinder accurate determination of the f-factor for a mixture of FeTi + Fe<sub>2</sub>Ti, by introducing a high uncertainty of relevant area fitting at temperatures approaching the Néel temperature. Thus the difficulty of producing FeTi without additional Fe<sub>2</sub>Ti, explains the lack of data in the literature regarding the f-factor of FeTi. Hence, future work on producing FeTi should concentrate on using an inert electrode arc melting technique to eliminate the problems of both oxygen contamination and the formation of Fe<sub>2</sub>Ti.

## References

- [1] N. N. Greenwood and T. C. Gibb in “*Mössbauer Spectroscopy*” (Chapman and Hall, London, 1971).
- [2] T. C. Gibb in “*Principles of Mössbauer Spectroscopy*” (Chapman and Hall, London, 1976).
- [3] G. P. Huffman, *Nucl. Instr. Meth.* **137** (1976) 267.
- [4] J. Bainbridge *Nucl. Instr. Meth.* **128** (1975) 531.
- [5] F. Salvat and J. Parellada *Nucl. Instr. Meth. B* **1** (1984) 70.
- [6] D. Liljequist, T. Ekdahl and U. Bäverstam *Nucl. Instr. Meth.* **155** (1978) 529.
- [7] G. D. Sandrock on “*The Metallurgy and Production of Rechargeable Hydrides*” in “*Hydrides for Energy Storage 3. Metal Hydrides - Industrial Applications*” (William Clowes and Sons Ltd, London, 1978).
- [8] G. K. Wertheim, J. H. Wernick and R. C. Sherwood, *Solid State Communications* **7** (1969) 1399.
- [9] W. C. Roman, *IEEE Transactions on Plasma Science* **14**(4) (1986) 370.
- [10] R. Knight, R. W. Smith and D. Apelian, *International Materials Reviews* **36**(6) (1991) 221.
- [11] J. Pelloth, R. A. Brand and W. Keune, *J. Magn. Magn. Mater.* **140-144** (1995) 59.
- [12] W. E. Wallace, *J. Chem. Phys.* **41** (1964) 3857.

# APPENDIX 1

## CEMSN2 PROGRAM

```
PROGRAM CEMSN2
DIMENSION EB(20),ES(20),WB(20),WS(20)
C
C OPEN(UNIT=1,NAME='CEMS.RES',TYPE='NEW')
C
C
C CEMSN2 CALCULATES PHASE SIGNALS AND SIGNAL RATIOS FOR
C A NON-ENRICHED 57-FE CEMS ABSORBER WITH A BULK PHASE B
C AND A SURFACE PHASE S. THE FILE CEMS.RES IS USED FOR THE
C PRINT-OUT OF THE RESULTS.
C
C
C
C NORMALLY LOCKED PARAMETERS SPECIFIED:
C *****
C
C DX=INTEGRATION STEP LENGTH IN FEA
C AFE=ATTENUATION LENGTH=1/YFE, WHERE YFE IS THE RESONANCE
C COEFFICIENT OF IRON. AFE IS IN ANGSTROM.
C DENSF=DENSITY OF IRON, G/CM3.
C
AFE=30000.
CK=0.8
CL=0.1
CA=0.53
CX=0.27
CG=0.1
RBK=3200.
RBL=9100.
RBA=2100.
DENSF=7.86
DX=10.
C
PRINT 136
136 FORMAT(1H1,////,' CEMSN2',/, ' *****',///,
*' ANSWER 1 FOR YES',/,
*' DO YOU WISH TO MODIFY ANY OF THE',/,
*' AFE,CK,CL,CA,CX,CG,RBK,RBL,RBA,DX ?')
READ *,I
IF(I.NE.1)GO TO 10
PRINT 137,AFE,CK,CL,CA,CX,CG,RBK,RBL,RBA,DX
```

```

137 FORMAT(/,' PRESENT VALUES: ',/,
* F7.0,5F5.2,3F6.0,F5.0,/,
*' GIVE NEW VALUES:')
  READ *,AFE,CK,CL,CA,CX,CG,RBK,RBL,RBA,DX
10 YFE=1./AFE
  WRITE(1,138)AFE,CK,CL,CA,CX,CG,RBK,RBL,RBA,DX
138 FORMAT(1H1,///,' CEMSN2 RESULTS ',/, ' *****',////,
*' STANDARD PARAMETERS AFE,CK,CL,CA,CX,CG,RBK,RBL,RBA,DX=',/,
* F7.0,5F5.2,3F6.0,F5.0)
  WRITE (1,139)
139 FORMAT(1H1,///,' FLEXIBLE PARAMETERS: ',/, ' *****',
*/)
  PRINT 140
140 FORMAT(///,' GIVE THE FOLLOWING PARAMETERS: ',/)
C
C
C  READ FLEXIBLE PARAMETERS
C  *****
C
C  IQ=0
C  Q=0.
C
C  PRINT 114,Q
114 FORMAT(' EFF.DENS.57-FE REL. IRON, B PHASE=',F6.3)
  READ *,FENB
  WRITE(1,114)FENB
C
C  PRINT 115,Q
115 FORMAT(' EFF.DENS.57-FE REL. IRON, S PHASE=',F6.3)
  READ *,FENS
  WRITE(1,115)FENS
C
C  PRINT 116,Q
116 FORMAT(' RECOIL-FREE FRACTION IN B PHASE=',F6.3)
  READ *,FB
  WRITE(1,116)FB
C
C  PRINT 117,Q
117 FORMAT(' DENSITY(G/CM3) OF S PHASE=',F6.3)
  READ *,DENS
  WRITE(1,117)DENS
C
C  PRINT 118,Q
118 FORMAT(' X-RAY PHOTO-ATTENUATION LENGTH (FEA), B
PHASE=',F10.0)
  READ *,DXB
  WRITE(1,118)DXB
C
C  PRINT 119,Q

```

```

119 FORMAT(' X-RAY PHOTO-ATTENUATION LENGTH (FEA), S
PHASE=',F10.0)
  READ *,DXS
  WRITE(1,119)DXS
C
  PRINT 120,Q
120 FORMAT(' GAMMA PHOTO-ATTENUATION LENGTH (FEA), B
PHASE=',F10.0)
  READ *,DNRB
  WRITE(1,120)DNRB
C
  PRINT 121,Q
121 FORMAT(' GAMMA PHOTO-ATTENUATION LENGTH (FEA), S
PHASE=',F10.0)
  READ *,DNRS
  WRITE(1,121)DNRS
C
  PRINT 122,Q
122 FORMAT(' RANGE OF XPE ELECTRONS CREATED IN B PHASE
(FEA)=',F10.0)
  READ *,RXPEB
  WRITE(1,122)RXPEB
C
  PRINT 123,Q
123 FORMAT(' RANGE OF XPE ELECTRONS CREATED IN S PHASE
(FEA)=',F10.0)
  READ *,RXPES
  WRITE(1,123)RXPES
C
  PRINT 124,Q
124 FORMAT(' RANGE OF GPE ELECTRONS CREATED IN B PHASE
(FEA)=',F10.0)
  READ *,RGPEB
  WRITE(1,124)RGPEB
C
  PRINT 125,Q
125 FORMAT(' RANGE OF GPE ELECTRONS CREATED IN S PHASE
(FEA)=',F10.0)
  READ *,RGPEB
  WRITE(1,125)RGPEB
C
  PRINT 126,IQ
126 FORMAT(' NUMBER OF LINES IN THE B PHASE SPECTRUM=',I2)
  READ *,NB
  WRITE(1,126)NB
C
  PRINT 127,IQ
127 FORMAT(' NUMBER OF LINES IN THE S PHASE SPECTRUM=',I2)
  READ *,NS

```

```

WRITE(1,127)NS
C
PRINT 128,Q
128 FORMAT(' WIDTH OF ALL LINES=',F10.2,/)
READ *,WIDTH
WRITE(1,128)WIDTH
C
DO 20 J=1,NB
C
PRINT 129,J,Q
129 FORMAT(' POSITION OF LINE NO',I3,' IN B SPECTRUM=',F10.2)
READ *,EB(J)
WRITE(1,129)J,EB(J)
C
PRINT 130,J,Q
130 FORMAT(' WEIGHT OF LINE NO',I3,' IN B SPECTRUM=',F8.5)
READ *,WB(J)
WRITE(1,130)J,WB(J)
C
20 CONTINUE
C
DO 30 J=1,NS
C
PRINT 131,J,Q
131 FORMAT(' POSITION OF LINE NO',I3,' IN S SPECTRUM=',F10.2)
READ *,ES(J)
WRITE(1,131)J,ES(J)
C
PRINT 132,J,Q
132 FORMAT(' WEIGHT OF LINE NO',I3,' IN S SPECTRUM=',F6.3)
READ *,WS(J)
WRITE(1,132)J,WS(J)
C
30 CONTINUE
C
PRINT 133,Q
133 FORMAT(/,' EFFICIENCY OF DETECTOR=',F6.3)
READ *,EFF
WRITE(1,133)EFF
C
PRINT 134
134 FORMAT(' INCREMENT STEP IN S PHASE THICKNESS (ANGSTROM) ?')
READ *,DD
C
PRINT 135
135 FORMAT(' MAXIMUM S PHASE THICKNESS (ANGSTROM) ?')
READ *,DMAX
C
C

```

```

C PRELIMINARY CALCULATIONS
C *****
C
C
C WRITE(1,141)
141 FORMAT(1H1,///  

* ' *****',///  

C
C CALCULATE ABSORBTION COEFFICIENTS:
C
C YRB=FENB*YFE
C YRS=FENS*YFE
C YNRB=1./DNRB
C YNRS=1./DNRS
C YXB=1./DXB
C YXS=1./DXS
C DRB=1./YRB
C DRS=1./YRS
C
C WRITE(1,112)DRB
C WRITE(1,113)DRS
C
C 112 FORMAT(' RESONANCE ATTENUATION LENGTH (FEA), B
PHASE=',F10.1)
C 113 FORMAT(' RESONANCE ATTENUATION LENGTH (FEA), S
PHASE=',F10.1)
C
C CALCULATE OBB AND OBS
C
C DO 80 J=1,2
C IF(J.EQ.1)NP=NB
C IF(J.EQ.2)NP=NS
C
C SUM=0.
C DO 90 JS=1,NP
C DO 90 JB=1,NB
C IF(J.EQ.1)E=EB(JS)
C IF(J.EQ.1)W=WB(JS)
C IF(J.EQ.2)E=ES(JS)
C IF(J.EQ.2)W=WS(JS)
C EPS=(EB(JB)-E)/WIDTH
C TERM=WB(JB)*W/(1.+EPS**2)
C 90 SUM=SUM+TERM
C SUM=SUM/2.
C
C IF(J.EQ.1)OBB=SUM
C IF(J.EQ.2)OBS=SUM
C
C 80 CONTINUE

```

```

C
C  CALCULATE "AVERAGE" ABSORPTION COEFFICIENTS
C
YBAV=YNRB+YRB*OBB
YSAV=YNRS+YRS*OBS
C
DBAV=1./YBAV
DSAV=1./YSAV
C
WRITE(1,1081)DBAV
WRITE(1,1082)DSAV
C
1081 FORMAT(' AVERAGE ATTENUATION LENGTH (FEA) FOR RECOIL-
LESS',/,
*' B PHASE GAMMA IN THE B PHASE=',F10.1)
1082 FORMAT(' AVERAGE ATTENUATION LENGTH (FEA) FOR RECOIL-
LESS',/,
*' B PHASE GAMMA IN THE S PHASE=',F10.1)
C
WRITE(1,110)OBB
WRITE(1,111)OBS
C
110 FORMAT(' OVERLAP INTEGRAL OBB=',E10.5)
111 FORMAT(' OVERLAP INTEGRAL OBS=',E10.5)
C
C  CALCULATE THE K(Y) FUNCTION VALUES BIX=K(YXB),
BINR=K(YNRB)
C  AND BIAV=K(YBAV)
C
CHI1=YNRB/YRB
C
CHI2=YNRB/YXB
CALL ZIB(CHI1,CHI2,NB,WB,BIX)
C
CHI2=1.
CALL ZIB(CHI1,CHI2,NB,WB,BINR)
C
CHI2=YNRB/YBAV
CALL ZIB(CHI1,CHI2,NB,WB,BIAV)
C
WRITE(1,109)BIX,BINR,BIAV
109 FORMAT(' X-RAY INTEGRAL K(YXB)=',E10.5,/,
*' RECOILING GAMMA INTEGRAL K(YNRB)=',E10.5,/,
*' RECOIL-LESS GAMMA INTEGRAL K(YBAV)=',E10.5)
C
C  CALCULATE COEFFICIENTS AX, ANR AND AR
C
AX=CX*BIX
ANR=CG*((1.-FB)*BINR+FB*BIAV)

```

```

AR=CG*FB*BIAV
C
WRITE(1,107)AX,ANR,AR
107 FORMAT(' AX=',E10.5,/, ' ANR=',E10.5,/, ' AR=',E10.5)
C
C
C CALCULATE COEFFICIENTS AXS, AXB, ANRS, ANRB, ARS AND ARB
C
AXS=AX*YXS/YRB
AXB=AX*YXB/YRB
ANRS=ANR*YNRS/YRB
ANRB=ANR*YNRB/YRB
ARS=AR*OBS*YRS/YRB
ARB=AR*OBB
C
WRITE(1,104)AXS,AXB
WRITE(1,105)ANRS,ANRB
WRITE(1,106)ARS,ARB
C
104 FORMAT(///, ' AXS=',E10.5, ' AXB=',E10.5)
105 FORMAT(' ANRS=',E10.5, ' ANRB=',E10.5)
106 FORMAT(' ARS=',E10.5, ' ARB=',E10.5,///)
C
C CALCULATE U(INF) VALUES
C
X=-DX/2.
UE=0.
UXPEB=0.
UGPEB=0.
C
70 X=X+DX
TK=TFUNC(X,RBK)
TL=TFUNC(X,RBL)
TA=TFUNC(X,RBA)
TXPEB=TFUNC(X,RXPEB)
TGPEB=TFUNC(X,RGPEB)
TE=EFF*(CK*TK+CA*TA*(1.-EFF*TK)+CL*TL)
C
UE=UE+TE*DX
UXPEB=UXPEB+TXPEB*DX
UGPEB=UGPEB+TGPEB*DX
C
IF(TXPEB.NE.0.)GO TO 70
IF(TGPEB.NE.0.)GO TO 70
IF(TE.NE.0.)GO TO 70
C
UXINB=UXPEB*EFF
UGINB=UGPEB*EFF
UEIN=UE

```

```

C
WRITE(1,102)X
WRITE(1,103)UE,UXINB,UGINB
102 FORMAT(' MAXIMUM EFFECTIVE ELECTRON RANGE (FEA)=' ,F10.0)
103 FORMAT(' UE(INF)=' ,F10.1,/,
* ' UXPEB(INF)=' ,F10.1,/,
* ' UGPEB(INF)=' ,F10.1)
C
C MAIN LOOP. CALCULATE SIGNAL RATIOS.
C *****
C
WRITE(1,200)
PRINT 200
200 FORMAT(1H1,///,' RESULTS:!',/, ' *****',/,
*' D(A) S/(S+B) B/(S+B) S B UE UXPE UGPE UGCE',
*//)
C
D=0.
DFE=0.
X=-DX/2.
UE=0.
UXPES=0.
UXPEB=0.
UGPES=0.
UGPEB=0.
C
C RATIOS R1=S/(S+B) AND R2=B/(S+B) ARE OBTAINED FOR THE
C SURFACE LAYER THICKNESS = D ANGSTROM
C
60 SI=FENS*UE
UXPE=AXS*UXPES+AXB*(UXINB-UXPEB)
UGPE=ANRS*UGPES+ANRB*(UGINB-UGPEB)
UGCE=ARS*UE+ARB*(UEIN-UE)
ATC=1.-YSAV*DFE
BI=FENB*(UEIN-UE+ATC*(UXPE+UGPE+UGCE))
R1=SI/(SI+BI)
R2=1.-R1
C
WRITE(1,101)D,R1,R2,SI,BI,UE,UXPE,UGPE,UGCE
PRINT 101,D,R1,R2,SI,BI,UE,UXPE,UGPE,UGCE
101 FORMAT(F6.0,2F7.3,6F7.1)
C
D=D+DD
IF(D.GT.DMAX)GO TO 100
DFE=D*DENS/DENSF
C
C WEIGHT FUNCTION INTEGRATION:
C
50 X=X+DX

```

```

TK=TFUNC(X,RBK)
TL=TFUNC(X,RBL)
TA=TFUNC(X,RBA)
TXPES=TFUNC(X,RXPES)*EFF
TXPEB=TFUNC(X,RXPEB)*EFF
TGPES=TFUNC(X,RGPES)*EFF
TGPEB=TFUNC(X,RGPEB)*EFF
TE=EFF*(CK*TK+CA*TA*(1.-EFF*TK)+CL*TL)
C
UE=UE+TE*DX
UXPES=UXPES+TXPES*DX
UXPEB=UXPEB+TXPEB*DX
UGPES=UGPES+TGPES*DX
UGPEB=UGPEB+TGPEB*DX
C
IF(X.GE.DFE)GO TO 60
GO TO 50
C
100 PRINT 201
201 FORMAT(' RESULTS ARE PRINTED IN FILE "CEMS.RES".')
C
STOP
END
SUBROUTINE ZIB(CHI1,CHI2,NB,WB,B)
DIMENSION WB(20),BV(20)
C
C THIS SUBROUTINE CALCULATES THE K(Y) FUNCTION
C
C DT=INTEGRATION STEP LENGTH IN DEGREES.
C
DT=1.
PI=3.141593
PII=PI/2.
DT=DT*PI/180.
C
C
DO 20 N=1,NB
W=WB(N)
C
T=-DT/2.
SUM=0.
C
10 T=T+DT
IF(T.GE.PII)GO TO 30
C=(COS(T))**2
A=CHI1+W*C
B=1.+CHI2+(CHI2/CHI1)*W*C
B=ALOG(B)
TERM=B/A

```

```

SUM=SUM+TERM
GO TO 10
C
30 BV(N)=W*SUM*DT
C
20 CONTINUE
C
SUM=0.
DO 40 N=1,NB
40 SUM=SUM+BV(N)
B=SUM/PI
C
RETURN
END
FUNCTION TFUNC(DEPTH,RANGE)
C
C THIS IS A SPECIAL LINEAR INTERPOLATION FUNCTION BASED
C ON MONTE CARLO SIMULATED ELECTRON SCATTERING DATA.
C
DIMENSION P(15),PD(15)
C
C DEPTHS (FEA) USED IN THE SIMULATION:
C
PD(1)=0.
PD(2)=50.
PD(3)=100.
DO 4 ID=1,12
RID=ID
I=ID+3
4 PD(I)=200.*RID
C
C SIMULATED WEIGHT FUNCTION (TRANSMISSION) VALUES:
C
P(1)=0.764
P(2)=0.687
P(3)=0.641
P(4)=0.566
P(5)=0.449
P(6)=0.340
P(7)=0.246
P(8)=0.165
P(9)=0.106
P(10)=0.066
P(11)=0.038
P(12)=0.019
P(13)=0.012
P(14)=0.0045
P(15)=0.0022
C

```

```

C  PUT ON A GENERAL DEPTH SCALE
C
  DO 10 I=1,15
10 PD(I)=PD(I)/3200.
C
C  REDUCE GIVEN DEPTH TO THIS SCALE
C
  X=DEPTH/RANGE
C
  DO 1 I=1,14
  II=I+1
  Y=PD(I)
  Z=PD(II)
1 IF(X.GE.Y.AND.X.LT.Z)GO TO 2
  TFUNC=0.
  GO TO 3
2 TFUNC=P(I)+((X-Y)/(Z-Y))*(P(II)-P(I))
C
3 RETURN
  END

```

## APPENDIX 2

### CEMSN2 RESULTS

#### CEMSN2 RESULTS

\*\*\*\*\*

STANDARD PARAMETERS AFE,CK,CL,CA,CX,CG,RBK,RBL,RBA,DX=  
30000. 0.80 0.10 0.53 0.27 0.10 3200. 9100. 2100. 10.

#### FLEXIBLE PARAMETERS:

\*\*\*\*\*

EFF.DENS.57-FE REL. IRON, B PHASE= 0.720  
EFF.DENS.57-FE REL. IRON, S PHASE= 1.000  
RECOIL-FREE FRACTION IN B PHASE= 0.800  
DENSITY(G/CM3) OF S PHASE= 7.870  
X-RAY PHOTO-ATTENUATION LENGTH (FEA), B PHASE= 200000.  
X-RAY PHOTO-ATTENUATION LENGTH (FEA), S PHASE= 200000.  
GAMMA PHOTO-ATTENUATION LENGTH (FEA), B PHASE= 200000.  
GAMMA PHOTO-ATTENUATION LENGTH (FEA), S PHASE= 200000.  
RANGE OF XPE ELECTRONS CREATED IN B PHASE (FEA)= 2100.  
RANGE OF XPE ELECTRONS CREATED IN S PHASE (FEA)= 2100.  
RANGE OF GPE ELECTRONS CREATED IN B PHASE (FEA)= 3200.  
RANGE OF GPE ELECTRONS CREATED IN S PHASE (FEA)= 3200.  
NUMBER OF LINES IN THE B PHASE SPECTRUM= 1  
NUMBER OF LINES IN THE S PHASE SPECTRUM= 6  
WIDTH OF ALL LINES= 0.30

POSITION OF LINE NO 1 IN B SPECTRUM= -0.11  
WEIGHT OF LINE NO 1 IN B SPECTRUM= 1.00000  
POSITION OF LINE NO 1 IN S SPECTRUM= -5.48  
WEIGHT OF LINE NO 1 IN S SPECTRUM= 0.205  
POSITION OF LINE NO 2 IN S SPECTRUM= -3.21  
WEIGHT OF LINE NO 2 IN S SPECTRUM= 0.225  
POSITION OF LINE NO 3 IN S SPECTRUM= -0.96  
WEIGHT OF LINE NO 3 IN S SPECTRUM= 0.070  
POSITION OF LINE NO 4 IN S SPECTRUM= 0.70  
WEIGHT OF LINE NO 4 IN S SPECTRUM= 0.070  
POSITION OF LINE NO 5 IN S SPECTRUM= 2.93  
WEIGHT OF LINE NO 5 IN S SPECTRUM= 0.225  
POSITION OF LINE NO 6 IN S SPECTRUM= 5.16  
WEIGHT OF LINE NO 6 IN S SPECTRUM= 0.205

EFFICIENCY OF DETECTOR= 1.000

CALCULATED PARAMETERS:

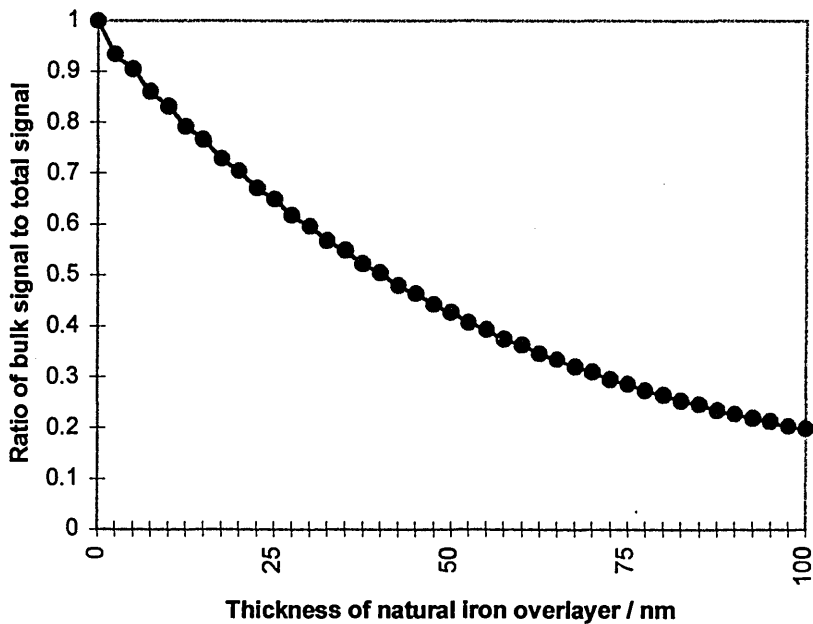
\*\*\*\*\*

RESONANCE ATTENUATION LENGTH (FEA), B PHASE= 41666.7  
RESONANCE ATTENUATION LENGTH (FEA), S PHASE= 30000.0  
AVERAGE ATTENUATION LENGTH (FEA) FOR RECOIL-LESS  
B PHASE GAMMA IN THE B PHASE= 58823.5  
AVERAGE ATTENUATION LENGTH (FEA) FOR RECOIL-LESS  
B PHASE GAMMA IN THE S PHASE= 186477.1  
OVERLAP INTEGRAL OBB=.50000E+00  
OVERLAP INTEGRAL OBS=.10878E-01  
X-RAY INTEGRAL K(YXB)=.11317E+01  
RECOILING GAMMA INTEGRAL K(YNRB)=.11317E+01  
RECOIL-LESS GAMMA INTEGRAL K(YBAV)=.50204E+00  
AX=.30555E+00  
ANR=.62796E-01  
AR=.40163E-01

AXS=.63657E-01 AXB=.63657E-01  
ANRS=.13083E-01 ANRB=.13083E-01  
ARS=.60678E-03 ARB=.20082E-01

MAXIMUM EFFECTIVE ELECTRON RANGE (FEA)= 6825.  
UE(INF)= 598.2  
UXPEB(INF)= 312.2  
UGPEB(INF)= 475.7

**Plot of Output Results for Natural Iron Deposited on a Type 304 Stainless Steel**



## RESULTS:

\*\*\*\*\*

D(A)	S/(S+B)	B/(S+B)	S	B	UE	UXPE	UGPE	UGCE
0.	0.000	1.000	0.0	458.1	0.0	19.9	6.2	12.0
25.	0.065	0.935	30.5	435.7	30.5	19.9	6.2	11.4
50.	0.096	0.904	45.2	424.9	45.2	19.9	6.2	11.1
75.	0.140	0.860	66.7	409.2	66.7	19.9	6.2	10.7
100.	0.168	0.832	80.6	398.9	80.6	19.9	6.2	10.4
125.	0.208	0.792	101.1	383.9	101.1	19.9	6.2	10.0
150.	0.234	0.766	114.4	374.1	114.4	19.9	6.2	9.8
175.	0.271	0.729	134.0	359.8	134.0	19.9	6.2	9.4
200.	0.295	0.705	146.7	350.4	146.7	19.9	6.2	9.2
225.	0.329	0.671	165.4	336.7	165.4	19.9	6.2	8.8
250.	0.351	0.649	177.5	327.8	177.5	19.9	6.2	8.6
275.	0.383	0.617	195.3	314.7	195.3	19.9	6.2	8.2
300.	0.403	0.597	206.9	306.2	206.9	19.9	6.2	8.0
325.	0.432	0.568	223.8	293.8	223.8	19.9	6.2	7.7
350.	0.451	0.549	234.8	285.7	234.8	19.9	6.2	7.4
375.	0.478	0.522	250.8	274.0	250.8	19.9	6.2	7.1
400.	0.495	0.505	261.2	266.4	261.2	19.9	6.2	6.9
425.	0.520	0.480	276.3	255.3	276.3	19.9	6.2	6.6
450.	0.536	0.464	286.1	248.1	286.1	19.9	6.2	6.4
475.	0.558	0.442	300.3	237.7	300.3	19.9	6.2	6.2
500.	0.573	0.427	309.4	230.9	309.4	19.9	6.2	6.0
525.	0.593	0.407	322.7	221.2	322.7	19.9	6.2	5.7
550.	0.607	0.393	331.3	214.9	331.3	19.9	6.2	5.6
575.	0.626	0.374	343.7	205.8	343.7	19.9	6.2	5.3
600.	0.638	0.362	351.7	199.9	351.7	19.9	6.2	5.2
625.	0.655	0.345	363.2	191.5	363.2	19.9	6.2	4.9
650.	0.666	0.334	370.6	186.1	370.6	19.9	6.2	4.8
675.	0.681	0.319	381.2	178.2	381.2	19.9	6.2	4.6
700.	0.691	0.309	388.1	173.2	388.1	19.9	6.2	4.5
725.	0.706	0.294	398.0	165.9	398.0	19.9	6.2	4.3
750.	0.715	0.285	404.3	161.3	404.3	19.9	6.2	4.1
775.	0.728	0.272	413.4	154.6	413.4	19.9	6.2	4.0
800.	0.736	0.264	419.2	150.4	419.2	19.9	6.2	3.8
825.	0.748	0.252	427.5	144.2	427.5	19.9	6.2	3.7
850.	0.755	0.245	432.8	140.3	432.8	19.9	6.2	3.6
875.	0.766	0.234	440.5	134.7	440.5	19.9	6.2	3.4
900.	0.773	0.227	445.4	131.1	445.4	19.9	6.2	3.3
925.	0.782	0.218	452.4	126.0	452.4	19.9	6.2	3.2
950.	0.788	0.212	456.9	122.7	456.9	19.9	6.2	3.1
975.	0.797	0.203	463.2	118.0	463.2	19.9	6.2	3.0
1000.	0.802	0.198	467.2	115.1	467.2	19.9	6.2	2.9

## APPENDIX 3

### FORTRAN PROGRAM USED FOR SOLVING THE DIFFUSION PROBLEM

```
C Numerical analysis of a diffusion problem using
C the explicit method
C F(I) - concentration at time torr
C G(I) - concentration at time torr + delta torr
DIMENSION F(200)
DIMENSION G(200)
WRITE(6,10)
10 FORMAT(' INPUT THE NUMBER OF INTERVALS')
READ(5,*)X
WRITE(6,20)
20 FORMAT(' INPUT THE NUMBER OF INTERVALS UPTO THE INTERFACE')
READ(5,*)K
DO 1 I=1,X
  IF(I.LE.K) THEN
    F(I)=1
  ELSE
    F(I)=0
  END IF
1 CONTINUE

WRITE(6,30)
30 FORMAT(' INPUT THE NUMBER OF ITERATIONS')
READ(5,*)Y
40 SUM=0
DO 2 I=2,X
  G(I)=.25*(F(I+1)-2*F(I)+F(I-1))+F(I)
  SUM=SUM+G(I)
2 CONTINUE
G(1)=(.025*K-SUM)
Y=Y-1
IF(Y.EQ.0) THEN
  GO TO 50
  ELSE
    DO 3 I=1,X
      F(I)=G(I)
3 CONTINUE
  GO TO 40
END IF
50 OPEN(10,FILE='DATF',STATUS='OLD')
DO 4 I=1,X
  WRITE(6,60)I,G(I)
60 FORMAT(' FOR INTERVAL ',I3,5X,' FRACTIONAL CONC=',F6.3)
  WRITE(10,70)I,G(I)
70 FORMAT(I3,10X,F6.5)
4 CONTINUE
CLOSE(10)
END
```

## APPENDIX 4

### PUBLICATIONS

*Studies of PVD Interfaces Generated by Ti Ions in a Steered Arc Discharge*

J. L. Davidson, J. S. Brooks, S. D. Forder and W. -D. Münz

*Surf. Coat. Technol.* (1997) accepted and scheduled for Vol. **101(2)**.

*A Mössbauer Spectroscopy Study of Ti-Fe Interfaces Generated by the PVD Process*

J. S. Brooks, J. L. Davidson, S. D. Forder, W -D. Münz and M. Larsson

*Thin Solid Films* (1997) accepted and scheduled for Vol. **312(1-2)**.

# STUDIES OF PVD INTERFACES GENERATED BY Ti IONS IN A STEERED ARC DISCHARGE

J. L. Davidson\*, J. S. Brooks, S. D. Forder and W.-D. Münz

\* School of Science, Sheffield Hallam University, Sheffield S1 1WB, U.K.

Materials Research Institute, Sheffield Hallam University, Sheffield S1 1WB, U.K.

The deposition of ceramic coatings of the type TiC/N on steels enhances the surface properties of the coated substrate. A critical stage in the ABS<sup>TM</sup> process, using the combined steered arc and unbalanced magnetron, is the titanium ion etch which improves the adhesion of the TiN coating to the substrate. Conversion electron Mössbauer spectroscopy (CEMS) has given evidence that the ion etch pretreatment involves the formation of phases including FeTi at a narrow interface region. To detect these phases it has been necessary to enrich substrates with the Mössbauer isotope <sup>57</sup>Fe.

The enriched <sup>57</sup>Fe substrates have been treated by a range of ion etch processes and then characterised by CEMS. The role of the FeTi in improving coating-substrate adhesion is not fully understood but current work is using XTEM, SNMS, AES etc. with CEMS to gain an understanding of the mechanisms involved.

# STUDIES OF PVD INTERFACES GENERATED BY Ti IONS IN A STEERED ARC DISCHARGE

J. L. Davidson\*, J. S. Brooks, S. D. Forder and W.-D. Münz

\* School of Science, Sheffield Hallam University, Sheffield S1 1WB, U.K.  
Materials Research Institute, Sheffield Hallam University, Sheffield S1  
1WB, U.K.

## INTRODUCTION

In recent years physical vapour deposition (PVD) methods have found widespread application in the deposition of hard ceramic coatings, e.g. TiN, TiCN and TiAlN. These coating methods include conventional and unbalanced magnetron sputtering, arc and electron beam evaporation. The coatings are extensively used to improve the friction and corrosion resistance and hardness of surfaces used for cutting and related applications. However, the details of the formation, structure and composition of relatively simple system layers, e.g. TiN, are not yet fully understood.

One of the most significant prerequisites for a high performance coating is good adhesion at the interface between the coating and the substrate material. The strength of this adhesion is dependent on the physical and chemical interactions between the coating and the substrate material. Poor adhesion has been attributed to poor interfacial contact, high compressive stress within the coating and a low degree of chemical bonding [1]. Therefore, the interface structure plays a significant role in determining the adhesive strength of the coating-substrate system. Hence it is of great importance to improve the understanding of the correlation between the interface structure and its related adhesion.

The Arc Bond Sputtering (ABS™) process has been shown to produce dense coatings having superior adhesion [2] compared with other competitive deposition methods. The essential difference offered by the ABS™ process is the etching pre-treatment of substrates with metal ions e.g. titanium ions. This pre-treatment process generates a graded interface consisting of a recrystallization zone extending down as far as 160 nm into the substrate [3].

In this study, conversion electron  $^{57}\text{Fe}$  Mössbauer spectroscopy (CEMS) [4] has been used to seek an understanding of the effect of the titanium ion etch treatment of steel substrates. Similar studies have used CEMS to investigate the interfaces of ceramic coatings deposited by PVD on iron [5]. However this process did not involve a metal ion etch stage. Unlike sputter depth profiling, CEMS is a non-destructive technique and does not involve the risk of modifying the original phase composition close to the interface. The technique detects resonantly excited conversion electrons and provides a distinction between iron-containing chemical environments within an information depth up to 300 nm. However, to detect a phase formation of a thickness in the order of nanometres, it has been necessary to enrich the near surface region of the mild steel substrates with the Mössbauer isotope  $^{57}\text{Fe}$ .

## **EXPERIMENTAL**

The substrates of bright mild steel (BS:1983:080A15) were polished to  $R_a \approx 0.05 \mu\text{m}$ . The substrates were ultrasonically cleaned in both industrial methylated spirit and acetone prior to the deposition of an estimated 25 nm  $^{57}\text{Fe}$  layer by evaporation under vacuum at  $2 \times 10^{-7}$  torr. Two  $^{57}\text{Fe}$  enriched substrates were annealed at 900 K for 90

minutes under argon in sealed fused silica ampoules, with polished titanium pieces acting as oxygen scavengers. A diffusion model [6] was used to predict the depth distribution of the  $^{57}\text{Fe}$  as a function of annealing parameters. The model was solved numerically by a standard iterative net method for a deposited 25 nm  $^{57}\text{Fe}$  layer as shown in Fig. 1. Verification of the thickness of the deposited  $^{57}\text{Fe}$  layer and the depth distribution of the  $^{57}\text{Fe}$  after annealing was provided by a VG microlab SIMS facility. Operating in the dynamic SIMS mode, depth profiles were obtained for the selected species using 4 keV  $\text{Ar}^+$  ions with a beam current in the range 200-400 nA. Diffusion of the  $^{57}\text{Fe}$  into the surface region was required for substrates that receive a typical 10 minute industrial Ti ion etch treatment. Without diffusion, the  $^{57}\text{Fe}$  would be removed by the surface sputtering generated by the etch process. Two samples, enriched in this way, were given different ion etch treatments at an Ar pressure of  $3 \times 10^{-3}$  mbar using a Hauzer HTC 1000-4 ABS<sup>TM</sup> chamber. The first sample was ion etched in an  $\text{Ar}^+$  plasma at 150 V and the second sample was Ti ion etched at a substrate bias voltage of 1200 V. In both experiments a thin Ti layer was then deposited at a bias voltage of 80 V. Three fold rotation was used throughout and the maximum temperature was 450 °C.

In further experiments, samples were used with an estimated 25 nm of  $^{57}\text{Fe}$  deposited on the surface. Samples were enriched in this way because for shorter Ti ion etch processes that were used,  $^{57}\text{Fe}$  removal is not as severe compared with longer etch processes. This enables  $^{57}\text{Fe}$  enrichment to be enhanced in the depth of interest. Ti ion etch treatments were performed under different residual Ar pressures at a substrate bias voltage of 1200 V. These experiments were performed for 45 seconds with no

substrate rotation and in order to sustain the arc at the lower gas pressure it was necessary to have the target shutter only half open. Further Ti ion treatments using similarly prepared samples were performed at the same bias voltage at an Ar pressure of  $7 \times 10^{-4}$  mbar for different lengths of time, 25 s and 300 s, using 3-fold substrate rotation. In all the Ti ion etch treatment processes the maximum temperature was 450 °C.

All of the treated samples were analysed by CEMS using a conventional constant acceleration mode Mössbauer spectrometer. The detection system comprised of a gas flow proportional counter using He/5% CH<sub>4</sub> [5]. The <sup>57</sup>CoRh Mössbauer source used was of 25 mCi initial activity. The Mössbauer spectra were fitted by a least squares Lorentzian fitting routine using a Silicon Graphics Indy workstation.

## **RESULTS AND DISCUSSION**

When observing CEM spectra it is usual to refer to the percent effect for each phase, as an indication of the amount of Fe-57 present in the different phases. The CEM spectrum of the annealed sample, Fig. 2(b), shows that no oxidation has taken place during the annealing. Although the signal has decreased relative to that of Fe-57 deposited on the sample prior to annealing, Fig. 2(a), the signal is enhanced compared to that of an unenriched mild steel, resulting in increased surface sensitivity.

The thickness of the deposited Fe-57 layer has been confirmed by dynamic SIMS, Fig. 3(a), and calibrating Talysurf measurements. After annealing, the dynamic SIMS shows that the level of Fe-57 has been increased above the natural level of 2.2% to a

depth of the order of 100 nm, Fig. 3(b). This result is consistent with the depth predicted by the diffusion model, Fig. 1.

The CEM spectra of the samples comparing the effects of Ar and Ti ion etching are shown in Fig. 4(a) and 4(b). Comparison of the percent effect for each etch process shows that the sample that has had a Ti ion etch treatment, Fig. 4(b), has a reduced percent effect due to the severity of the metal multi-ionised ion etch. In addition the formation of FeTi phase can be seen. A further CEM spectrum was obtained for this sample at a lower velocity range in order to improve the resolution in the region of interest, Fig. 5. From this spectrum it can be seen that both the amorphous and crystalline phase are present. The hyperfine parameters associated with these phases are given in Table 1. There is good agreement with the measurements of Chien and Liou [7].

The CEM spectra showing the comparison of the Ti etch under differing residual gas pressures, Fig. 6(a) and (b), show the formation of iron carbonitride and low levels of magnetite,  $\text{Fe}_3\text{O}_4$  ( $H_{\text{eff}} = 477$  and  $442$  kG for sites A and B). The formation of these phases is due to the sputtering of surface debris from the shutter, and redeposition on to the samples. The percent effect for samples where the etch was carried out at a lower gas pressure is 41% compared with 50% for the etch at a higher gas pressure. This indicates that more Fe-57 has been removed from the surface when a lower gas pressure is used, showing the greater effect of the Ti ion etch under these conditions.

The CEM spectra of the two samples Ti ion etched for different lengths of time are shown in Fig. 7(a) and 7(b). For the 25 s Ti ion etch the presence of magnetite and a low level of FeTi interaction is seen, Fig 7(a). By contrast the 300 s Ti ion etch shows the removal of the magnetite phase and a more significant formation of both amorphous and crystalline FeTi phases, Fig 7(b).

## **SUMMARY**

Improved surface sensitivity of the CEMS technique can be achieved either by Fe-57 deposition, or deposition and annealing, chosen to suit the nature of subsequent experiments in the coating chamber.

It has been possible to use CEMS to detect and identify phases formed by various ion etch processes. The results indicate that oxides and carbonitrides, that can be formed during the initial stages of the Ti ion etch process, are removed after longer etch processes.

After a longer Ti ion etch a significant formation of amorphous and crystalline FeTi occurs. However the role of the FeTi phase in the adhesion of surface ceramic coatings requires further investigation.

## **ACKNOWLEDGEMENTS**

We acknowledge the work of Mr Kevin Blake of the Materials Research Institute at Sheffield Hallam University, for obtaining the SIMS spectra.

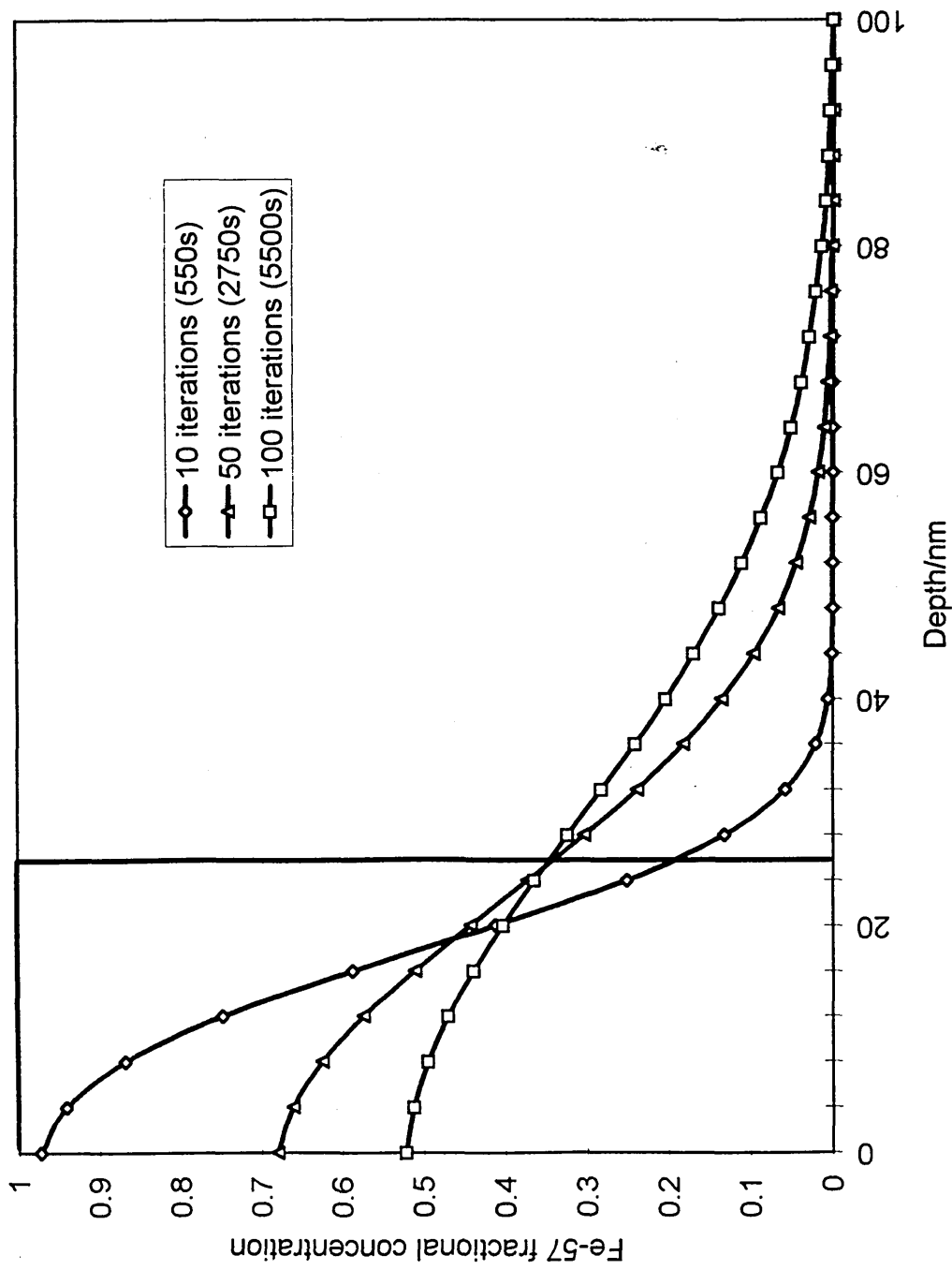
## REFERENCES

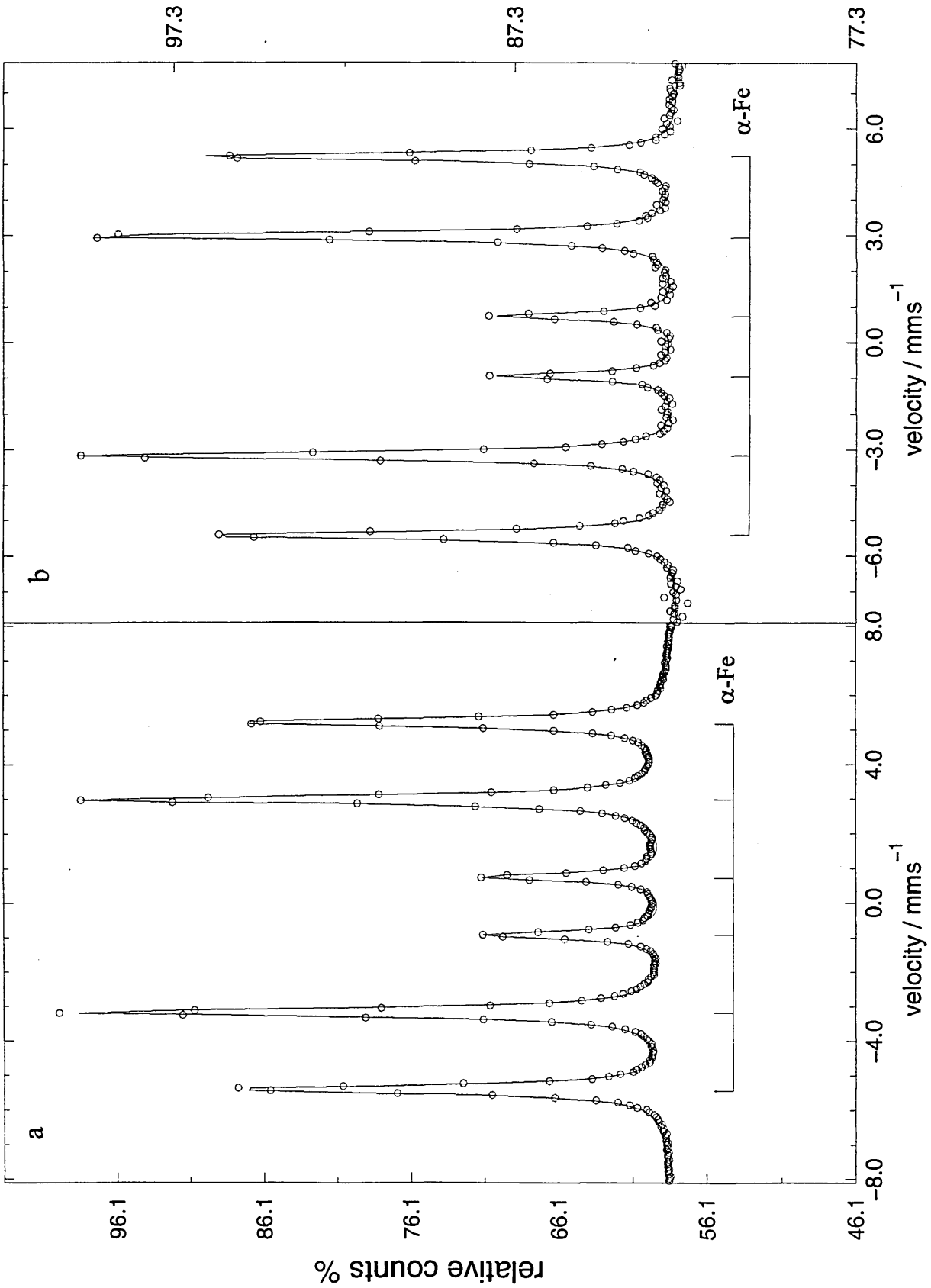
- [1] C. C. Cheng, A. Erdermir and G. R. Fenske, *Surf. Coat. Technol.* **39/40** (1989) 365.
- [2] W. -D. Münz, J. F. M. Hauzer, D. Schulze and B. Buil, *Surf. Coat. Technol.* **49** (1991) 161-167.
- [3] G. Häkansson, L. Hultmann, J. -E. Sundgren, J. E. Greene and W. -D. Münz, *Surf. Coat. Technol.* **48** (1991) 51-67.
- [4] J. A. Sawicki, *Mat. Sci Eng.* **69** (1985) 501-517.
- [5] D. Hanzel, W. Meisel, D. Hanzel, P. Griesbach, B. Navinsek, P. Panjan and P. Gütlich, *J. Vac. Sci. Technol. A* **11(6)** (1993) 3034.
- [6] J. S. Brooks and S. C. Thorpe, *Hyp. Int.* **47** (1989) 159-178.
- [7] C. L. Chien and S. H. Liou, *Phys. Rev. B* **31(12)** (1985) 8238-8241.

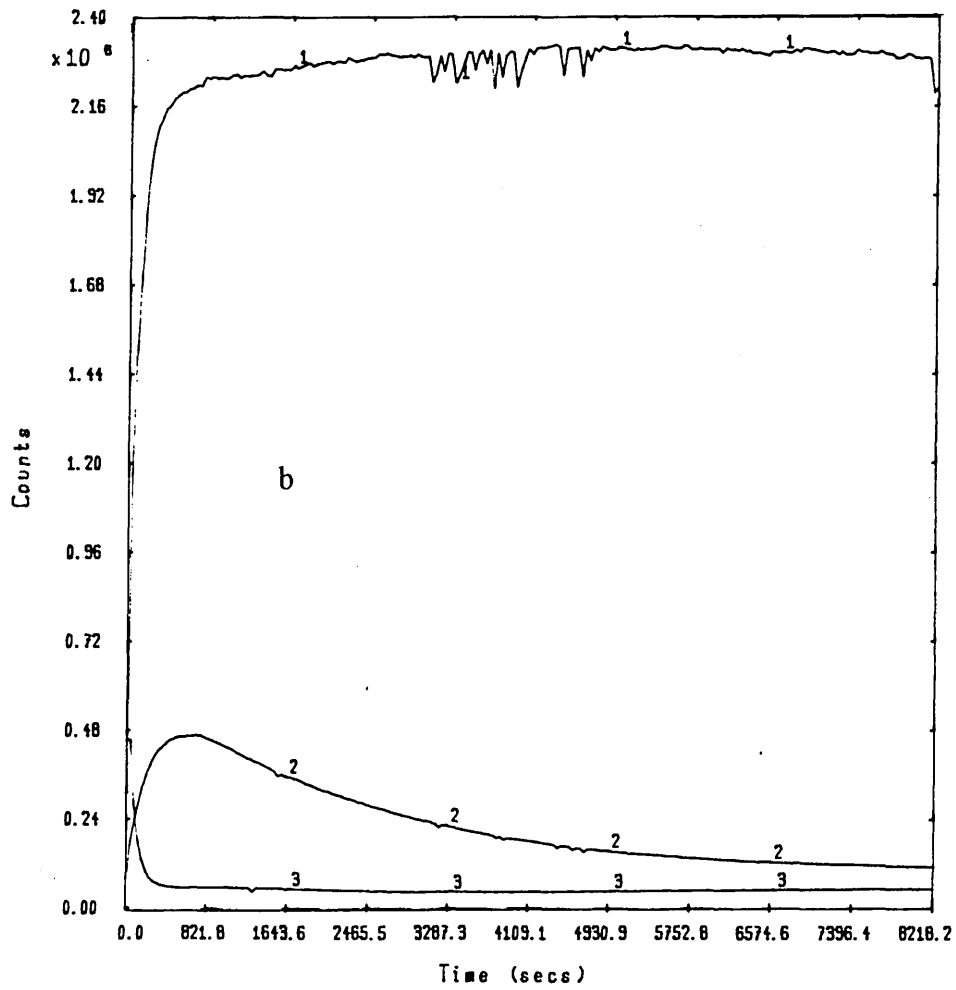
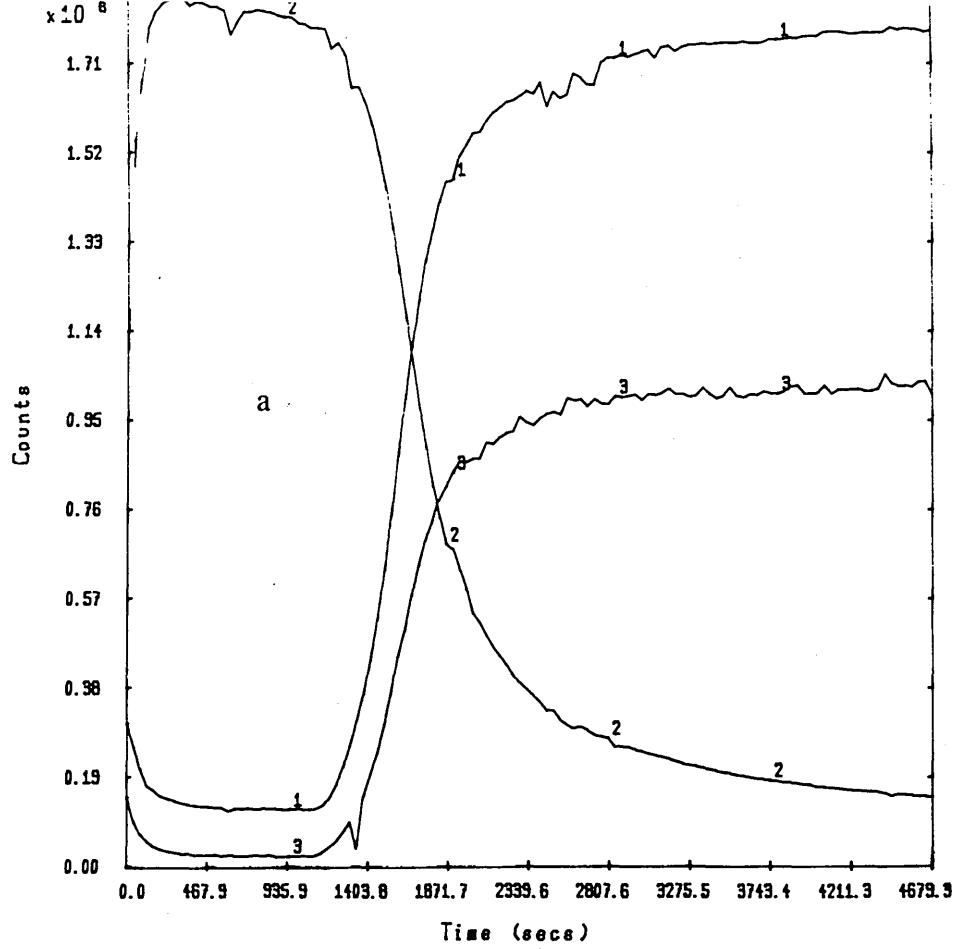
IS / mm s <sup>-1</sup>	QS / mm s <sup>-1</sup>	H <sub>eff</sub> / kG	Γ/2 / mm s <sup>-1</sup>	Phase
0.00	-	330	0.12	α-Fe
-0.16	0.34	-	0.18	FeTi-a
-0.15	-	-	0.22	FeTi-c

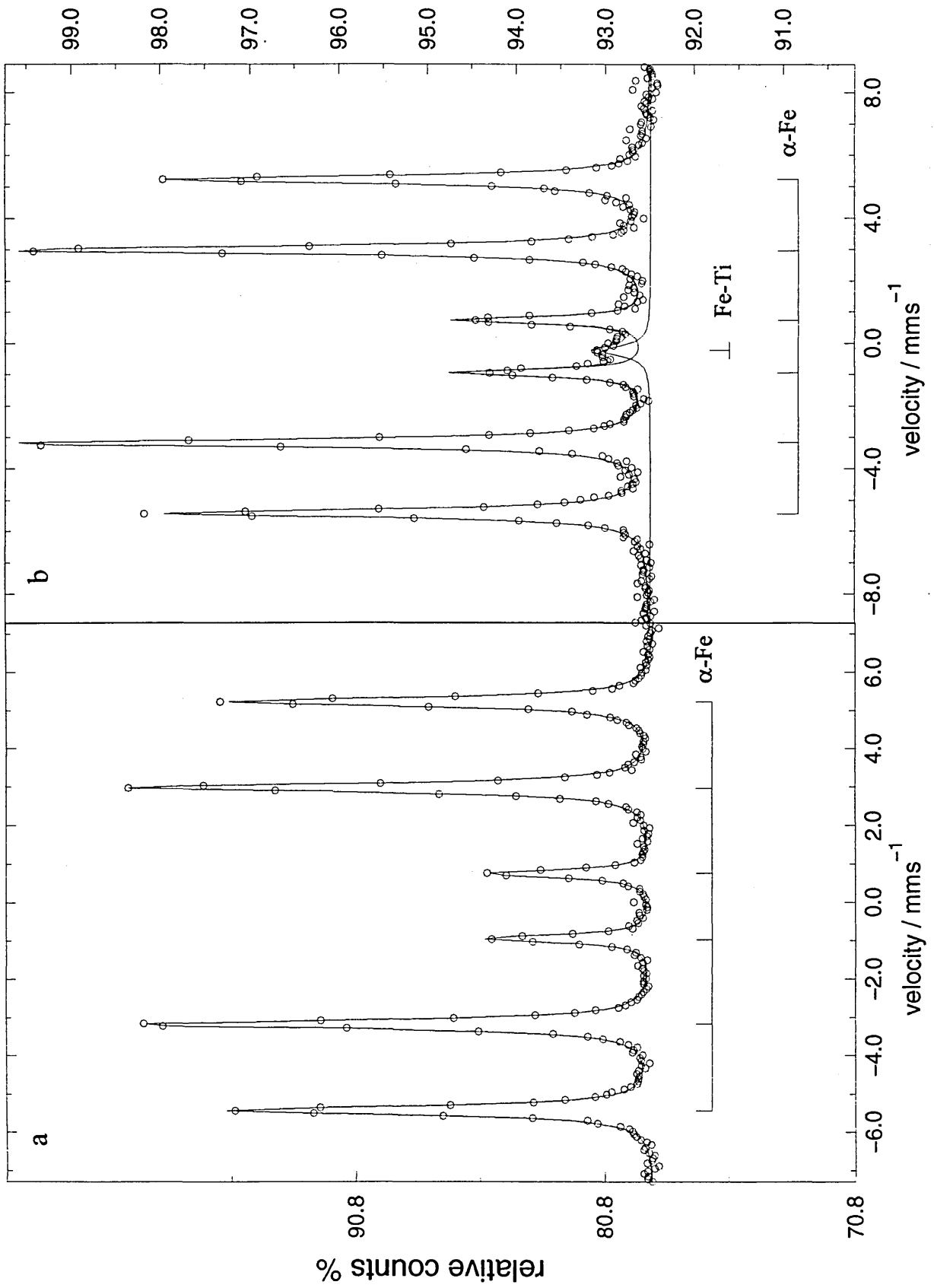
Table 1 Hyperfine parameters relative to α-Fe of the phases present after a Ti ion pre-treatment followed by the deposition of a thin Ti layer.

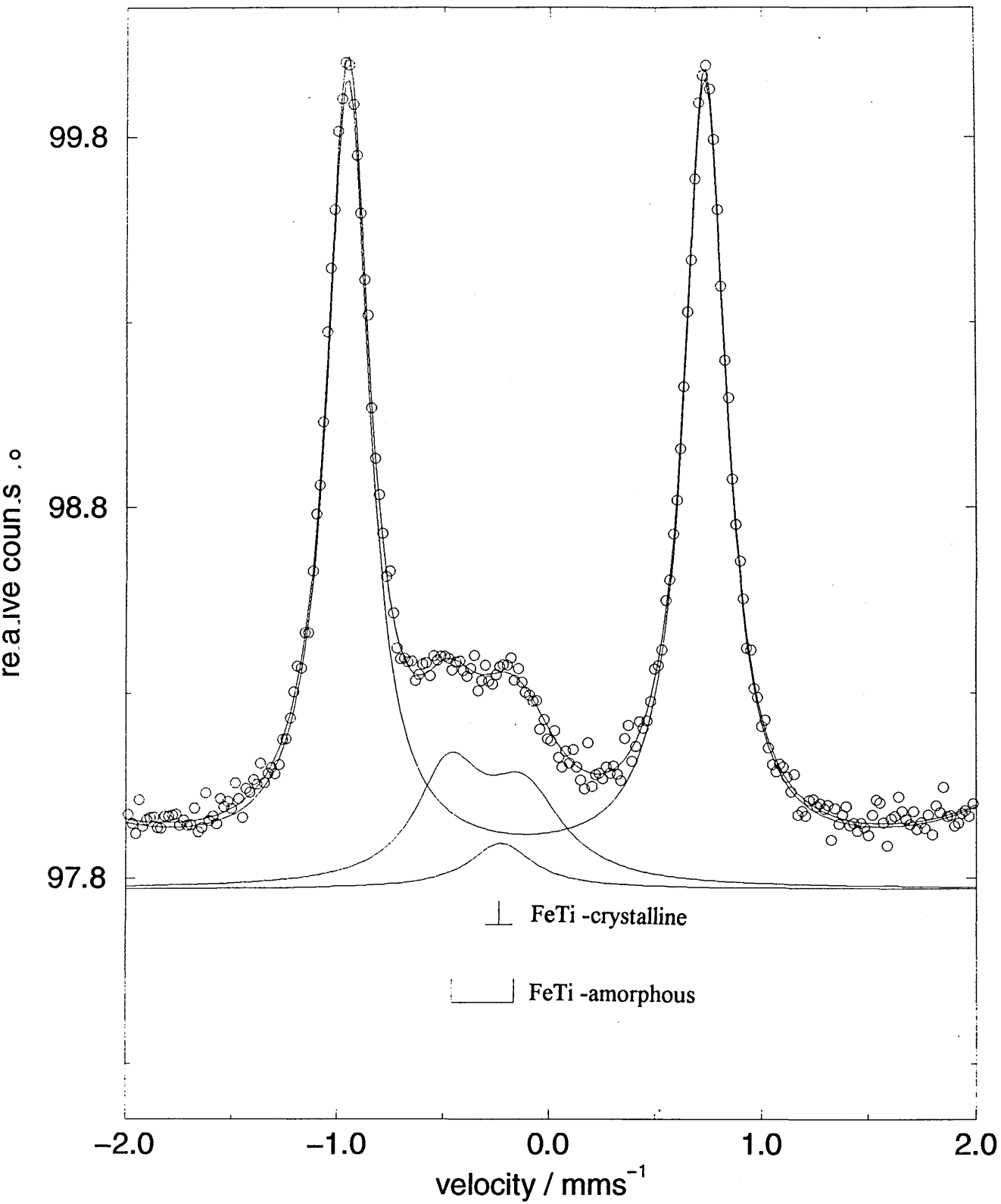
- Fig. 1 Fractional concentration of  $^{57}\text{Fe}$  as a function of depth for a mild steel annealed at 900 K.
- Fig. 2 Comparison of  $^{57}\text{Fe}$  enrichment - (a) deposited and (b) after annealing.
- Fig. 3 Dynamic SIMS of (a)  $^{57}\text{Fe}$  deposited and (b) after annealing.  
1 - Fe56, 2 - Fe 57 and 3 - Mn.
- Fig. 4 CEM spectra of (a) Ar ion etch followed by the deposition of a thin Ti layer and (b) Ti ion etch followed by the deposition of a thin Ti layer.
- Fig. 5 CEM spectrum of Ti ion etch followed by the deposition of a thin Ti layer - lower velocity range.
- Fig. 6 Comparison of Ti ion etch performed under different Ar gas pressures - (a)  $6 \times 10^{-5}$  and (b)  $3 \times 10^{-3}$  mbar.
- Fig. 7 Comparison of Ti ion etch for different times - (a) 25 s and (b) 300 s.

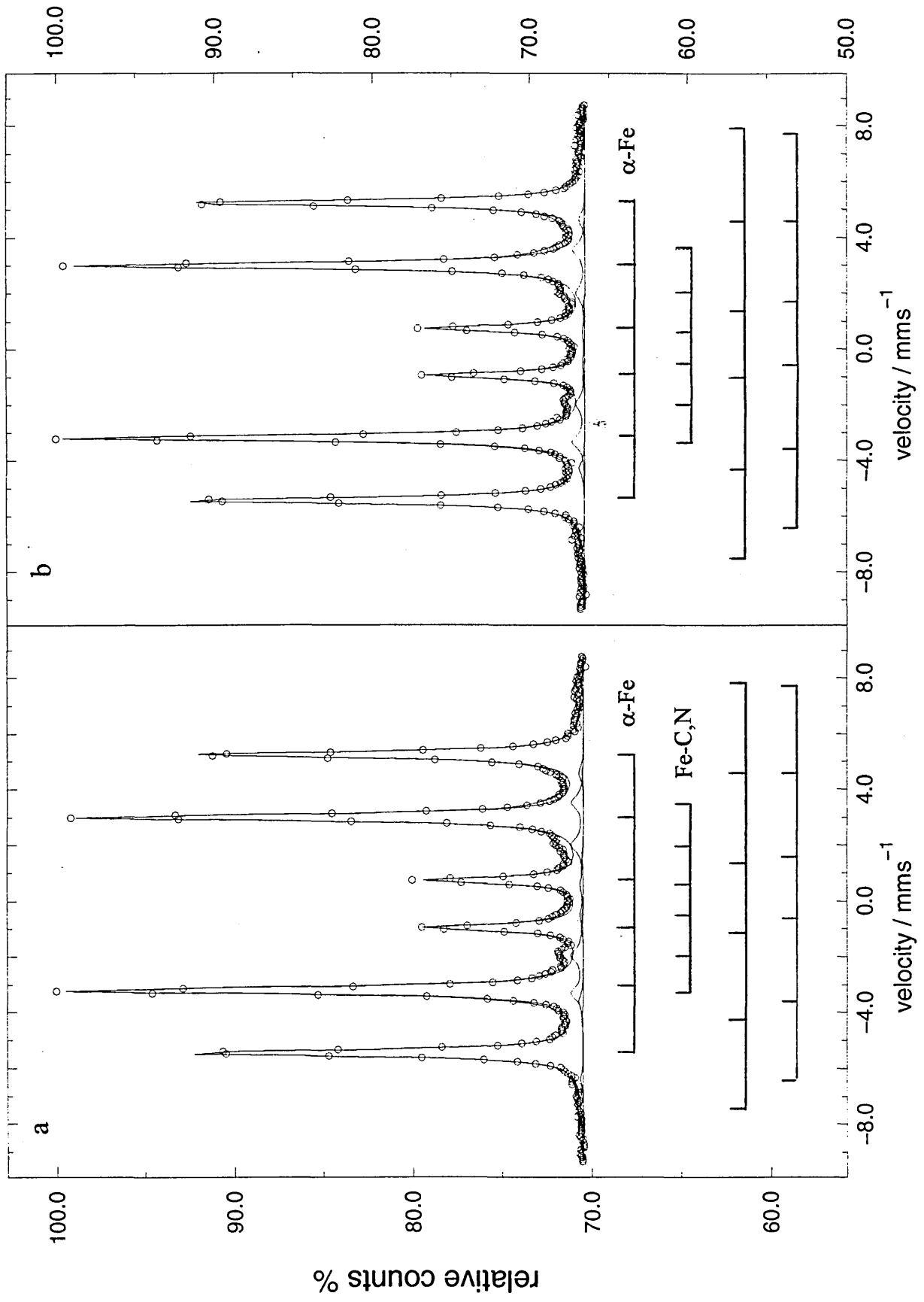


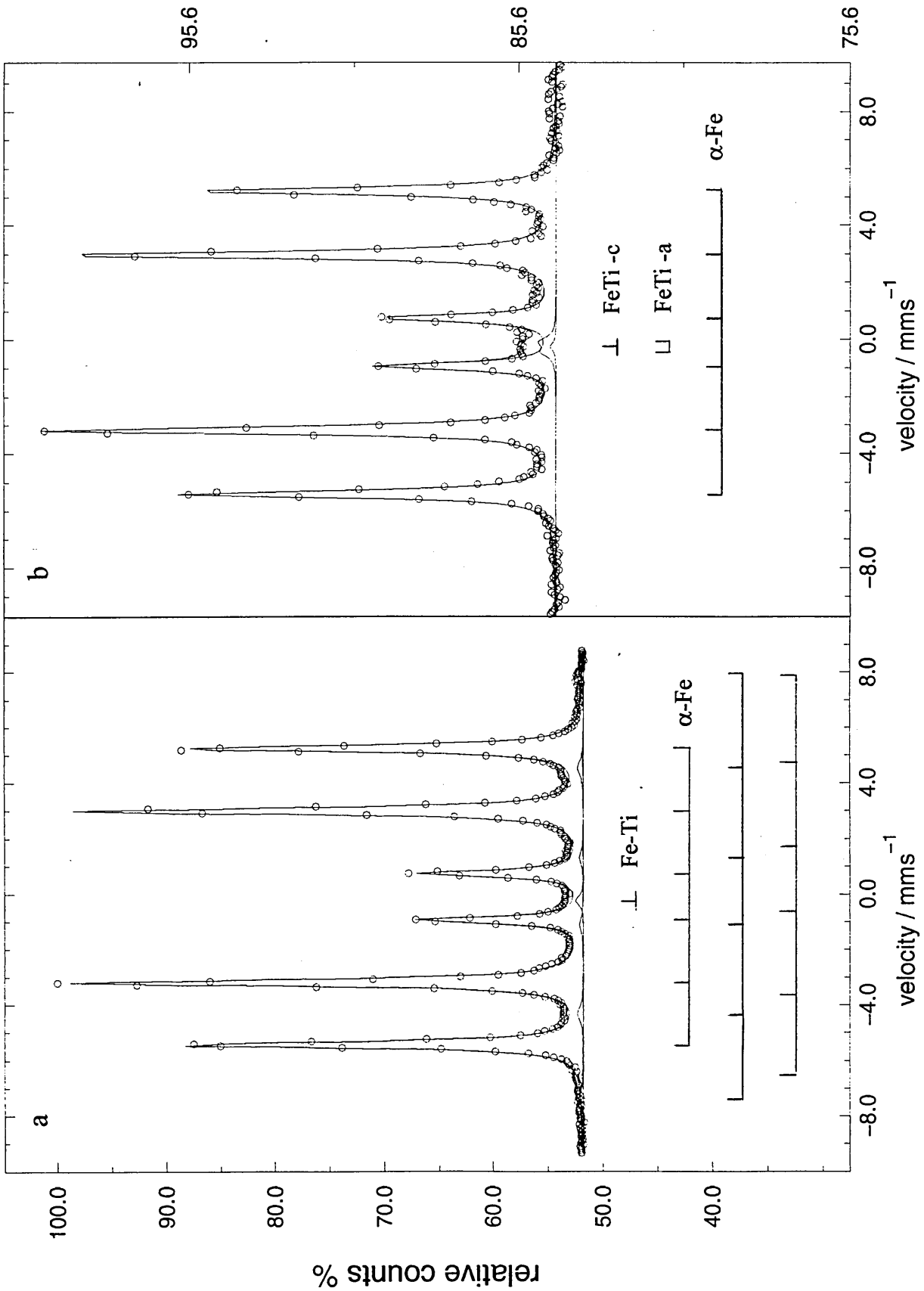












## A Mössbauer Spectroscopy Study of Ti-Fe Interfaces Generated by the PVD Process

J. S. Brooks<sup>a</sup>, J. L. Davidson<sup>b</sup>, S. D. Forder<sup>a</sup>, W.-D. Münz<sup>a</sup> and M. Larsson<sup>c</sup>

<sup>a</sup>Materials Research Institute, Sheffield Hallam University, Sheffield S1 1WB, U.K.

<sup>b</sup>School of Science and Mathematics, Sheffield Hallam University, Sheffield S1 1WB, U.K.

<sup>c</sup>Department of Materials Science, Materials Science Division Box 534, University of Uppsala, S-751 21 Uppsala, Sweden.

The deposition of hard coatings of the type TiC/N on steels enhances the surface properties of the coated substrate. Steel substrates have been pre-treated by the Arc Bond Sputtering process (ABS<sup>TM</sup>), which uses a combined steered arc and unbalanced magnetron arrangement. A critical stage of the ABS<sup>TM</sup> process is the titanium ion etch which improves the adhesion of the TiN coating to the substrate. This work uses conversion electron Mössbauer spectroscopy (CEMS) to study the phase formations in the near surface region of mild steel substrates after various Ti ion etch pre-treatments using the steered arc discharge within the ABS<sup>TM</sup> process. The work has also investigated a second method using a Balzers BAI 640R coating unit. Appropriate enrichment using the Mössbauer isotope <sup>57</sup>Fe has been used, enhancing the interfacial sensitivity of the CEMS technique to detect and identify phases formed by various ion etch processes. The results for the ABS<sup>TM</sup> pre-treatments indicate that oxides and carbonitrides that may be formed during the initial stages of the Ti ion etch, are removed after a longer etch. For a conventional 10 minute Ti ion etch pre-treatment a significant formation of both a crystalline FeTi and a Ti rich amorphous phase occurs. The existence of the crystalline phase has also been confirmed by X-ray diffraction. For comparison, samples that had been pre-treated and coated in the Balzers process show some evidence of the FeTi amorphous phase and the development of an iron carbonitride, often identified as  $\epsilon$ -Fe<sub>2-3</sub>(CN).

# A MÖSSBAUER SPECTROSCOPY STUDY OF Ti-Fe INTERFACES PRODUCED BY THE PVD PROCESS

J. S. Brooks<sup>a</sup>, J. L. Davidson<sup>b</sup>, S. D. Forder<sup>a</sup>, W.-D. Münz<sup>a</sup> and M. Larsson<sup>c</sup>

<sup>a</sup> Materials Research Institute, Sheffield Hallam University, Sheffield S1 1WB, U.K.

<sup>b</sup> School of Science and Mathematics, Sheffield Hallam University, Sheffield S1 1WB, U.K.

<sup>c</sup> University of Uppsala, Department of Materials Science, Materials Science Division  
Box 534, S-751 21 Uppsala, Sweden.

## INTRODUCTION

Physical Vapour Deposition (PVD) methods have been widely used to deposit hard coatings to improve the surface properties for engineering applications. Several methods have been used to reactively deposit the hard compounds of metal alloys e.g. TiN, TiCN and TiAlN. One method, Arc Bond Sputtering (ABS<sup>TM</sup>) has been shown to produce dense coatings having superior adhesion [1]. This process uses a steered arc discharge to generate metal ions e.g. titanium ions, to provide an etching pre-treatment of the substrates prior to coating by unbalanced magnetron sputtering. The process has been shown to generate a recrystallization zone extending down as far as 160 nm into the substrate and an approximately 20 nm thick interface layer consisting primarily of FeTi [2].

Another process has combined triode ion plating with in-situ plasma Ar and N nitriding to improve the wear characteristics of metal injection moulding dies [3]. This duplex process is particularly well suited to this application and has the advantage of producing  $\epsilon$  compound layers showing no increase in the carbon content of the diffusion zone. This diminishes any carbide embrittlement problems when nitriding steels with a high carbon content and improves the corrosion resistance of the coated steel [4]. A detailed description of the process has been reported by Bergmann *et al.*[3-5].

This work uses conversion electron  $^{57}\text{Fe}$  Mössbauer spectroscopy (CEMS) [6] to study the phase formations in the near surface region of mild steel substrates after various Ti etching pre-treatments using the steered arc discharge within the ABS<sup>TM</sup> process. Unlike sputter depth profiling, CEMS is a non-destructive technique and does not involve the risk of modifying the original phase composition close to the interface. The technique detects resonantly excited conversion electrons and provides an identification of different iron-containing chemical environments within an information depth up to 300 nm. For a comparison with the ABS<sup>TM</sup> Ti ion etched substrates, a sample has been Ar ion etched and coated with Ti using a Balzers BAI 640R coating unit. In both cases it has been necessary to improve the surface sensitivity of the CEMS technique by enriching the substrate with the Mössbauer isotope  $^{57}\text{Fe}$ .

## EXPERIMENTAL

The substrates of bright mild steel (BS:1983:080A15) were polished to  $R_a \approx 0.05 \mu\text{m}$ . The substrates were ultrasonically cleaned in both industrial methylated spirit and acetone prior to the deposition of an estimated 25 nm  $^{57}\text{Fe}$  layer by evaporation under vacuum at  $2 \times 10^{-7}$  torr.  $^{57}\text{Fe}$  enriched substrates were then annealed at 900 K for 90 minutes under argon in sealed fused silica ampoules, with polished titanium pieces acting as oxygen scavengers. A diffusion model [7] was used to predict the depth distribution of the  $^{57}\text{Fe}$  as a function of annealing parameters. The model was solved numerically by a standard iterative net method for a deposited 25 nm  $^{57}\text{Fe}$  layer. Verification of the thickness of the deposited  $^{57}\text{Fe}$  layer and the depth distribution of the  $^{57}\text{Fe}$  after annealing was provided by a VG microlab SIMS facility and has been reported elsewhere [8]. Diffusion of the  $^{57}\text{Fe}$  into the surface region was required for substrates that receive a typical 10 minute industrial Ti ion etch treatment. Without diffusion, the surface deposited  $^{57}\text{Fe}$  would be fully removed by the surface sputtering generated by the etch process. Samples, enriched in this way, were subjected to different ion

etch treatments at an Ar pressure of  $3 \times 10^{-3}$  mbar using a Hauzer HTC 1000-4 ABS<sup>TM</sup> coater. The first sample was Ti ion etched at a substrate bias voltage of 1200 V followed by the deposition of a thin Ti layer at a substrate bias voltage of 80 V. A second sample was Ti ion etched under the same conditions but without the deposition of the Ti layer. Three fold rotation was used throughout and the maximum temperature was 450 °C.

In further experiments, samples were used with an estimated 25 nm of <sup>57</sup>Fe deposited on the surface without any subsequent annealing. Samples were enriched in this way because for the shorter Ti ion etch processes that were used, <sup>57</sup>Fe removal is not as severe compared with longer etch processes. These samples were Ti ion etched at the same bias voltage of 1200 V at an Ar pressure of  $7 \times 10^{-4}$  mbar for different lengths of time, 25 s and 300 s, using 3-fold substrate rotation. Similarly prepared samples were Ti ion etched under different residual Ar pressures at a substrate bias voltage of 1200 V. These experiments were performed for 45 seconds with no substrate rotation, and in order to sustain the arc at the lower gas pressure it was necessary to have the target shutter only half open. In all the Ti ion etch treatment processes the maximum temperature was 450 °C.

For a comparison with the ABS<sup>TM</sup> process, a sample was treated using a BAI 640R Balzers coating unit [5]. Prior to treatment, the mild steel substrate was <sup>57</sup>Fe enriched in the manner described previously, except the deposited <sup>57</sup>Fe layer was estimated to be 40 nm and the annealing process was carried out for only 45 minutes. The predicted diffusion profile of the <sup>57</sup>Fe was felt to be appropriate for a typical Ar etch process preventing excessive removal of the Mössbauer isotope and hence maintaining surface sensitivity. The <sup>57</sup>Fe enriched sample was heated to 600 K for 60 minutes prior to Ar etching for 3 minutes at a substrate negative bias voltage of 200 V. This was followed by the deposition of a thin Ti layer at a negative

bias voltage of 100V for 40 s at an Ar pressure of  $1.2 \times 10^{-3}$  mbar. The emission current of the electron beam gun was held constant at 0.4 A and plasma enhancement was obtained using the high current plasma beam maintained at 80 A.

All of the treated samples were analysed by CEMS using a conventional constant acceleration mode Mössbauer spectrometer. The detection system comprised of a gas flow proportional counter using He/5% CH<sub>4</sub> [7]. The <sup>57</sup>CoRh Mössbauer source used was of 25 mCi initial activity. The Mössbauer spectra were fitted by a least squares Lorentzian fitting routine using a Silicon Graphics Indy workstation.

The most important feature of the Mössbauer effect [9] is that it allows the analysis of the hyperfine structure of nuclear transitions. This is achieved by exploiting the precise energy resolution provided by the Mössbauer effect for the <sup>57</sup>Fe system. The observed linewidths are comparable with or less than the interaction energies between the nuclei and the extra-nuclear electric and magnetic fields. These interactions between the nucleus and the surrounding environment are known as the hyperfine interactions. Three types of hyperfine interactions exist, the isomer shift (IS), the quadrupole splitting (QS) and the magnetic Zeeman splitting ( $H_{\text{eff}}$ ). Several review articles [10, 11] describe the hyperfine interactions in detail. Each measured hyperfine interaction provides information regarding the chemical and physical environment of the <sup>57</sup>Fe nucleus. The isomer shift relates to any change in the s-electron density at the nucleus which may arise from a change in valency and hence provides information regarding the chemical bonding of the <sup>57</sup>Fe atom. The quadrupole splitting provides information regarding the spin state and the atomic distribution geometry and the magnetic Zeeman splitting confirms the presence of any magnetic ordering within the compound under study. Thus CEMS using <sup>57</sup>Fe can observe chemical and magnetic

interactions of Fe atoms in the near surface or interfacial region, and hence can be used to study and Fe-Ti interactions that may occur in the Ti etch process.

## RESULTS AND DISCUSSION

The CEM spectrum obtained from an  $^{57}\text{Fe}$  enriched sample after a Ti ion etch followed by the deposition of a thin Ti layer by the ABS<sup>TM</sup> method is shown in Fig. 1(a) This shows an intense sextet pattern due to the magnetically ordered  $\alpha$ -Fe of the substrate material along with FeTi amorphous and crystalline phases. It can be seen that no oxides are present after a 10 minute industrial Ti ion etch pre-treatment process provided by the ABS<sup>TM</sup> method. A further CEM spectrum shown in Fig. 1(b) of the same sample was obtained at a lower velocity range in order to improve the resolution in the region of interest. The low intensity of each FeTi phase is due to the small quantity of phase formation. Further evidence of the crystalline phase can be seen from a typical XRD trace using Cu K $\alpha$  radiation shown in Fig. 2. The observed Mössbauer hyperfine parameters associated with these phases are given in Table 1. There is good agreement with the measurements of Chien and Liou [12] and the work of Stupel *et al.* [13]. In the case of the amorphous phase,  $\text{Fe}_x\text{Ti}_{1-x}$ , the Mössbauer hyperfine parameters depend greatly on the concentration  $x$ . This dependence has been investigated experimentally by Sumiyama *et al.* [14] and Liou *et al.* [15] for amorphous alloys prepared by rf sputtering using Fe and Ti targets simultaneously. Also the concentration dependence has been predicted in a range of amorphous alloys with varying  $x$  concentration by van der Kraan *et al.* [16]. From their prediction model and by using our measured isomer shift hyperfine parameter for the detected amorphous  $\text{Fe}_x\text{Ti}_{1-x}$  phase, the concentration  $x$  has been determined to be approximately  $x=0.3$ . This indicates a high level of titanium implantation into the near surface region and subsequent Fe-Ti interaction during the pre-treatment process.

The CEM spectra of the two samples Ti ion etched for different lengths of time are shown in Fig. 3(a) and 3(b). For the 25 s Ti ion etch the presence of magnetite,  $\text{Fe}_3\text{O}_4$  and a low level of Fe-Ti interaction is seen, Fig 3(a). By contrast the 300 s Ti ion etch shows the removal of the magnetite phase and a more significant formation of both amorphous and crystalline FeTi phases, Fig 3(b).

The CEM spectra showing the comparison of the Ti etch under differing residual gas pressures, Figs. 4(a) and (b), show the formation of iron carbonitride and low levels of magnetite ( $H_{\text{eff}} = 477$  and  $442$  kG for sites A and B). The formation of these phases is due to the sputtering of surface debris from the shutter, and redeposition on to the samples. It should be noted that in order to sustain the arc at the lower gas pressure it was necessary to have the target shutter covering half the target, to generate a defined positive electrode with respect to the cathodic target. This positioning of the shutter is not usual in the ABS<sup>TM</sup> process, but was necessary for just these two experiments. When observing CEM spectra it is usual to refer to the percent effect for each phase, as an indication of the amount of  $^{57}\text{Fe}$  present in the different phases. The percent effect for samples where the etch was carried out at a lower gas pressure is 41% compared with 50% for the etch at a higher gas pressure. This indicates that more  $^{57}\text{Fe}$  has been removed from the surface when a lower gas pressure is used, showing the greater effect of the Ti ion etch under these conditions.

The CEM spectrum obtained from an  $^{57}\text{Fe}$  enriched sample followed by the deposition of a thin Ti layer at a bias voltage of 100 V using the Balzers BAI 640R coating unit is shown in Fig. 5(a). This spectrum clearly shows an additional sextet pattern which could be attributed to the early growth stages of the compound layer  $\epsilon\text{-Fe}_{2.3}(\text{CN})$ . From the relative intensities of the Mössbauer resonance lines within the sextet, it follows that the iron carbonitride grows on

the substrate with a magnetisation parallel to the sample surface. Similar carbonitride have been observed by CEMS after the sputter deposition of Ti and TiN layers using a Balzers Sputron device by Hanzel *et al.* [17]. A further CEM spectrum shown in Fig. 5(b) of the same sample at a lower velocity range shows the formation of a small quantity of the amorphous phase  $\text{Fe}_x\text{Ti}_{1-x}$ . The quantity of the observed phase is less evident compared with the samples treated by the ABS<sup>TM</sup> method. However, it should be noted that a true quantitative comparison of  $\text{Fe}_x\text{Ti}_{1-x}$  formation between the two coating methods is difficult due to differences in the detected CEMS signal as a consequence of the nature of the produced conversion electrons in the sample under study. Most significantly the number of resonantly produced electrons by the Mössbauer effect depends on the remaining  $^{57}\text{Fe}$  enrichment level within the depth of interest and this remaining enrichment level will differ as a result of the severity of etching with either low energy Ar ions or higher energy multi-ionised Ti. This may cause observed differences in the magnitude of the relative phase components in the CEM spectrum. Also different contribution effects of the relative phase components may arise due to the deposited Ti layer generating detectable secondary electrons by a method described by Tricker *et al.* [18]. This is of particular importance since the thickness of the deposited Ti layer by each process may be different and hence will contribute differently to the relative phase components of the associated CEM spectra.

## SUMMARY

The technique of backscattered Conversion Electron Mössbauer Spectroscopy (CEMS) using enrichment of the substrate with the Mössbauer active isotope  $^{57}\text{Fe}$  has been shown to be a valuable tool to study the interaction of ions with a steel substrate. Surface enrichment, followed by appropriate annealing which diffuses the  $^{57}\text{Fe}$  atoms into the near surface region of the substrate, can enhance the interfacial sensitivity of the technique and allow the chemical

interaction between arriving ions and the iron lattice to be studied. In particular CEMS has been used to detect phases formed by specific metal ion etch processes produced by the ABS<sup>TM</sup> process. In a conventional 10 minute ion etch pre-treatment followed by a very short sputter deposition of Ti, clear evidence was found for the formation of an Fe-Ti crystalline phase and a titanium rich amorphous phase. The existence of the crystalline phase was confirmed by X-ray diffraction. Investigation of the surface region after very short ion etch times (<25s) revealed the presence of iron oxides ( $\text{Fe}_3\text{O}_4$ ) as a surface contaminant with some evidence of Fe-Ti interactions, while after 300s the oxide is fully removed and the Fe-Ti phases are well established. The dynamic nature of the deposition and resputtering that is occurring at the surface during the metal ion etch phase appears to result in a maximum level of formation of the Fe-Ti phases at a time approaching 300 s. Beyond this time, phase formation and resputtering appear to have reached an equilibrium.

An interesting observation was made when the effect of Ar partial pressure was investigated. In order to stabilise the arc, the shutters were partly covering the target and resulted in a high level of unwanted FeCN at the surface. Such unwanted phases are unlikely to assist in achieving good adhesion and would normally not be present in an ABS<sup>TM</sup> process. The study showed that at lower gas pressure, there is less scattering of the Ti ions and hence most effective etching.

For comparison, an alternate pre-treatment strategy was investigated with samples that had been pre-treated and coated in a Balzers process. Here, some evidence of an Fe-Ti amorphous phase was shown, but the significant phase development was the Fe-C,N, often identified as  $\epsilon\text{-Fe}_{2-3}(\text{CN})$  [3].

## REFERENCES

- [1] W. -D. Münz, J. F. M. Hauzer, D. Schulze and B. Buil, *Surf. Coat. Technol.* **49** (1991) 161.
- [2] G. Häkansson, L. Hultmann, J. -E. Sundgren, J. E. Greene and W. -D. Münz, *Surf. Coat. Technol.* **48** (1991) 51.
- [3] N. Dingremont, E. Bergmann and P. Collignon, *Surf. Coat. Technol.* **72** (1995) 157.
- [4] N. Dingremont, E. Bergmann, M. Hans and P. Collignon, *Surf. Coat. Technol.* **76/77** (1995) 218.
- [5] E. Bergmann, *Surf. Coat. Technol.* **57** (1993) 133.
- [6] J. A. Sawicki, *Mat. Sci Eng.* **69** (1985) 501.
- [7] J. S. Brooks and S. C. Thorpe, *Hyp. Int.* **47** (1989) 159.
- [8] J. L. Davidson, J. S. Brooks, S. D. Forder and W. -D. Münz, *Surf. Coat. Technol.* (1996) in the press.
- [9] R. L. Mössbauer, *Z. Physik* **151** (1958) 24.
- [10] N. N. Greenwood, T. C. Gibb, "Mössbauer Spectroscopy", Chapman Hall, London (1971).
- [11] H. Frauenfelder, "The Mössbauer Effect", W. A. Benjamin, New York (1962).
- [12] C. L. Chien and S. H. Liou, *Phys. Rev. B* **31**(12) (1985) 8238.
- [13] M. M. Stupel, M. Ron and B. Z. Weiss, *J. Appl. Phys.* **47** (1976) 6.
- [14] K. Sumiyama, H. Yasuda and Y. Nakamura, *J. Phys. Cond. Matt.* **2** (1990) 3595.
- [15] S. H. Liou and C. L. Chien *J. Appl. Phys.* **55**(6) (1984) 1820.
- [16] A. M. van der Kraan and K. H. J. Buschow, *Phys. Rev. B* **27**(5) (1983) 2693.
- [17] D. Hanzel, W. Meisel, D. Hanzel, P. Griesbach, B. Navinsek, P. Panjan and P. Gütlich, *J. Vac. Sci. Technol. A* **11**(6) (1993) 3034.
- [18] M. J. Tricker, L. A. Ash and T. E. Cranshaw, *Nucl. Instr. and Meth.* **143** (1977) 307.

## LIST OF FIGURES

- Fig. 1 CEM spectra of (a) 10 minute Ti ion etch at 1200 V bias followed by the deposition of a thin Ti layer at a bias voltage of 80V and (b) lower velocity range.
- Fig. 2 XRD trace of a 10 minute Ti ion etch at 1200 V bias.
- Fig. 3 Comparison of Ti ion etch for different times - (a) 25 s and (b) 300 s.
- Fig. 4 Comparison of Ti ion etch performed under different Ar gas pressures - (a)  $6 \times 10^{-5}$  and (b)  $3 \times 10^{-3}$  mbar.
- Fig. 5 CEM spectra of (a) 3 minute Ar ion etch followed by a 40 s deposition of Ti at a bias voltage of 100 V using the Balzers BAI 640R coating chamber and (b) lower velocity range.

Phase	IS (mm s <sup>-1</sup> )	QS (mm s <sup>-1</sup> )	H <sub>eff</sub> (kG)	Relative Spectral Area (%)
$\alpha$ -Fe	0.00	-	330.5	97.5
FeTi-crystalline (fig. 1)	-0.15	-	-	0.8
FeTi-amorphous (fig. 1)	-0.20	0.34	-	1.7
FeTi-crystalline <sup>a</sup>	-0.15	-	-	-
Fe <sub>x</sub> Ti <sub>1-x</sub> (0.3 ≤ x ≤ 0.8) <sup>b</sup>	-0.14 to -0.22	0.29 to 0.36	-	-

<sup>a</sup>From M. M. Stupel *et al.* [13].

<sup>b</sup>From S. H. Liou and C. L. Chien [15].

Table 1 Hyperfine parameters relative to  $\alpha$ -Fe of the phases present after a Ti ion etch at a substrate bias voltage of 1200 V followed by the deposition of a thin Ti layer using the ABS<sup>TM</sup> process.

